

**Nanostructured surfaces for sensing heavy metals and radionuclides in aqueous systems**

David James Robert Conroy

Submitted in accordance with the requirements for the degree of  
Doctor of Philosophy

Millner Biosensors and Biocatalysis laboratory

The University of Leeds  
Faculty of Biological Sciences  
School of Biomedical Sciences

October 2012

The candidate confirms that the work submitted is his/her own, except where work which has formed part of jointly authored publications has been included.

The contribution of the candidate and the other authors to this work has been explicitly indicated below. The candidate confirms that appropriate credit has been given within the thesis where reference has been made to the work of others.

‘This copy has been supplied on the understanding that it is copyright material and that no quotation from the thesis may be published without proper acknowledgement.

© 2012 The University of Leeds and David James Robert Conroy

## **Acknowledgements**

Jointly authored materials formed the book chapter ‘Novel targets and mechanistic studies on impedance interrogated affinity sensors’, acknowledged and included in section 8.1, co-authored by Paul A. Millner, Rebecca L Caygill, David J.R. Conroy, Muhammad A. Shahidan

Thanks to the EPSRC research council and the DIAMOND (Decommissioning, Immobilisation and Management of Nuclear Waste for Disposal) consortium for funding this project. Thanks to all the people who without this project wouldn't have been possible. This includes, but not limited to;

Thank you to Andrew Nelson and Rik Brydson whos guidance and supervision helped me through the BSc Nanotechnology as well as Rob, Alex and, Phil and our time together in the undergraduate days. A special thanks to Zachary Coldrick whose inspiration and guidance during the MSc Bionanotechnology started my interest in biosensors, which later led to me undertaking this PhD.

Alex, Henry, Morsaline and Emma for starting me off in the lab and being an inspiration to what you can get done with a little ingenuity when things don't go to plan. Ash, Bex and Mark were the early day colleagues who worked with me through the daily grind, made the laboratory what it is and kept each other going throughout our PhDs, before being joined by Jim, Nat, Jack and Asif in the later days.

A huge thank you goes to all the people who helped me beg, borrow and access equipment in a number of facilities across campus unofficially when the official channels failed. This includes Steve Maude, Thibaut Charpentier, Rik Brydson, Andrew Nelson, Simon Biggs, Olivier Cayre and Chris Hodges.

Thank you to both of my supervisors, Doug who always had the time to offer help and guidance, gave advice on any aspect of the project and offer critical analysis and teach me the professionalism of research, any who put me back on the rails towards the project goals when needed. Thanks to Paul whose guidance, character and support got me through these four years, who gave me the freedom to take the research in the direction I wanted, who was always there to pick my up and keep me going when things were down and ideas were reaching dead ends.

A special mention to all the people outside the PhD circle, who kept me sane and social through the four years of research. This includes the film soc guys; Mat, Adam, Jason and Tom with our weekly pub outings. Also, all the guys from Chinese class who again kept me motivated every Wednesday evenings with our pub or meal nights and kept me going when things were tough. A big thank you to Adrian, Fran, Andy and Geoff. Thank you to my parents and sister for supporting me along the way.

Without these eight years of friends, colleagues and networking the progress made wouldn't have been possible.

## Abstract

An interdisciplinary approach was used to engineer a range of nanostructured surfaces with specificities for a number of radioactive waste contaminants that are typical of low level legacy contamination at sites across the UK. Specifically, analytes  $^{238/234}\text{UO}_2^{2+}$ ,  $^{90}\text{Sr}^{2+}$  and  $^{137}\text{Cs}^+$ .

Because traditional mercury based electrochemical methods lacked the specificity to differentiate individual analytes from complex solutions, combining electrochemical impedance spectroscopy with receptor molecules of desired specificity was used to create sensors with specificity and sensitivity to these radionuclides and which could give responses in real time.

For  $\text{UO}_2^{2+}$ , combining the evolved uranyl sequestering ability of the surface layer protein (SLP) from the bacterial strain *Bacillus sphaericus* JG-A12 allowed sub nanomolar levels of uranyl to be monitored in real time using the capacitive component of impedance at low frequency, whilst being largely selective against contaminant divalent cations. Whilst this approach, based on two tethering mechanisms for the SLP, has potential for fabrication of bespoke biosensors for other metal analytes, because of the lack of available metal binding proteins with appropriate cation specificity, alternative synthetic hosts were investigated as receptors.

A number of macrocycles, including crown ethers and lariat ethers with specificity to either  $^{90}\text{Sr}^{2+}$  or  $^{137}\text{Cs}^+$  were obtained commercially and chemically modified, or chemically synthesised, to permit surface tethering to sensor electrodes. Combining these tethered synthetic hosts with real time cyclic voltammetry, electrochemical impedance and microgravimetric interrogation methods revealed some interesting interfacial phenomena and gave insight into host interactions with the electrode surface. However, this approach did not yield devices that could be used to empirically quantify binding  $^{90}\text{Sr}^{2+}$  or  $^{137}\text{Cs}^+$ .

Accordingly, an alternative approach of combining engineered surfaces that had high surface areas and metal ion specificity, with direct quantification of analyte by  $\beta$  or  $\gamma$  counting of the captured radionuclide was investigated using  $\beta$  counting for  $^{90}\text{Sr}^{2+}$  and  $\gamma$  counting for  $^{137}\text{Cs}^+$ .

This allowed differentiation and quantification of  $^{90}\text{Sr}^{2+}$  or  $^{137}\text{Cs}^+$  ions from their non-radioactive isotopes which exist naturally and abundantly in the environment. Functionalised silanes allowed metal chelator functionality to be deposited onto bulk silica surfaces,

polymeric nanofibres and silica nano – and micro- particles. Whilst the bulk surfaces and nanofibres were able to bind significant amounts of isotopes, at very low level analyte concentrations typical of contaminated ground water, reproducibility between batches was poor.

However, the functionalised nanoparticles performed well, binding significant amounts of radionuclide and exhibiting high saturation limits. They were also able to bind low levels of radionuclide in complex analyte solutions such as synthetic groundwater. Bifunctional chelators particles were also made which allowed simultaneous deposition of a solid scintillant. This allowed simultaneous binding and quantification of radioisotopes without the need of scintillation fluid for counting of  $\beta$ -particles from  $^{90}\text{Sr}^{2+}$ .

## **Rationale**

The need for long term ground water radionuclide monitoring is essential to determine the presence and spread of radioactive legacy waste that has escaped failed containment vessels into the environment. The existing process involves sending an engineer out to suspected contaminated sites, a bore hole being dug into the ground and ground water samples being pumped to the surface. These samples are then typically sent to an external laboratory for mass spectrometry elemental analysis to confirm or deny the presence of radionuclides. Because of legal and safety requirements regarding the vaporising and aerosol dispersion of radioactive materials, very few sites are able to perform the desired analysis even if the equipment is available. The process is labour intensive, costly, laborious and slow, having a turn around time of weeks to months. As a result the need for a rapid, low cost, continual method for detection of radionuclides is clearly desirable, the motivation for this research.

Because of funding from the DIAMOND consortium, the Sellafield site was used as a model of expected contaminants and groundwater composition. However, again because of legal and access restrictions with obtaining and transporting radioactive waste from such a site, the designed biosensors were tested in synthetic groundwater of elemental composition matching published Sellafield data. Because exact groundwater radionuclide concentrations are not made public, average radionuclide activities were compiled from extensive analysis of annual external groundwater analysis reports of the surrounding waters of Sellafield. Using this data, the bio- chemo- sensors, functionalised nanoparticles and nanofibres could be tested for a valid response in conditions a field deployed device would be expected to encounter.

## Contents

Acknowledgements.....	II
Abstract.....	IV
Rationale.....	VI
Contents.....	VII
List of Tables.....	XIV
List of Tables.....	XXIV
Abbreviations.....	XXVII
<b>1 : General Introduction.....</b>	<b>1</b>
1.1. Groundwater contamination.....	2
1.2. Ground water composition.....	3
1.3. Ground water contaminants.....	3
1.4. Current remediation technologies and the need for biosensing.....	6
1.5. Bioremediation.....	8
1.6. Biosensing Techniques.....	9
1.6.1. Optical biosensors.....	10
1.6.1.1. Surface Plasmon Resonance.....	10
1.6.1.2. Total internal reflection imaging ellipsometry (TIRIE).....	11
1.6.2. Electrochemical biosensors.....	11
1.6.2.1. Amperometric biosensors.....	11
1.6.2.2. Mediatorless amperometric sensors.....	12
1.6.2.3. Amperometric mediated biosensors.....	13
1.6.2.4. Common oxygen and water based reactions in electrochemical reactions.....	14
1.6.2.5. Amperometric direct electron transfer biosensors.....	15
1.6.3. Potentiometric biosensors.....	15
1.6.4. Impedance biosensors.....	16
1.6.4.1. Equivalent Circuits.....	18
1.6.4.2. Randles circuit.....	18
1.6.4.2.1. Interfacial potential and Helmholtz theory.....	19
1.6.4.2.2. Guoy-Chapman theory.....	20
1.6.4.2.3. Stern theory.....	21

1.6.4.2.4.	DLVO.....	21
1.6.4.2.5.	Electrical Double layers .....	21
1.6.4.2.6.	Colloidal Stability .....	21
1.6.4.2.7.	Thickness of the molecular double layer .....	22
1.6.4.2.8.	Solution resistance, IR drop and constant phase elements	24
1.6.4.2.9.	Polarisation resistance, $R_p$ .....	25
1.6.4.2.10.	Warburg impedance.....	25
1.6.4.3.	Nyquist plots.....	26
1.6.5.	Cyclic voltammetry .....	27
1.7.	Approaches to metal ion binding .....	29
1.7.1.	Biosensors and the application of electrochemistry .....	29
1.7.2.	Mercury based polarography .....	29
1.8.	Protein-metal binding and supra-molecular chemistry .....	33
1.9.	Protein-metal binding and biotechnology .....	36
1.9.1.	Metallohistins, metallothionein, phyto-chelatins and metallochaperones.....	36
1.9.2.	Metal binding proteins and homologous sequences .....	37
1.10.	Metal binding and peptide engineering .....	40
1.11.	Sensitivity and selectivity: biological vs chemical receptors .....	42
1.12.	Metal Chelation.....	43
1.12.1.	Introduction.....	43
1.12.2.	Conditions of Chelation .....	43
1.12.3.	Ligand donor atoms .....	43
1.12.4.	Ligand donor groups .....	43
1.12.5.	Colour in chelates .....	45
1.12.6.	Groups with affinity for metal ions.....	45
1.12.7.	Ligands with one acidic and one basic group .....	46
1.12.8.	Ligands with two acidic groups .....	47
1.12.9.	Multidentate ligands.....	48
1.12.10.	Complexones.....	49
1.12.11.	Properties of ethylenediaminetetraacetic acid .....	51
1.13.	Conclusions.....	53
<b>2</b>	<b>: S-layer protein based biosensors for uranyl ions.....</b>	<b>54</b>
2.	Chapter overview .....	55

2.1. Metal binding proteins for biosensing .....	56
2.1.1. Surface layer proteins .....	57
2.1.2. Metallo proteins and uranyl binding - <i>Bacillus sphaericus</i> S-layer JG-A12 .....	57
2.1.3. Bushmaster <i>Meta muta muta</i> metalloproteins.....	58
2.2. Analyte forms and uranyl speciation .....	60
2.3. Experimental .....	61
2.3.1. Reagents.....	61
2.3.2. Electrochemical Setup .....	61
2.4. SLP tethering Mechanisms .....	62
2.4.1. Biotin-Neutravidin mSAM layer .....	62
2.4.2. mSAM stability measurements at varying MHDA : biotin-caproyl-DPPE ratios .....	63
2.4.3. Bioconjugation using 4-ATP sulfo-SMCC layer .....	63
2.4.3.1. Blocking the SLP chelating sites .....	64
2.4.4. Bioconjugation using 4-MTP and isocyanate silane.....	65
2.5. Analytical methods .....	66
2.5.1. Atomic Force Microscopy .....	66
2.5.2. X-ray photoelectron spectroscopy .....	66
2.5.3. Scanning electron microscopy .....	67
2.5.4. Native gel PAGE and SDS PAGE of S-layer protein.....	67
2.5.5. S-layer protein sizing using size permeation gel chromatography .....	68
2.5.6. Electrochemical analysis.....	69
2.5.6.1. Deposition of 4-ATP SAM .....	69
2.5.6.2. Conductivity of deposited 4-ATP SAM .....	72
2.5.6.3. Biosensor response of 4-ATP SAM based uranyl biosensor .....	74
2.5.6.4. SLP biosensor fabricated on DropSens electrodechips .....	78
2.5.6.5. DropSens electrode cleaning.....	78
2.5.6.6. Stabilisation the DropSens reference electrode .....	80
2.5.7. Surface analysis of 4-ATP S-layer biosensor .....	83
2.5.8. Cyclic voltammetry of 4-ATP vs 4-MTP tethering method .....	86
2.5.9. Impedance analysis and Randle's fitting comparison of 4-ATP vs 4-MTP tethering method .....	88
2.5.10. Biosensor response and binding analysis – uranyl compounds, interfering analytes, non specific receptors and inhibition .....	90

2.5.10.1.	Kinetic binding analysis.....	94
2.5.11.	Blocking of SLP phosphates and carboxy groups .....	95
2.5.12.	Life Time trials .....	97
2.6.	Conclusion .....	99
<b>3</b>	<b>: Crown ethers – potential synthetic receptors for metal ions .....</b>	<b>101</b>
3.1	Chapter overview .....	102
3.2	Introduction to macrocycles.....	103
3.2.1	Therapeutics and analyte targeting .....	105
3.2.2	Hosts specific to the lanthanide series .....	105
3.2.3	$^{90}\text{Sr}^{2+}$ extraction in the nuclear industry.....	107
3.2.4	$^{90}\text{Sr}^{2+}$ strontium extraction procedures.....	108
3.2.5	$^{137}\text{Cs}^{+}$ extraction in the nuclear industry .....	110
3.2.6	Uranium extraction and the nuclear industry .....	111
3.2.7	Summary .....	112
3.3	Crown ethers and chemosensing.....	112
3.3.1	Amperometric crown ether chemosensors .....	112
3.3.2	Chromogenic crown ether chemosensors .....	114
3.3.3	Chiral crown ether chemosensors .....	115
3.3.4	Mass based crown ether chemosensors.....	116
3.3.5	Ionic liquids and chemosensors .....	117
3.4	Experimental .....	120
3.4.1	Experimental overview .....	120
3.4.2	Reagents .....	121
3.4.3	Crown ether chemistry - modification of crown ether side arms. 121	
3.4.4	Crown ether synthesis .....	124
3.5	Analytical methods .....	126
3.5.1	Electrochemical Impedance Spectroscopy .....	126
3.5.2	Quartz crystal microbalance .....	126
3.5.3	Nuclear magnetic resonance .....	126
3.5.4	Mass Spectroscopy.....	127
3.6	Electrode preparation .....	127
3.6.1	Electroactive surface area calculation from piranha cleaning using the Cottrell equation.....	127
3.6.2	Liquid metal electrodes.....	128

3.6.3	Ionic liquid preparation.....	130
3.6.4	SAMs on QCM electrodes for crown ether insertion .....	131
3.6.5	SAMs of DOPC on HgPt electrodes .....	132
3.7	Results.....	133
3.7.1	Crown ether synthesis .....	133
3.7.2	Direct tethering of crown ethers to electrodes via thiol bonding. ....	135
3.7.3	Optimisation of ionic liquid synthesis .....	135
3.7.4	Non aqueous electrochemistry to determine transport ability of crown ether seeded ionic liquid .....	137
3.7.5	Ionic liquid retention of DC18C6 $^{90}\text{Sr}^{2+}$ and $^{90}\text{Y}^{2+}$ .....	140
3.7.6	Mercury-platinum amalgam electrodes .....	142
3.7.7	Crown ether insertion into SAMs on HgPt electrodes.....	143
3.8	Conclusion .....	154
<b>4</b>	<b>: Functionalised nanoparticles for chelation of radionuclides.....</b>	<b>157</b>
4.1	Chapter overview .....	158
4.2	Functionalised nanoparticles.....	158
4.3	Functionalised silanes .....	159
4.4	Silanol condensation theory .....	160
4.5	Silica nanoparticles .....	161
4.6	Bifunctional silica particles.....	162
4.7	Nanoparticle dispersity .....	163
4.8	Long term stability of nanoparticles .....	164
4.9	Experimental.....	165
4.9.1	Experimental overview .....	165
4.9.2	Reagents.....	165
4.10	Analytical methods .....	166
4.10.1	Photon correlation spectroscopy of nanoparticles .....	166
4.10.2	Field emission gun tunnelling electron microscopy of silica particles.....	166
4.10.3	Fourier transform infrared spectroscopy.....	166
4.10.4	Accurate determination of nanoparticle chelation .....	167
4.10.5	Centrifuge assays for $^{90}\text{Sr}^{2+}$ and $^{137}\text{Cs}^+$ binding.....	168
4.10.6	Gamma radiation of $^{137}\text{Cs}^+$ .....	170
4.10.7	Beta counting of $^{90}\text{Sr}^{2+}$ .....	171
4.11	Methods.....	171

4.11.1	Direct nucleation of silica nanoparticles.....	171
4.11.2	Prehydrolysis nucleation of silica nanoparticles.....	172
4.11.3	Fabrication of mercapto-and sulphonate- silica particles ...	172
4.11.4	EDTA silica particles.....	173
4.11.5	Dye core particles. ....	173
4.11.6	Nanoparticle and scintillant seeded agarose gels.....	174
4.11.7	Commercial functionalised resins.....	175
4.12	Results and Discussion .....	176
4.12.1	Synthesis of silica particles.....	176
4.12.2	EDTA silane hydrolysis and condensation.....	182
4.12.3	Synthesis of functionalised nanoparticles using a two step prehydrolysed silane method .....	182
4.12.4	Effects of varying solution component on nanoparticle growth 183	
4.13	Particle characterisation .....	185
4.13.1	Sulphydryl quantification with Ellman's reagent.....	185
4.13.2	FEG TEM and EDX surface analysis of functionalised silica nanoparticles .....	187
4.13.3	Confirmation of nanoparticle functionalisation by FTIR ...	190
4.13.4	Nanoparticles seeded with scintillant and embedded in agarose gels	194
4.13.5	ATR-FTIR of bifunctional solid scintillant chelator particles	194
4.13.6	Radioisotope saturation binding of particles and scintillation counting.....	205
4.13.7	Particle stability .....	210
4.13.8	Bifunctional particles.....	210
4.13.9	Bifunctional particles and scintillation binding .....	213
4.14	Commercial resins binding of $^{90}\text{Sr}^{2+}$ and $^{137}\text{Cs}^+$ .....	214
4.14.1	Commercial resins and $^{137}\text{Cs}^+$ binding.....	217
4.14.2	Performance in synthetic groundwater with low level radionuclide contamination.....	218
4.15	Conclusion .....	220
<b>5</b>	<b>: High surface area nanofibres as affinity sorbents .....</b>	<b>222</b>
5.1	Chapter overview .....	223
5.2	Silane reaction methods .....	224
5.3	Experimental .....	228

5.3.1	Experimental overview .....	228
5.3.2	Reagents.....	228
5.4	Methodology .....	229
5.4.1	Surface preparation .....	229
5.4.2	Silane condensation for functional surface coatings.....	229
5.4.3	Nanofibre formation.....	230
5.5	Analytical methods .....	232
5.5.1	Nanofibre diameter sizing analysis via FEG-TEM microscopy..	232
5.5.2	Fourier transform infrared spectroscopy analysis of bulk surfaces	232
5.5.3	Focused ion beam analysis for silane deposition depth .....	232
5.5.4	Secondary Ion Mass Spectroscopy of bulk surfaces for functionalisation.....	233
5.6	Results and discussion .....	234
5.6.1	Secondary ion mass spectroscopy.....	234
5.6.2	Fourier transform infrared spectroscopy of surfaces .....	236
5.6.3	Thickness of deposited silane layers - FIB TEM analysis .....	240
5.6.4	Functionalised surfaces and bining of radionuclides .....	242
5.6.5	Fibre size visualisation and size change after silanisation .....	248
5.7	Functionalised nanofibres and radionuclide saturation binding .....	251
5.8	Commercial resins and binding of radionuclides from contaminated synthetic ground water.....	253
5.9	Conclusion .....	254
<b>6</b>	<b>: Conclusions, discussion and future work .....</b>	<b>255</b>
6.1	Project summary .....	256
6.2	Future work.....	257
<b>7</b>	<b>References .....</b>	<b>259</b>
<b>8</b>	<b>Appendix – Publications.....</b>	<b>278</b>
8.1	Young investigator of the year nomination .....	279
8.2	Sensors publication .....	283

## List of Tables

Figure 1-1- Sellafield site groundwater monitoring network. Highlighting the monitoring wells, the separation area and site perimeter.

Figure 1-2 - Summary of the membrane pumps in (A) *S. cerevisiae* and (B) *E. coli*. (A) Arsenic ArsAB pump functions similar to ABC transporters, with potential from amperometric sensors used to extrude Ar (III). The Acr3p pump extrusion system removes As(III) ions, the proton potential gradient for this process generated from Pma1p which generates ADP and extrudes H<sup>+</sup> ions. Metal enzymes that convert metal ions to alternate oxidation states can be detected by potentiometric based cyclic voltammetry, while binding and conformational changes observed by impedance. (B) Arsenate [As(V)] ions enter cells via phosphate transporters (Pit and Pst) and Pho84p in *E. coli*. This can activate a resistance protein via the (ars) operon. Transcription of arsR is induced by As(V) ions and resistance (ars) operon. ArsR, regulates the expression of the arsABC a membrane pump which pumps out s(III) ions. Before the levels are toxic to the bacteria. Glpf and Pslp are also thought to be involved in As(III) removal.

Figure 1-3 – Typical reaction mechanism of GOD amperometric biosensors for the detection of glucose by production of H<sub>2</sub>O<sub>2</sub> from the reduction of β-D-glucose to gluconolactone.

Figure 1-4- Equivalent circuit components. Frequency dependent impedance (A) can be modelled as a solution resistance and pseudo capacity (B) or a charge transfer resistance and a Warburg impedance component (C).

Figure 1-5- The equivalent Randles circuit.

Figure 1-6 - Double layer ion distribution absorbed at an interface moving towards bulk.

This consists of the inner ( $\sigma_i$ ) and outer ( $\sigma_d$ ) Helmholtz planes.

Figure 1-7 – Calculated Debye lengths for a monovalent 1 : 1 counterion buffer. The inset is a magnification of the length scale region that will be observed using a millimolar strength buffer.

Figure 1-8 - Nyquist plot showing equivalent circuit components. Regions of mass transfer and kinetic control are found at low and high frequencies respectively.

Figure 1-9 – Current observed for a linear potential sweep of Nernstian (reversible) reaction.

Figure 1-10 - Common geometries of molecules and their corresponding coordination number. The central atoms (pink) show the following coordination geometries and coordination numbers. Linear (2), trigonal planar (3), tetrahedral geometry (4), square planar (4), trigonal bipyramidal (5), square pyramidal (5) and octahedral (6).

Figure 1-11 - Examples of supra-molecular host guest recognition. Incorporation of tetrathiafulvalene (TTF) molecule into a variety of tested host systems.

Figure 1-12 - Conserved residue sequences between a number of metal binding proteins. Note conservation of residue sequences of lysine (K), aspartate (D), histidine (H) and cysteine (C).

Figure 1-13 - Three dimensional structure of the CadC binding peptide and the 2 alpha helical binding domains for Cd<sup>2+</sup>.

Figure 1-14 - Engineered alpha helical peptides and the exposed chelating sulphur binding site mechanisms between peptide arrays. Tetrahedral ions satisfy all sites while Cd<sup>2+</sup> ions

have been shown to bind 3 sites with the fourth satisfied by water hydrogen bonding in spite of the entropically less favourable conditions .

Figure 2-1 – Chapter two hierarchy outlining the methods used to create the uranyl biosensor.

Figure 2-2 - Proposed binding mechanism of uranyl to JG-A12 SLP. Binding occurs to carboxyl groups in a bidentate orientation, and also to phosphate groups in a monodentate fashion.

Figure 2-3 – The conserved sequences between a number of snake venom metalloproteins. 1, N-terminal region (metalloproteinase domain) of the high molecular weight haemorrhagic I-IRIB from *Trimeresurus flavoviridis* 2, low molecular weight haemorrhagic protein HR2a from *T. flavoviridis* ; 3, non-haemorrhagic metalloproteinase Hz from *T. flavoviridis* ; 4, haemorrhagic metalloproteinase toxin d from *Crotalus atrox* and 5, haemorrhagic factor LHFII from *Lachesis muta muta*.

Figure 2-4 – Uranyl speciation in aqueous systems as a function of pH. In standard ground water (pH5) uranium will be in the  $UO_2^{2+}$  state.

Figure 2-5 - mSAM incorporation of SLP by MHDA/biotin-caproyl-DPPE mSAM, deposited with a Neutravidin layer that binds to pre-biotinylated SLP.

Figure 2-6 - Porous membrane model with molecular linkers of 1.5 nm length binding SLP through a stable permeable membrane as maleimide groups covalently bind to thiols on protein cysteine residues.

Figure 2-7 - Schematic of the protocols used to modify proposed SLP analyte binding carboxylates and phosphates sites. (A), phosphate modification by carbodiimide reaction in the presence of amine. (B), modification of carboxylates with TRIS using carbodiimide mediated process.

Figure 2-8- Silane linker bioconjugation. A SAM of 4-mercaptothiophenon has a hydrolysed silane layer condensed onto the available hydroxyls leaving the isocyanate to form a covalent bond with free amines on the SLP.

Figure 2-9 – (A) SDS PAGE sizing of S-layer protein. Wells correspond to (1) molecular weight markers, (2) 1 mg/ml SLP, (3) 1mg/ml S-layer boiled (4) 1/5 dilution (5) 1/5 boiled (6) 1/10 dilution (7) 1/10 dilution boiled. (B) Size exclusion chromatography calibration galactosidase with sizes 66 kDa, 160 kDa, 280 kDa, and 466 kDa respectively. A Superdex 200 10 / 300 GL column was used (13  $\mu$ m particles resolution 10 - 6000 kDa) at a pump speed of 1.0 ml / min, max pressure 15 bar (217 psi, 1.5 MPa). 50  $\mu$ L protein samples were injected containing approximately 0.1 to 10  $\mu$ M protein and pumped through the porous matrix.

Figure 2-10 - Nyquist fitting to Randles circuit of 4-ATP monolayer assembling on gold with time. (A) Nyquist double semicircle plots of increasing incubation times. (B), a reminder of how the Randles circuit s are extrapolated.

Figure 2-11 – Comparison of glucose oxidase amperometric sensors; 4-ATP, 4-MTP isocyanate silane SAM sensor surfaces versus bulk absorbed PEI polymer used to tether GOx enzyme.

Figure 2-12 -Nyquist plot of impedance of s-layer conjugated electrode in increasing uranyl nitrate. 0 V applied vs AgAgCl, 10 mM PBS supporting electrolyte, 51 points calculated using an 0.01 V rms potential.

Figure 2-13 – (A) Real and (B) imaginary impedance components of impedance response with frequency of S-layer conjugated electrode in increasing uranyl nitrate concentrations (B) Imaginary impedance response under same conditions. 0V applied vs AgAgCl, 10 mM PBS supporting electrolyte, 51 points calculated 0.01 V rms.

Figure 2-14 – (A) Diagram of the general DropSens electrode (DRP-C223A) configuration. The DRP-C223A DropSens electrodes have a screen printed gold working electrode of 1.6 mm diameter, Ag/AgCl reference electrode and platinum counter.

Figure 2-15 – Cleaning effects on DropSens electrodes, 30 min in stated conditions before a 50 mv/s in 10 mM PBS containing 10 mM ferricyanide scan to observe redox response. Bare gold electrode no cleaning method, 2 min piranha, 1:1 methanol : acetone, 1% Decon 90, sonicated 1:1 methanol : acetone, chromic acid, sonicated chromic acid.

Figure 2-16 – (A) and (B), two independent batches of AgAgCl modified DRP-C223A electrodes showing and improvement in stability of the electrodes. Redox peak potentials on an uncleaned electrode in ferricyanide compared to those of each cleaning method.

Figure 2-17 – Microscopy analysis of bare gold and constructed 4-ATP JG-A12 biosensor. Left to right: 2D representation, 3D topographical view, surface roughness histogram. (A) AFM of bare gold electrode (2  $\mu\text{m}$  x 2  $\mu\text{m}$  area), (B) AFM of JG-A12 surface layer of biosensor (2  $\mu\text{m}$  x 2  $\mu\text{m}$  area). (C) SEM of biosensor surface.

Figure 2-18 – Cyclic voltammetry showing passivation of electrode surface with biosensor construction; (A), Bare gold, 4-ATP, sulfo-SMCC, JG-A12; (C), Bare gold, 4-MTP.isocyanate silane, JG-A12. (Triplicate scans with standard deviation, 10 mM FCC in 10 mM PBS, -0.4 to 0.6 V, 50 mV/s); B) and (D) Extrapolated potentials and currents for FCC redox reactions after each layer was deposited onto gold P3 electrodes.

Figure 2-19 -Triplicate averages were taken from Nyquist scans. (51 point calculated across a frequency range of 250 kHz to 0.1 Hz in a solution electrolyte of 10 mM PBS containing 10 mM ferricyanide). Electrochemical parameters extracted based on Randles equivalence.

Figure 2-20- Real time capacitance response to uranyl biosensor using JG-A12 surface layer protein host receptor. (A) Response of biosensor to different uranyl compound. The data show no differentiation between uranyl compounds as all are able to bind with the  $\text{UO}_2^{2+}$  in the +6 oxidation state. (B) Response of biosensor to a range of interfering divalent cations (nickel nitrate, caesium sulfate, cadmium nitrate, cobalt chloride, average uranyl response). Response is typically 10–30 % lower than response to uranyl ions.

Figure 2-21 – Kinetic binding models of uranyl to JG-A12 electrode; (C), modified SLP protein response to  $\text{UO}_2^{2+}$ ; (D), Effect of using non-specific proteins as the sensing agent. Biosensors were constructed and the response to  $\text{UO}_2^{2+}$  monitored (casein sensor response, BSA sensor response, BSA sensor response with carboxylates blocked, average uranyl response of SLP biosensor for comparison). The percentage decrease in  $-Z''$  was calculated as previously. Sequential analyte injections were performed over a six hour period.

Figure 2-22 - A weak pair of peaks at 365 and 373 eV were observed and identified as Ag 3d3/2 and Ag 3d5/2 peaks. Detailed scans of the C 1s, the Au 4f were taken, baselines were fitted and the peak's areas compared to give relative atomic percentages, summarised in Table 2-4.

Figure 2-23 - Figure of chrono impedance at 1 Hz, response to increasing uranyl nitrate aliquots. (A) A newly made electrode, exhibiting minimal noise. (B) 1 week old electrode

stored in 10 mM PBS has reduced sensitivity and a significantly increased noise ratio due to salt crystal formation and possible reduced protein activity.

Figure 3-1 - Chapter three hierarchy outlining the methods used to use synthetic macrocycle hosts as potential components for chemosensors. Figure 3-2 – Examples of the three broad macrocycle categories; crown ether, lariat ether cryptand / podand.

Figure 3-3 - Figure of bifunctional chelators (A) DOTA and (B) a derivative of DTPA, a linear octadentate polyaminocarboxylates that has been most studied to date.

Figure 3-4 - Bifunctional chelators, Serum albumin targeting vectors, enzyme and protein targeting.

Figure 3-5 – Lariat crown ethers (A) dicyclohexano-18-crown-6 lariat ether, (B) DtBuCH18C6 used in the  $^{90}\text{Sr}^{2+}$  SREX process.

Figure 3-6 – Cryptand calix[4]arene-bis(crown-6), an excellent chelator for both strontium and caesium with a preference to the latter, is unusually water soluble and able to hold two ions simultaneously stabilised by the phenol core and the upper and lower rings.

Figure 3-7 – Examples of lariat crown ether discussed. (A) Dibenzo-21-crown-7 and cryptands and (B) calix[4]-bis-2,3-naphtho-crown-6 have high specificity for  $\text{Cs}^+$  extraction.

Figure 3-8 - Methods of tethering crown ethers to electrodes. (A) synthesis from monomers containing a functionalised spacer allowing orientated covalently linkage to a gold substrate, or (B) post synthesis modification of the crown ether such as adding a hydrophobic tail.

Figure 3-9 – Ionisable chromoionophores allow pH dependent switching between the bound 'off' state and the unbound 'on state' of the inner crown ether core.

Figure 3-10 - Example of (A) a chromogenic steroidal crown compound, modified to have (B) a cholesterol tail attached. Upon addition of an alkali metal or ammonium cations the helical pitch of the formed liquid crystals changed resulting in a change in maximum absorbance wavelength shown in (C). A range of amine analyte compounds tested showed large  $\lambda\text{R}$  differences between D- and L-isomers is observed for ammonium ions having bulky substituent's (such as phenyl and indolyl).

Figure 3-11 – Schematic of  $^{90}\text{Sr}^{2+}$  extraction using ionic liquids at an electrode interface. Ions in the aqueous phase are immiscible to the ionic liquid, similarly the hydrophobic crown ethers are immiscible to the aqueous phase. As a result selective ion transport only occurs across the interface as the host has specificity to the analyte.

Figure 3-12 – Side arm modification of aza-18-crown-6 with hydrophobic cholesterol moiety. This allows the host to be inserted into SAMs via intercalation.

Figure 3-13 - 2-Iminothiolane modification of aza-18-crown-6 for direct conjugation to a gold substrate via the available thiol group.

Figure 3-14 - Modified of 4-Carboxybenzo-18-crown-6 to linker 4-ATP for chemisorptions onto a gold substrate.

Figure 3-15 – Strontium resorcinol calixarene binder 2,c-8,c-14,c-20-tetraundecyl-4,6,10,12,16,18,22,24-octahydroxyresorc[4]arene, trivial name resorcinol calixarene. The tails are perpendicular to the central cavity.

Figure 3-16 – Caesium binder pentacyclo [19.3.1.13,7.19,13.115,19] octacosal(25), 3,5,7 (28),9,11,13 (27),15,17,19(26),21,23-dodecaene-4,6,10,12,16,18,22,24-octol, trivial name calix[4]resorcinarene.

Figure 3-17 – Schematic of the P10 electrode exhibiting radial diffusion from an array of micro spots.

Figure 3-18 - Ionic liquid composed of tributylmethylammonium chloride ( $\text{Bu}_3\text{MeN}^+\text{Cl}^-$ ) and N-lithiotrifluoromethanesulfonimide ( $\text{Li}^+\text{Tf}_2\text{N}^-$ ).

Figure 3-19 - 16-mercaptohexadecanoic acid used as the component of SAMs on gold for QCM interrogation and crown ether insertion.

Figure 3-20 – Polar lipid DOPC used as a hydrophobic insertion layer on mercury coated platinum for crown ethers.

Figure 3-21 – NMR spectra of (A) successful linkage of 4-carboxybenzo 18-crown-6 to 2-MEA, and (B – F) component molecules.

Figure 3-22 - NMR spectra of successful cholesterol aza-18-crown-6 synthesis. (A), Cholesterol aza-18C6; (B), triethylamine; (C), cholesterol chloroformate; (D), aza-18C6. Samples analysed in Chloroform-d, 99.8% (Isotopic) containing 0.03 % v/v TMS, in 300 MHz tubes.

Figure 3-23 – Mass spec confirmation of cholesterol tethered aza-18-crown-6 synthesis at a Mw to charge ratio of 676.

Figure 3-24 - Oxidation of ferrocenium in acetonitrile to ferrocene around 0.2 V, the base signal used to test Hg-Pt electrodes with fabricated pseudo AgAgCl reference electrode. Performed using 10 mM ferrocenium in acetonitrile solution at a scan rate of 50 mV/s.

Figure 3-25 – Scintillation counting of DC18C6 IL coated HgPt electrodes that have chelated  $^{90}\text{Sr}^{2+}$  and  $^{90}\text{Y}^{2+}$  ions. Twelve samples under identical conditions but at the energy spectra interrogated to determine the amounts of each isotope bound simultaneously. Green bars are scintillation counting after 24 h, red bars the same samples counted after 48 h.

Figure 3-26 - (A) A schematic of the platinum and gold P4 electrodes used. (B) A platinum electrode under a held potential in mercuric nitrate solution undergoes amalgam plating. Deposition is monitored as the flow of charge with time. (C) Successful P4 Hg electroplating on platinum (left) and (D) microscopically on a P10 microscopic array electrode.

Figure 3-27 - Successful DOPC deposition on to HgPt electrodes. Rapid real time cyclic voltammetry shows peaks corresponding to SAM poration, reorientation, desorption and resorption. The upper peaks correspond to a solution DOPC diffusing and desorbing from the electrode surface.

Figure 3-28 - Real-time cyclic voltammetry of 4-carboxy-benzo18-crown-6 interaction with DOPC SAM on a Hg-Pt electrode

Figure 3-29 - Real time rapid CV of DOPC SAM recovery with time from increasing concentrations of crown ether. At low concentrations peak recovery shows host elution, while at high concentrations permanent displacement and reorientation of the SAM occur. Arrows indicate the directional shift of the peaks with time. Resorption peaks show a negative shift, decrease and then broadening and recovery at low concentrations suggesting crown ether layer formation in lipid.

Figure 3-30 Effect of crown ether insertion on the DOPC characteristic -0.94 V lipid reorientation and -1.0 V phase transformation peaks. (A) and (B) show the -0.94 reorientation peak (C) and (D) the -1.0V phase transition. (A) and (C) show the lateral deviation in potentials of the observed phenomena while (B) and (D) show changes in peak height.

Figure 3-31 – QCM measurements were made on Maxtek 1 inch AT cut crystals coated with a gold electrode. Fundamental frequency was around 6 MHz and  $\Delta f$  was converted to  $\Delta m_{\text{mass}}$  using Maxtek software. The following additions were made (A), 3 mg / ml free cholesterol; (B), cholesterol aza-18-crown-6 (10 mg/ml in EtOH); (C), attempted cholesterol aza-18-crown-6 insertion (10 mg/ml in EtOH in 10 % (v/v) chloroform) which resulted in stripping of the MHDA base SAM.

Figure 3-32 - Insertion of resorcalix[4]arene into a MHDA SAM. Figure numerals indicate solutions flowed over the surface; (i) dH<sub>2</sub>O; (ii), ethanol; (iii), 10 mg resorc[4]alixarene in 10:1 (v/v) ethanol : acetone; (iv), ethanol; (v), dH<sub>2</sub>O; (vi), 1 mM Sr(NO<sub>3</sub>)<sub>2</sub>; (vii), dH<sub>2</sub>O; (viii), 1 mM EDTA; (ix), 1 mM Sr(NO<sub>3</sub>)<sub>2</sub>; (x), dH<sub>2</sub>O; (xi), 1 mM EDTA; (xii), dH<sub>2</sub>O.

Figure 4-1 - Chapter four hierarchy outlining the methods used to create chelator particles with a high specificity particularly to <sup>90</sup>Sr<sup>2+</sup> with greater binding capacity than a number of commercial resins and functionalised nanofibres.

Figure 4-2 - The basic schematic of a bioconjugatable, hydrolysable silane used to nucleate the silica particles. The most common unfunctionalised forms are TEOS (tetraethyl orthosilicate) or TMOS (tetramethyl orthosilicate).

Figure 4-3 - APTS condensation onto hydroxyl surface via silanol bond formation. This method allows large surface areas to be coated on hydroxyl coated surfaces (glass, silica, metal oxides etc) with a wide range of functionalities.

Figure 4-4 - Increasing ratios of oils (dinonyl : dibutyl) with a sample dye added. (A) before centrifugation, (B) after 1 min 13,000 RPM.

Figure 4-5 – (A) Theoretical and (B) experimentally observed emission peaks as <sup>137</sup>Cs<sup>+</sup> decays either to <sup>137</sup>mBa, then <sup>137</sup>Ba emitting a  $\gamma$  emission, or directly to <sup>137</sup>Ba via  $\beta$  emission. The 30 keV emission was used to identify <sup>137</sup>Cs<sup>+</sup> decay.

Figure 4-6 – Theoretical decay emission routes for <sup>90</sup>Sr<sup>2+</sup> via a high energy beta emission decaying to <sup>90</sup>Y, then a further high energy beta emission, or a further low energy beta and gamma emission to the stable form <sup>90</sup>Zr.

Figure 4-7 - Summary of the functional groups on modified silica particles. Basic hydroxyl groups (A) were modified to (B) alkyne, (C) isocyanate, (D) methacrylate, (E) ferrocene, (F) mercapto, (G) sulfonate, (H) carboxylic acid, (I) amine or (J) EDTA functionality.

Figure 4-8 - Silica nanoparticle nucleation as a function of parameter. The reaction solution contained 5 % (v/v) TEMOS, 100  $\mu$ l APTS, 3 % (v/v) H<sub>2</sub>O in ethanol. (A) Improved narrower size distribution of amino nanoparticle growth using a controlled temperature Huber water bath at 20 °C  $\pm$  0.5 °C. (n = 3). (B) Dependence of silica nucleation on dispersion solvent (2 independent batches, n = 3 in each) (C) Effects on stability of nanoparticle from purification and solvent redispersion (n = 3).

Figure 4-9 - Image of mercapto silica nanoparticles, 20 h nucleation of TEOS at room temperature on a Stuart gyro-shaker, speed 8, as a function of pH.

Figure 4-10 - Image of EDTA silica particles nucleated at different pH. Particles were grown for a 20 h nucleation of TEOS at room temperature on a Stuart gyro-shaker speed 8.

Figure 4-11 – Nanoparticle growth at RT as a function of solution components. Components varied were (A), ammonia; (B), water; and (C), amino silane varied as a % (v/v) ratio of the total volume. (D) shows as overlay comparison of the 3 variables. Constant parameters used were 5 % (v/v) ammonia, 5 % (v/v) water or 2 % (v/v) silane. (n = 3  $\pm$  S.D).

Figure 4-12 - Calibration curve for thiol quantification on mercapto silica particles using Ellman's reagent. Thiols cleave the DNTB disulfide bond to give 2-nitro-5-thiobenzoate(NTB-), which ionizes to the NTB<sup>2-</sup>-dianion, a yellow product that adsorbs at 412 nm in a 1:1 stoichiometry reaction.

Figure 4-13 - Figure of bare TEOS silica particles. (A) Photon correlation spectroscopy sizing (n = 5), average size = 127.3 nm, S.E.M = 0.171 (B) EDX elemental analysis shows silicon, oxygen and copper (C) and (D) TEM images of dried particles on a carbon substrate. Figure 4-14 - Figure of EDTA functionalised particles, prehydrolysis method, 4 h RT nucleation.

Figure 4-15 - FTIR spectra of functionalised nanoparticles dispersed in a KBr matrix. Particle functionalities were; (A), carboxylic acid; (B), EDTA, condensed onto TEOS particles.

Figure 4-16 - FTIR spectra of functionalised nanoparticles dispersed in a KBr matrix. (A) mercapto and (B) amine groups condensed onto tetraethyl orthosilicate particles.

Figure 4-17 - Schematic of solid scintillant EDTA/phenyl functionalised chelator particles. Upon the EDTA arms chelating a <sup>90</sup>S<sup>2+</sup> ion, an emitted β particle excites phenyl groups in close proximity which emit a photon of light during de-excitation that allow scintillation counting without traditional scintillation cocktails.

Figure 4-18 - ATR-FTIR transmission spectra of functionalised particles. Lines correspond to TEOS unfunctionalised particles, TEOS particles with solid scintillant trimethoxyphenylsilane. Inset a schematic of particle structure shown in Figure 4-17.

Figure 4-19 - ATR-FTIR transmission spectra of functionalised particles. Lines correspond to: TEOS unfunctionalised particles, TEOS particles with trimethoxyphenylsilane and a chelator functionality, TEOS particles with EDTA functional group only. Inset a schematic of particle structure shown in Figure 4-17.

Figure 4-20 - ATR-FTIR transmission spectra of functionalised particles. Lines correspond to: TEOS unfunctionalised particles, TEOS particles with trimethoxyphenylsilane and a chelator functionality, TEOS particles with functional sulfonic acid group only. Inset a schematic of particle structure shown in Figure 4-17.

Figure 4-21 - ATR-FTIR transmission spectra of functionalised particles. Lines correspond to: TEOS unfunctionalised particles, TEOS particles with trimethoxyphenylsilane and a chelator functionality, TEOS particles with functional thiol group only. Inset a schematic of particle structure shown in Figure 4-17.

Figure 4-22 - ATR-FTIR transmission spectra of functionalised particles. Lines correspond to: TEOS unfunctionalised particles, TEOS particles with trimethoxyphenylsilane and a chelator functionality, TEOS particles with functional amine group only. Inset a schematic of particle structure shown in Figure 4-17.

Figure 4-23 - ATR-FTIR transmission spectra of functionalised particles. Lines correspond to: TEOS unfunctionalised particles, TEOS particles with trimethoxyphenylsilane and a chelator functionality, TEOS particles with functional alkyne group only. Inset a schematic of particle structure shown in Figure 4-17.

Figure 4-24 - ATR-FTIR transmission spectra of functionalised particles. Lines correspond to: TEOS unfunctionalised particles, TEOS particles with trimethoxyphenylsilane and a

chelator functionality, TEOS particles with functional isocyanate group only. Inset a schematic of particle structure shown in Figure 4-17.

Figure 4-25 – Functionalised chelator nanoparticles and sequestering ability for aqueous  $^{90}\text{Sr}^{2+}$ . (A) Ratios of isotope remaining in the upper tube segment unbound (red) and isotope chelated by the nanoparticles (green) to show reproducibility between samples. (B) Relative CMP and mass of  $^{90}\text{Sr}^{2+}$  bound as a function of pH; green, pH 11; blue, pH 7; red, pH 2; black, pH 1. (C) Total bound  $^{90}\text{Sr}^{2+}$  as a function of pH; black, pH 1; red, pH 2; blue, pH 7; green, pH 11.

Figure 4-26 - Functionalised chelator nanoparticles and sequestering ability to aqueous  $^{137}\text{Cs}^+$  ions. Bars correspond to pH used; black, pH 1; red, pH 2; blue, pH 7; green, pH 11.

Figure 4-27 - Co-condensation of two functional silanes onto precursor silica core particles (4h growth, 24 h condensation). (A) Particle size distribution as a function of functional monomer varied. Amounts of phenyl silane and functional monomer added, in ml, were; 0  $\mu\text{l}$ :100  $\mu\text{l}$  (no phenyl silane, functional monomer only); black, 20  $\mu\text{l}$ :80  $\mu\text{l}$ ; red, 40  $\mu\text{l}$ :60  $\mu\text{l}$ ; blue, 60  $\mu\text{l}$ :40  $\mu\text{l}$ ; green, 80  $\mu\text{l}$ :20  $\mu\text{l}$ ; purple 100  $\mu\text{l}$ :0  $\mu\text{l}$  (phenyl silane only, no functional monomer). (B) Particle size distribution as a function of the two functional silane volumes used. Bars correspond to functionalised silane used; black, EDTA; red, amine; blue, isocyanate; alkyne, green; purple, mercapto silane. 400 sizing scans were obtained from the 5 silanes combined with 6 ratios of silanes, (n = 10 per average).

Figure 4-28 -Bifunctional scintillant chelator particles. Particles comprising of phenyl functionalised silica, and a chelators group (EDTA, amine, isocyanate, alkyne, mercapto or sulfonate) were tested under saturation conditions with  $^{90}\text{Sr}^{2+}$  solutions and counted without traditional scintillation cocktail.

Figure 4-29 - Radioisotope saturation binding experiments of  $^{90}\text{Sr}^{2+}$  using a range of weak and strong cation resins. After 1 h with shaking, the resin was recovered by centrifugation, and added to 5 ml of scintillation fluid. In each case, the left bar shows data from medium at pH 7 whilst the right hand media was at pH 1.

Figure 4-30 – Saturation binding ability of six commercial resins to high concentrations of  $^{137}\text{Cs}^+$  ions. Mass of ions extrapolated from calibrated radioisotope stock shown on the right axis.

Figure 4-31 – Chelating ability of functionalised silica particles. (A), phenyl scintillant particles; (B), chelator only particles without scintillant; (C), commercial resins. A known mass of particles or resin was incubated in 50  $\mu\text{L}$  of synthetic groundwater. Levels of  $^{90}\text{Sr}^{2+}$  and  $^{137}\text{Cs}^+$  were chosen on the basis of typical activities around Sellafield. Black bars correspond to samples counted with Emulsi Safe scintillation cocktail, red bars without.

Figure 5-1 - Chapter four hierarchy, outlining the methods used to deposit chelator groups using functional silanes onto a range of surfaces including electrospun nanofibres for high surface area sorbents.

Figure 5-2 – Examples of hydrolysable functionalised silanes; (A), 3-aminopropyltriethoxysilane (APTES) and (B), 3-aminopropyltrimethoxysilane (APTMS).

Figure 5-3 - The bare (—) and effective charge densities (----) of a planar glass substrate according to Hiemstra et al [212]. (A), solid surfaces used; (B), a 1  $\mu\text{m}$  silica sphere, assuming a density 8 nm<sup>-2</sup> of chargeable sites, a pK value of 7.5 for the silanol dissociation, and a Stern capacity of 2.9 F/m<sup>2</sup> [216].

Figure 5-4 - EDTA affinity surface preparation from two dimensional silane condensation growth on planar hydroxyl coated surfaces.

Figure 5-5 - Secondary ion mass spectroscopy analysis of functionalised surfaces. (A), positive and (B) negative scans of an aluminium base layer with generated hydroxyl base layer. An aluminium substrate was then modified with the desired functional silane including (C) carboxylate and sulfonate.

Figure 5-6 - Bare aluminium surface. (A), microscope image of aluminium surface, 1 min piranha treated hydroxyl layer. (B), triplicate FT-IR transmission mode scans of three different areas per sample. The sample was prepared by abrasion with 200  $\mu\text{m}$  diamond powder before a 1 min piranha wash to create a surface hydroxyl coating.

Figure 5-7 - Carboxysilane on aluminium substrate. Surfaces were prepared at pH 5.5, 4 h RT deposition of 5 % (v/v) silane, 2 % (v/v) water in ethanol. (A), microscope image of aluminium surface, 1 min piranha treated hydroxyl layer. (B), triplicate FT-IR transmission mode scans of three different areas per sample.

Figure 5-8 - EDTA silane on aluminium. (A), microscope image of aluminium surface imaged. (B), triplicate FT-IR transmission mode scans of three different areas per sample. Sample prepared as 5 % (v/v) EDTA-silane reacted in 2 % (v/v) dH<sub>2</sub>O in ethanol as a 4 h surface condensation reaction to AlOH surface layer.

Figure 5-9 - Carboxysilane condensed on aluminium. (A), microscope image of aluminium surface. (B), triplicate FT-IR transmission mode scans of three different areas per sample. Samples were prepared as 5 % (v/v) carboxysilane reacted in 2 % (v/v) dH<sub>2</sub>O in ethanol for 4 h. A EDAC/sulfo-NHS reaction to bond amino acid taurine was performed to form a sulfonic acid coated surface.

Figure 5-10 - FIB etching and cross section analysis of EDTA silane layer deposited onto silicon dioxide substrate. (A), surface overview; (B), trench etched into the sample with Pt resist layer; (C), magnification of the Pt-organic-silica interface and sizing of organic silane layer.

Figure 5-11 - Functionalised EDTA glass capillaries and saturation binding quantities of <sup>90</sup>Sr<sup>2+</sup> under analyte flow as a function of pH. Samples were background corrected and compared to an unfunctionalised capillary. •, scintillation fluid only control, •, unfunctionalised glass capillary control. Other bars are identically prepared EDTA functionalised capillaries (EDTA 1 - 5) are shown to illustrate inter batch variation.

Figure 5-12 - Functionalised mercapto and sulfonate glass capillaries showing saturation binding of <sup>90</sup>Sr<sup>2+</sup> under analyte flow at pH 7. Samples triplicates versus an unfunctionalised glass capillary to account for nonspecific binding are shown.

Figure 5-13 - Functionalised glass capillaries and saturation binding with <sup>137</sup>Cs<sup>+</sup> under analyte flow pH 7. Sample triplicates (functionalised capillary 1-3) with the average with SD to illustrate batch variation are shown.

Figure 5-14 - Saturation binding and reusability of EDTA coated capillaries. Five identical samples (EDTA 1 - 5) were used in repeated binding and debinding experiments. Green bars show <sup>90</sup>Sr<sup>2+</sup> binding. Red bars show the amount remaining after a low pH acidic wash to reprotonate chelator sites. Percentages show the percent removal of <sup>90</sup>Sr<sup>2+</sup> ions after each wash. (A), the initial binding saturation of <sup>90</sup>Sr<sup>2+</sup> ions; (B), the second saturation amount of <sup>90</sup>Sr<sup>2+</sup> ions, of reused samples under identical conditions.

Figure 5-15 - Five identical EDTA capillaries under repeated saturation and washing. Bars correspond to; initial incubation with  $^{90}\text{Sr}^{2+}$ ; after a 10 min pH1 10 mM PBS wash; second initial incubation with  $^{90}\text{Sr}^{2+}$ , a 20 mins pH 1 wash (no competing salt); a 10 min 0.1 M HCl wash with 0.1 M NaCl and a third initial incubation with  $^{90}\text{Sr}^{2+}$ .

Figure 5-16 - FEG SEM images of FT 4 nanofibres. Left to right shows increasing magnification of fibres (1 k, 10 k and 100 k). Fibres used were (A), bare fibres; (B), as (A) with isocyanate modification; (C), as (B) with 4 % (v/v) EDTA silane; (D), as (B) with 40 % (v/v) EDTA silane.

Figure 5-17 - Change in fibre diameter as a function of chemical modification. Diameters were averaged from a minimum of  $n=5$  sampling at a 10,000 magnification. Fibre diameter sizing averages based on SEM analysis. (A), fibre diameter averages as a function of fibre modification. (B), diameter comparison of all fibre types as a function of silane modification.

Figure 5-18 - Binding of  $^{90}\text{Sr}^{2+}$  and  $^{137}\text{Cs}^+$  ions by functionalised nanofibres. 2.5 cm square panels of fibres were incubated in synthetic ground water spiked with  $^{90}\text{Sr}^{2+}$  and  $^{137}\text{Cs}^+$  ions to give a total activity of 10 kBq. Samples were incubated for 1 h.  $n=5$  per sample. Black bars show binding of unfunctionalised bare fibres in comparison to 5 identical functionalised samples. (A), binding of  $^{137}\text{Cs}^+$  ions; (B), binding of  $^{90}\text{Sr}^{2+}$  ions; (C), relative amounts of  $^{90}\text{Sr}^{2+}$  (red bars) and  $^{137}\text{Cs}^+$  (green bars) bound.

Figure 5-19 - Beta counting response of commercial resins incubated in Sellafield low level radioisotope contaminated synthetic ground water ( $n=3$  per resin). 50  $\mu\text{l}$  of resin was incubated with 50  $\mu\text{l}$  of spiked SGW which contained  $1\text{ kBq L}^{-1}$   $^{90}\text{Sr}^{2+}$  and  $0.1\text{ kBq L}^{-1}$   $^{137}\text{Cs}^+$  ions.

## List of Tables

Table 1-1 – Radionuclide contamination levels compiled using annual analysis reports to model accurate synthetic groundwater systems for appropriate testing of sensor and chelator surfaces.	5
Table 1-2 - Table of common natural amperometric redox probes and potentials reactions occur.	13
Table 1-3 – Oxygen and hydrogen based redox reactions that can contribute to electrochemical current in aqueous systems.	14
Table 1-4 - The lowest detection limits for a range of electro-analytical techniques [59].	33
Table 1-5 - Table of important ligand electron donor groups available in metal chelation.	44
Table 1-6 – A selection of bidentate and monodentate chelators.	47
Table 1-7 – Decreasing stability of chelation complexes for diacidic chelators	48
Table 1-8 - Table of multidentate amine ligands of increasing stability due to the ‘wrap around’ sterics mobility possible from a longer carbon back bone. Carboxylic variations reduce competitive protonation problem of polyamine chelates.	49
Table 1-9 – Complexone chelators based on onimidodiacetic acid.	50
Table 1-10 – Table of formation and stability of aqueous EDTA complexes	52
Table 2-1 – Summary of redox potential deviation and drift of DropSens electrodes from screen printed reference electrode problems. Shown in Figure 2-16 C.	82
Table 2-2 – Summary of extrapolated redox current potentials from Figure 2-21.	88
Table 2-3 – Fitted binding kinetic parameters of SLP biosensor in response of uranyl. Two models were used, one site total and non-specific and two site total and non-specific.	94
Table 2-4 - Gold and carbon XPS spectrum of electrodes that were either bare, coated with a functioning biosensor or a chemically blocked biosensor.	96
Table 3-1 - Comparison of a number of crown ethers with the ionic diameter of various metal cations [108].	104
Table 3-2 – A summary of ionic liquid salts used for electrochemical biosensors [161].	118

Table 3-3 Determination of the inter batch amount of ionic liquid produced. Weighing after each solvent evaporation and washing step allows the amounts of liquid removed, precipitate extracted and final volume of ionic liquid to be determined.	136
Table 3-4 – Collated standard redox potentials of a range of analytes expected in contaminated ground water (aqueous systems vs standard hydrogen electrode, +0.197 for Ag/AgCl/Sat. KCl) [45, 46, 171].	138
Table 3-5 – Summary table of macrocycle molecules and subsequent successful modifications used in this chapter.	155
Table 4-1 - A summary table of potential spurious bands that frequently are seen from poor sample preparation, sampling technique or other phenomena.	167
Table 4-2 - Organic molecules used as scintillants for beta radiation.	168
Table 4-3 - Commercial resins compared.	175
Table 4-4 – Dried mass yield of 40 °C nucleated functionalised silica, which resulted in particles, surface coatings and bulk aggregates. The average mass of particles in mg is given (n =3).	176
Table 4-5 - ATR-FTIR summary for unfunctionalised TEOS silica particles, and general troughs common in all particles.	196
Table 4-6 - ATR-FTIR summary for trimethyl(phenyl)silane functionalised TEOS silica particles, common to all bifunctional particle spectra.	197
Table 4-7 - FTIR summary for triethoxysilylpropylmaleamic acid functionalised TEOS silica particles.	198
Table 4-8 - ATR-FTIR summary for 3-[(Trimethoxysilyl)propyl] ethylenediaminetriacetic acid functionalised TEOS silica particles.	198
Table 4-9 - ATR-FTIR summary for sulfonic acid functionalised TEOS silica particles.	199
Table 4-10 – ATR-FTIR summary for 3-mercaptopropyltrimethoxysilane functionalised TEOS silica particles.	201
Table 4-11 – ATR-FTIR summary for aminopropyltrimethoxysilane functionalised TEOS silica particles.	202

Table 4-12 – ATR-FTIR summary for (O-(propargyloxy)-N-(triethoxysilylpropyl)urethane functionalised TEOS silica particles.	203
Table 4-13 – ATR-FTIR summary for 3-Isocyanatopropyltriethoxysilane functionalised TEOS silica particles.	204
Table 4-14 – Functionalised NP and $^{90}\text{Sr}^{2+}$ saturation, normalised per mass of particles ( $\mu\text{g}^{-1}$ $^{90}\text{Sr}^{2+}$ bound per $\mu\text{g}^{-1}$ NP).	207
Table 4-15 – Summary table of theoretical $\text{pK}_a$ values of functional groups used on functionalised nanoparticles.	209
Table 4-16 – Commercial resin saturation binding of $^{90}\text{Sr}^{2+}$ . Mass of analyte bound per mass of resin calculated at each pH. Mean data are shown, $n = 3$ .	216
Table 4-17- Comparison of normalised $^{90}\text{Sr}^{2+}$ saturation binding data at pH 1 and pH 7 for the four chelator nanoparticles and four commercially available resins ( $\mu\text{g}^{-1}$ $^{90}\text{Sr}^{2+}$ bound per $\mu\text{g}^{-1}$ NP).	216
Table 4-18 – Table of normalised $^{137}\text{Cs}^+$ binding saturation data for commercial resins. Figures normalised showing $\mu\text{g}^{-1}$ $^{137}\text{Cs}^+$ bound $\mu\text{g}^{-1}$ resin.	218
Table 5-1 – Growth conditions controlled during nanofibres growth: polymer injection rate, growth temperature and relative humidity.	231
Table 5-2 – Normalised background corrected saturation binding data of EDTA functionalised capillaries. Bound $^{90}\text{Sr}^{2+}$ is extrapolated to counts per min or as a mass per $\text{mm}^2$ of capillary surface.	243
Table 5-3 - Normalised saturation binding data of functionalised capillaries at pH 7. Bound $^{90}\text{Sr}^{2+}$ is extrapolated to counts per min or as a mass per $\text{mm}^2$ of capillary surface area.	244
Table 5-4- Normalised saturation binding data of functionalised capillaries. Bound $^{137}\text{Cs}$ is extrapolated to counts per min or as a mass per $\text{mm}^2$ of capillary surface area.	245
Table 5-5 – Nanofibre diameter averages as a function of silane modification. Summary of Figure 5-17 B. Empty values are because fibre diameter grew too large.	251

## Abbreviations

4-ATP	4-aminothiophenol
4-MTP	4-mercaptothiophenol
ASV	Anodic stripping voltammetry
ATR-FTIR	Attenuated total reflectance Fourier transform infrared spectroscopy
Biotin-cap-DPPE	1,2-dipalmitoyl- <i>sn</i> -glycero-3-phosphoethanolamine-N-(cap biotiny)
BOBCalix6	bis(tert-octylbenzo-crown-6
BPPF <sub>6</sub>	N-butylpyridinium hexafluorophosphate
Bu <sub>3</sub> MeN <sup>+</sup> Cl <sup>-</sup> crown ether	Tributylmethylammonium chloride Crown ether
Calix[4]resorcinarene	Pentacyclo [19.3.1.13,7.19,13.115,19] octacosal(25), 3,5,7 (28),9,11,13 (27),15,17,19(26),21,23-dodecaene-4,6,10,12,16,18,22,24-octol
CCC	Critical coagulation concentration
Cionic liquidEs	carbon ionic liquid electrodes octyl(phenyl)-N, N-dibutyl carbamoylmethyl phosphine oxide
CMPO	calix[4]-bis-2,3-naphtho-crown-6
CNC	caustic-side solvent extraction
CSSX	crystalline silico-titanate
CST	Cyclic voltammetry
CV	Dibenzo-21-crown-7
DB21C7	1,2-Cyclohexylenedinitrotetraacetic acid
DCTA	Dimethyl sulfide
DMS	Dimethyl sulfoxide
DMSO	Deoxyribonucleic acid
DNA	1,4,7,10-tetraazacyclododecane-1,4,7,10-tetraacetic acid
DOTA	Dual polarisation interferometry
DPI	Disintegrations per minute
DPM	Diethylenetriaminepentaacetic acid
DTPA	Dithiothreitol
DTT	Ethyl-3-(3-dimethylaminopropyl)carbodiimide
EDC/EDAC	Ethylenediamine-N,N'-bis(2-hydroxyphenylacetic acid)
EDDHA	Ethylenediaminetetraacetic acid
EDTA	Ethylene glycol tetraacetic acid
EGTA	Electrochemical Impedance Spectroscopy
EIS	triethylamine
Et <sub>3</sub> N	X-ray absorption fine-structure
EXAFS	

FEGTEM	Field emission gun tunnelling electron microscopy
FIB	Focused ion beam
FITC	Fluorescein isothiocyanate
FT	Fibre type
FTIR	Fourier transform infrared spectroscopy
GFP	Green fluorescen protein
HCL	Hydrochloric acid
Hg-ISE	Mercury ion selective electrode
HMDE	Hanging mercury drop electrode
HPLC	High performance liquid chromatography
HRP	horseradish peroxidase
IHP	Inner Helmholtz plane
ionic liquid	Ionic liquid
LC	Liquid crystal
Li <sup>+</sup> Tf <sub>2</sub> N <sup>-</sup>	N-lithiotrifluoromethanesulfonimide
LoD	Limit of detection
MeCN	Acetonitrile
MHDA	16-Mercaptoundecanoic acid
Mie scattering	Lorenz–Mie–Debye solution scattering
Native/SDS-PAGE	Sodium dodecyl sulfate polyacrylamide gel electrophoresis
NMR	Nuclear magnetic resonance
NPP	Normal Pulse Polarography
NTA	Nitrilotriacetic acid
OCP	Open circuit potential
OHP	Outer Helmholtz plane
PBR	Permeable reactive barrier
PCS	Photon correlation spectroscopy
PEI	Polyethyleneimine
POPOP	1,4-bis(5-phenyloxazol-2-yl) benzene
PP	Pulse Polarography
PPO	2,5-Diphenyloxazole
RST	Reverse spectrum transform
RTionic liquid	room temperature ionic liquid
SAM	Self assembled monolayer
SANS	Shallow angle neutron scattering
SEM	Scanning electron microscopy
SHE	Standard hydrogen electrode
SIMS	Secondary Ion Mass Spectroscopy
SLP	Surface layer protein
SPR	Surface plasmon resonance
SREX	strontium extraction process
sulfo-NHS	N-hydroxysulfosuccinimide
sulfo-SMCC	4-(N-Maleimidomethyl)cyclohexane-1-carboxylic acid 3-

	sulfo-N-hydroxysuccinimide ester
TBP	tributylphosphate
TBP	tributyl phosphate
TDMI-Tf <sub>2</sub> N,	1-tetradecyl-3- methylimidazolium
TEMOS	Tetramethyl orthosilicate
TEOS	Tetraethylorthosilicate
TIRE	Total internal reflection ellipsometry
TIRIE	Total internal reflection imaging ellipsometry
TMS	3-(trimethylsilyl)propionic-2,2,3,3-d <sub>4</sub> acid sodium
TOPO	trioctylphosphine oxide
TPB	1,1,4,4-tetraphenyl-1,3-butadiene
Traut's	2-Iminothiolane
	Polyethylene glycol p-(1,1,3,3-tetramethylbutyl)-phenyl ether
Triton X-100	
tSIE	Transformed spectral index of an external source
TTF	Tetrathiafulvalene
UNEX	UNiversal EXtraction
UREX	Uranium Recovery by Extraction
W/O	Water-in-oil (emulsion)

# **1 : General Introduction**

---

## 1.1. Groundwater contamination

In the UK hazards arise from fuels, materials and wastes produced from United Kingdom Atomic Energy Authority (UKAEA) and British Nuclear Fuels plc (BNFL) dating back to the 1940s and 1960s as well as Magnox power stations from the 1950s to 1970s. Analysis of the problem of ground water contamination is not a simple one especially in the UK as institutions are not obliged to reveal sensitive waste management data. Without detailed knowledge of the problem and the specifications needed design of a practical biosensor is not possible. As a result, models for ground water contamination in the UK are often based on American data which is freely available. The Drigg site in the North West of England is a nuclear processing site owned by Sellafield (previously British Nuclear Fuels). This is one site that does disclose information on soil analysis and allows a realistic model of the environmental contamination to be made. By-products from the nuclear fission process are radionuclides  $^{238}\text{U}$ ,  $^{99}\text{Tc}$ ,  $^{90}\text{Sr}$  and  $^{137}\text{Cs}$ . These are commonly present in plumes after reprocessing as are technetium Tc(VII) and Ra ions. Tc particularly causes problems for remediation.  $^{99}\text{Tc}$  is bioavailable as a sulfate analogue when oxidised to form the pertechnetate ( $\text{Tc(VII)O}_4^-$ ) anion. In this form it is highly mobile for bioaccumulation, working its way into the food chain [1].

Further complications arise when these cations bind to form oxy-anions. Other substances that may interact are a number of natural compounds in soils and ground water as well as erosion compounds from well monitoring sites. High level radioactive waste is buried with the intention of the radioactive decay over significant periods of time. Even minor leakage and radionuclide migration through container vessels can result in disastrous ramifications for the environment [2].

A number of other metals common in agricultural soils, namely Zn, Cd, Pb and Cu add to the complexity of competing ions [3] which hinder a number of current analytical techniques as the samples require pre-treatment in strong acids. Most current sensing mechanisms in the laboratory do not account for the number of interfering co-contaminants and environmental variables that the devices will have to face.

More in-depth analysis of American groundwater from Maynardville Limestone and Bear Creek Area radionuclide contaminated sites shows a significant number of competing anions

(NH<sub>4</sub><sup>+</sup>, Cl<sup>-</sup>, F<sup>-</sup>, kjeldahl nitrogen, NO<sub>3</sub><sup>-</sup>, NO<sub>2</sub><sup>-</sup>, SO<sub>4</sub><sup>2-</sup>), over 30 organic species and nearly as many inorganic ions.

## 1.2. Ground water composition

As a model of simulant groundwater that will mimic the operational conditions of the prototype sensors, groundwater conditions analysed in Permo-Triassic sedimentary rocks and underlying Ordovician metavolcanic basement were used as a suitable model. While data for Sellafield is usually difficult to obtain, a summary of 19 boreholes spanning 52 km<sup>2</sup> were published during a 1990's project [4] identifying a potential host for a nuclear waste repository due to the low permeability of the rocks in the area. In this model, Na, K, Ca, Mg, Sr, Cl, SO<sub>4</sub>, HCO<sub>3</sub>, Br, <sup>18</sup>O/<sup>16</sup>O, <sup>2</sup>H/<sup>1</sup>H, <sup>3</sup>H, <sup>14</sup>C, <sup>13</sup>C/<sup>12</sup>C, <sup>36</sup>Cl/<sup>35</sup>Cl, <sup>87</sup>Sr/<sup>86</sup>Sr, <sup>34</sup>S/<sup>32</sup>S, <sup>4</sup>He and inert gases Ne, Ar, Kr and Xe were all reported.

In 2006, a simplified synthetic ground water system containing mainly the natural soil minerals has been used in research systems; Drigg synthetic ground water (SGW) at pH 7.35 contains KCl, MgSO<sub>4</sub>.H<sub>2</sub>O, MCl<sub>2</sub>, H<sub>2</sub>O, CaCO<sub>3</sub> sodium silicate, NaNO<sub>3</sub>, NaCl and NaHCO<sub>3</sub> [5]. Even within this small system the analysis needed must show high specificity to a number of metal ions and minerals as well as being able to function with high levels of organic materials over prolonged time periods. Binding experiments used to test the chelator nanoparticles and nanofibres (Chapters 5 and 6) were tested using synthetic Drigg groundwater as a model for potential interferents and co-sorbents.

## 1.3. Ground water contaminants

After extensive communications with various Nuclear UK bodies via the DIAMOND consortium no set figures of radioisotope contamination concentrations were obtained, suggesting these figures are either confidential or simply not known due to the large scale and ongoing deterioration of stored legacy waste. However, for a realistic model to test sensors in operational environments, a combination of internal Sellafield monitoring documentation [6], World Health Organisation limits (WHO) [7] and Sellafield land quality reports [6, 8] was used to derive an average of activities taken from bore hole samples across the Sellafield separation area. Typically data is reported in Bq<sup>-1</sup> rather than chemical concentrations (M).

The 2010 WHO analysis of groundwater samples [7] indicated total alpha activities were below the WHO drinking water guideline level ( $0.5 \text{ Bq l}^{-1}$ ), with only 5 Sellafield wells exceeding this amounts (Figure 1-1).

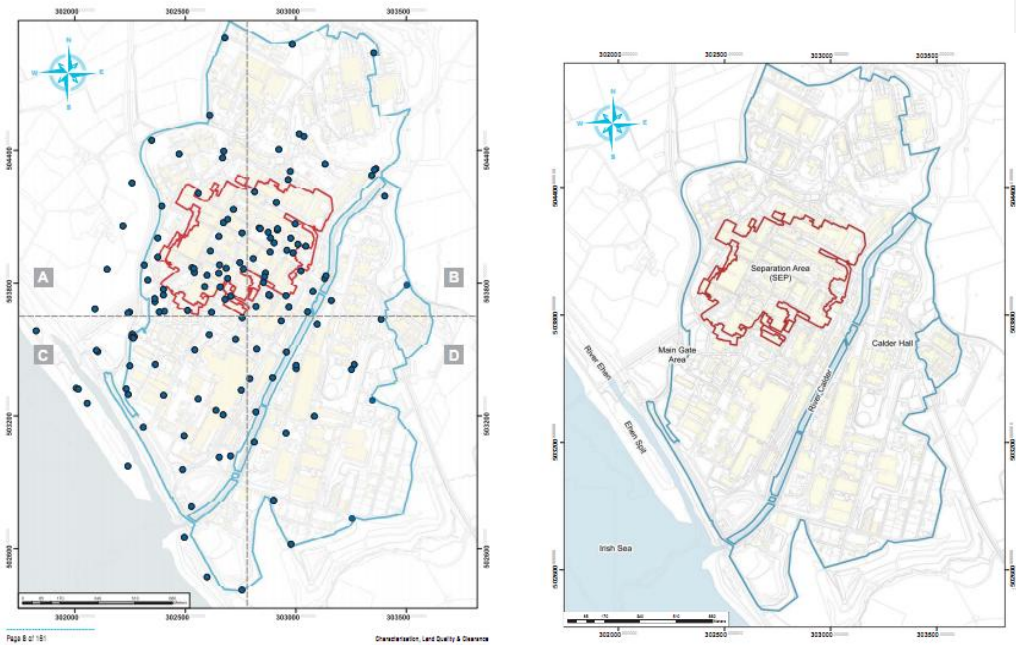


Figure 1-1- Sellafield site groundwater monitoring network. (•) monitoring wells, (—) the separation area, (—) the site perimeter.

The annual average in one monitoring well reached  $96.2 \text{ Bq l}^{-1}$ . Uranium isotopes (particularly  $^{234}\text{U}$  and  $^{238}\text{U}$ , but with lesser contributions from  $^{235}\text{U}$  and  $^{236}\text{U}$ ) dominated the  $\alpha$  activity across the site. Lower activities of other  $\alpha$  - emitting radioactive isotopes including  $^{239/240}\text{Pu}$ ,  $^{237}\text{Np}$ ,  $^{241}\text{Am}$  and  $^{226}\text{Ra}$  were measured in groundwater. The highest total observed  $\beta$  activity was  $1620 \text{ Bq l}^{-1}$ . A number of  $^{90}\text{Sr}$  sites exceeded the  $^{90}\text{Sr}$  guidelines ( $10 \text{ Bq l}^{-1}$ ), maximum plutonium levels observed were 'low' at a maximum of  $0.46 \text{ Bq l}^{-1}$ ,  $^{99}\text{Tc}$  below  $0.5 \text{ Bq l}^{-1}$  (limit  $100 \text{ Bq l}^{-1}$ ). Weak beta emitter  $^3\text{H}$  had annual average values from three monitoring wells in the area which exceed the WHO drinking water guideline level of  $10,000$

Bq l<sup>-1</sup>. The highest annual average activities are from monitoring wells located outside the south-west corner of the separation area with averages up to 38 750 Bq l<sup>-1</sup>. Overall groundwater data from the 2010 data released does not show significant changes compared to the previous three years.

The figures summarised in Table 1-1 when stated as total α emitters comprised of <sup>226</sup>Ra, <sup>235</sup>U, <sup>236</sup>U, <sup>237</sup>Np, <sup>238</sup>U, <sup>239</sup>Pu, <sup>240</sup>Pu and <sup>241</sup>Am. Total beta emitters comprises compounds, <sup>90</sup>K, <sup>90</sup>Sr <sup>137</sup>Cs and <sup>241</sup>Pu, while total weak beta emitters include tritium, <sup>14</sup>C, <sup>36</sup>Cl, <sup>99</sup>Tc and <sup>129</sup>I [8].

Table 1-1 – Radionuclide contamination levels compiled using annual analysis reports to model accurate synthetic groundwater systems for appropriate testing of sensor and chelator surfaces.

Primary isotopes in Sellafield [6]	WHO drinking water limits (Bq l <sup>-1</sup> ) [7]	Observed averages in Sellafield from 04/09 to 03/2010 (Bq l <sup>-1</sup> )	Emission	2010 analysis level comparison [8]	Geological grid reference [8]
<sup>234</sup> U and <sup>238</sup> U, but with lesser contributions from <sup>235</sup> U and <sup>236</sup> U	<sup>238</sup> U 10  <sup>236</sup> U 1  <sup>235</sup> U 1  <sup>234</sup> U 10	Max: <sup>238</sup> U 10.00 - 55.0 .  Majority 0.006 - 0.01  Max: <sup>236</sup> U 2.9  Max: <sup>235</sup> U 2.1  Max: <sup>234</sup> U 50	Alpha	Mainly below this level.	p47 <sup>236</sup> U P48 <sup>238</sup> U p45 <sup>235</sup> U p45 <sup>234</sup> U
<sup>239/240</sup> Pu, <sup>237</sup> Np, <sup>241</sup> Am and <sup>226</sup> Ra	1	Max: <sup>239</sup> Pu 0.02 - 0.0  Majority 0.0037 - 0.005  <sup>237</sup> Np Max 0.05 - 0.1	Alpha	Mainly below this level.  No <sup>237</sup> Np, above WHO level.	<sup>239</sup> Pu p49  <sup>237</sup> Np p49
<sup>90</sup> Sr	10	Max 100.00 - 1000.00  Several 100.00 - 1000.0	Beta	Above WHO threshold.	p53

		Majority 0.12 - 1.0			
<sup>137</sup> Cs	10	2 Majority of bore holes 0.10 - 0.2	Beta		p54
<sup>99</sup> Tc	100	Majority 0.04-5 Max observed 100.00 - 200.0	Beta	Several sites exceeded WHO guidelines.	p56
<sup>3</sup> H	5.6	Majority of bore holes 100.00 - 500.00 Max 20000.00 - 40000.0	Beta	Several sites exceeded WHO guidelines.	p55
<sup>14</sup> C	100	Max: 20.00 - 35.0	Beta	No values exceeded WHO levels	p 57
<sup>129</sup> I	100	Max: 1.0 - 2.0 2.0 Majority 3.0 0.03 - 0.1	Beta and gamma	No values exceeded WHO levels	p 59

A number of radionuclide species needed to be detected have been identified as have their realistic activities the sensor will need to respond to. To place radioactive waste contamination into context, a brief summary of current remediation technologies is presented to justify the need for biosensing application.

#### **1.4. Current remediation technologies and the need for biosensing**

Groundwater contamination throughout Europe is a common problem. Application of technological advances for ground water remediation is often determined by cost-effective and risk management policies. There are 3 methods of waste removal. Degradation involves chemical or biological agents applied to decompose the contaminants or form harmless

products. Precipitation can be used to form insoluble contaminant compounds that flocculate or sediment from solution. Sorption is the immobilisation of the contaminant by absorption or complex formation to the substrate or a barrier material. Implementation of these methods is currently achieved by three remediation strategies. There are: (I) natural attenuation systems that use reactive elemental reducing agents that induce abiotic reductive degradation of substances, (II) wetland systems (large land areas saturated with water including mine effluents) and (III) permeable reactive barriers (PRB) for ground water remediation which are increasingly used.

PRB contain reactive elemental complexes such as iron, activated carbon and zeolites, which participate in redox and chemical coupling reactions with the contaminant in question. There has been some success with chromate removal using iron PRBs, as has mercury removal with copper shavings, which induced flocculation. However, these barriers treat the plume and not the source.

Even if a solution to the problem exists, economical and political restrictions often resist implementation. Underground utilities, property boundaries, site logistics, human health and safety and compromising ground conditions hinder the implementation of successful remediation technologies. The PRBs, the most promising of the three strategies, still faces a number of problems. Target contaminants need to bind the material so that it cannot be easily re-released back into the ground water, but at some point can be safely removed if the barrier material is to be reused. Formation of surface coatings gradually decrease the PRB permeability efficiency over time [9]. Uranium ions have been observed as a notable cause of this affect. Reactivity of the barriers requires the contaminants to be known prior to the barrier being installed and the binding of expected contaminants can be hindered by co-contaminants. Stability of these materials often needs to extend over a timescale of years as well as being environmentally compatible. Currently, little is known about the long term affects of such PRB implementation.

Because of these problems, remediation of groundwater effluents is not straight forward even with promising technologies. In such situations as these, the application of biosensing technologies is the most practical implementation to continually monitor a target site when complete remediation is not possible.

## 1.5. Bioremediation

An alternative approach to engineered systems is the use of bacterial absorbing agents. Bioremediation is the removal of toxins from the environment by microorganisms. It is often more cost effective and sometimes the only practical method available. One of the problems with environmental pollutant removal is that many metal ions bond with sulphides to form insoluble complexes. Depending on the metal concentration, bacterial organisms can oxidise these compounds; this strategy is used for the extraction of copper sulphate from copper sulphide ores to create highly water soluble compounds. The use of bacteria significantly increases the rate of oxidation on surface exposed ores making removal now a practical scenario. However the method is not suitable for all metals. For example, copper and iron in the form of pyrrhite (FeS) and covellite (CuS) can be remediated while molybdenum ores cannot [10]. Scrap iron, for example, can be used with *Acidithiobacillus ferrooxidans* to produce Fe<sup>3+</sup> solutions from pyrite to oxidise more sulphide minerals [11]. UO<sub>2</sub> (Uraninite) in particular, is highly insoluble until it has been oxidised by *Acidithiobacillus ferrooxidans* using iron and O<sub>2</sub> as an electron acceptor. In cases where toxicant species cannot or will not be removed, for means of practicality or cost, biosensing to monitor concentration levels and movement is a practical alternative.

## 1.6. Biosensing Techniques

Biosensors are the integration of electronic circuits with organic biological recognition components to create a selective and sensitive sensing device for a specific analyte. They consist of three parts; a binding receptor, a transducer to conduct the signal and an output device to convert the detected signal usually in the form of current, potential or impedance. A summary of a typical amperometric or potentiometric bacterial sensor is summarised in Figure 1-2 using bacterial membrane transporters [12].

The signal interrogation method varies, thus a brief overview of the main interrogation methods of sensors is presented and their application to metalloid sensing is presented with the focus on electrochemical sensing as this covers a significant amount of the work presented.

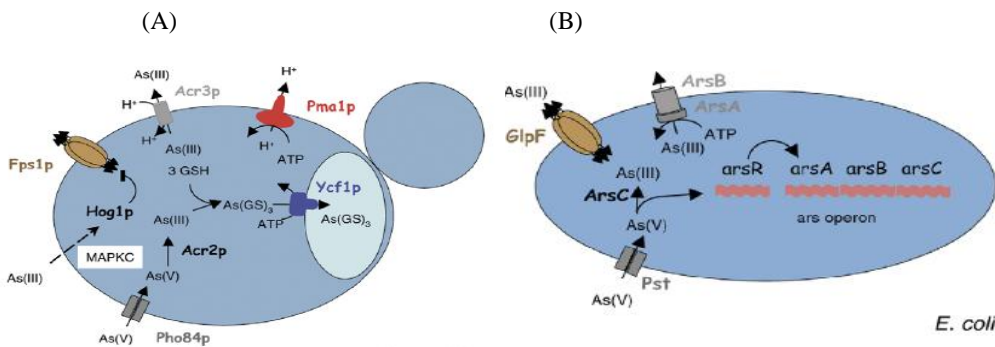


Figure 1-2 - Summary of the membrane pumps in (A) *S. cerevisiae* (B) *E. coli*. (A) Arsenic ArsAB pump functions similar to ABC transporters, with potential from amperometric sensors used to extrude Ar (III). The Acr3p pump extrusion system removes As(III) ions, the proton potential gradient for this process generated from Pma1p which generates ADP and extrudes  $H^+$  ions. Metal enzymes that convert metal ions to alternate oxidation states can be detected by potentiometric based cyclic voltammetry, while binding and conformational changes observed by impedance. (B) Arsenate [As(V)] ions enter cells via phosphate transporters (PiT and Pst) and Pho84p in *E. coli*. This can activate a resistance protein via the (ars) operon. Transcription of arsR is induced by As(V) ions and resistance (ars) operon. ArsR, regulates the expression of the arsABC a membrane pump which pumps out s(III) ions. Before the levels are toxic to the bacteria. Glpf and Ps1p are also thought to be involved in As(III) removal.

### **1.6.1. Optical biosensors**

Optical sensors typically use photon based emission or quenching as a method of analyte detection. Whole cell bacterial biosensors have been engineered to fluoresce in the presence of specific heavy metal ions [13]. Using the *luxCDABE* promoter, fluorescence was activated in the species *Alcaligenes eutrophus* when mM copper concentrations were present.

Similarly, the regulatory sequence from the *cadA* gene of plasmid *pI258* was used to insert the firefly luciferase gene into *Staphylococcus aureus* [14]. Limits of detection (LoD) for cadmium, lead and antimony were 10 nM, 33 nM and 1 nM respectively which are impressively low. While optical equipment has the resolution to detect single photons and thus, in theory, an individual molecule's emission, electrochemistry cannot say the same for single electron transfers. However, implementation of optical sensors is not always practical. Also, a limited number of bacteria-analyte interactions are applicable and the approach has the disadvantage that extensive signal to background data manipulation is often needed. Impedance based sensing provides a practical compromise.

#### **1.6.1.1. Surface Plasmon Resonance**

Surface plasmon resonance (SPR) is the localised phenomena that electrons undergo under light stimulation. If the light frequency interacting with the surface layer of electrons matches, resonance valence electrons are excited locally emitting an evanescent wave parallel to the interface, while the bulk of light is reflected perpendicularly. This phenomenon alters the materials local dielectric permittivity, and also the refractive index ( $n$ ) allowing interfacial phenomena such as layer by layer sensor deposition [15], binding constant extrapolation, and more recently changes in magnetic properties to be observed. Nanoparticles, because of their high surface area to volume ratio, exhibit an enhanced SPR effect and can be modelled by Mie (Lorenz–Mie–Debye solution) scattering theory [16]. While there are examples that show SPR can monitor protein-protein or antibody antigen interactions [17], the small molecule detection required for the length scale of ions is below the detection limits of the technique. As a result SPR was not used as an interrogation method.

### 1.6.1.2. Total internal reflection imaging ellipsometry (TIRIE)

Ellipsometry, like SPR is a non destructive optical technique used to observe changes in interfacial phenomena in thin films. TIRIE is also able to monitor refractive index changes and dielectric properties and is able to probe below the wavelength diffraction limit, and is currently popular for large throughput pathogen detection [18], immunoarray screening [19] and other biomedical applications [20].

## 1.6.2. Electrochemical biosensors

### 1.6.2.1. Amperometric biosensors

Amperometric biosensors are those that use a current generated by movement of an ionic or redox species as the detection mechanism. Three broad classes exist; the unmediated, mediated or direct electron transfer. To date they are the most extensively used and successful in terms of transition from laboratory to commercialisation, predominantly in medical diagnostics [21]. These sensors function by using a working electrode acting as the anode or cathode to determine analyte concentrations from the current generated in a known reaction mechanism.

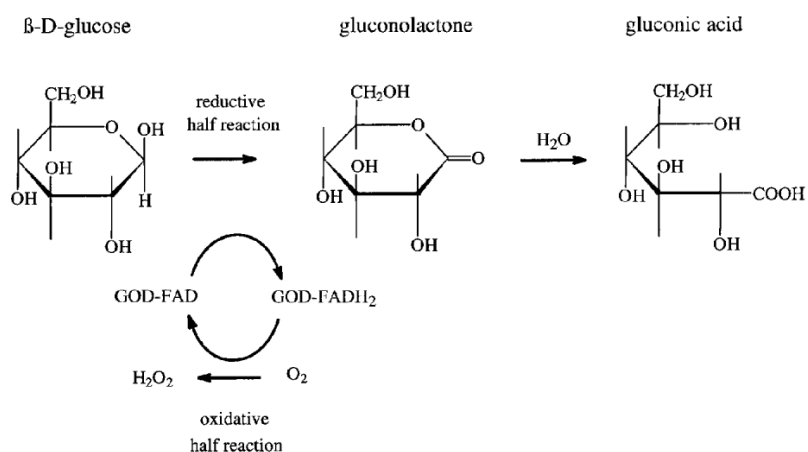


Figure 1-3 – Typical reaction mechanism of GOD amperometric biosensors for the detection of glucose by production of H<sub>2</sub>O<sub>2</sub> from the reduction of  $\beta$ -D-glucose to gluconolactone.

The analytical amperometric biosensor is the glucose sensor which is catalysed by glucose oxidase [22]. Glucose oxidase biosensors produce a 1:1 stoichiometry between oxygen and glucose converted from a reductive half reaction with two protons and electrons transferred from  $\beta$ -D-glucose to the enzyme yielding d-gluconolactone which hydrolyses to gluconic acid (Figure 1-3). The reduced enzyme is then regenerated in a two proton half reaction to yield  $H_2O_2$ . The current generated by the oxidation of  $H_2O_2$  against a calibration curve is used to determine the glucose concentration present in a sample.

The earliest amperometric electrode was an oxygen sensor by Clark in 1956 [23]. He developed this system as the first enzyme based electrode using glucose oxidase as an enzymic transducer, entrapping the enzyme in a permeable dialysis membrane.

### 1.6.2.2. Mediatorless amperometric sensors

These sensors measure the concentrations of enzymic products with the substrate decreasing as products are generated. For example, in glucose oxidation:

Substrate + oxidised enzyme  $\Rightarrow$  reduced enzyme + product

where:  $S + EFAD \Leftrightarrow EFADS \Rightarrow EFADH_2 + \text{product}$

The substrate plus enzyme in oxidised form is reduced (+ 2e) and converted to flavin adenine dinucleotide  $H_2$ .

Subsequently  $EFADH_2 + O_2 \Rightarrow EFAD + H_2O_2$

Here the reduced FAD cofactor in the enzyme is regenerated and results in  $H_2O_2$

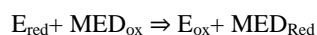
Generation. This product like the glucose oxidase sensor is oxidised against a known calibration to determine the analyte concentration.

Most of these sensors work using -0.7 V cathodic reduction or +0.65 V anodic oxidation of  $H_2O_2$  [24]. These sensors are limited however by substrate diffusion to and from the electrode, to and from the electrode active site and oxygen/ $H_2O_2$  diffusion [25]. A range of enzymes and analytes can be quantified in this way; lactate oxidase for lactate[26] alcohol

oxidase/catalase for ethanol [27], xanthine oxidase for hypoxanthine [28], lysine oxidase for lysine [29].

### 1.6.2.3. Amperometric mediated biosensors

These biosensors use alternative (non-enzyme) mediators or oxidising agents as electron carriers. These are typically low potential, (typical  $E_m < 0$  V) artificial molecules so the effects of oxygen are minimised, that transport electrons between a molecule's redox centre and electrode.



The most common mediators that are used in the many electrochemical experiments include the reversible ferricyanide  $[\text{Fe}(\text{CN})_6]^{3-}$  / ferrocyanide  $[\text{Fe}(\text{CN})_6]^{4-}$  redox couple, and the irreversible oxidation of ferrocene  $\text{Fe}(\text{C}_5\text{H}_5)_2$ , for non aqueous experiments. Other alternatives are summarised in Table 1-2:

Table 1-2 - Table of common natural amperometric redox probes and potentials reactions occur.

Reaction	E (V)
Acetone – propan-2-ol	-0.43
$\text{H}^+ - \text{H}_2$	-0.42
Acetate aldehyde – ethanol	-0.20
Cystine – cysteine	-0.22
$\text{O}_2 - \text{H}_2\text{O}_2$	+0.31

Mediator based systems are used with an applied voltage that does not exceed the oxygen reduction potential ( $\text{O}_2 + \text{H}_2\text{O} + 2\text{e}^- \leftrightarrow \text{HO}_2^- + \text{OH}^-$  at -0.076 V and  $\text{O}_2 + \text{H}_2\text{O} + 2\text{e}^- \leftrightarrow \text{HO}_2^- + \text{OH}^-$  at -0.076 V). Ideally the mediator should not react with oxygen, the rate of mediator

electron transfer should be fast relative to its transport rate, and ideally not influenced by pH. However, in many systems oxygen can be used as the mediator if a redox probe is not used. Buffered experiments often use oxygen as the current generator while ferricyanide based experiments in many cases use argon purging to remove bulk oxygen. This ensures the ‘bulk’ current is due to  $[\text{Fe}(\text{CN})_6]^{3-/4-}$  and not a composite signal that is prone to drift and fluctuations. While a truly oxygen current free is difficult to achieve deaeration ensures that this current contribution is magnitudes lower than the main signal from biosensor interrogation.

#### 1.6.2.4. Common oxygen and water based reactions in electrochemical reactions

In an aqueous electrochemical system, regardless of deaeration, a current will be generated due to oxygen and hydrogen being present in the system from the atmosphere and diffusion or dissociation of water. Table 1-3 shows a summary of common reactions and the potentials they occur versus the standard hydrogen electrode (SHE).

Table 1-3 – Oxygen and hydrogen based redox reactions that can contribute to electrochemical current in aqueous systems.

Reaction	$E^{\circ}$ / (V) vs SHE
$\text{O}_2 + 2\text{H}^+ + 2\text{e} \leftrightarrow \text{H}_2\text{O}_2$	0.695
$\text{O}_2 + 4\text{H}^+ + 4\text{e} \leftrightarrow 2\text{H}_2\text{O}$	1.229
$\text{O}_2 + \text{H}_2\text{O} + 2\text{e} \leftrightarrow \text{HO}_2^- + \text{OH}^-$	-0.076
$\text{O}_2 + 2 \text{H}_2\text{O} + 2\text{e} \leftrightarrow \text{H}_2\text{O}_2 + 2\text{OH}^-$	-0.146
$\text{O}_2 + 2 \text{H}_2\text{O} + 4\text{e} \leftrightarrow 4\text{OH}^-$	0.401
$\text{O}_3 + 2\text{H}^+ + 2\text{e} \leftrightarrow \text{O}_2 + \text{H}_2\text{O}$	2.076
$\text{O}_3 + \text{H}_2\text{O} + 2\text{e} \leftrightarrow \text{O}_2 + 2\text{OH}^-$	1.24
$\text{O}(\text{g}) + 2\text{H}^+ + 2\text{e} \leftrightarrow \text{H}_2\text{O}$	2.421
$\text{OH} + \text{e} \leftrightarrow \text{OH}^-$	2.02
$\text{HO}_2^- + \text{H}_2\text{O} + 2\text{e} \leftrightarrow 3\text{OH}^-$	0.878

### **1.6.2.5. Amperometric direct electron transfer biosensors**

In these systems, also known as bioelectrocatalytic systems, electrons transfer directly between enzyme and electrode without a carrier. The rate of electron transfer is related to the potential drop, and the physical distance between the enzyme redox-centre and electrode [30]. One of the earliest examples by Kuwana [31] used an indium tin oxide electrode to show direct electron transfer between mitochondrial protein cytochrome c and the electrode. More recent sensors include cholinesterase [32], membrane bound dehydrogenases [33], cellobiose dehydrogenases [34] and haemoglobin [35] used for electron transfer. Amperometric sensors are discussed in more detail in Chapter 2.

### **1.6.3. Potentiometric biosensors**

Potentiometric systems use a change in electric field across an electrode to detect analytes on interest. These systems differ to, and should not be confused with potentiostatic sensors that measure current. The earliest potentiometric sensor, the pH sensor detects  $H^+$  ions across a glass membrane, the specificity of these electrodes dependent on the selectivity of a porous membrane. As well as molecular analytes, potentiometric systems allow surface interrogation of systems such as lipid SAMs on the working electrode [36] with adsorption, poration [29] and conformational changes detected as a change in potential or capacitance.

Miller's early study using a HMDE [37] monitored interactions of the lipid heads with a number of molecules. When lipids self assemble to form a monolayer, the hydrophobic tails align to the mercury with the polar heads facing outwards. The interactions in the head group region are of importance to determine changes of the monolayer structure and permeability. These studies showed that molecules could self assemble into ordered structures at an interface and be interrogated by application of an electric field. Since then SAMs assembled on mercury have been extensively studied allowing real time monitoring of hydrophobic compound insertion [38], lipid phase transitions [39] and protein insertion into [40]. While difficult to quantify specific analytes, potentiometric interrogation is sensitive to interfacial changes at a sensor interface than that cannot be easily detected by other methods. Because of the ability to detect significant interfacial changes, potentiometric sensors are being increasingly used with recombinant antibody technologies with specific antibodies created for biosensor applications [41] for a wider range of analytes including pesticides

(terbuthylazine) [42], bacterial (*Escherichia coli*) [43], antibiotic resistance ( $\beta$  lactamase) [44]. Potentiometric sensors are discussed in more detail in Chapter 3.

#### 1.6.4. Impedance biosensors

When a potential is applied to an electrode, ions of opposite charge are attracted to the interface creating a charged layer of ions, termed the electrical double layer. The closest distance of approach is a balance between electrostatic attraction between electrode counter ions of attractive and repulsive charge. The distance of this double layer is dependent on potential, concentration and ion valency and the charged double layer is analogous to a capacitor.

Impedance based electrochemistry applies a sinusoidal potential to this system. By monitoring the amplitude and resulting phase shift in the observed current at the interface, interfacial phenomena can be modelled as a combination of parallel capacitive and resistive circuit elements. Systems without an analyte or mediator behave like a series RC circuit [45] while mediator based systems can be modelled as a Randles resistor and capacitor parallel circuit [46]. Normally substantial data interpretation is needed but surface adsorption, deposition and binding are quantifiable with this technique. The scans are also generally non destructive to analyte or electrodes providing suitable potentials are used.

Resistance (R) is the ability of a component to resist electrical flow, the fundamental relation Ohms law (Equation 1-1):

$$R = \frac{E}{I} \quad (1-1)$$

However this model's basic assumptions are that current and potential are in phase with each other, that resistance is independent of frequency and the relationship is true for all currents and potentials. This is flawed when a biosensor surface is considered. Impedance accounts for these real life parameters to realistically model a system's ability to resist current flow. Application of an alternating potential to a system will result in a change to these parameters. In a theoretical pure resistor (R), impedance (Z) is equal to the resistance (Equation 1-2):

$$Z = R \quad (1-2)$$

In a theoretical pure capacitor impedance is inversely proportional to the product of frequency ( $\omega$  in radians  $2\pi f$ ), capacitance (C) and  $j$  the imaginary component (Equation 1-3).

$$Z = \frac{1}{j\omega C}$$

(1-3)

Electrochemical impedance spectroscopy (EIS) is a method of interrogating a surface's proportion as a function of current dissipation with frequency. Impedance therefore is the ratio of current change to a incremental applied voltage.

Impedimetric sensors work on empirical electronic systems which model the ideal Ohms law conductors to actual imperfect electronics. An RC circuit models the phase shift between the input and output a.c signal as a function of real and imaginary components. This shift in signals comes from a frequency dependence of the electronics. Conductance and capacitance are other forms to represent impedance. Using a pure resistor model, no phase shift is observed,  $\theta = 0$  and the equation for impedance is Ohms law (Equation 1-4);

$$z = \frac{V_m}{I_m}$$

( 1-4 )

Using a pure capacitor, then the total resistance is a product of resistance (R) added to reactance ( $jX$ , where  $j = \sqrt{-1}$ ) the model accounting for the imaginary component and phase shift in the a.c signal (Equation 1-5):

$$Z = R + jX$$

(1-5)

Combining the pure capacitor and resistor model for a series RC circuit the actual impedance is given by Equation 1-6:

$$Y = \frac{V \sin \omega t}{I_m \sin(\omega t + \theta)}$$

(1-6)

Admittance (Y), an alternative way of displaying impedance (I) is the inverse of impedance (Z) which is the addition of conductance and susceptance (B) which is the product of frequency multiplied by the current (Equation 1-7).

$$Y = \frac{1}{Z} = G + jB$$

(1-7)

Impedance is measured at a range of frequencies under voltage excitation due to parasitic impedances that can exist between an electrode in solution, thus impedance is a function of frequency,  $Z(\omega)$ .

### 1.6.4.1. Equivalent Circuits

The electrochemical models discussed are represented as equivalent circuits of resistors and capacitors as impedance to a small sinusoidal excitation potential causes current to flow of phase and amplitude identical to component models (Figure 1-4).

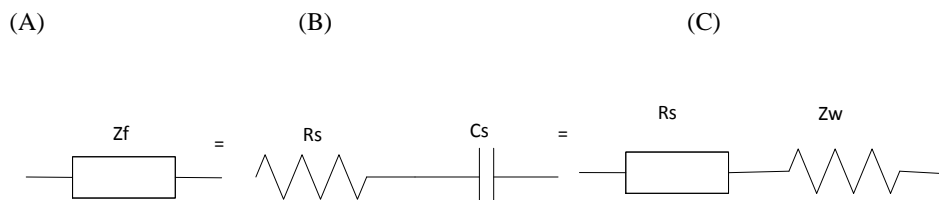


Figure 1-4- Equivalent circuit components. Frequency dependent impedance (A) can be modelled as a solution resistance and pseudo capacity (B) or a charge transfer resistance and a Warburg impedance component (C).

Figure 1-4 shows general capacitance  $Z_f$  (as frequency dependent components cannot be modelled by pure R and C components) which can be modelled as either of two equivalent components; (B) a serial  $R_{ct}$  charge transfer resistance and  $C_s$  pseudo capacity or (C)  $Z_w$  Warburg impedance and a  $C_s$  pseudo capacity component. Of the two models Figure 1-4 B is preferred as the Randles circuit parallel branch and is usually used to model impedance data. The full Randles circuit is discussed next.

### 1.6.4.2. Randles circuit

A frequency dependent circuit is often modelled by the Randles circuit as the total contributions to current in an electrochemical cell (faradaic current, charging current) can be modelled by a capacitor ( $C_d$  double layer capacitance) (Figure 1-5).

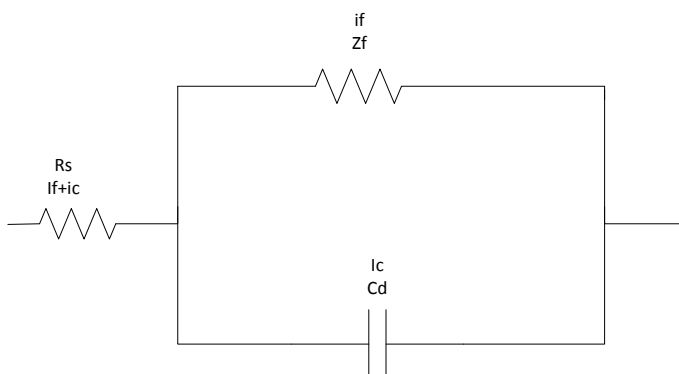


Figure 1-5- The equivalent Randles circuit.

The equivalent Randles circuit that can model faradaic impedance processes as a series resistor and Warburg impedance component in parallel to a capacitor, which is in series to a second resistor. As all these currents pass through the solution with its own resistance ( $R_\Omega$  or  $R_s$ ) a second resistor is used in series. Solution resistance,  $R_\Omega$ , and double layer capacitance,  $C_d$ , however are model components. These components do not truly model faradaic impedance because of the frequency phase shift. Therefore, only at a single frequency the Randles circuit is able to model an electrochemical system effectively. At multiple frequencies these models become empirical and more detached from experimental data, and it is possible to have multiple equivalent circuits for the same system.

### 1.6.4.2.1. Interfacial potential and Helmholtz theory

At the interface between electrode and solution there is an electrical potential. This is composed of electrolyte ions and their associated electrical charge. Assuming these ions undergo no electroactive reactions, the ions redistribute to achieve an overall electrical neutrality. Ions of attractive charge will approach the electrode to a distance of the ion's radius plus one hydration layer. The presence of repulsive ions forms a second diffuse layer, the distance of which is governed by electrostatic repulsion. These two layers were first modelled by Hermann von Helmholtz who modelled these layers in terms of Van der Waals forces and he termed these layers the Inner Helmholtz plane (IHP,  $\sigma^i$ ) and Outer Helmholtz

plane (OHP  $\sigma^d$ ) respectively analogous to a parallel plate capacitor (Figure 1-6). This approach effectively models the IHP as a linear potential drop from electrode to IHP, but does not account for diffusion, interfacial adsorption and solvent interactions.

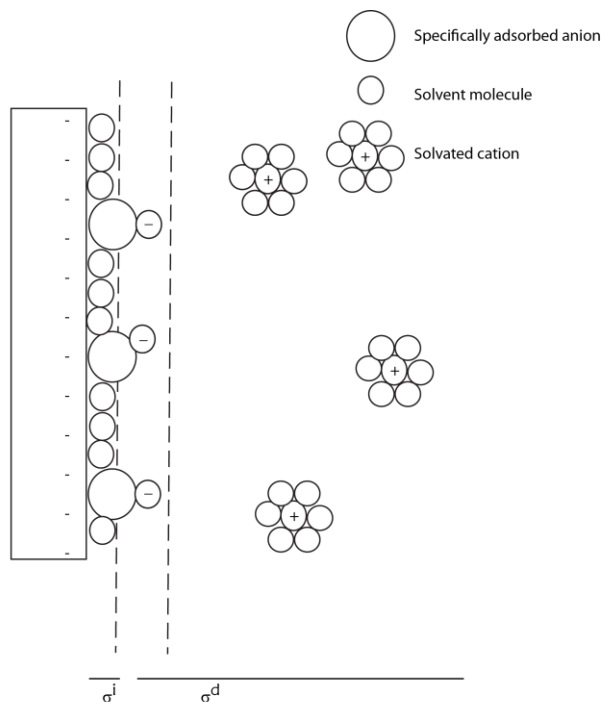


Figure 1-6 - Double layer ion distribution adsorbed at an interface. This consists of the inner ( $\sigma^i$ ) and outer ( $\sigma^d$ ) Helmholtz planes. Redrawn from [47].

### 1.6.4.2.2. Guoy-Chapman theory

Guoy-Chapman theory models interfacial charge as a sum of ions of opposite ionic charge in solution to the interfacial charge. Counter ions are not rigid, but are more diffuse within limits of their counter potential. This second layer charge and concentration affects the double layer thickness.

$$C = C_0 e^{\frac{\psi z e}{kT}} \quad (1-8)$$

The balance between forces of surface counter ions,  $C$ , and the bulk solution counter ion concentration  $C_0$  is modelled by (Equation 1-8) where  $z$  is the charge on the ion,  $e$  is the

charge of a proton,  $k$  is the Boltzmann constant and  $\psi$  is the potential of the charged surface. Whilst more accurately modelling the OHP as an exponential decay with distance this model's assumptions only work for monovalent ions and that molarity is 1:1 with activity.

#### **1.6.4.2.3. Stern theory**

Stern theory is a combination of Helmholtz and Guoy-Chapman theories. The Stern layer models ions as non finite size point charges and modifies the IHP, limiting the distance ions can approach the electrode. This is known as the slipping plane, also known as the zeta potential ( $\psi$ ).

#### **1.6.4.2.4. DLVO**

Derjaguin and Landau theory was a further modification of double layer theory combining attractive Van der Waals and electrostatic repulsion of the double layer counter ions (DLVO theory). Electrostatics are modelled on mean field approximation (charge potential energy is much smaller than thermal energy ( $kBT$ , where  $kB$  is Boltzmann constant and  $T$  temperature).

#### **1.6.4.2.5. Electrical Double layers**

It should be noted that these surface approximations are based on the assumption that no electron transfer occurs at the interface. Electrical double layers that are present at electrodes under applied potentials, and become polarised away from the OCP no longer satisfy this assumption once electrochemical reactions occur. Once redox reactions begin to occur these models no longer accurately model the system like the surface layer protein biosensor (Chapter 2). For static, no electron transfer systems such as the affinity silica nanoparticles (Chapter 4) and sorbent surfaces (Chapter 5) double layer theory accurately models the solution interface.

#### **1.6.4.2.6. Colloidal Stability**

Double layer theory extends to the stability of colloids such as the silica nanoparticles discussed in Chapter 4. Natural lyophilic colloids such as proteins and poly electrolytes are stable because there is an energetic potential barrier which prevents coagulation. Many solutions have a critical coagulation concentration, CCC. At this concentration double layer repulsion is reduced so that collisions occur and particles coagulate.

Experimentally, in terms of forces applied to an electrode, under applied potentials, or during cyclic voltammetry on a stationary electrode of constant area, a charging current builds up at

the electrode. As potential changes, the charging current ( $i_c$ ) flows (Equation 1-9), where  $C_d$  is the double layer capacitance ( $Fcm^2$ ),  $A$  the electrode area and  $v$  the scan rate (Vs). While the peak current  $i_p$  varies with the square root of the scan rate ( $v^{1/2}$ ) (for electrodes under linear diffusion),  $i_c$  varies with  $v$  so  $i_c$  becomes more important at higher scan rates. To minimise this, a consistent scan rate was used for cyclic voltammetry and a small set rms voltage of 10 mV was used for impedance work.

$$i_c = AC_d v \therefore C_d = \frac{i_c}{Av} \quad (1-9)$$

#### 1.6.4.2.7. Thickness of the molecular double layer

It is important to understand the region of ionic interaction at a sensor or nanoparticle interface. IUPAC defines the diffuse layer as the region in which non-specifically adsorbed ions are accumulated and distributed by action of the electric field and thermal motion. Counter and co-ions in immediate contact with the surface are located in the Stern layer. Ions farther away from the surface form the diffuse layer or Gouy layer, as shown previously in Figure 1-6.

In contrast, the diffusion layer is defined as the region in the vicinity of an electrode where the concentrations are different from their value in the bulk solution, and is dependant on the applied scan rate and the diffusion coefficient of the redox analyte used, and is related to the Cottrell equation. This phenomena is experimentally defined, while the double layer is not.

It is important to know the thickness of the double layer, the region of interaction of ions and analyte in electrolyte to fully understand the sensor interface which can be determined experimentally, and detailed in Equation 1-11.

It is important that the analyte being detected, for example uranyl ions, is magnitudes lower than the supporting electrolyte concentration, otherwise the observed signal will occur via bulk compression of the Inner Helmholtz plane (IHP) and not interfacial changes at the biosensor interface.

Several attempts at simulations of model diffusion layers are available [45] that model physical phenomena at the electrode. One model by Faulkner shown in Equation 1-10 relates  $J_{max}$ , the maximum flux of species to an electrode, to a species diffusion coefficient,  $D_t$  and

the distance from the electrode,  $x$ . When  $D_i$  is less or equal to 0.5, the double layer is affected to a distance of six times the square root of the diffusion coefficient.

$$J_{max} = \frac{6(Dt)^{\frac{1}{2}}}{\Delta x} + 1 \quad (1-10)$$

An experiment running for time  $t$  will alter the bulk concentration for a distance no larger than about  $6(Dt)^{1/2}$  from the electrode surface.

Experimentally the extent of the double layer, also called the Debye Length ( $\kappa^{-1}$ ) is determined by Equation 1-11:

$$\kappa^{-1} = \sqrt{\frac{\epsilon_r \epsilon_0 k_b T}{2N_A e^2 I}} \quad (1-11)$$

where  $I$  is electrolyte concentration (M),  $\epsilon_r$  the dielectric constant/relative permittivity,  $\epsilon_0$  is permittivity of free space ( $8.854 \times 10^{-12} \text{ Fm}^{-1}$ ),  $k_b$  the Boltzman constant ( $1.3806503 \times 10^{-23} \text{ m}^2 \text{ kg s}^{-2} \text{ K}^{-1}$ ),  $N_A$  is Avagadro's number ( $6.022 \times 10^{23} \text{ mol}^{-1}$ ),  $e$  the charge of an electron ( $1.602 \times 10^{-19} \text{ C}$ ).

As this equation is derived from the Grahame equation, it is valid for low potentials below 25 mV [48]. The equation models the interface and salt layer as two plates of a capacitor and states that the magnitude of the Debye length depends solely on the properties of the liquid and not the surface, its charge or potential in a 1 : 1 cation : anion electrolyte.

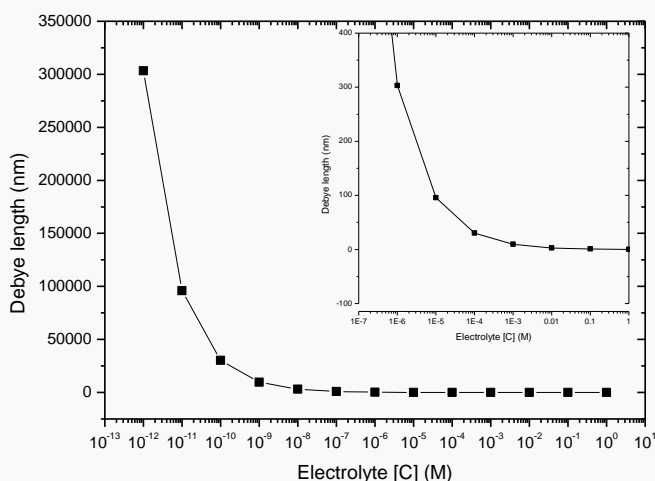


Figure 1-7 – Calculated Debye lengths for a monovalent 1 : 1 counterion buffer. The inset is a magnification of the length scale region that will be observed using a millimolar strength buffer.

Equation 1-11 was used to calculate the Debye distance for a monovalent 10 mM buffer such as typically used in experiments (Figure 1-7). It shows that sensor response comes from only interactions within 30.3 nm of the surface and not the bulk solution. In comparison, a 100 mM buffer the Debye length extends to only 0.96 nm while at 1 mM it interacts to a distance of 9.57 nm. High salt concentrations compress the double layer while lower ones create a more diffuse layer.

#### 1.6.4.2.8. Solution resistance, IR drop and constant phase elements

A current flowing from the bulk solution to the electrode encounters a resistance from the ions in solution ( $R_{\Omega}$ , also  $R_s$ ). These ions do not undergo electroactive reactions, thus  $R_s$  should remain constant as long as the amount of electrochemical species generated at the electrode is magnitudes lower than the bulk concentration.

In electrochemical systems, a voltage drop occurs across the solution. This voltage drop is a product of resistance ( $R$ ) of current ( $I$ ) passing through the solution. Experimentally, its effects are observed as broadening of the redox peaks due to the reduction in conductivity and a change between the observed and theoretically thermodynamically derived redox

potential of an electroactive species. In experimental terms a higher potential is needed than derived to drive the required reaction to account for this  $iR$  drop.

A constant phase element is a correction factor to more accurately model the equivalent electrical components and their imperfections discussed in modelling capacitance and its phase dependence. Its impedance,  $Z_{CPE}$ , is calculated as:

$$Z_{CPE} = \frac{1}{Y_{CPE}}$$

Where  $Y_{CPE}$  is the admittance constant phase element and is related to  $1/Z$  at 1 rad/s.

Experimentally CPE are used when using GPES software for fitting of equivalent circuit parameters. A value of zero to one is possible, with a perfect capacitor approaching a value of one and a perfect resistor a value of zero. A value exceeding or significantly below one indicated a poor fit from the modelling parameters in extrapolating the double layer capacitance,  $C_{dl}$  and was not used.

#### **1.6.4.2.9. Polarisation resistance, $R_p$**

The open circuit potential is the difference in electrical potential between the internal and external reference points when no external potential is applied and the circuit is open [45]. When an electrode potential is forced away from this open circuit potential, an electrode becomes polarised. If polarisation is sufficient depending on the ionic species present in solution, current is generated, electrons are transferred and electrochemical reactions occur. A resistance to this current flow also builds up because of the opposing counter ions termed polarisation resistance ( $R_p$ ).

#### **1.6.4.2.10. Warburg impedance**

The Warburg impedance models the bulk solution diffusion on a planar to semi-infinite distance. It behaves as a constant phase element i.e. an imperfect capacitor, with a phase of  $45^\circ$ , independent of frequency. The Warburg component retards current flow in a system due to the frequency effects on ions. At high frequencies, its effects are minimal as ions only have a short time to react to the applied field, but at low frequencies, ions diffuse further affecting the bulk solution and convection. It is observed in Nyquist plots as the tail of a semicircle, occurring at a  $45^\circ$  phase shift only when a redox species is present.

### 1.6.4.3. Nyquist plots

Nyquist plots allow the total impedance of a system (Equation 1-12) to be measured as a function of frequency and electrical parameters such as solution resistance  $R_\Omega$ , double layer capacitance  $C_d$ , and pseudo capacity  $C_s$  to be measured directly as opposed to using a single frequency and needing to extrapolate these values individually from equivalent circuits.

$$Z = \frac{R_B - j}{\omega C_B} = Z_{Re} - jZ_{Im} \quad (1-12)$$

where  $Z$  is the total impedance  $R_B$  the bulk resistance  $C_B$  the bulk capacitance,  $Z_{Re}$  the real impedance component,  $Z_{Im}$  the imaginary impedance component,  $j$  the square root of -1 and  $\omega$  equal to  $2\pi f$ .

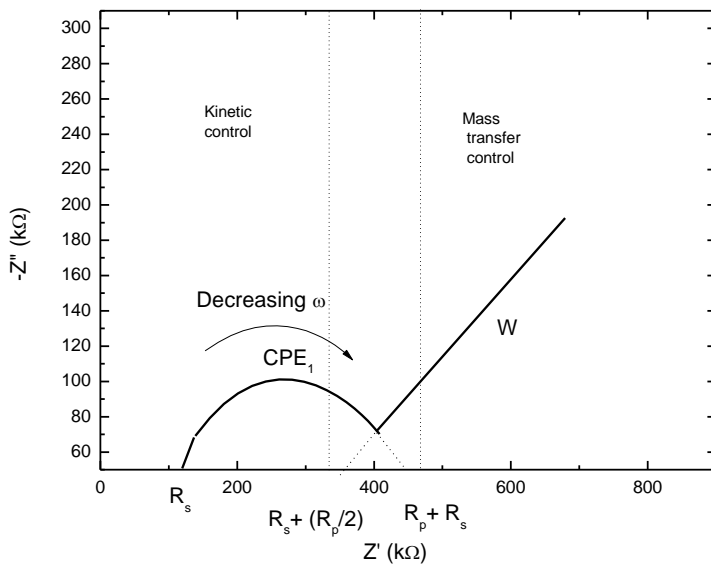


Figure 1-8 - Nyquist plot showing equivalent circuit components. Regions of mass transfer and kinetic control are found at low and high frequencies respectively.

An applied voltage induces a current in the system under study and the response is monitored at a range of frequencies. Thus impedance can be expressed as a complex function represented as the sum of the real  $Z'(\omega)$  and imaginary  $-Z''(\omega)$  components of resistance and capacitance. Plotting the real part on the X axis and the imaginary part on the Y axis of a

graph creates a Nyquist plot (Figure 1-8). Thus a vector of length  $|Z|$  with the angle between this vector and the x-axis is  $\omega$  ( $2\pi f$ ) corresponding to the impedance at a particular frequency.

Fitting data to a Nyquist format (Figure 1-8) shows how the electrical components of a species such as a monolayer or the organic layer of a biosensor can be extrapolated. The first semicircle intercept gives  $R_s$  ( $R_\Omega$ ), the solution or electrolyte resistance. The second intercept is the combined charge transfer resistance  $R_{ct}$  and solution resistance  $R_\Omega$ . Thus  $R_{ct}$  is derived by the second intercept minus  $R_\Omega$ . The Warburg component (W) occurs in faradaic systems and limits current flow due to diffusion constraints. This component has less effect at high frequencies but contributes significantly to low frequency impedance in the mass transport region.

### **1.6.5. Cyclic voltammetry**

Cyclic voltammetry is a powerful tool for interrogating reactions at an electrode interface. In cyclic voltammetry a linear scan is applied to an electrode and reversed by switching the direction of the scan at a certain time or potential. Consider an electrode in solution with an electroactive species. If a potential is applied that is more positive than  $E^{o'}$ , current begins to flow as reduction of the electroactive species occurs. As the potential grows more negative beyond  $E^{o'}$ , the surface concentration of active species drops, analyte flow drops to almost zero due to a depletion layer forming, mass transfer to and from the electrode, reaches its maximum as does the peak potential ( $E_p$ ). The current then drops and a peak shaped scan like Figure 1-9 is observed. If the potential is reversed in the positive direction, oxidation occurs assuming the redox probe undergoes a reversible Nernstian reaction. As the potential passes back through  $E^{o'}$  there is a temporary neutral balance of oxidise and reduced species. As the potential becomes more positive, more oxidation occurs and an anodic current flows until the same process repeats. Surface concentration drops, flux increases, followed by surface current and the potential drops.

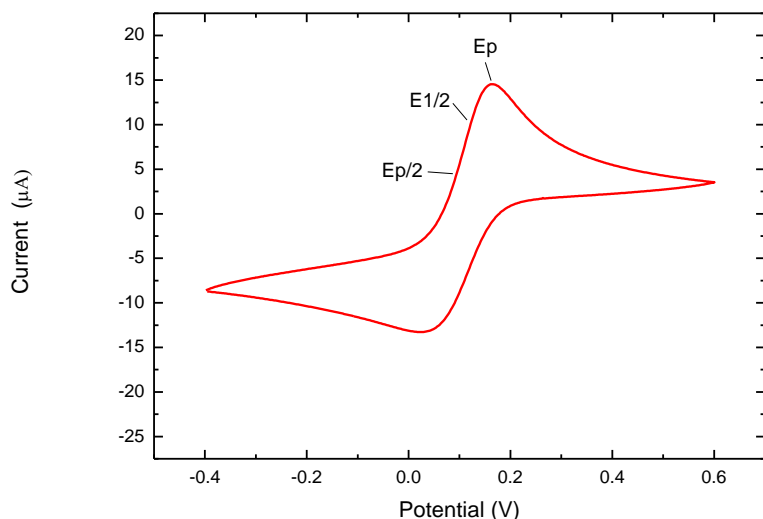


Figure 1-9 – Cyclic voltammogram of the current observed for a linear potential sweep of Nernstian (reversible) reactions. Performed using a scan rate of 50 mVs, with electrolyte 10 mM PBS containing 10 mM ferricyanide.

The peak current in a cyclic voltammogram is given in Equation 1-13:

$$i_p = 0.4463 \left( \frac{F^3}{RT} \right)^{1/2} n^{3/2} A D_o^{1/2} C_o^* v^{1/2} = (2.69 \times 10^5) A D_o^{1/2} C_o^* v^{1/2} \quad (1-13)$$

where  $F$  is faraday's constant, the charge on one mole of electrons,  $n$  the no of electrons transferred,  $A$  the electrode area ( $\text{cm}^2$ ),  $D_o$  the diffusion coefficient ( $\text{cm}^2/\text{s}$ ),  $C_o^*$  the bulk concentration of redox species,  $v$  the scan rate ( $\text{V/s}$ ),  $i_p$  peak current (A).

Because the peak observed can be broad and the true potential difficult to determine, often an alternative potential is used at  $i_p/2$ , called the half peak potential at  $E_p/2$  is used (Figure 1-9).

$$E_p - E_{p/2} = 2.20 \frac{RT}{nF} = \frac{56.5}{n} \text{mV at } 25^\circ\text{C} \quad (1-14)$$

The relation of peak potential and half peak to  $n$ , the number of electrons transferred in the redox reaction is given by Equation 1-14. As  $i_p/v^{1/2}C_o^*$  is essentially a constant depending on  $n^{3/2}$  and  $D_o^{1/2}$  the parameter  $n$  can be estimated for an unknown redox reaction. Thus

Equation 1-14 shows that the peak potential ( $E_p$ ) is independent of scan rate ( $v$ ), peak current ( $i_p$ ) and is proportional to the square root of the scan rate ( $v^{1/2}$ ). This electrochemical analysis was used to test electrode cleaning performance and biosensor deposition. If the peak current with a redox mediator is proportional to the square root of scan rate, then a clean electroactive electrode is present. As the active surface area is reduced, the current flow is reduced as a function of deposition.

## **1.7. Approaches to metal ion binding**

### **1.7.1. Biosensors and the application of electrochemistry**

Regardless of the recognition mechanism of the sensor which may use proteins, peptides or supra-molecules, a system to convert and use the analyte signal to a quantifiable form is needed to see if such biorecognition elements are operating in this way. A number of analytical electrochemical tools using a standard 3 electrode set up can be used.

### **1.7.2. Mercury based polarography**

Electrochemistry is broadly defined as the study of chemical reactions at an interface under an applied potential. Non-faradaic systems involve no electron transfer and conventionally used potential or impedance based measurements to observe interfacial changes. This approach is often used to model interactions in organic monolayers or the effect of toxins on these [36]. The faradaic approach relies on chemical reactions between redox species and often produces a current based signal proportional to the analyte concentration. The current observed in the system is a combination of the redox species in parallel with resistive and capacitive elements due to molecular double layer (as discussed in Impedance equivalent circuits). A complex multi-model system can explain, electrode kinetics but fundamentally these forces determine the limit of detection for the following techniques.

Polarography is the voltammetric measurement of a system governed by analyte diffusion and convectional mass transport. The limiting current observed is directly proportional to the analyte concentration. Traditionally the technique is used on a hanging mercury drop electrodes (HMDE) which uses a spherical Hg drop extruded from a glass as the working

electrode. Particularly advantageous, the working surface area can be increased or decreased in proportion to the capillary force applied and allows rapid regeneration of a fresh electrode.

Mercury based electrochemistry is, along with hydrogen electrochemistry, one of the earliest electrochemical approaches used, and unlike hydrogen systems, is still regularly used. A potential is applied between working and counter electrodes and measured against the reference. A range of interrogation profiles can then be applied to interrogate the sample.

Normal pulse polarography (NPP) has the advantages of having a minimal background capacitance current and removes the problem of a varying potential ramp by applying a series of potential steps of varying amplitude. Current measurements are made near the end of each pulse which allows the interfering charging current to dissipate via exponential decay (decay  $\propto \text{time}^{1/2}$ ) allowing the faradaic current to be determined and offers typical LoDs of  $10^{-7}$  M [49]. However, because of this decay depletion of the limiting current occurs with time and this method has been superseded by other PP methods.

Differential pulse polarography (DPP) is similar to NPP, the difference being each potential step has the same amplitude while the applied potential increases anodically each time. Therefore the current obtained is a combination of linear ramp and square wave systems. The current here is measured just before the step and just before the end of the ramp (step drop). The analytical current is the difference between the two removing the charging current addition. A typical LoD is of the magnitude  $10^{-10}$  M [49].

Anodic stripping voltammetry (ASV) is a similar technique but offers greatly superior sensitivity. The initial step where the Hg electrode is held at a negative potential to form amalgams with cationic analytes still remains. However, a linear ramp rate typically of 2 to  $100 \text{ mV s}^{-1}$  rather than square wave potential is used to reoxidise the analyte and generate the signal current. As a first approximation, the analyte concentration is determined by dividing the observed current by the number of electrons needed to reoxidise the analyte cation to a neutral metal atom. This is because the number of moles of analyte adsorbed in the amalgam drop is proportional to the peak current [50]. Because of its impressive LoD limit ASV and its variants are now the main choice for trace metal analysis. This is especially so since advances are being made in electrode miniaturisation and composition.

Chapman [50] performed ASV on a vibrating microelectrode using single step deposition. Traditional macroscopic electrodes use stirring to increase mass transport to the electrode,

thereby enhancing deposition and the signal obtained. However, the use of microelectrodes showed the opposite and greater sensitivity was obtained without stirring due to the smaller electrode area and a thinner diffusion layer. Increasing vibrating frequency offered up to 4 nM sensitivity to copper ions. As a result, many newer electrodes are scaled down to the micron level for greater mass transport effects.

Traditional methods of detecting metal ions such as atomic fluorescence spectroscopy and coupled plasma mass spectroscopy are laboratory only specialised devices that are inappropriate as practical portable devices in the field [51]. Protein-small molecule interactions can be measured by dual polarisation interferometry (DPI) a method that relies on optical interference within two waveguides. Essentially a change in refractive index is measured to determine mass and thickness changes at an interface. Similarly the quartz crystal microbalance (QCM) is another successful tool for monitoring interactions resulting in small mass changes. In this technique, discussed in Chapter 3, binding is detected as a resonant frequency change as species bind at the interface of a non centrosymmetric crystal. As well as mass changes, structurally significant conformational changes that occur on binding can be identified, such as antibody-antigen interactions [52]. Other techniques such as shallow angle neutron scattering (SANS), X-ray scattering and X-ray crystallography have been largely unsuccessful as a method of monitoring binding and are criticised as artificial, as the original system has been significantly altered due to the required processing steps. Current analytical tools are generally laboratory based, need an expert knowledge system and are costly.

Attempts have been made to create a practical portable measurement system using ASV on gold microelectrodes [53]. The ability to co-determine As (III) and As (V) using specific pre-treatment by chemically reducing As (III) to As (V) was proven. Allowing simultaneous determination of multiple ionic states in a single technique is certainly advantageous and is an emerging trend, but a common problem highlighted was sensitivity to interfering lead, iron and nickel ions. Gold wire electrodes also showed success in determining mercury and copper using ASV in 0.01M HCl but showed interference from bromide and chloride ions [54].

Evolution of the traditional HMDE has occurred because of the toxicity of mercury and associated hazards in handling large quantities of the material. However there has yet to emerge another electrode that offers a renewable, uniform, atomically flat, polishing free

surface that has such a wide interrogation window. As a result, novel approaches to creating films, static drops or coatings of smaller, less hazardous volume of mercury with the same or enhanced properties of bulk mercury electrodes are now in use. A diverse number of metal ions can be analysed using mercury electrodes; static mercury drops can co-determine complex metal ion solutions of multiple valences. For example, Cr (VI), Pb (II), Sn (II), Sb (III) Cu (II) and Zn (II) [55] have been determined within the same solution.

A cutting edge variant of the mercury electrode uses a mercury ion selective electrode (Hg-ISE) [56]. This allowed a LoD  $3.31 \times 10^{-6}$  M for metal ions showing that by controlling fundamental parameters, reducing area and increasing mass transport sensitivity can be greatly enhanced. There is much literature specifically on sensing of 'heavy' metals particularly chromium, lead, copper, zinc and mercury. Beyond these elements, research on systems giving high sensitivity and selectivity for other metals is currently limited. Due to the legal and safety legislations needed for laboratories to handle radioactive sources literature dealing with radioisotope binding is very sparse.

One notable success using Van den berg's pre-reduction steps was an example of AdSV detection for uranium complexes [57]. By reducing U (VI) to U (V) using cupferron complexation, a detection limit of 0.1 mg/L was achieved. Pre-treatment steps in many cases are deemed necessary to remove interfering organics or competing ions that would otherwise cause the sensor to give false readings. A new bismuth coated electrode was promoted but the 'lower toxicity' claim as compared to mercury electrodes was questionable. The anodic range of bismuth was notably narrower too, which limits the practical interrogation window [58]. A brief review of electrochemical techniques has been presented to show the high sensitivity to a chosen analyte possible through purely electrochemical means. These approaches are summarised in Table 1-4.

Table 1-4 - The lowest detection limits for a range of electro-analytical techniques [59].

Technique	Lowest Detection Limit / M
Normal polarography	$5 \times 10^{-3}$
Cyclic Voltammetry	$1 \times 10^{-5}$
Sampled DC polarography	$1 \times 10^{-5}$
Normal pulse polarography	$10^{-7}$ - $10^{-8}$
Differential pulse polarography	$10^{-8}$ - $5 \times 10^{-5}$
Square-wave polarography	$1 \times 10^{-8}$
Anodic Stripping Voltammetry	$10^{-10}$ - $10^{-11}$

Trace metal analysis often needed to the magnitudes of parts per million (ppm) or even per billion (ppb) in the case of radionuclides. A real time analysis system must have dynamic response, allow reusable electrodes with a long life span and still offer some mechanism to differentiate between analytes. Because this is not possible for the reasons discussed with mercury based electrochemistry, alternative binding hosts will now be discussed.

## 1.8. Protein-metal binding and supra-molecular chemistry

The binding mechanism of a good bio- or chemo-sensor depends on the fundamental chemistry between analyte and host. An individual ion or molecule's complexing ability is dependent on its electronic configuration and the number of attachment points to its central atom, consequently determining the orientation of the electron pairs around the atom to maximise distance, forming a conformation imposed by electrostatic repulsion. A slight complication is that the size and charge of the central atom influences the distance between the bonding pairs; the charge radius ratio determines the arm length of a molecule and the overall volume in three dimensional space that the molecule occupies. Common geometries of molecules are shown in Figure 1-10.

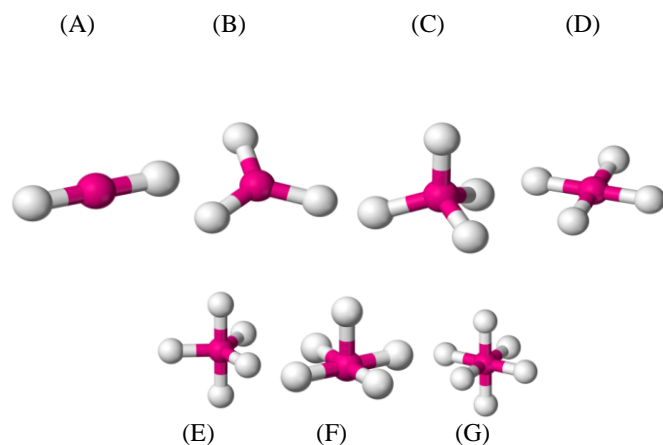


Figure 1-10 - Common geometries of molecules and their corresponding coordination number. The central atoms (pink) show the following coordination geometries and coordination numbers; (A), linear (2); (B), trigonal planar (3); (C), tetrahedral geometry (4); (D), square planar (4); (E), trigonal bipyramidal (5); (F), square pyramidal (5); and (G) octahedral (6).

Supra-molecular chemistry explains intermolecular interactions via weak van-der-Waals, electrostatics and steric recognition, which are the fundamental forces between host and guest molecules. Self assembly of molecules occurs due to solvent-molecule interaction and the hydrophobic effect. Thus, the key to successful stable binding of component molecules to form a desired complex is the matching of the number of hydrogen bond donor and acceptor sites, interlocking steric sites and size interaction of the molecules. A subset of this area uses chelation chemistry, where specific metal coordination of the analyte or guest is used to recognise and bind specific host molecules.

The classic supra-molecular example is the crown ether host, a circular molecule with the inner hole allowing individual metal ion docking if size and charge consideration allow. These are discussed extensively in Chapter 3. A current development of this classic system is the cyclophane-type crown ether the tetrathiafulvalene molecule (TTF) (see Figure 1-11). Variants have increasingly used metal binding for application such as molecular switches [60]. Their  $\pi$  electron donating capabilities are useful in metallic charge transfer systems. However, their specificity is limited to a geometrical-charge system. The molecule can be reversibly oxidized to cation or di-cation forms at usable potentials giving it many practical

advantages for reversible switching systems observed using optical fluorescence and nuclear magnetic resonance. In combination with impedance or optical methods such systems could be adapted to biosensing. A modification of the standard calixerine system for binding radionuclides showed selectivity for the gamma emitter  $^{137}\text{Cs}^+$  cation while ignoring  $\text{K}^+$  and  $\text{Na}^+$  ions [61].

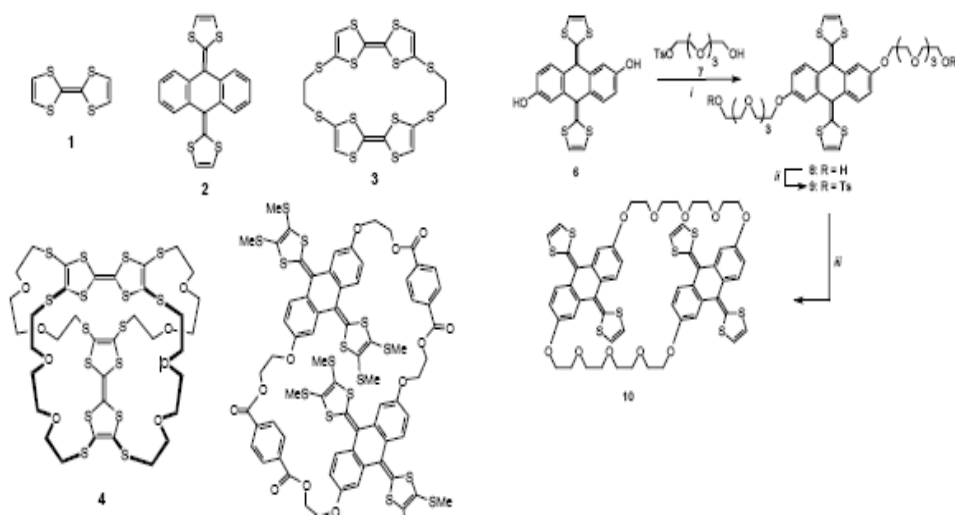


Figure 1-11 - Examples of supra-molecular host guest recognition. Incorporation of tetrathiafulvalene (TTF) molecule into a variety of tested host systems [60].

More recent developments which were originally aimed at diagnostic, therapeutic and pharmaceutical applications of radionuclide tracer binding could potentially be adapted to biosensing transducer mechanisms. Complexes of La (III) ions Gd, Eu, Sm and Ce were bound to vectors that then targeted and bound to specific tissues, cells, proteins or nucleic acid sequences. These bifunctional chelates use one binding site for the metal ion and a second for the target binder. The fundamental molecule is the bis-anhydride fDTPA that contains 3 amines and 4 oxygen binding sites suitable for lanthanide binding [62]. These examples further show that by controlling the steric and charge configuration, a number of proposed hosts can be made to bind to chosen targets. If mechanisms can be found for binding to an electrode surface or insertion into a SAM layer these systems would theoretically work well with impedance sensors.

A number of supramolecular systems were identified as being potential radionuclide binders. The binding mechanisms of these systems can be engineered due to the low 3D complexity as compared to protein engineering. These molecules however are expensive and require extensive chemical synthesis with hazardous compounds. Furthermore, attachment of the host ligands to a substrate must not inhibit the binding properties of the molecule.

## **1.9. Protein-metal binding and biotechnology**

Genetic recombination is a useful biotechnological tool that is of increasing use for generating proteins with desirable qualities. With an increasing number of bacterial genomes being analysed an increasing number of sequences are being identified and used in biotechnology for the engineering of biological components.

It is possible to use recombinant DNA biotechnologies to endow viable microbial cells with foreign heterologous properties without the need to destroy and purify the cells. The addition of novel cell surface proteins is now becoming a feasible option for whole cell biosensors. As well as introducing mechanisms to bind fluorophores such as green fluorescent protein (GFP) Tanaka [63] showed by inserting membrane based proteins that covalently bind to the outer membrane of the cell wall, an anchoring mechanism to bind external agents from peptides, biocatalysts and enzymes was shown to be possible.

Currently however, protein engineering is better understood and more likely to yield short term results. There are a number of metal binding protein classes that are currently under analysis, each responsible for homeostasis, bioaccumulation or binding. These will now be discussed.

### **1.9.1. Metallohistins, metallothionein, phyto-chelatins and metallochaperones**

Metallohistins are a recently identified class of histidine rich metal binding proteins found in the plant *Alnus glutinosa*. Two identified peptides AgNt84 (a 4 region, 99 amino acid peptide) and Ag164 (an 86 amino acid homolog) are known to bind multiple divalent cations including  $Zn^{2+}$ ,  $Cu^{2+}$ ,  $Co^{2+}$ ,  $Cd^{2+}$  and  $Hg^{2+}$ . These proteins have been combined with a modified microcantilever system for real time concentration measurements [64]. Successful

binding caused a detectable deformation in the cantilever showing some selectivity with binding to  $Zn^{2+}$  but not  $Mn^{2+}$  ions.

Metallothionein and phyto-chelatins are an area of expanding research. Metallothionein genes have been identified but few have been isolated and analysed for metal binding. Metallothioneins of aquatic hyphomycetes *Fontanospora fusiramosa* and *Flagellospora curta* Metallothionein were exposed to  $Cu^{2+}$ ,  $Cd^{2+}$ , or  $Zn^{2+}$  [65]. *Flagellospora curta* metallothionein bound more  $Cu^{2+}$  and  $Cd^{2+}$ , the believed mechanism due to the presence of low molecular weight peptides containing glutathione (a natural antioxidant tripeptide formed from glutamic acid, cysteine and glycine, phytochelatin) which acted as the  $Cu^{2+}$  and  $Zn^{2+}$  binding domains.

Phyto-chelatins are metal chelating peptides important in heavy metal regulation in certain plants, fungi and bacteria and contain the sequence  $(\gamma\text{-Glu-Cys})_n\text{-Gly}$  [66]. Examples have been found to bind copper and zinc for storage in both eukaryotes and prokaryotes [65]. Nonetheless, all examples so far show little selectivity.

### **1.9.2. Metal binding proteins and homologous sequences**

Metallochaperones sequester metals in the cytoplasm and deliver them to specific associated proteins. Examples include the nickel chaperone that carries  $Ni^{2+}$  to urease [67] and farataxin chaperone that delivers iron ions to heme clusters. Periplasmic protein (PCuAC) is known to bind and deliver Cu (I) ions to subunit II of *Thermus thermophilus* ba(3) oxidase. The CopZ chaperone interacts with protein CopA, chaperone TorD, a molybdenum transporter, and four accessory proteins for nickel transport (UreD, UreE, UreF, and UreG) to form the nickel-containing active site in the urease apoprotein (UreABC) [68].

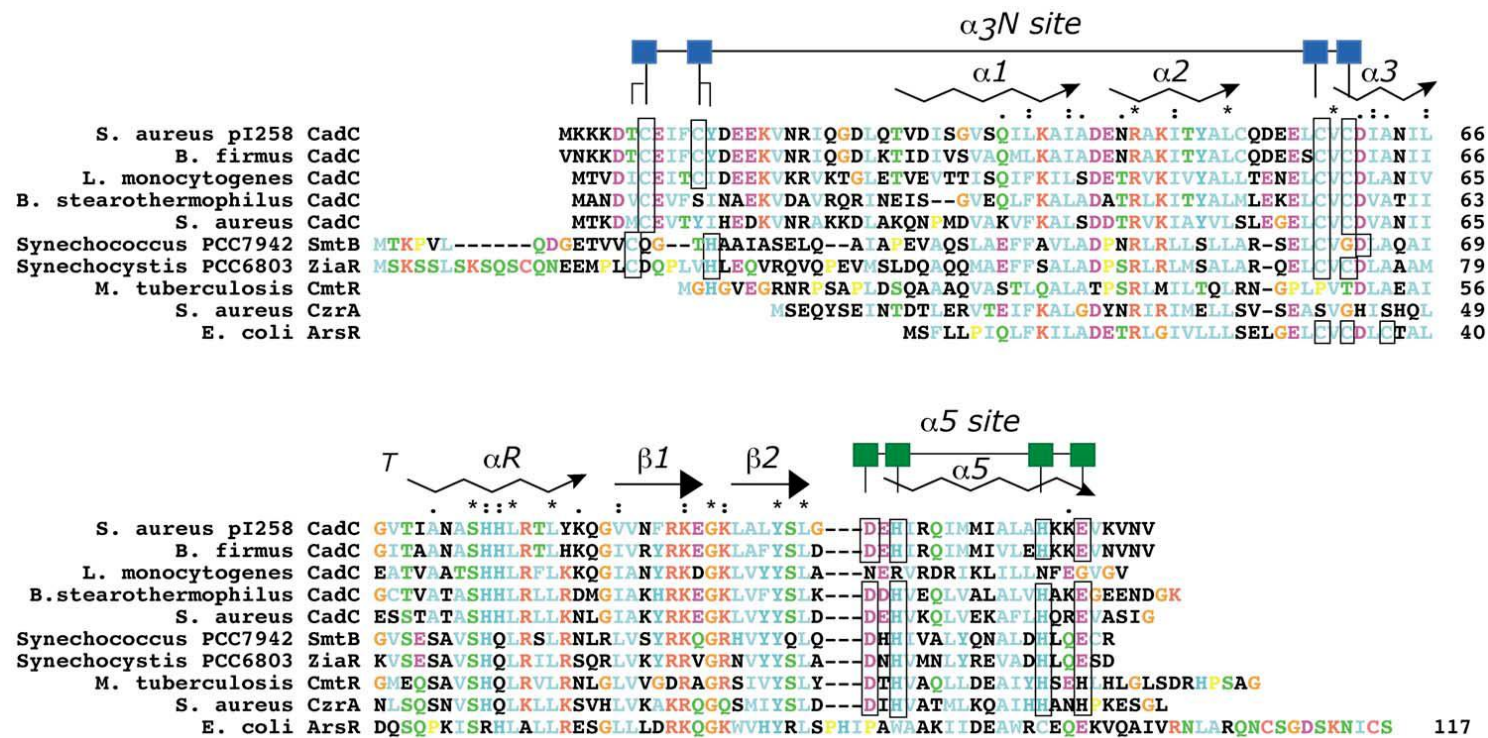


Figure 1-12 - Conserved residue sequences between a number of metal binding proteins. Note conservation of residue sequences of lysine (K), aspartate (D), histidine (H) and cysteine (C) ([65]).

*Staphylococcus aureus* plasmid *pI258-CadC* encodes the CadC protein that, binds a number of heavy metal divalent ions including Cd (II), Pb (II), Bi (III) and Zn (II). Two distinct metal-binding sites have been identified; a thiolate-rich alpha (3) N site composed entirely of cysteine residues that bind larger metal ions such as Cd (II), Pb (II) and Bi (III), and a second C-terminal alpha (5) site at the dimer interface, containing no cysteine residues that binds smaller, harder metal ions such as Co(II) and Zn(II) [69]. Elucidation of the genetic sequence and comparison to a number of other metal binding proteins including SmtB (tetrahedral coordination zinc binding), ZiaR (zinc and cadmium (II) binding), CrzA (zinc binding) shows consistent cysteine residue placement to create metal binding sites upon peptide folding into a 3 dimensional protein. An example is shown by the alignment of CadC sequences (Figure 1-12) whilst Figure 1-11 shows the 2 proposed binding sites within CadC.

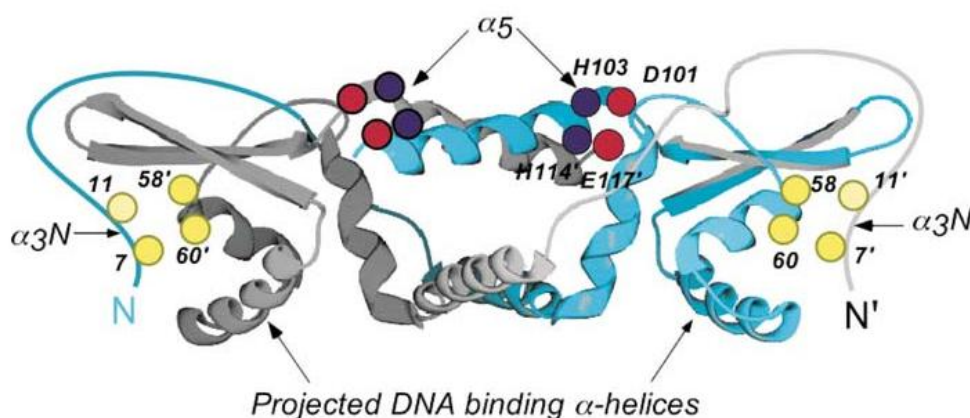


Figure 1-13 - Three dimensional structure of the CadC binding peptide and the 2  $\alpha$  helical binding domains for  $\text{Cd}^{2+}$ .

A similar set of metal binding proteins have been shown to bind various valence states of the metalloid arsenic in *Ochrobactrum tritici* [70]. These studies show that to a degree, most biological metal binding is related to specific ion size and charge density range as the mechanisms of selectivity. The range of metal binding proteins is currently limited to those in biological processes such as Fe, Ni, Cu, Mb, and Zn. For individual analyte detection, proteins with greater specificity are needed and for a wider range of analytes. These binding proteins are beginning to be found by analysing specific bacterial strains that have evolved in

toxic environments. The arsenic-ATPase pumps of *Escherichia coli* are composed of subunits ArsA, the catalytic sector of the pump and ArsB, the transmembrane channel. Together they form an As (III) translocating pump that removes As<sup>3+</sup> and also <sup>137</sup>Cs<sup>+</sup> from the cell cytosol. If the ArsA gene is isolated without the ArsB gene it can still be expressed, to yield a soluble As (III) binding protein. The ArsA subunit contains 2 homologous halves connected by a 25 residue linker. Binding of As (III) or Sb (III) to 3 specific cysteine residues causes a conformational change in the system [71] causing a detectable output signal that could potentially be used with impedance systems for real time biosensing. Trans-acting repressor, ArsD has been identified and is encoded by the operon *arsRDABC*. ArsD encodes a 120 residue monomer that confers resistance to As and Sb ions in *E.coli*. ArsD was observed to increase the ArsA affinity at lower concentrations, activating the pump at significantly lower trivalent cation concentrations. A 60 fold increase in sensitivity from 1.2 mM to 20 μM was found [72].

ArsD selectivity was further confirmed when its structure was identified and binding interrogated. The ArsD monomer has two-pairs of vicinal cysteine residues, Cys12-Cys13 and Cys112-Cys113. As a homodimer, the structure contained 4 vicinal pairs. However rather than pairs acting as individual binding sites, interaction and displacement studies of metal ions showed that displacement at one site inhibited release at the others. [71]. This example shows, that in some cases, specifically evolved proteins show complex sequential and selective binding as opposed to simple charge-co-ordination recognition.

## **1.10. Metal binding and peptide engineering**

The limiting factor for biological based biosensors is currently the lack of knowledge in understanding the details of metal binding mechanisms within proteins. The few that have been analysed have been discussed in detail. Attempts have begun to engineer peptides specifically with the ability to bind specific metals of known co-ordination chemistry as opposed to searching for natural sequences in bacteria. A polypeptide is essentially just a linear arrangement of amino acid residues that assemble into a more complex 3 dimensional arrangement.

A number of similarities behind metal binding sequences have been highlighted and begun to be used in generating such synthetic peptides. Cysteine and histidine rich sequences Gly-His-

His-Pro-His-Gly (named HP) and Gly-Cys-Gly-Cys-Pro-Cys-Gly-Cys-Gly (named CP) have been engineered into the LamB proteins and expressed in *E. coli*. The resulting recombinant proteins have been shown to bind divalent  $\text{Cd}^{2+}$  but not  $\text{Cu}^{2+}$  or  $\text{Zn}^{2+}$  [73]. Similarly, binding peptides of motif  $(\text{Glu-Cys})_n\text{Gly}$  (termed synthetic phytochelatins) engineered into *E. coli* were believed to bind  $\text{Hg}^{2+}$  ions more effectively than did metallothioneins [74]. These examples highlight the ability of cysteine-rich peptides to bind metal ions. However, they often lack specificity to the ions they bind and this can cause problems for specific recovery and removal of ions afterwards [75].

Cysteine derivatives of the TRI peptide family ( $\text{Ac-G(LKALEEK)}_4\text{G-NH}_2$ ) are known to bind metal ions with a trigonal geometry. Increasing complexity to the next level creates protein subunits, the helix or beta barrel. A repeat of a seven amino acid motif like in this sequence, known as a heptad, is known to assemble into an alpha helical conformation. By substituting the leucines for cysteine residues that contain sulphur groups the resulting peptide self assembles into an alpha helix with outer exposed chelation sites that have been engineered to appear at a specific inter-sulphur distance on the sequence (Figure 1-14). An alpha helix will be generated as long as the first and fourth residues are hydrophobic (leucine or isoleucine) and the others hydrophilic. Thus, between adjacent peptide domains are created for metals with 4 binding sites; tetrahedral structures [76].

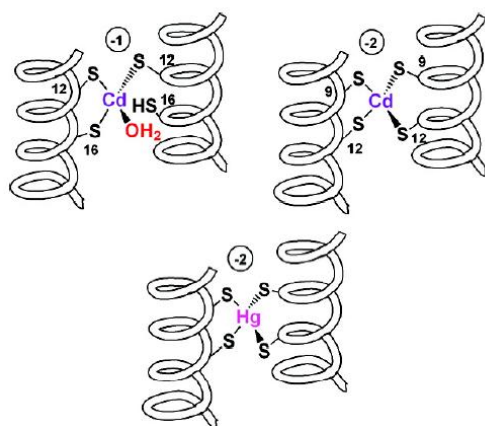


Figure 1-14 - Engineered  $\alpha$  helical peptides and the exposed chelating sulphur binding sites between peptide arrays [76]. Tetrahedral ions satisfy all sites while  $\text{Cd}^{2+}$  ions have been shown to bind three sites, with the fourth satisfied by water hydrogen bonding in spite of the entropically less favourable conditions.

Even a slight alteration in peptide length with spacer residues affects the assembled conformation. Engineering peptides is not simply done by recognition of binding motifs alone. An extended engineered motif -Cysd-X-X-X-Cysa (a and d are sites of possible cysteine side chain addition) with one additional spacer residue occurs in TRionic liquid9CL12C. Addition of metal ions stabilised these bundles by binding to the 4 cysteine sulphur groups although under some distortion, but behaved similar to the metallochaperone HAH1, the transporter that regulates copper homeostasis [77]. The ability to coordinate with homoleptic tetrahedral cadmium complexes, commonly exhibited by metal ores was shown. This method opens up a huge realm for possibilities to engineer metal binding proteins, although because the technique works on satisfying charge and co-ordination chemistry there will be limited specificity. Any metal of tetrahedral geometry within a size limit is likely to bind. If a method to assemble the peptides, for example at controlled distances in a self assemble monolayer, or the peptides can be bound to an electrode substrate, then there is potential for introducing some size selectivity to the ions bound.

### **1.11. Sensitivity and selectivity: biological vs chemical receptors**

Regardless of the binding mechanism chosen for the sensor, a minimal range of sensitivity is essential and specific to the application. The LoD of biological biosensors compared to electrochemical equivalents has shown that generally, biobased sensors lag behind (e.g. ASV fM levels compared to  $\mu\text{M}$  for the ArsD protein).

However fM level metal detection has been shown by combining the 2 heavy metal proteins, GST-SmtA and MerR, over expressed in *E.coli* [78]. Using a 3 electrode electrochemical setup, a working electrode which contained these proteins was bound to a gold substrate via a self assembled thiol monolayer. While MerR selectively binds mercury, GST-SmtA potentiostatic measurements confirmed GST-SmtA bound  $\text{Cu}^{2+}$ ,  $\text{Cd}^{2+}$ ,  $\text{Hg}^{2+}$ , and  $\text{Zn}^{2+}$  ions. Control electrodes of bovine serum albumin or urease did not detect these metals. fM concentrations were detectable using capacitance data obtained from impedance scans showing conformational change of the immobilized protein upon successful binding. Thus a combination of biological recognition for selectivity and high sensitivity is achievable if combined with electrochemical techniques.

## **1.12. Metal Chelation**

### **1.12.1. Introduction**

Metal complexes are associations of a metal atom or ion and a second species known as the ligand. Ligands which form complexes with metals are *chelating agents* while the complexes formed are termed *metal chelates*. These can be stable in solid or liquid state and are characterised by two valences, auxiliary and principal. Auxiliary valency is the number of ligand atoms bound to the metal, equal to the co-ordination number. The primary valency, also called the oxidation state ( $1^+$ ,  $2^+$ ,  $3^+$ ) typically have co-ordination numbers of 4 or 6, with less common values of 2, 3, 5, 7, 8, 9 and even 10 possible [79].

### **1.12.2. Conditions of Chelation**

The metal ion acts as an electron acceptor and the ligand an electron donor, ie behaving as a ligand Lewis base and a metal Lewis acid. Competing reactions influence the rate and ability of chelation. Metal ions can undergo hydrolysis releasing hydrogen ions in to solution that can then result in protonation of ligands reducing chelation towards the metal ion.

### **1.12.3. Ligand donor atoms**

For chelation to occur the ligand must have at least two donor atoms capable of bonding to the metal ion. For this to occur, that is, elements that act as donors must be more electronegative, ie to the right side of the periodic table (group V – nitrogen, phosphorus, arsenic, antimony, group VI – oxygen, sulphur selenium, tellurium, while the group VII halogens often behave individually as mononuclear complexes).

### **1.12.4. Ligand donor groups**

Basic groups, those containing an atom with a group of lone electron which may interact with a metal ion or proton are shown in the first two columns in Table 1-5. At low pH, competitive protonation of the ligand may be so extensive that donor atoms, some or all, are completely inhibited in binding to the metal ion. Acidic groups that lose a proton and interact with a metal ion are shown in columns three and four of Table 1-5.

Table 1-5 - Table of important ligand electron donor groups available in metal chelation.

Important basic ligand donor groups		Important acidic ligand donor groups		Coloured chelate groups that may interfere with scintillation	
Structure	Name	Structure	Name	Structure	Name
-NH <sub>2</sub>	amine	-CO <sub>2</sub> H	Carboxylic	C=O	Carbonyl
-NH	imino	-SO <sub>3</sub> H	Sulphonic	C=S	Thioketo
-N=	tertiary acyclic or hetro-cyclic nitrogen	-PO(OH) <sub>2</sub>	phosphoric	-CH=N-	Azomethine
=O	carbonyl	-OH	Enolic, phenolic	-N=N-	Azo
-O-	ether, ester	=N-OH	oxime	-N=O	Nitroso
=N-OH	oxime	-SH	Thioenolic, thiophenolic	-NO <sub>2</sub>	Nitro
-SH	Thioenolic, thiophenolic				

π-bonding occurs when metal d-orbital electrons interact with vacant ligand orbital's, resulting in a metal to ligand electron transfer. However, in σ-bonding the reverse occurs and an electron is transferred from ligand to metal. Steric restrictions also influence binding and therefore, the donor atoms must be spatially available. Those linked to two carbons are particularly flexible, while bulky side groups hinder the closest approach of the metal ion.

As well as electron transfer, many chelating agents lose protons to form anions that coordinate to the metal ion (eg glycine forms the glycinate ion). Bidentate ligands (those with donating groups of different composition) are often more stable and easier to prepare. Generally, the more available donor atoms capable of binding to a metal ion the more stable the chelate complex will be.

### 1.12.5. Colour in chelates

There are a number of mechanisms that cause a range of metal chelates to express strong vibrant colours, due to absorbance in the visible region of the electromagnetic spectrum. While this can be useful for an immediate visual confirmation of binding, these chelates will interfere with scintillation counting of  $\beta$  radiation.

These mechanisms include; (I), d-d transitions; metal empty, filled or half occupied orbitals and the transition between them; (II), transition with ligands ( $\pi^* \leftarrow \pi$ ) excitation from low to high energy orbitals. Organic ligands, due to delocalised  $\pi$  electron pairs, absorb UV light and shorter wavelengths. Such chromophoric groups that may interfere with scintillation are summarised in columns 3 and 4 of Table 1-5. This problem is increased if phenolic rings are introduced such as those in solid scintillants. In contrast, the problem is minimised if such groups are separate from the chelator, which is why chelation groups and solid scintillants were incorporated on to particles or surfaces as independent components. This was to minimise ( $\pi^* \leftarrow \pi$ ) bonding and coloured products. (III), Charge transfer transitions occur when an electron is transferred from ligand to metal, effectively reducing it, or in the reverse direction, oxidising it, both resulting in strong absorption bands.

Aromatic compounds themselves act as capable chelators due to the low lying vacant  $\pi$  orbitals that interact with filled metal d-orbitals causing a metal to ligand bond, (eg, 2,2',-bipyridyl 1,10-phenanthroline and phenylenebis(dimethylarsine) [80]) and can be used directly for colourimetric detection of micro molar levels of Cu (I) and Fe (II) ions respectively.

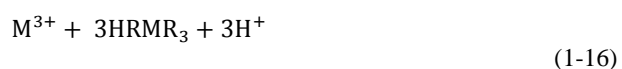
### 1.12.6. Groups with affinity for metal ions

There are a number of common ligands in regular use. Common simple organic metal chelators include oxalic acid, ethylenediamine and glycine. Iminodiacetic acid is tetra dentate, forming a four bond coordination, leaving a further three bonds free. Nitriloacetic acid is a sexadentate molecule and interacts with a metal ion through four bonds leaving two available. ETDA is sexadentate and typically coordinates five bonds with the metal ligand, with one remaining bond for other interactions. NTA and EDTA form three and five chelate rings when all their donor atoms are chelated creating highly stable complexes with only a single ligand molecule.

Traditional 'weak' metal ion exchangers are metal ion exchange resins. These include diethylammoniummethyl (DEAE) groups (anions) and carboxy methyl (CM) (cations). 'Strong' ion exchangers are sulfonate (S) (cation), sulfopropyl (SP) groups (cation) and quaternary ammonium ethyl (QAE) (anion) groups. 'Weak' and 'strong' exchangers do not refer how strongly a complex binds to a ligand. Strong ion exchangers are essentially independent of pH, while for weak exchangers, the charge held and protonation state varies with pH.

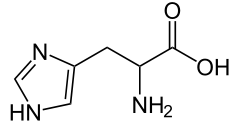
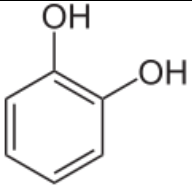
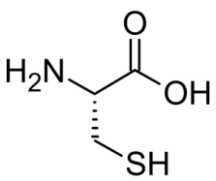
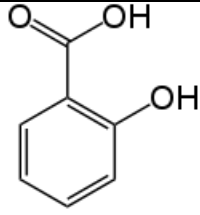
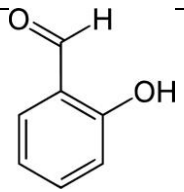
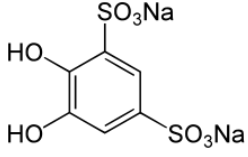
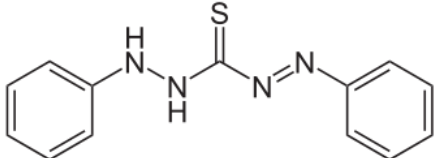
### 1.12.7. Ligands with one acidic and one basic group

These chelates often interact with a metal ion to form a neutrally charged species as both oxidation and chelation number is satisfied. Divalent ions with a coordination number of four react as shown in Equation 1-15, while trivalent ions with a coordination number of six follow Equation 1-16.



There are a number of biological molecules that also form stable chelates. The  $\alpha$ -amino acid glycine, between pH 4 and 9, occurs in a zwitterionic state and forms a five membered ring with a metal ion. Histidine and cysteine similarly act as good chelators due to the  $NH_2$  and  $SH$  groups, the histidine additionally having an imidazole. A summary of other biological metal affinity ligands is presented in Table 1-6.

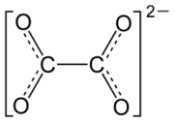
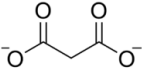
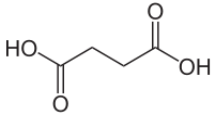
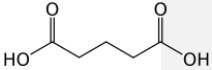
Table 1-6 – A selection of bidentate and monodentate chelators.

Ligands with one acidic and one basic group		Ligands with two acidic groups	
Histidine		Catechol	
Cysteine		Salicylic acid	
Salicylaldehyde		Tiron	
Dithizone			

### 1.12.8. Ligands with two acidic groups

These chelates are made from inorganic acids as well as organic ligands including  $\text{CO}_3^{2-}$ ,  $\text{SO}_4^{2-}$ ,  $\text{PO}_4^{3-}$  and  $\text{CrO}_4^{2-}$ . Chelation comes from the electronegative oxygens interacting with a cation. Nitrates and perchlorates too can act as metal binders. The simplest organic dibasic acid is oxalic acid. Table 1-7 shows a rare exception to the ‘more, donor groups the more stable the complex’ rule. As complexity of these acids increases, the stability of the chelate complexes (and stability constants) actually decreases.

Table 1-7 – Decreasing stability of chelation complexes for diacidic chelators.

Oxalate >	Malonate >	Succinate >	Glutarate >
			

### 1.12.9. Multidentate ligands

Multidentate ligands contain two or more different donor atoms, typically oxygen or nitrogen. While these structures can be complex, they commonly have flexible carbon backbones forming five membered rings with varying functional group. The simplest, ethylene diamine consists of a hydrocarbon backbone adjacent to primary amine groups.

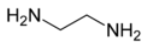
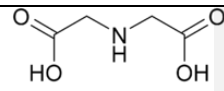
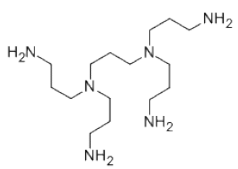
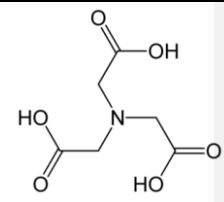
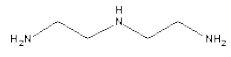
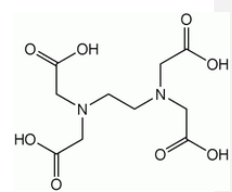
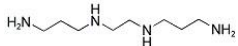
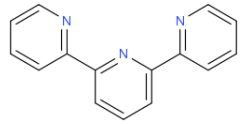
Increasing the number of carbon atoms and amines we have structures as shown in Table 1-8. However, simply increasing donor atoms from di-, tri- to penta-dentate does not necessarily make a more suitable co-ordination ligand. n-n'-di-2 aminoethyl ethylene diamine (Table 1-8, column one) is highly stable and available in quinque- to sexadentate forms. However, increasing the number of nitrogens causes increasing basicity, so increasing pH resulting in competitive protonation or metal hydroxide precipitation. This is overcome if oxygens are incorporated in the molecule such as imidodiacetic acid or nitrilotriacetic acid (Table 1-8 column two).

Porphin and corrin molecules are planar cyclic organic molecules found in nature with Huckel based stability (when the number of  $\pi$ -electrons is  $4n + 2$  or greater, where n is the number of  $\pi$ -electrons. If satisfied, a a stable ring complex forms. These molecules have enhanced chelating abilities due to high degrees of  $\pi$ -electron delocalisation. Iron porphyrins are found in haemoglobins and peroxidases, magnesium porphin in chlorophyll. Both evolved as biological catalyts, and they undergo reversible redox processes, either adding oxygens to haemoglobin or photon absorption in photosynthesis.

Another class of chelates are produced from Schiff bases via the condensation of primary amines with active carbonyl groups. These form five or six membered rings around a metal

ion. However, many of these systems are templated around the metal ion. That is, they form only in the presence of the desired metal ion, and are thus unsuitable as sorbents.

Table 1-8 - Table of multidentate amine ligands of increasing stability due to the 'wrap around' sterics mobility possible from a longer carbon back bone. Carboxylic variations reduce competitive protonation problem of polyamine chelates.

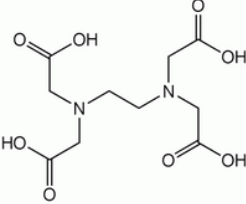
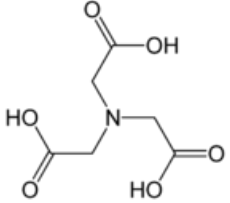
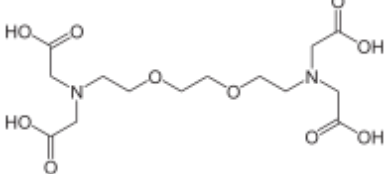
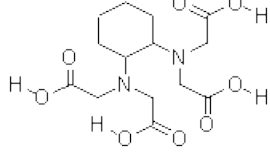
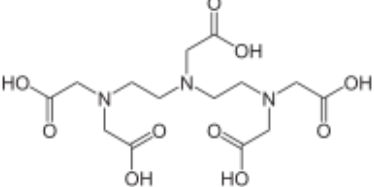
Multidentate polyamine ligands		Multidentate ligands	
Ethylene diamine		Imidodiacetic acid	
1,2,3,4 tetra aminobutane		Nitrilotriacetic acid	
n-2 aminoethyl ethylene diamine		Ethylenediaminetetraacetic acid	
n-n'-di-2-(aminoethyl) ethylene diamine		2,2',6',2''-terpyridylhuckel rule	

### 1.12.10. Complexones

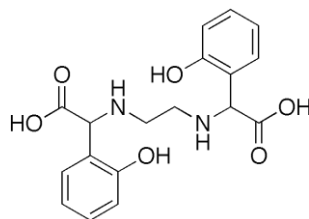
Aminopolycarboxylic acids are an effective class of chelating binders derived from glycine. While increasing carboxyalkyl arms increase the size and complexity of the binders, they are all based around the same amine and carboxylic acid functionalities. Their binding strength comes from the stable, water soluble compounds they form. Table 1-9 shows a range of these

compounds based on imidodiacetic acid. NTA and EDTA are included again as they are both aminopolycarboxylic compounds derived from imidodiacetic acid.

Table 1-9 – Complexone chelators based on imidodiacetic acid.

Aminopolycarboxylic chelators	Structure
Ethylenediaminetetraacetic acid (EDTA)	
Nitrilotriacetic acid (NTA)	
Ethylene glycol tetraacetic acid (EGTA)	
1,2-Cyclohexylenedinitrilotetraacetic acid (DCTA)	
Diethylenetriamine pentaacetic acid (DTPA)	

Ethylenediamine-N,N'-bis(2-hydroxyphenylacetic acid) (EDDHA)



### 1.12.11. Properties of ethylenediaminetetraacetic acid

Because EDTA is readily available and is a relatively cheap chelator, its availability as a functionalised silane allowed the generation of high affinity chelating surfaces. Its properties are discussed in detail to understand how the functionalised surfaces, nanofibres and nanoparticles function.

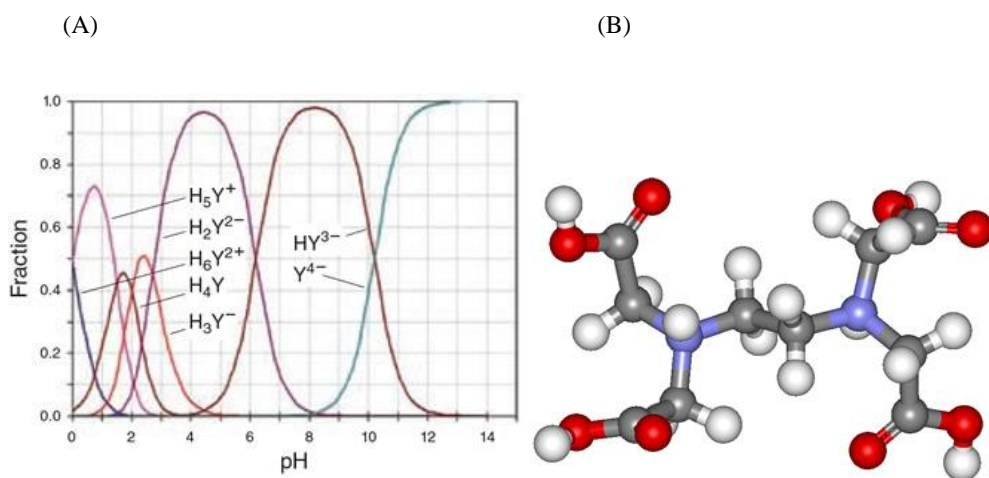


Figure 1-15 – (A), EDTA protonation states as a function of pH. [211]; (B), molecular model of EDTA (H<sub>6</sub>EDTA<sup>2+</sup>). Atom colours are standard CPK; ●, oxygen; ●, nitrogen; ●, carbon and ●, hydrogen.

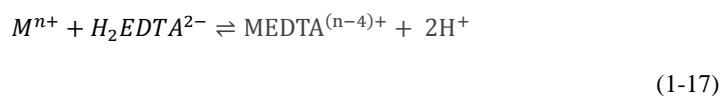
The protonated neutral form of EDTA, H<sub>4</sub>EDTA, has a low solubility in water (0.2 g in 100 ml at 22 °C). Proton association constants for the various anionic forms of EDTA are presented in Table 1-10 corresponding to the EDTA fractions observed in solution and shown

in Figure 1-15 A. A molecular cartoon of the chelating arm orientation is shown in Figure 1-15 B.

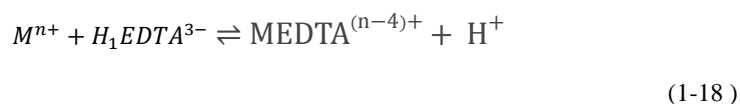
Table 1-10 – Table of formation and stability of aqueous EDTA complexes.

Components and products	Equilibrium	Proton association constant [81] [82]
$H_4EDTA \rightleftharpoons H_3EDTA^- + H^+$	$K_4 = \frac{[H_4EDTA]}{[H_3EDTA^-][H^+]}$	(20 °C in 0.1 M KNO <sub>3</sub> ) lg k <sub>4</sub> =2.07
$H_3EDTA \rightleftharpoons H_2EDTA^{2-} + H^+$	$K_3 = \frac{[H_3EDTA^-]}{[H_2EDTA^{2-}][H^+]}$	lg k <sub>3</sub> =2.75
$H_2EDTA^{2-} \rightleftharpoons H_1EDTA^{3-} + H^+$	$K_2 = \frac{[H_2EDTA^{2-}]}{[H_1EDTA^{3-}][H^+]}$	lg k <sub>2</sub> = 6.24
$H_1EDTA^{3-} \rightleftharpoons EDTA^{4-} + H^+$	$K_1 = \frac{[H_1EDTA^{3-}]}{[EDTA^{4-}][H^+]}$	lg k <sub>1</sub> = 10.34

Two protons are lost below pH 4 from the first two carboxyl groups. Proton dissociation from the nitrogens occurs around pH 5, the second at pH 9. Between pH 3 and 5 the EDTA dominant form exists as H<sub>2</sub>EDTA<sup>2-</sup>. In a 1:1 stoichiometry binding with a metal ion, the complex formed between pH 3 and 5 is shown in Equation 1-17, while the complex formed between between pH 7 and 10 is shown in Equation 1-18:



Between pH 7-10 metal ions form the complex:



### **1.13. Conclusions**

The need for radionuclide biosensing is clear to not only compensate for the lack of techniques for absolute remediation but to work in parallel with them in long term real-time monitoring. While absolute radionuclide ground water figures are not available, model limits, groundwater simulants and co-contaminants have been outlined based on Sellafield annual reports. An extensive overview of the different type of biosensor has been presented with their scope, limitations or potentials with regards to metal ion sensing. In particular electrochemical techniques have been highlighted as an area of potential. While traditional mercury based stripping techniques have been shown to work for individual ion detection these often fail in complex solutions due to analyte signal overlap and electrode poisoning from permanent amalgam layers forming. A multidisciplinary approach using a range of potential host molecules, that importantly have the desired specificity and selectivity, is most likely to produce functional biosensors. Proteins and supramolecular hosts were shown the most suitable.

## **2 : S-layer protein based biosensors for uranyl ions**

---

## 2. Chapter overview

A successful uranyl sensor was created using the surface layer protein (SLP) JG-A12. Uranyl ions noncovalently interact with surface phosphates and carboxylates on this protein. This was monitored in real time as a low frequency impedimetric response. Various tethering methods were used to tether this host molecule while retaining functionality. This included; (a) nonspecific bulk polymer absorption on carbon electrodes, (b) the classic biotin-neutravidin assembly system on a self assembled monolayer (SAM). This is followed by Neutravidin mediated coordination of the biotin tagged sensing component; (c) 4-aminothiophenol and (d) 4-MTP based SAM approaches. Each method aimed to to create highly ordered uniform and reproducible surfaces on gold electrodes. A hierarchy summary of the methods used in this chapter are summarised in Figure 2-1.

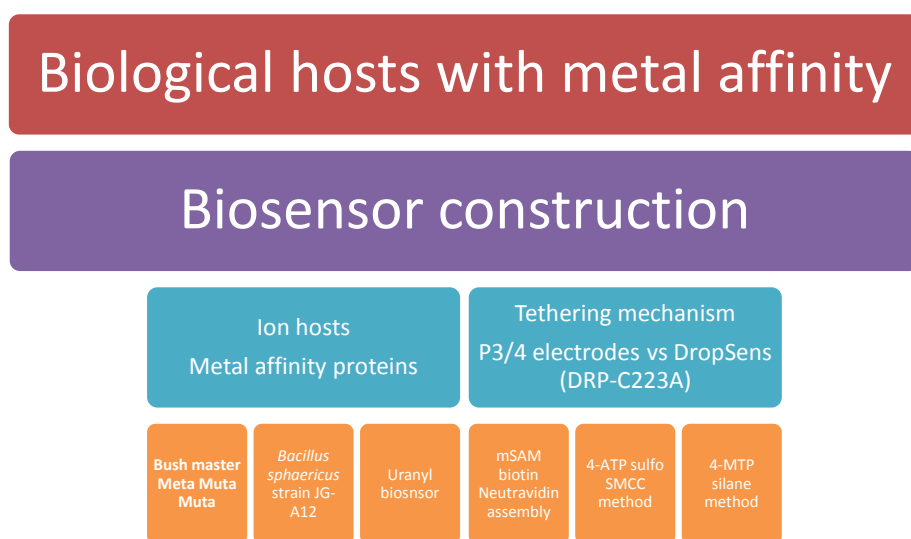


Figure 2-1 – Chapter two hierarchy outlining the methods used to create the uranyl biosensor.

## 2.1. Metal binding proteins for biosensing

Metallochaperones are a class of proteins that sequester metals in the cytoplasm and deliver them to specific associated proteins. If gene sequences for relevant metallo proteins have been identified then the potential to produce bulk quantities of such proteins is of great interest to biosensing technology. Numerous proteins that bind metals are found in biochemical pathways are already identified. These include the nickel chaperone that carries  $\text{Ni}^{2+}$  to urease [67], (UreABC), the ferritaxin chaperone that delivers iron ions to heme clusters. The periplasmic protein PCuAC is known to bind and deliver Cu (I) ions to subunit II of *Thermus thermophilus ba(3) oxidase* [68]. The CopZ chaperone interacts with protein CopA, chaperone TorD, a molybdenum transporter, and four accessory proteins for nickel transport (UreD, UreE, UreF, and UreG) to form the nickel-containing active site in the urease apoprotein. *Staphylococcus aureus* plasmid *pI258-CadC* encodes the CadC protein that, binds a number of heavy metal divalent cations including Cd(II)/Pb(II)/Bi(III)/Zn(II). Two distinct metal-binding sites have been identified; a thiolate-rich  $\alpha(3)$  N site composed entirely of cysteine residues that bind larger metal ions such as Cd(II), Pb(II) and Bi(III), and a second C-terminal  $\alpha(5)$  site at the dimer interface, containing no cysteine residues that binds smaller, harder metal ions such as Co(II) and Zn(II) [69].

These few examples show that for biologically active metals a vast range of metal binding proteins occur and have been identified with common binding sequences of typically lysine, aspartate, histidine and cysteine as key binding residues. While they could all have potential as biosensor recognition elements they would offer little specificity with many of them binding multiple metals, leading to potentially giving false positives or inability to differentiate between multiple analytes.

While a few bacterial strains have been identified as resilient and able to sequester uranium; *Pseudomonas stutzeri*, *Neurospora sitophila*, *Streptomyces albus* and *Streptomyces viridochromogenes* [83] the specific mechanisms and binding sites of very few are understood. Bacteria regulate their responses to metal ions by a number of mechanisms. Membrane pumps use an electrochemical potential to pump out metal ions from the bacterial cytoplasm to maintain ion concentrations below toxic levels. Alternatively, many bacterial species have evolved specific membrane proteins externally, or internal chaperone proteins that bind and sequester proteins to minimise uptake or transport them into metabolic response pathways [12].

### 2.1.1. Surface layer proteins

The surface layer is a monomolecular layer that is part of the cell envelope found in many bacteria. It is composed of proteins or glycoproteins. Surface layer proteins form two-dimensional crystalline arrays of protein subunits, generally forming four types of 2-D lattices. There are: oblique (p1 or p2 symmetry), triangle (p3 symmetry), square (p4 symmetry) or hexagonal (p6 symmetry) [84] arrangements. Their functions can include cell adhesion, protection from feeding by protozoa or phagocytes, virulence factors, antigenic properties, anchoring sites, receptors for phages and porin function [85]. Because structure and function vary, their assembly mechanism have been difficult to elucidate. However in some strains of *Thermus thermophilus* three genes, a repressor and two that code for the S-layer have been shown to regulate different types of s-layer dependent on oxygen supply [86]. X-ray photoelectron spectroscopy (XPS) importantly showed that the 2D assembly mechanism and chelation effect is independent of transcription and transport, and depends on inter-protein interaction and heavy metal association, frequently mediated by calcium or sodium saturation [87]. It is this property that can be harnessed for biosensor application.

### 2.1.2. Metallo proteins and uranyl binding -*Bacillus sphaericus* S-layer JG-A12

The *Bacillus sphaericus* strain JG-A12 is believed to have naturally evolved due to chronic exposure to uranium mining waste piles near the town of Johanngeorgenstadt (Saxony, Germany) and shows an intrinsic resilience to uranyl ions [88]. Compared to similar strains of bacteria JG-A12 was reported to bind  $\text{UO}_2^{2+}$  with higher specificity than its neighbours. Early reports claimed JG-A12 offered specificity only to  $\text{UO}_2^{2+}$  making it an ideal metal receptor. However, subsequent work [87] monitored the interaction of this strain with 19 heavy metal ions (Al, Ba, Cd, Co, Cr, Cs, Cu, Fe, Ga, Mn, Ni, Rb, Si, Sn, Sr, Ti, U, and Zn). While having little or no affinity to many JG-A12 SLP bound  $\text{Cu}^{2+}$ ,  $\text{Pb}^{2+}$ ,  $\text{Al}^{3+}$ , and  $\text{Cd}^{2+}$  as well as  $\text{UO}_2^{2+}$ . Thus, while not offering complete specificity to uranium it binds to a fewer number of interfering cations.

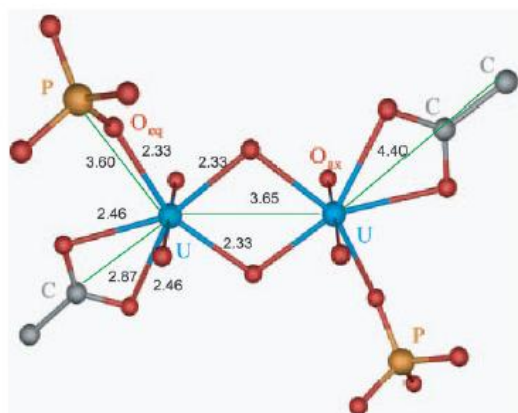


Figure 2-2 - Proposed binding mechanism of uranyl to JG-A12 SLP. Binding occurs to carboxyl groups in a bidentate orientation, and also to phosphate groups in a monodentate fashion [87].

The binding mechanism has been elucidated by X-ray absorption fine-structure (EXAFS) analysis. It is believed that the U (IV) ion is coordinated to carboxyl groups in a bidentate fashion with an average distance between the U atom and the C atom of  $2.88 \pm 0.02 \text{ \AA}$  and phosphate groups in a monodentate fashion with an average distance between the U atom and the P atom of  $3.62 \pm 0.02 \text{ \AA}$  (Figure 2-2). Because of the high potential for the JG-A12 SLP to bind uranyl a sample was obtained from Dr Katrin Pollmann laboratory (Dresden, Germany) and was used to develop a uranyl biosensor.

### 2.1.3. Bushmaster *Meta muta muta* metalloproteins

Another potential source for metalloproteins is from animal venoms as they contain a number of common components. In particular a wide range of snake venoms contain proteolytic, clotting and hemorrhagic factors that attacking basement membranes and the walls of blood vessels once entering the blood stream of prey. There was much interest in toxicology journals in the mid 1980's in snake venom analysis as the ability to sequence proteins and produce vaccines became increasingly viable.

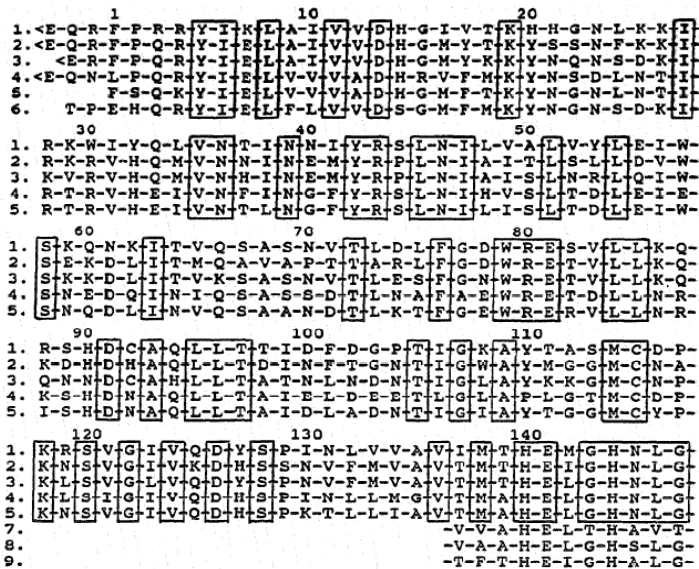


Figure 2-3 – The conserved sequences between a number of snake venom metalloproteins. 1, N-terminal region (metalloproteinase domain) of the high molecular weight haemorrhagic I-IRIB from *Trimeresurus flavoviridis* 2, low molecular weight haemorrhagic protein HR2a from *T. flavoviridis* ; 3, non-haemorrhagic metalloproteinase Hz from *T. flavoviridis* ; 4, haemorrhagic metalloproteinase toxin d from *Crotalus atrox* and 5, haemorrhagic factor LHFII from *Lachesis muta muta*.

In particular, as shown in Figure 2-3 [89] comparing the conserved regions of a number of metalloproteinases reveals leucines, alanine, threonine, aspartic acid and lysine. The crude venom of the bushmaster *Lachesis muta muta* pit viper native to the forested regions of equatorial South America has been noted to bind aqueous uranyl ions [90].

Two independent groups, MacCordick [90] and Sánchez [91] proposed that venom proteins could bind uranyl ions. This was inferred from mass spectroscopy inference and gene sequencing in crude *Meta muta muta* venom. Two specific metalloproteins were identified in the crude venom; hamorrhagic factor I a 100 kDa glycoprotein and hamorrhagic factor II, a 22 kDa low molecular weight protein [89]. Because of the focus of the research journal, this was never followed further. Crude venom was purified using high-performance liquid chromatography (HPLC). However, because the binding proteins were only present at low concentration, obtaining practical amounts for use as uranyl sequestering components was impractical. Amounts of the uranyl binding proteins were identified and purified but this approach was not followed further.

## 2.2. Analyte forms and uranyl speciation

Actinides such as uranium, thorium, neptunium and plutonium have complex aqueous chemistry as a number of oxy-anions and are stable as a function of pH (Figure 2-4). Because of their chemical instability these metals do not occur in their elementary form in nature. A number of sources state they cannot be obtained naturally, and only generated by salt solution electrolysis [92].

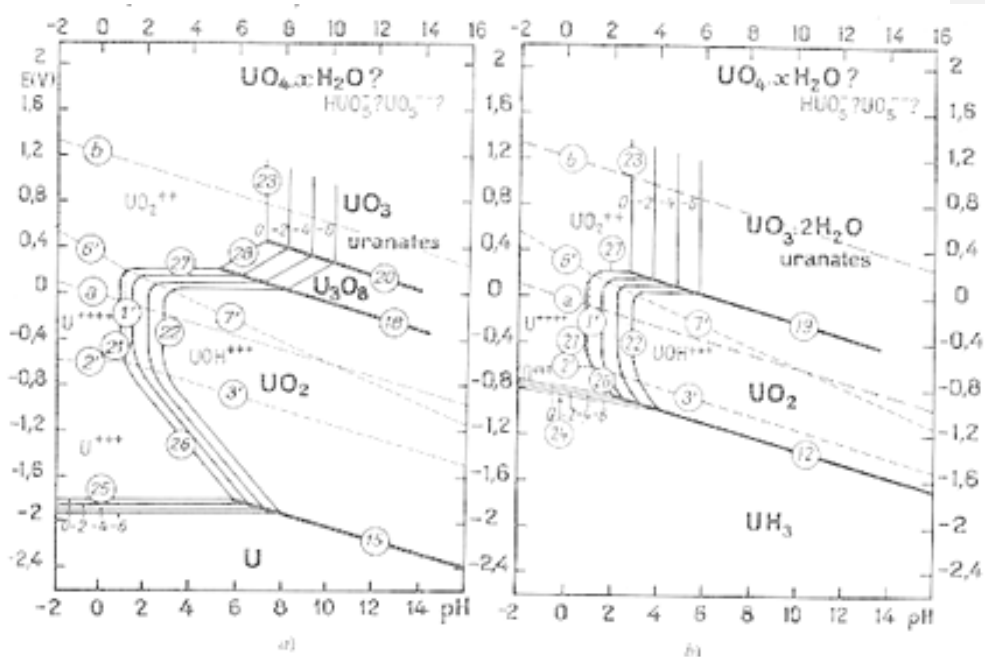


Figure 2-4 –Uranyl speciation in aqueous systems as a function of pH. In standard ground water (pH5) uranium will be in the  $\text{UO}_2^{2+}$  state [9].

While the most common forms of uranium are triuranium octaoxide  $\text{U}_3\text{O}_8$  and uranium dioxide ( $\text{UO}_2$ ) a number of other compounds such as uranium trioxide ( $\text{UO}_3$ ), uranium monoxide ( $\text{UO}$ ), diuranium pentoxide ( $\text{U}_2\text{O}_5$ ), and uranium peroxide ( $\text{UO}_4 \cdot 2\text{H}_2\text{O}$ ) also exist in nature. In tetravalent form  $\text{U}^{4+}$  and  $\text{UOH}^{3+}$  forms complex with the acids  $\text{HCl}$ ,  $\text{H}_2\text{SO}_4$ ,  $\text{H}_3\text{PO}_4$  and  $\text{COOH}_2$ . Plutonium complexes with anions nitrates, chlorides, sulphites, carbonates,

citrates and peroxygenated complexes. As with strontium and alkali earth metals these elements are strongly electronegative, well below the stability domain of water and act as reducing agents forming trivalent cations in strong acid solutions. In alkaline solutions they form hydroxides. A number of uranyl salts are formed from reaction with the acids  $\text{H}_2\text{SO}_4$ ,  $\text{HNO}_3$  and with hydrogen peroxide. In the presence of a strongly acidic environment, most actinide oxides dissolve to form hexavalent metal ions.  $\text{UO}_2^{2+}$ ,  $\text{NpO}_2^{2+}$ ,  $\text{PuO}_2^{2+}$ , pentavalent  $\text{MO}_2^+$  are unstable at low pH and do not occur in practical amounts with the exceptions of  $\text{NpO}_2^+$  and  $\text{AmO}_2^+$ .

## 2.3. Experimental

### 2.3.1. Reagents

SLP from strain *Lysinibacillus sphaericus* JG-A12 was provided by Dr Katrin Pollmann, Institute of Radiochemistry, Forschungszentrum Dresden - Rossendorf, Germany. The transducers used were designs P3 and P4 [93] comprising a 1 mm diameter gold working electrode fabricated on a  $\text{SiO}_2$  coated Si wafer over a Ti adhesion layer. These were sourced from the Tyndall institute, Cork. The reagents 4-aminothiophenol (4-ATP), mercaptothiophenol (4-MTP), 4-(N-maleimidomethyl)cyclohexane-1-carboxylic acid 3-sulfo-N-hydroxysuccinimide ester sodium salt (sulfo-SMCC), 16-mercaptohexadecanoic acid (MHDA) and biotin-N-hydroxysulfosuccinimide (biotin-NHS), (3-isocyanatopropyl)triethoxysilane (isocyanate silane) were obtained from Sigma-Aldrich. Biotin-caproyl-DPPE was obtained from Avanti Polar lipids whilst Neutravidin was acquired from Pierce. All other solvents and buffers unless stated obtained from Sigma-Aldrich.

### 2.3.2. Electrochemical Setup

EIS was performed on PGSTAT100 FRA and microAutolabIII/FRA2 systems. Experiments were performed with a gold P3 or dual P4 working electrode, an Ag / AgCl reference electrode and a solid platinum counter electrode, in a classic 3 electrode system. Phosphate buffered saline solution at pH 7.0 comprising 140 mM NaCl, 2.7 mM KCl, 0.1 mM  $\text{Na}_2\text{HPO}_4$  and 1.8 mM  $\text{KH}_2\text{PO}_4$  was used as the supporting electrolyte. A range of cleaning methods was used for preparation of the gold electrodes and then the amperometric response monitored by

cyclic voltammetry scans in 10 mM PBS containing 5 mM potassium ferricyanide as the redox probe.

The cleaning protocols that were tested were: (a), ethanol wash and sonication; (b), 15 min UV irradiation followed by ethanol wash; (c), ozone treatment followed by an ethanol wash; (d), 2 mins in a piranha solution; (e), (7:3 v/v sulphuric : hydrogen peroxide); (f), 5 mins in a 7:3 (v/v) piranha solution and (g), 15 mins in a 1:1 piranha solution. Piranha solution gives an aggressive treatment that erodes metal with excessive use, and thus reduced electrode life span with extended use, but it also offered the most powerful method of organic removal from electrode surfaces. The optimum method was found to be a 2 min clean in a 7:3 (v/v) piranha solution.

## **2.4. SLP tethering Mechanisms**

Three different tethering mechanisms were used to bind the host SLP protein to gold substrates and the response interrogated with EIS.

### **2.4.1. Biotin-Neutravidin mSAM layer**

For mSAM preparation initially a 10 : 1 biotin-caproyl-DPPE to MHDA molar ratio was used. For this 44  $\mu\text{L}$  of 10 mg/ml MHDA in  $\text{CHCl}_3$  was added to 10 ml ethanol to form a 0.5 mM/500  $\mu\text{M}$  stock solution. To this 52.5  $\mu\text{L}$  of biotin-caproyl-DPPE was added from a 10 mM stock in  $\text{CHCl}_3$  to create a total working concentration of 50  $\mu\text{M}$  biotin-caproyl-DPPE and a 10:1 molar ratio of MHDA : biotin-caproyl-DPPE. Electrodes were incubated overnight to prepare the mSAM. Biotinylated SLP was bound to a Neutravidin protein layer that was preassembled on a MHDA:DPPE mSAM [94]. In the present work N-hydroxysuccinimide activated carboxy biotin was used to biotinylate the SLP. The protein was dialysed for 24 hrs against PBS to remove interferants such as azides that act as biocides to enhance protein storage lifespan. Biotin/S-layer protein ratios tested were 1000, 100 and 10 to 1. A 10 : 1 ratio with a 30 min incubation time was found to be optimal for binding. Biotin tagged SLP and free unreacted biotin were separated and purified on a PD-10 Desalting column (Sephadex G-25). A schematic of this assembly mechanism is shown in Figure 2-5.

### 2.4.2. mSAM stability measurements at varying MHDA : biotin-caproyl-DPPE ratios

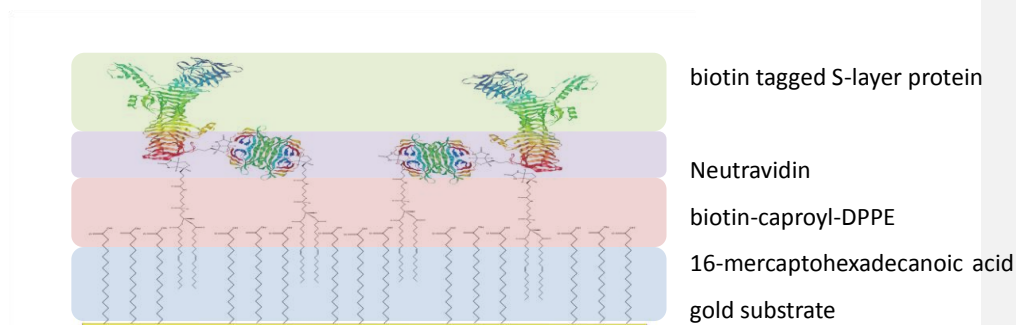


Figure 2-5 - mSAM incorporation of SLP by MHDA/biotin-caproyl-DPPE mSAM, deposited with a Neutravidin layer that binds to pre-biotinylated SLP.

Varying ratios of biotin-caproyl-DPPE : MHDA were prepared in 10 ml ethanol to be absorbed on gold P3 electrodes. The mSAM was interrogated over a frequency range 250 kHz to 0.25 Hz. Fifty data points were measured to monitor self assembly. Readings were taken immediately upon electrode immersion into the component solution to monitor adsorption, assembly or stability as a function of capacitance or  $-Z''$ , the imaginary component of impedance.

### 2.4.3. Bioconjugation using 4-ATP sulfo-SMCC layer

Cleaned electrodes were incubated in 10 mM 4-ATP in ethanol solution for 4 h. Hourly Nyquist scans showed that while a significant amount of 4-ATP bound within the first hour, stabilisation and molecular ordering occurred sometime after 4 h. To attach sulfo-SMCC the electrodes were then incubated in a 5 mM sulfo-SMCC in PBS pH 7.0 for a minimum of 1 h. Sulfo-SMCC binds to amine groups of the 4-ATP monolayer; its maleimide groups are then free to bind cysteine thiol groups on the SLP. Once the supporting layer had been prepared, the electrodes were further incubated for a minimum of 1 h in 1 mg/ml protein and stored in 10 mM PBS at room temperature. Electrodes were interrogated after each deposition step to confirm successful layer deposition. A schematic representation of this assembly mechanism is shown in Figure 2-6.

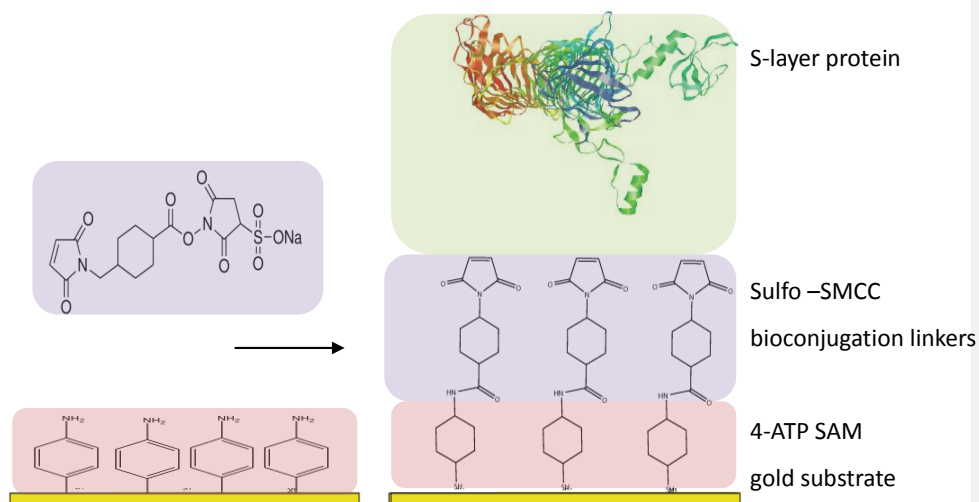


Figure 2-6 - Porous membrane model with molecular linkers of 1.5 nm length [95] binding SLP through a stable permeable membrane as maleimide groups covalently bind to thiols on protein cysteine residues.

### 2.4.3.1. Blocking the SLP chelating sites

Two alternative binding mechanism of uranyl ions to JG-A12 SLP have been proposed; one is through carboxyl and phosphate groups in a bidentate manner, the second via phosphate groups in a monodentate mechanism, unique to JG-A12 SLP [87]. To confirm the impedance response change was due to the specificity of JG-A12 SLP to uranyl ions these sites were chemically modified (Figure 2-7).

Phosphate blocking was achieved by phosphoramidate modification which added an amine to the phosphate groups (Figure 2-7 A). This was performed by incubating at S-layer coated electrode in 5 mM ethylenediamine with 1-ethyl-3-(3-dimethylaminopropyl) carbodiimide under alkaline conditions (pH 7–10). Carboxyl groups were blocked by modification of acyl groups that created 3 terminal hydroxyls that introduced electrostatic and steric hindrance to analyte cations that attempted to bind (Figure 2-7 B). This was achieved by incubating an SLP bound electrode in 0.1 M MES pH 4.7 with 0.1 M TRIS with 10 mg/ml 1-ethyl-3-(3-dimethylaminopropyl) carbodiimide for 4 h at room temperature.

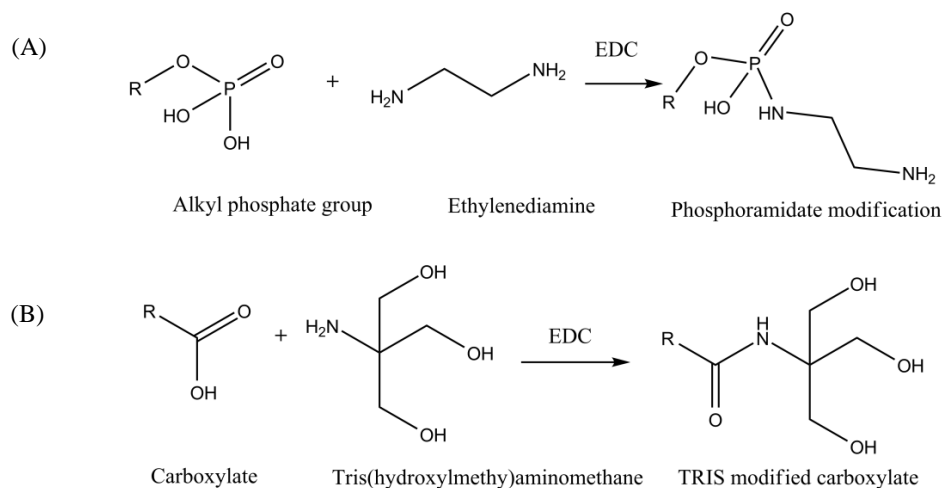


Figure 2-7 - Schematic of the protocols used to modify proposed SLP binding carboxylates and phosphates sites. (A), phosphate modification by carbodiimide reaction in the presence of amine. (B), modification of carboxylates with TRIS using a carbodiimide mediated process.

Successful blocking of the SLP binding sites was confirmed by XPS and inhibition of the biosensor response to uranyl ions.

#### 2.4.4. Bioconjugation using 4-MTP and isocyanate silane

Bioconjugation using this method used a bare gold electrode in a 4 h incubation of the base layer solution which contained at a concentration of 5mM 4-MTP in ethanol. A further 4 h reaction of functional silane 5 % (v/v) in ethanol was hydrolysed and condensed on to the surface via silanol linkage. The available isocyanate groups then reacted with free amine groups forming a covalent linkage to the receptor protein (Figure 2-8).

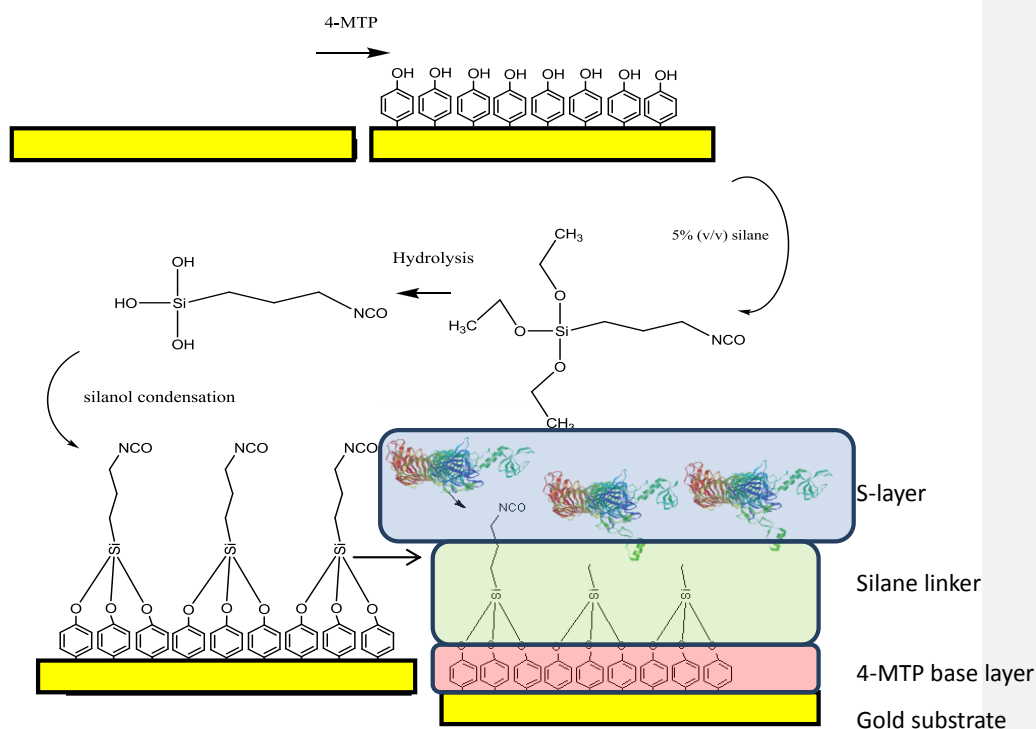


Figure 2-8 - Silane linker bioconjugation. A SAM of 4-mercaptothiophenol has a hydrolysed silane layer condensed onto the available hydroxyls, leaving the isocyanate to form a covalent bond with free amines on the SLP.

## 2.5. Analytical methods

### 2.5.1. Atomic Force Microscopy

Atomic force microscopy (AFM) was performed using a Nanoscope IV Pico scope force module with the help of Dr Hodges, School of Process, Environmental and Materials Engineering in the Faculty of Engineering at the University of Leeds. Data was analysed with alternative software WSxM 5.0 development 5.2 [96].

### 2.5.2. X-ray photoelectron spectroscopy

X-ray photoelectron spectroscopy was performed on a VG Escalab 250 XPS using a 500  $\mu\text{m}$  spot size and 150 W power Monochromated Al K $\alpha$  X-ray source. QCM analysis was carried

out using a Maxtek RQCM instrument using 5 MHz, 1 in. diameter AT cut crystals with Au coated surfaces. Real time deposition studies were obtained by setting up a flow through system using a 100  $\mu$ l flow chamber and flow speed of 220  $\mu$ L min<sup>-1</sup>.

### **2.5.3. Scanning electron microscopy**

Scanning electron microscopy was performed on a Philips XL30 SEM. Samples were dried and sputter coated with a 5nm conductive layer of gold or platinum. Typical working conditions were a 200k x magnification, a 3 mm working distance and a 3 kV accelerating voltage.

### **2.5.4. Native gel PAGE and SDS PAGE of S-layer protein**

Polyacrylamide gel electrophoresis is a technique that allows the separation of proteins based on electrophoretic mobility. A 10 % (w/v) gel allows separation of proteins in the range 20 kDa to 3 MDa which should have allowed identification of the proposed 126 kDa SLP monomer [87] and some lower aggregates. However, native gels appeared blank suggesting a staining problem or that the protein was not entering the gel. It is known that highly phosphorylated protein have problems with common stains such as Coomassie and silver [88]. For such proteins a staining agent such as Spyro Ruby has been suggested. However, use of an SDS-PAGE gel with the use of elevated temperatures and SDS to unfold and denature the proteins, removed problems of aggregation and successfully stained proteins to be imaged (Figure 2-9 A).

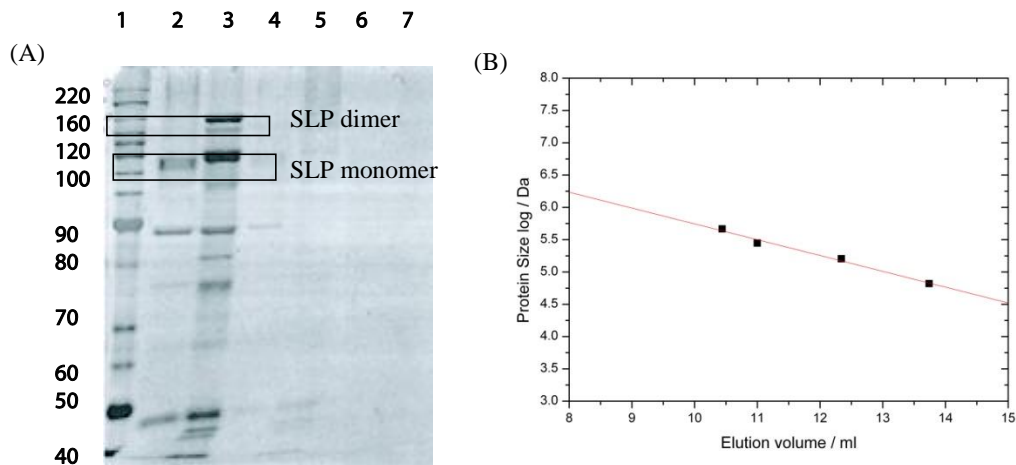


Figure 2-9 – (A) SDS PAGE sizing of S-layer protein. Wells correspond to (1) molecular weight markers, (2) 1 mg/ml SLP, (3) 1 mg/ml S-layer boiled (4) 1/5 dilution (5) 1/5 boiled (6) 1/10 dilution (7) 1/10 dilution boiled. (B) Size exclusion chromatography calibration curve using bovine serum albumin, glucose oxidase, acetyl choline esterase and  $\beta$  galactosidase with sizes 66 kDa, 160 kDa, 280 kDa, and 466 kDa respectively. A Superdex 200 10 / 300 GL column was used (13  $\mu$ m particles resolution 10 - 6000 kDa) at a pump speed of 1.0 ml / min, max pressure 15 bar (217 psi, 1.5 MPa). 50  $\mu$ L protein samples were injected containing approximately 0.1 to 10  $\mu$ M protein concentrations and pumped through the porous matrix.

### 2.5.5. S-layer protein sizing using size permeation gel chromatography

High performance liquid chromatography (HPLC) uses a porous matrix similar to PAGE to separate proteins. The main difference is that the former separates on hydrodynamic size rather than charge to subunit ratio. The sample is pumped through a column containing agarose - dextran cross linked porous particles. This technique is without the denaturing effects of SDS and shows proteins in the native state thereby allowing aggregation effects to be observed.

Figure 2-9B shows the calibration curve of standards used; bovine serum albumin, glucose oxidase, acetyl choline esterase and  $\beta$  galactosidase of sizes 66 kDa, 160 kDa, 280 kDa, and 466 kDa respectively. The expected 126 kDa monomer shown by SDS PAGE (Figure 2-9A) was expected at an elution volume of 14 ml. However, this was only observed at a protein

concentration of 1  $\mu\text{M}$  or lower supporting the idea that there is a critical aggregation concentration below which the monomeric form is favourable. At 1  $\mu\text{M}$  and 10  $\mu\text{M}$  a 740 kDa peak was observed in all fractions suggesting a hexameric aggregate. To ensure a monodisperse sample for protein deposition, a protein supernatant sample was centrifuged at 10,000  $\times g$  for 30 min was retested in the HPLC column. Elutants showed that a monodisperse sample remained while the heavier aggregates sedimented.

Computational analysis using UniProt software analysis predicted the isoelectric point of the 126 kDa JG-A12 monomer as 5.10. A protein monomer contains 125 negatively charged residues (aspartic acid and glutamic acid) and 103 positively charged residues (arginine and lysine). Therefore at pH 7 the protein should carry a slight overall negative net charge.

## **2.5.6. Electrochemical analysis**

Deposition, assembly and organisation of the 4-ATP base layer was monitored with hourly EIS interrogation on cleaned gold P3 electrodes in a cell containing 10 mM 4-ATP in ethanol. Using fitting of parameters based on a Randle's equivalent model, electrochemical parameters were extrapolated.

### **2.5.6.1. Deposition of 4-ATP SAM**

To determine the optimum monolayer assembly of the base layer, sequential impedance scans were taken every 60 minutes for 8 h (Figure 2-10 A) and the corresponding equivalent circuit components extrapolated. Two semicircles appear with the components fitted according to the model in Figure 2-10 B. The left high frequency region corresponds to the absorbed 4-ATP, the right unbound 4-ATP within the Debye length (calculated in Chapter 1 as 30 nm - see Figure 1-7) interacting with the electrode and responding to the applied field at lower frequencies (extrapolated in Figure 2-10 D). This corresponded to the mass transfer component of analyte diffusing to, and from, the surface. Both peaks showed a stable solution resistance with minor change as excess ferricyanide and 4-ATP were in solution (Figure 2-10 C and D, see  $R_s$ , ■).

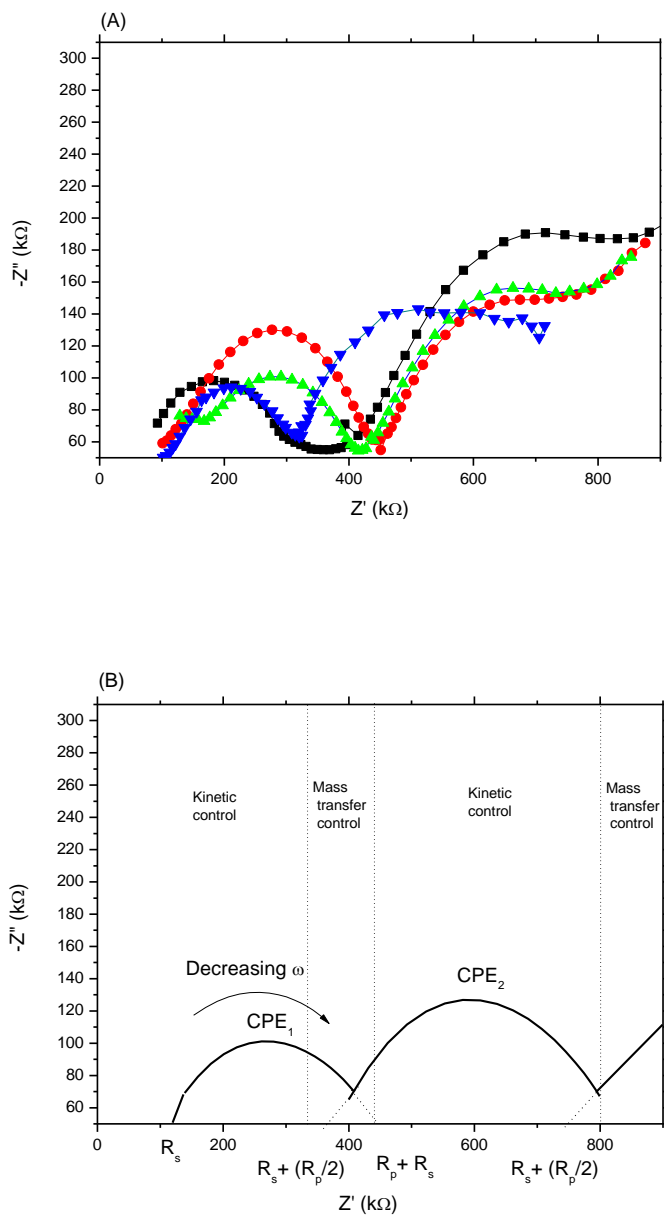


Figure 2-10 - Nyquist fitting to Randles circuit of 4-ATP monolayer assembling on gold with time. (A) Nyquist double semicircle plots at  $\bullet$ , 1 h;  $\blacktriangle$ , 2 h;  $\blacktriangledown$ , 3 h;  $\blacksquare$ , 4 h incubation times. (B), a reminder of how the Randles circuit components are extrapolated.

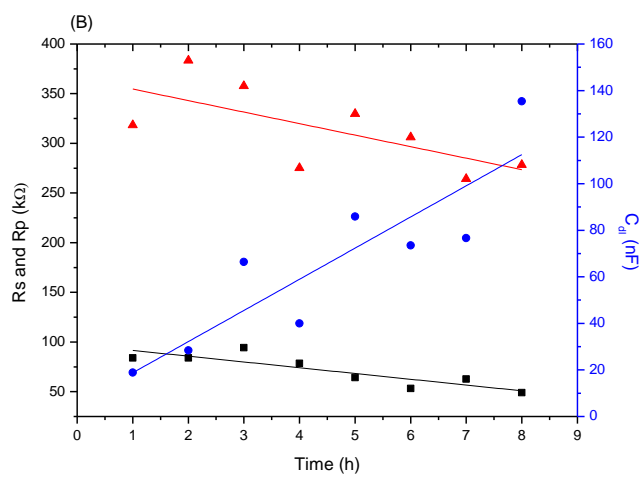
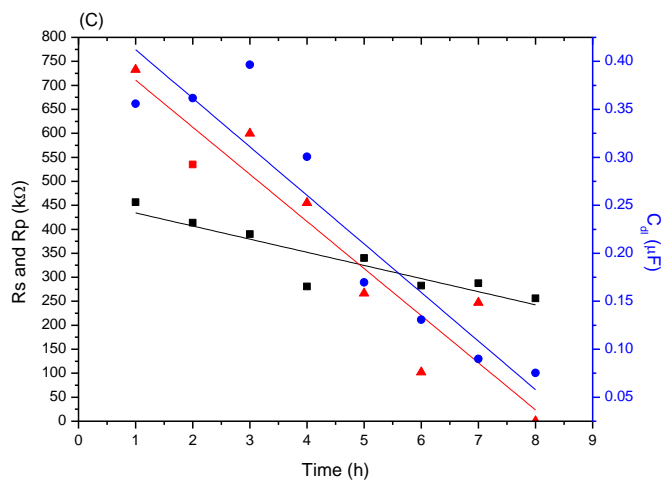


Figure 2-10 C - Nyquist fitting to Randles circuit of 4-ATP monolayer assembling on gold with time. (C) and (D) correspond to extrapolated Randles circuit equivalent components ( $R_s$ ,  $R_p$  and  $C_{dl}$ ) of semicircles 2 and 1 respectively.

Whilst there was still some decreasing capacitance beyond a 4 h incubation, only a subsequent 10 nF deviation in  $C_{dl}$  was observed up to the complete 8 h incubation (Figure 2-10 D,  $C_{dl}$  ▲). Rinsing of electrodes and scans in fresh ferricyanide showed a stable layer formation and 4 h was chosen as the minimal incubation time for the base layer.

The second semicircle (Figure 2-10 C) showed a linear decrease of capacitance as ferricyanide was reduced and diffused away from the electrode, as did the polarisation resistance. In contrast the second semicircle, representing unbound species, showed continual but relatively small decrease in  $R_p$  and  $R_s$  (520 k $\Omega$  and 530 k $\Omega$  respectively) as the ions from the Inner Helmholtz plane to bulk solution were continually changing.

Figure 2-10 D showed bulk absorption within the first hour and then small flux in solution and layer resistance due to reorientation of the layer (a change of 25 k $\Omega$  in  $R_p$  and 28 k $\Omega$  in  $R_s$  respectively). However, capacitance continued to increase over the 8 h period (a change in  $C_{dl}$  from 18 to 137 nF), but this is attributed to Inner Helmholtz ions interacting with the absorbed layers, as this stabilised when the electrode was transferred to PBS alone.

Rinsing electrodes deposited after a set number of hours and interrogation with CV confirmed that beyond 4 h no significant change in base the layer was observed. Accordingly a 4 h base layer incubation time was subsequently used.

### 2.5.6.2. Conductivity of deposited 4-ATP SAM

To test the conductivity of the 4-ATP (■) and 4-MTP (△) surfaces amperometric sensors were created by tethering the enzyme glucose oxidase with either sulfo-SMCC or isocyanate silane onto gold P3 electrodes. These were compared to a conventional electrostatic binding method using the bulk polymer, PEI (○) (Figure 2-11). Sequential aliquots of glucose were added and the anodic oxidation of the catalytic product  $H_2O_2$  monitored at +0.65V, with the base corrected current extrapolated. Comparison of the base glucose sensors, 4-ATP, 4-MTP and PEI respectively, showed currents of 132, 85 and 78 nA per mM glucose (Figure 2-11).

Because all systems used a 1:1 stoichiometry between analyte (glucose) and product ( $H_2O_2$ ) the difference in current comes from the sensor interface and variation in conductivity. Compared to the PEI sensor, a significantly higher current was observed for the 4-MTP sensor (36% higher current per M glucose than the PEI surface). This showed that a controlled low concentration and short condensation time results in SAM linkage to 4-MTP

hydroxyls and not inter-silane linkage that would create a completely insulating layer (as shown in Chapter 5 on functionalised nanofibres). The 4-ATP linkers were expected to be the most conducting, and showed a significant improvement in conduction (69% current per M glucose compared to PEI surface) due to the closer proximity of enzyme to electrode and higher conductivity.

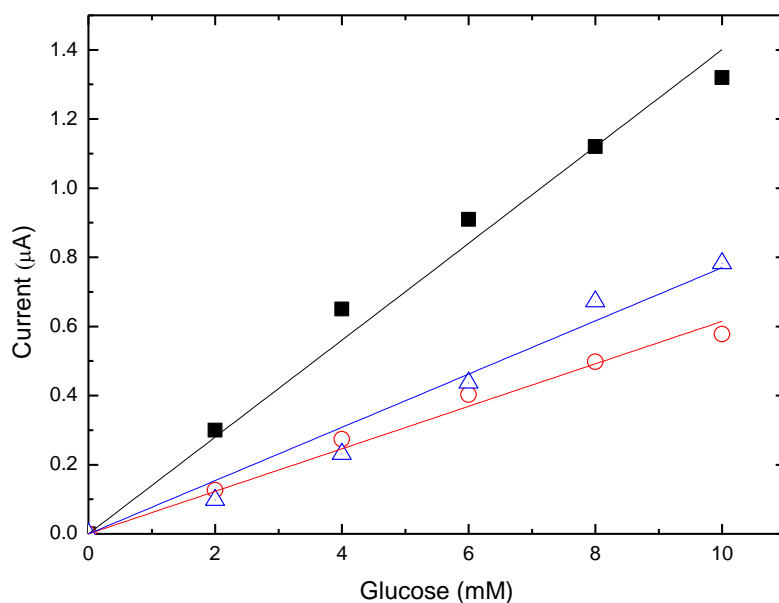


Figure 2-11 – Comparison of glucose oxidase amperometric sensors; (■) 4-ATP, (△) 4-MTP isocyanate silane SAM sensor surfaces versus (○) bulk absorbed PEI polymer used to tether GOx enzyme.

### 2.5.6.3. Biosensor response of 4-ATP SAM based uranyl biosensor

SLP loaded electrodes assembled using the 4-ATP base layer were equilibrated for 1 h before use in 10 mM PBS. EIS experiments were performed with the standard electrode setup; W.E (Au P3), R.E (AgAgCl), crown ether (Pt). Readings were taken at 0 V, with 10 mM PBS supporting electrolyte, or at 0.4 V in the same buffer containing 5 mM ferricyanide. 51 points were calculated over a frequency range of 250 kHz to 0.1 Hz using a 0.01 V rms potential. Three readings with a 10 min delay between successive scans were used to determine system stability and an average taken. After each sequential uranyl nitrate addition the cell was stirred for 30 min and allowed to equilibrate for 5 min before the next 3 EIS scans were performed.

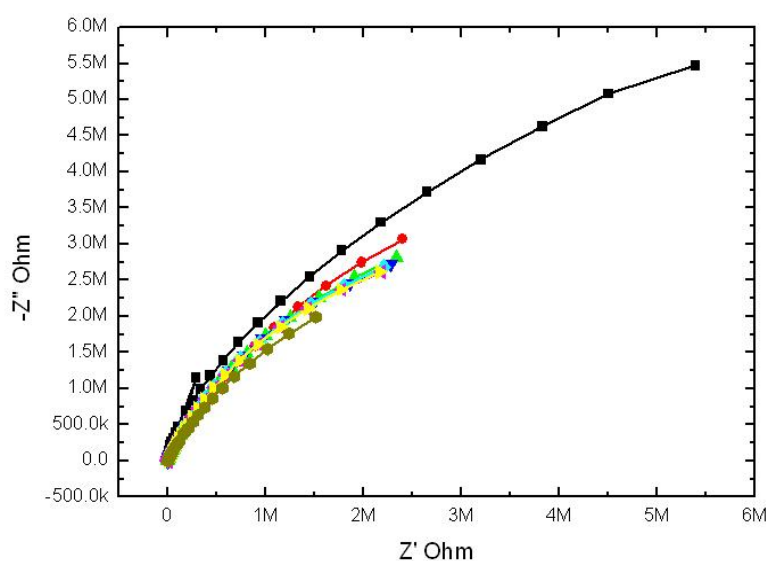


Figure 2-12 -Nyquist plot of impedance of s-layer conjugated electrode in increasing uranyl nitrate concentrations (• S-layer, •  $10^{-11}$  M, •  $10^{-10}$  M, •  $10^{-9}$  M, •  $10^{-8}$  M, •  $10^{-7}$  M, •  $10^{-6}$  M, •  $10^{-5}$  M ). 0 V applied vs AgAgCl, 10 mM PBS supporting electrolyte, 51 points calculated using a 0.01 V rms potential.

The Nyquist response of the SLP bioconjugated electrodes differed significantly from the semicircles observed for mSAM deposited layers (Figure 2-12). This is because the adsorbed molecular layers, while forming ordered structures do not create a complete insulating barrier with a finite capacitance separating the electrode from electrolyte. Deposition steps on to mSAMs can be directly extrapolated from impedance data as a repression or expansion in the observed semicircle. Thus, the altered constant phase element and electron transfer resistance components were observed as the permeability altered at low frequency. Initial interrogations of the Nyquist plot shows some minor fluctuation in the  $C_{dl}$ , but this was not reproducible enough to be used as the biosensor signal

Briefly returning to the fundamentals; the capacitance between electrode and an ion in solution is modelled as series of capacitors (Equation 2-1).

$$\frac{1}{C} = \frac{1}{C_{mod}} + \frac{1}{C_{dl}} \quad (2-1)$$

Where  $C_{mod}$  is the modifier layer of absorbed species and  $C_{dl}$  the natural double layer occurring at a liquid-electrode interface modelled by Gouy Chapman – Stern theory.

Binding of nanomolar levels of atoms to this Stern layer will cause a small disruption to the outer Helmholtz plane of the Guoy-Chapman model. Because these processes occur on the Angstrom scale they are difficult to detect over other dominating processes.

$$\frac{1}{C_{dl}} = \frac{1}{C_{protein}} + \frac{1}{C_{analyte}} \quad (2-2)$$

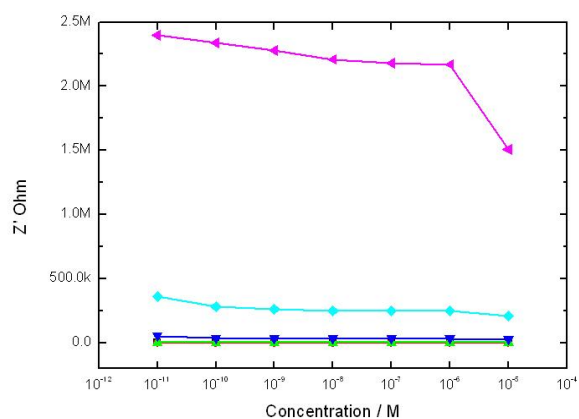
Binding of analytes to the absorbed molecular layers caused an increase in modified layer capacitance (extending the closest distance of approach of a molecule, likely increasing the resistive component of the Inner Helmholtz plane (IHP) and causing a decrease in double layer capacitance due to a compression of the double layer (Equation 2-2). The most

dominant of these opposing processes will determine if binding causes an increase or decrease in the  $C_{dl}$ .

Analyte binding caused a disruption in the interfacial double layer and the hydrated / salt layer in the OHP. Plotting the Nyquist data as a function of concentration response to different frequencies allowed this disruption to be quantified (Figure 2-13).

At high frequencies increasing concentrations of uranyl nitrate binding to the SLP layer showed little deviation in response in both the real and imaginary components. However, at low frequencies a linear decrease was observed in impedance. A larger response at lower frequencies was due to poration of the interface now observable because the measurement time was longer than the electron transfer time, and the signal was an interrogation of the mass transfer region, not the electron transfer region.

(A)



(B)

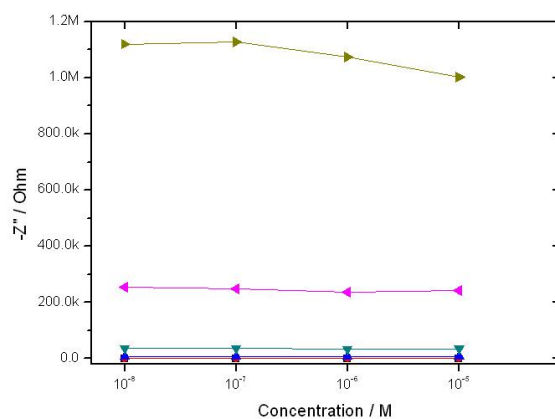


Figure 2-13 – (A) Real and (B) imaginary impedance components of impedance response with frequency of S-layer conjugated electrode in increasing uranyl nitrate concentrations; (● 10 kHz, ● 1 kHz, ● 100 kHz, ● 10 Hz, ● 1 Hz ● 0.1 Hz). (B) Imaginary impedance response under same conditions (● 10 kHz, ● 1 kHz, ● 100 kHz, ● 10 Hz, ● 1 Hz ● 0.1 Hz). 0 V applied vs AgAgCl, 10 mM PBS supporting electrolyte, 51 points calculated 0.01V rms.

#### 2.5.6.4. SLP biosensor fabricated on DropSens electrodechips

An alternative to the P3 and P4 electrodes was obtained from Dropsens (DRP-C223A). Each electrodechip consists of three self contained screen printed electrodes within each individual electrode (Figure 2-14). This new electrode design consisted of W.E: 1.6 mm diameter gold, crown ether: gold, R.E: silver, printed with high temperature curing inks and a base ceramic substrate of dimensions L33 x W10 x H 0.5 mm. The aim was to produce cheaper, scalable sensors that were more reproducible and consistent than the P3 and P4 variants.

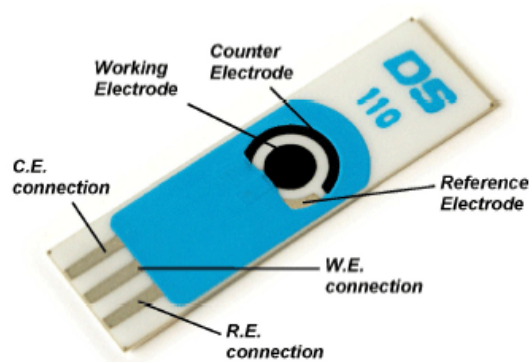


Figure 2-14 – Diagram of the general DropSens electrodechip (DRP-C223A) configuration. The DRP-C223A DropSens electrodes have a screen printed gold working electrode of 1.6 mm diameter, Ag/AgCl reference electrode and platinum counter.

#### 2.5.6.5. DropSens electrode cleaning

The cleaning method for the DropSens electrodes was optimised in similar fashion to the P3/P4 cleaning trials, six cleaning methods were used on electrodes as supplied and then the cyclic voltammetry response using a supporting electrolyte of 10 mM PBS containing 10 mM ferric anide were obtained (Figure 2-15). Cleaning methods used were; (a), 7 : 3 sulfuric acid : hydrogen peroxide; (b), 1 % Decon 90; (c), chromic acid; (d), chromic acid with sonication; (e), 50 : 50 acetone : methanol and (f), 50 : 50 acetone : methanol with sonication.

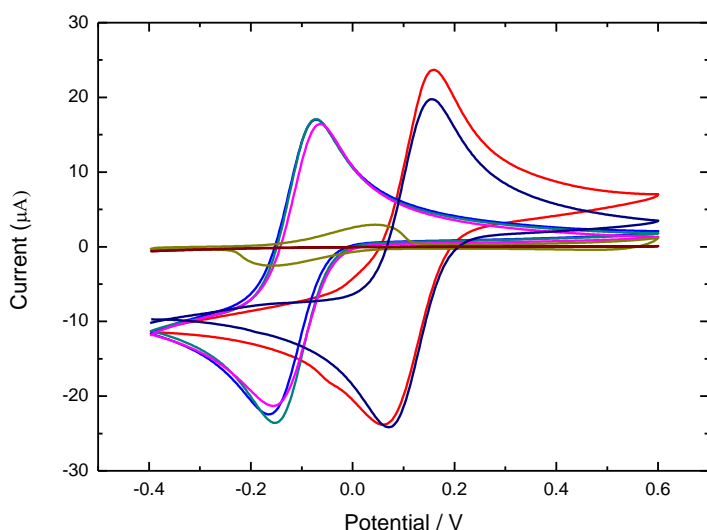


Figure 2-15 – Cleaning effects on DropSens electrodes, 30 min in stated conditions before a 50 mv/s in 10 mM PBS containing 10 mM ferricyanide scan to observed redox response. (—) Bare gold electrode no cleaning method, (—) 2 min piranha, (—) 1:1 methanol : acetone, (—) 1% Decon 90, (—) sonicated 1:1 methanol : acetone, (—) chromic acid, (—) sonicated chromic acid.

Electrodes cleaned by five of the six methods showed a significant drift in the redox peaks by up to 250 mV after cleaning. Chromic acid completely disrupted both the redox potentials and currents the observed suggesting erosion of reference electrode and was too harsh a treatment. Decon 90 was suitable for removing inorganic contaminants but residual surfactant interfered with the biosensor construction. While the organic solvent wash initially looked like it gave the most stable electrode response, subsequent repeats showed significant drift in the observed redox peaks. Interrogation of buffer components and the drift potential highlighted that chloride from the buffer was binding to the silver reference generating a AgAgCl electrode. This resulted in the observed shift in redox potentials, returning the redox potentials closer to the potentials observed using the P3/P4 experiments which used an external 3 M KCl AgAgCl (the standard electrode potential,  $E_o$  vs SHE is  $0.230V \pm 10 \text{ mV}$  [45]). If this shift was consistent the potential difference could be accounted for manually by comparing redox values between individual electrodes (silver  $E_o$  - 0.7996V [97]). However, the reference was unstable throughout individual experiments and

measurements with the DRP-C223A electrodes; thus they are useless as reproducible, stable electrodes for sensor use. Because of these problems piranha cleaning was found to be the best at removing contaminants but rapidly eroded the printed inks resulting in electrodes only reusable one or two times before complete dissolution occurred.

#### **2.5.6.6. Stabilisation the DropSens reference electrode**

The observed drift seen in DropSens electrodes was presumed due to the instability of the silver reference, due to electrolyte species binding or reacting. To counter this problem a 1 h incubation of the electrodes in 1 M HCl to create a bound saturated Ag/AgCl salt layer was introduced. While stability improved significantly (Figure 2-16 A) inter electrode batch comparisons still showed variation with a smaller amount of drift (Figure 2-16 B). Over 10 CV scans, the oxidation peak drifted within a 32 mV window and the reduction peak potential drifted over a 46 mV range (Figure 2-16 C, blue lines, O for oxidation and rectangles for reduction).

Addition of further chloride ions by use of KCl was used to see if the reference had stabilised following the HCl wash. However, traces still showed a drift to more positive potentials ( $E_{ox}$  to + 17mV and  $E_{red}$  to + 30 mV). The drifting reference problem could not be sufficiently solved. This coupled with problems of the blue insulator layer exhibiting variable resistance to piranha cleaning caused problems of complete wetting when using hydrophobic compounds. This resulted in coverage of all three electrodes (e.g. 4-MTP or 4-MTP in EtOH), rather than just the desired working electrode. It was decided that the DropSens electrodes were unsuitable, and that the P3/P4 electrodes were superior because of the separate (off chip) reference and counter electrode that were robust, more resistant to contamination and did not suffer degradation like the printed organic inks.

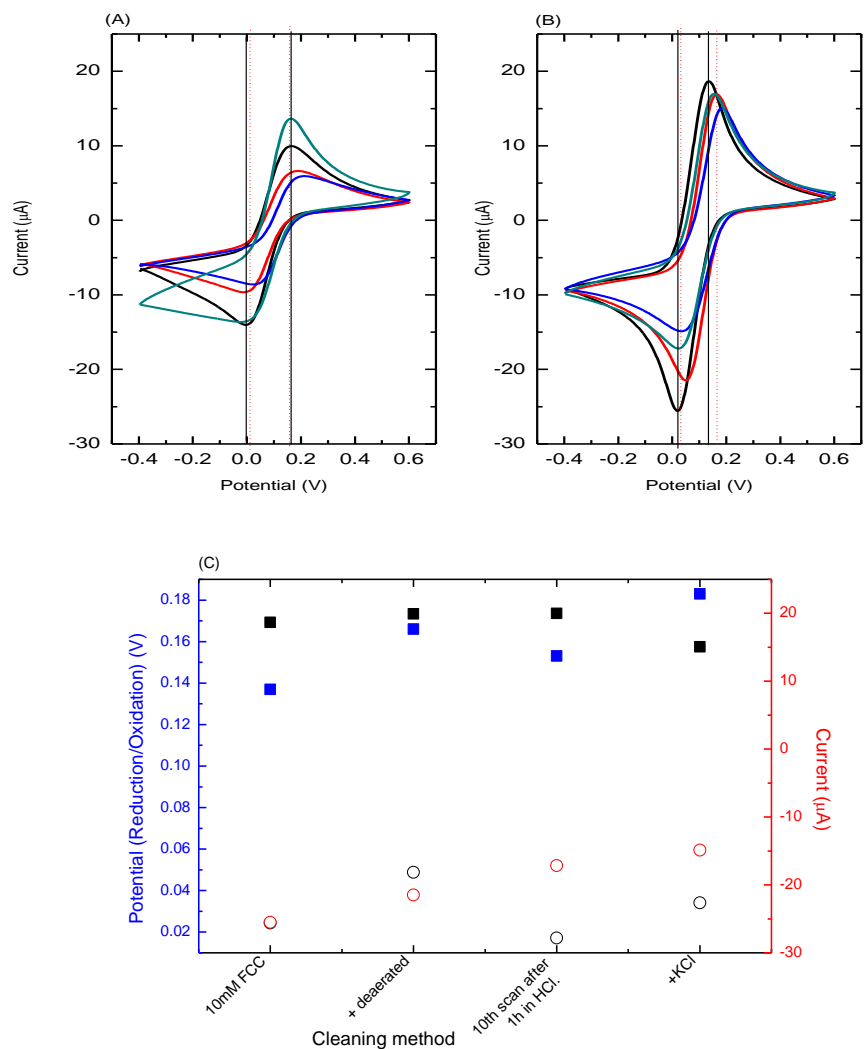


Figure 2-16 – (A) and (B), two independent batches of AgAgCl modified DRP-C223A electrodes showing improvement in stability of the electrodes. (A) (■) 10mM ferricyanide in dH<sub>2</sub>O, (●) deaerated, (■) +KCl, (■) 10th scan after 1h in HCl. (B) (■) 10mM ferricyanide in dH<sub>2</sub>O, (●) +KCl, (■) 10th scan after 1h in HCl. Vertical lines (—) Redox peak potentials on an uncleaned electrode in ferricyanide (.....) redox potential peak drift from cleaning treatment (1h HCl). (Average Red E:  $0.0022\text{V} \pm 0.0064\text{ SE}$  Oxid:  $0.138\text{V} \pm 0.0063\text{ SE}$ ,  $n=4$  in both). (C) Extrapolated redox potentials and peaks from each treatment. Taken from batch A (Figure A). Symbols; ○ for oxidation and ■ for reduction. Lines colour coded to axes; blue for potentials on left axis, red for currents on right axis.

Table 2-1 – Summary of redox potential deviation and drift of DropSens electrodes from screen printed reference electrode problems. Shown in Figure 2-16 C.

Electrode interrogation	Colour	Left peak (○ oxidation)		Right peak (■ reduction)	
		Potential (V)	Current (μA)	Potential (V)	Current (μA)
10 mM ferricyanide in dH <sub>2</sub> O	—	0.024	-25.494	0.137	18.665
+ deaerated	—	0.049	-21.469	0.166	19.901
10th scan after 1h in HCl.	—	0.017	-17.166	0.153	19.968
+KCl	—	0.034	-14.873	0.183	15.048

Using CV experiments that contained 10 mM ferricyanide in deionised water, PBS and individual buffer components it was possible to confirm that the drift component resulted from chloride ions reacting with the silver reference with the overall reaction  $\text{Ag}^0(\text{s}) + \text{Cl}^- \leftrightarrow \text{AgCl}(\text{s}) + \text{e}^-$  (Table 2-1). Similar to the non-aqueous electrochemistry systems used in early crown ether experiments (Chapter 3) a saturated silver chloride pseudo-reference was made from immersing the silver references in 1M HCl to form a saturated Ag/AgCl that can be condensed by an ethanol wash. After reaction with HCl acid, submerged reference electrodes remain silver coated, but a black residue formed on one of the three silver contacts suggesting an unknown reaction occurred on the impure silver layer. Extended acid incubation weakened the blue insulating layer that began to peel, even to parts of the electrode not submerged in acid. Air based storage over similar time scales did not result in the black layer forming. An unknown gaseous ‘fuming HCl reaction’ is the likely cause from elimination of alternative possibilities. Silver is known to tarnish in the presence of sulfonates i.e in sulphuric acid, but not hydrochloric, and should be stable in water or oxygen. The reaction still occurs but at a slower rate on ferricyanide scanned electrodes stored in oxygen. A simple oxide coating would normally be removed by weak acid and physical abrasion. The black residue was resistant to organic solvents, whilst aqueous physical abrasion with fine abrasive removes some of the contaminant but resulted in the contact pad layers to break off.

### **2.5.7. Surface analysis of 4-ATP S-layer biosensor**

To complement electrochemical characterisation of the biosensor performance, atomic force and electron microscopy was used to interrogate the sensor surface and observe structural changes occurring upon each layer deposition.

AFM is not the traditional analysis method for organic or soft surfaces because of the nature of the system. Both 'contact' and 'tapping' modes were used but contact mode repeatedly resulted in tip contamination and image degradation or sample damage. As a result images presented were made in tapping mode. Contact mode is where the cantilever is rastered across the surface of a sample with deviations in the tip height proportional to the force applied and contours of the sample (silicon or silicon nitride tips applied at  $80 \text{ nM}^{-1}$ ). Tapping mode is where the tip is oscillated at a set frequency (320 kHz) and height across the sample and deviations from optimum oscillations occur from near-field repulsive and attractive forces, Van der Waals forces and electrostatics. This information is used to generate 2D or 3D topographical representations of the surfaces. P4 electrodes were analysed either bare after a 2 min piranha wash or during layer by layer biosensor construction, summarised in (Figure 2-17 A and B).

Two dimensional surface

Three dimensional surface

Surface roughness

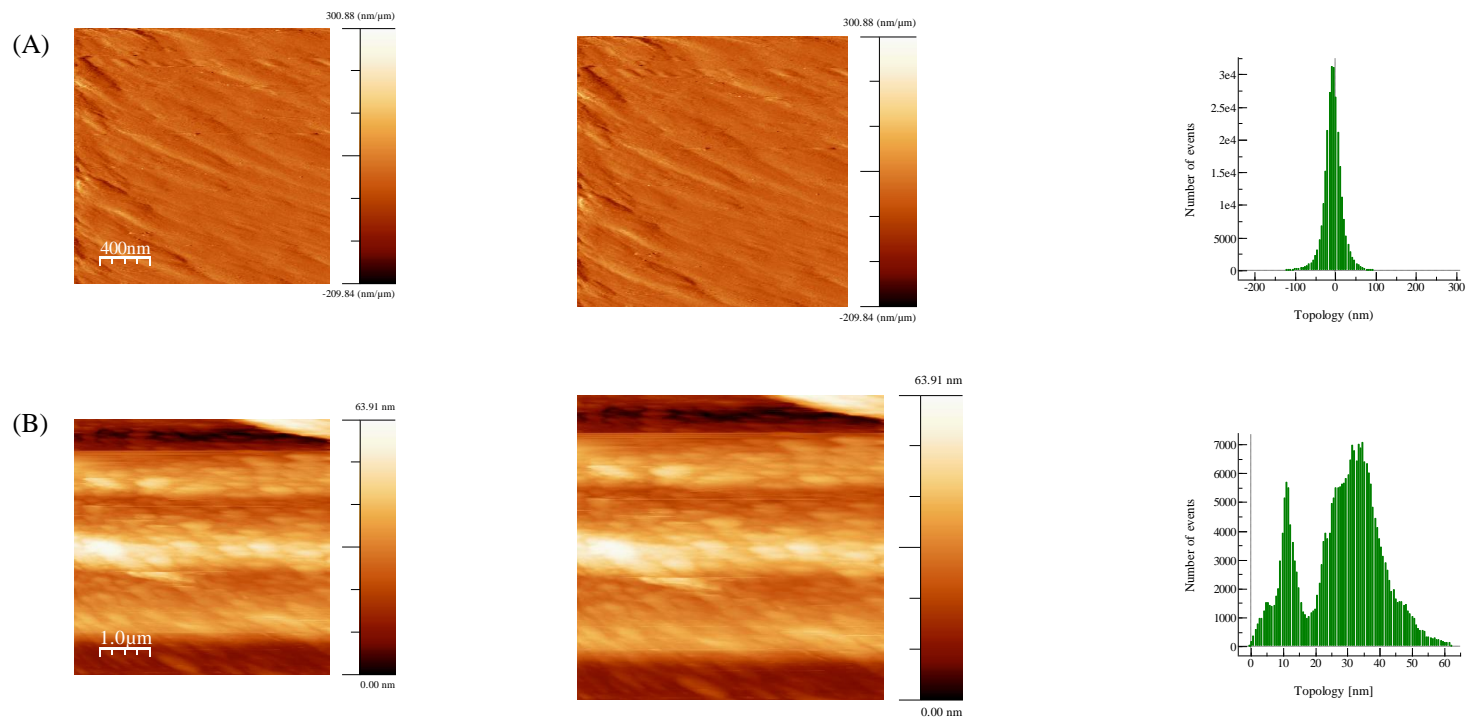


Figure 2-17 - Microscopy analysis of bare gold and constructed 4-ATP JG-A12 biosensor. . Left to right: 2D representation, 3D topographical view, surface roughness histogram. (A), AFM of bare gold electrode (2 μm x 2 μm area); (B), AFM of JG-A12 surface layer of biosensor (2 μm x 2 μm area); (C), SEM of biosensor surface.

(C)

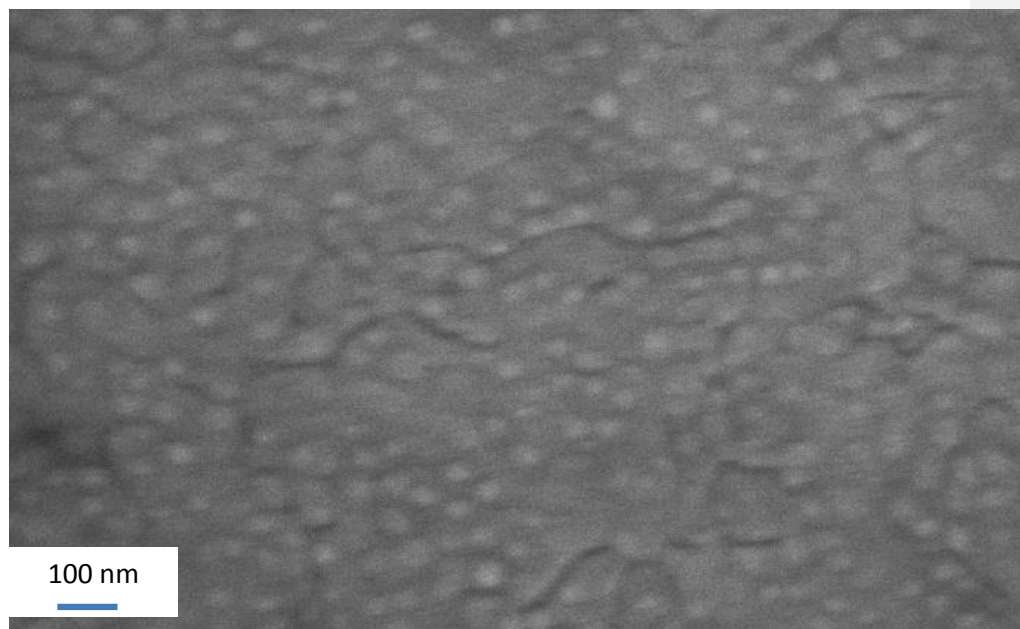


Figure 2-17 – Microscopy analysis of bare gold and constructed 4-ATP JG-A12 biosensor. Left to right: 2D representation, 3D topographical view, surface roughness histogram. (A) AFM of bare gold electrode ( $2\ \mu\text{m} \times 2\ \mu\text{m}$  area), (B) AFM of JG-A12 surface layer of biosensor ( $2\ \mu\text{m} \times 2\ \mu\text{m}$  area). (C) SEM of biosensor surface.

The bare gold electrode showed a surface roughness peak to trough of around 200 nm although many troughs were less than 50 nm. This roughness is significant compared to the expected thickness of the biosensor and is far from atomically flat. Repeated scans showed reproducible stable features confirming no organic or contaminants remained. No significant difference between 4-ATP and sulfo-SMCC layers were observed, as the expected height change calculated from computational modelling was below the limits of the machine (linker layer 1.5 nm, S-layer protein 12.5 nm by 7.2 nm [98]). However variations between the bare gold and functioning sensor were observed as shown in Figure 2-17 B. AFM negative mode surface rastering showing fluid like behaviour with repulsion from tip resulting in trench formation. Unfortunately, because of this fluid like nature, the protein aggregate domains could not be well imaged and sized but were confirmed by the parallel trench formation typically ranging between 30 and 40 nm suggesting protein aggregated rather than formed a monolayer. While previous work by Hays [94] and Billah [99] had success imaging lipid

domains in this way, Caygill [100] while trying to image viral sensors suffered the same difficulties imaging organic layers. SEM analysis (Figure 2-17 C) further confirmed the theory of protein aggregates with spherical regions ranging 20 – 40 nm. However, it is important to note that wet AFM is more indicative of the biosensor in its natural state, while SEM samples were dried where some aggregation may be due to the lyophilisation process. Atmospheric AFM, a method where a biological sample can be imaged in its more natural state by increasing humidity to saturation within the microscope chamber, can allow biological samples to be imaged in their natural folded state.

### **2.5.8. Cyclic voltammetry of 4-ATP vs 4-MTP tethering method**

The changes in conductivity using ferricyanide CV during each stage of biosensor assembly is shown in Figure 2-18. From the drop in current comparing bare gold electrodes to modified electrodes, the 4-ATP linkers are far more conducting (-17.46 to -13.36  $\mu\text{A}$ ) and suited to amperometric systems than the 4-MTP (-17.44 to -4.94  $\mu\text{A}$ ) system which shows a significant reduction in current, and shows greater variation showed by error bars. The 4-ATP linking mechanism followed almost linear current response with each successive deposition step (Figure 2-18 B, reduction current ■ dropping by 10.44  $\mu\text{A}$  compared to the bare electrode, oxidation current a 7.54  $\mu\text{A}$  drop). The 4-MTP system however shows significant reduction in both redox currents (Figure 2-18 D, ○ and ■) upon 4-MTP layer adsorption with minor change upon silane linker, which was expected to be the most insulating layer, then protein layer. In both systems the standard deviation between measurements is significantly smaller than those observed by the DropSens electrodes with little drift in the observed redox peaks (Section 2.5.6.6). Because of the smaller currents seen using an oxygen probe the 4-ATP was used as the optimum system for the JG-A12 system. However the 4-MTP system is shown to be stable and reproducible with high current systems such as ferricyanide (Figure 2-18 C).

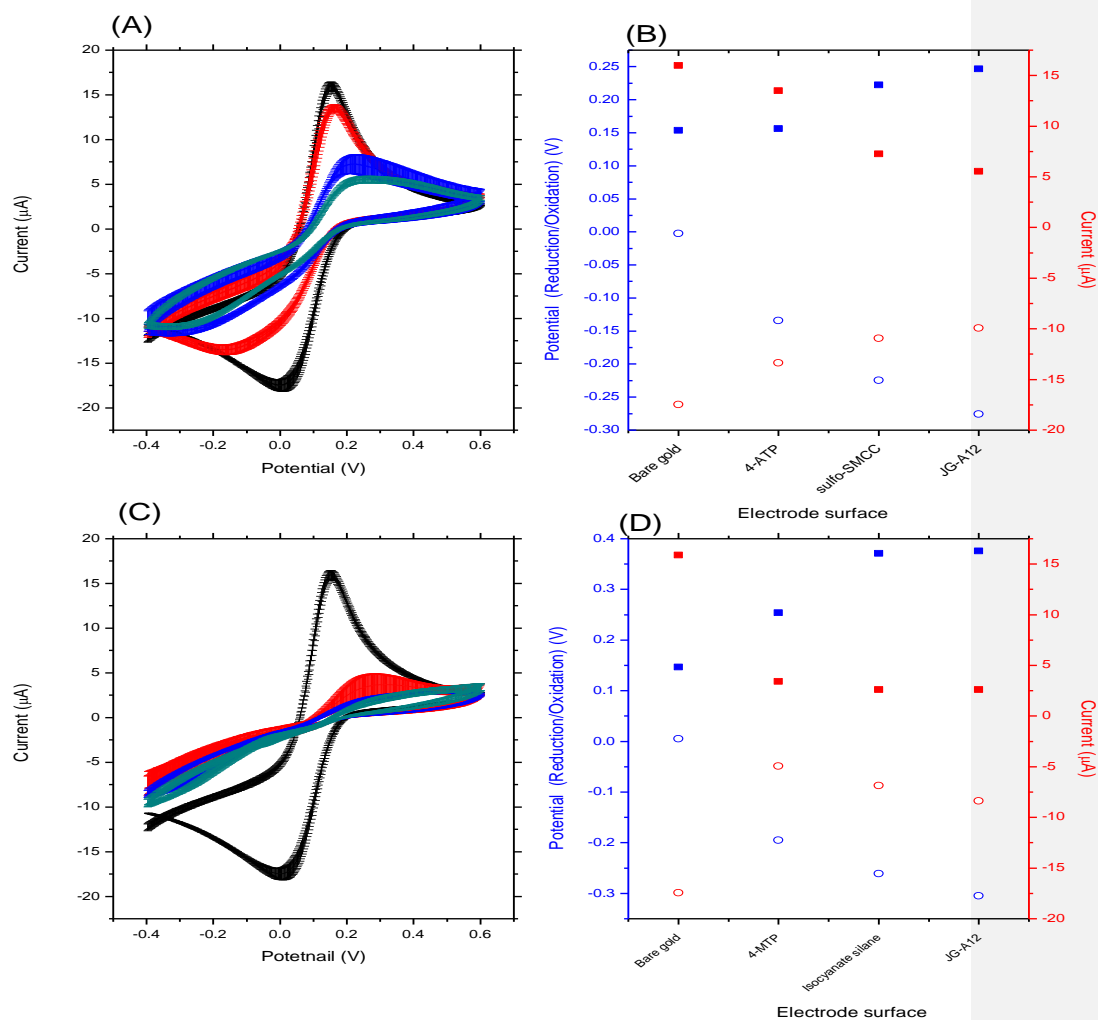


Figure 2-18 - Cyclic voltammetry showing pasivation of electrode surface with biosensor construction. (A) — Bare gold, — 4-ATP, — sulfo-SMCC, — JG-A12. (C) — Bare gold, — 4-MTP, — isocyanate silane, — JG-A12. (Triplicate scans with standard deviation, 10 mM ferricyanide in 10 mM PBS, -0.4 to 0.6V, 50mV/s). (B) and (D) extrapolated potentials and currents for ferricyanide redox reactions after each layer was deposited onto gold P3 electrodes. Symbols;  $\circ$  for oxidation and  $\blacksquare$  for reduction. Lines colour coded to axes; blue for potentials on left axis, red for currents on right axis.

Table 2-2 – Summary of extrapolated redox current potentials from Figure 2-21.

Curve	Graph legend	Left peak (○ oxidation)		Right peak (■ reduction)	
		Potential (V)	Current (μA)	Potential (V)	Current (μA)
Bare Gold	—	-0.002	-17.463	0.154	15.970
4-ATP	—	-0.134	-13.364	0.156	13.499
sulfo-SMCC	—	-0.225	-10.921	0.222	7.252
JG-A12	—	-0.276	-9.920	0.247	5.533
Bare Gold	—	0.005	-17.443	0.146	15.871
4-MTP	—	-0.195	-4.949	0.254	3.426
isocyanate silane	—	-0.261	-6.853	0.371	2.599
JG-A12	—	-0.305	-8.384	0.376	2.619

### 2.5.9. Impedance analysis and Randle's fitting comparison of 4-ATP vs 4-MTP tethering method

Extrapolated Randles component analysis shows the variation in components with SLP biosensors constructed from different base layers. The 4-ATP linker method is compared to the 4-MTP method (Figure 2-19). Both 4-ATP and 4-MTP are small aromatic molecules that will assemble in ordered arrays due to  $\pi$ - $\pi$  stacking between adjacent molecules. This allows diffusion and conduction between them creating highly conducting surfaces (0.95 M $\Omega$  and 0.83 M $\Omega$  (■ R<sub>p</sub>) respectively). The variation of the current and surface charge is from the different functional groups of each base molecule, free amines on 4-ATP compared to hydroxyls on the 4-MTP. Sulfo-SMCC is not expected to bond inter-molecularly, but high silane concentrations that rapidly hydrolysis can result in intermolecular bonding and bulk insulating layers (see Chapter 5 high surface area sorbents). However, 2 h incubation in 1% silane, 3% H<sub>2</sub>O in ethanol was mild enough to ensure the bulk of three available silanol groups condense onto the 4-MTP sites. This created a porous conducting layer shown by the low R<sub>p</sub> resistance. If significant inter silane condensation occurred complete surface passivation and a higher R<sub>p</sub> would have been observed.

JG-A12 layers showed layers of 1.67 μF and 2.10 μF (○ C<sub>dl</sub>) capacitance and 0.22 M $\Omega$  and 0.16 M $\Omega$  (■ R<sub>p</sub>) resistance respectively. No significant change in solution resistant was observed showing both tethering mechanisms were stable under the potential ranges used. There is significantly larger standard deviation in sensors created using the isocyanate linker

(also shown in Figure 2-19) between three electrode batches, due presumably to larger variations in the amount of S-layer protein bound. As a result, the 4-MTP method was used for biosensor analyte interrogation, but the 4-MTP method still has potential application but currently shows greater variation in the amount of protein bound.

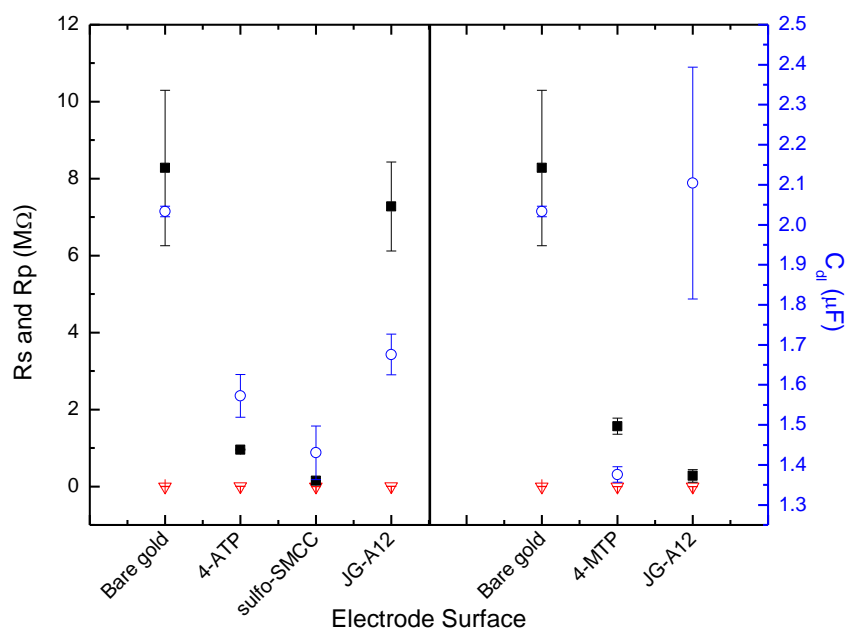


Figure 2-19 -Triplicate averages were taken from Nyquist scans. (51 point calculated across a frequency range of 250 kHz to 0.1 Hz in a solution electrolyte of 10 mM PBS containing 10mM ferricyanide). Electrochemical parameters extracted based on Randles equivalence. Symbols correspond to  $\circ$   $C_{dl}$ ,  $\nabla$   $R_s$ ,  $\blacksquare$   $R_p$ . Left shows the 4-ATP method, right the 4-MTP silane method.

### **2.5.10. Biosensor response and binding analysis – uranyl compounds, interfering analytes, non specific receptors and inhibition**

The response of the prototype sensor was tested with a range of uranyl compounds, as well as known interfering analytes and other divalent cations. This was to confirm there were no false positive responses from other ion species. These results are summarised in Figure 2-20.

Binding of uranyl ions from any compound to the protein layer resulted in a large decrease in the imaginary impedance component, significantly more than other interfering divalent cations, which saturated around 40 %  $\Delta -Z''$  (Figure 2-20 A).

Significant charge build up at the interface from analyte binding appeared to compress the molecular double layer showing the greater selectivity of the JG-A12 SLP to  $\text{UO}_2^{2+}$  than other analytes ( $\text{Ni}^{2+}$ ,  $\text{Cs}^+$ ,  $\text{Cd}^{2+}$ ,  $\text{Co}^{2+}$  on Figure 2-20 B). Analytes for which JG-A12 SLP had a lower affinity caused a smaller decrease in imaginary impedance, typically around 10–20%.

Figure 2-21 A shows individual and combined functional group blocking on a functioning SLP biosensor. While there is some limited response when only 1 binding site is chemically blocked suggesting some monodentate binding, the complete binding inhibition by blocking both functional groups supports a dominating bidentate mechanism. Experiments also showed that uranyl binding was reversible as would be predicted since the interaction mechanism is non-covalent. Previously uranyl saturated biosensors that were briefly washed with buffer showed complete removal of uranyl ions which strongly implies rapid on and off rates of binding for the  $\text{UO}_2^{2+}$  ions binding to the SLP.

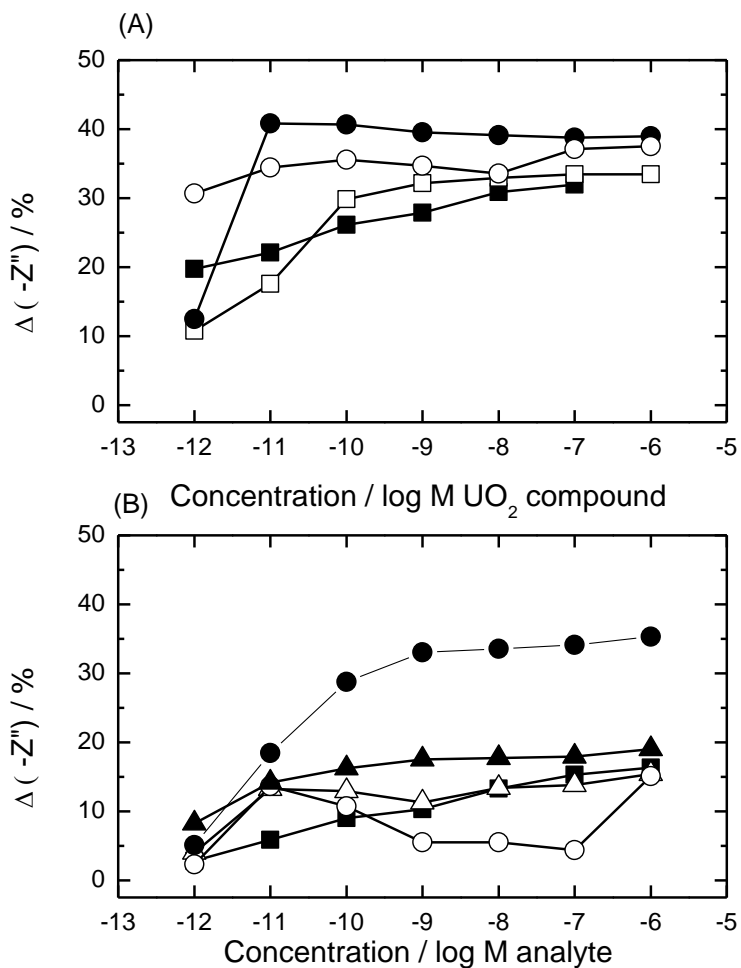


Figure 2-20- Real time capacitance response to uranyl biosensor using JG-A12 surface layer protein host receptor. (A) Response of biosensor to different uranyl compound (■ uranyl nitrate on six hour old electrode, □ uranyl nitrate response from a seven day old electrode, ● natural uranyl nitrate response, ○ uranyl acetate response). The data show no differentiation between uranyl compounds as all are able to bind with the  $UO_2^{2+}$  in the +6 oxidation state. (B) Response of biosensor to a range of interfering divalent cations (■ nickel nitrate,  $\Delta$  caesium sulfate, ○ cadmium nitrate,  $\blacktriangle$  cobalt chloride, ● average uranyl response). Response is typically 10–30 % lower than response to uranyl ions.

To confirm this apparent selectivity for  $\text{UO}_2^{2+}$  was due to binding by the JG-A12 SLP a number of controls were performed using alternative protein layers and binding site modification (Figure 2-21 B). Sequential uranyl aliquots were added to a bare electrode in buffer in comparison showed a  $-Z''$  response 3 orders of magnitude lower showing that there is some double layer capacitive component from unbound uranyl ion-gold interaction but it is significantly lower than the main signal. The signal stability of a bare electrode in buffer only was monitored over 6 h and was stable within 2 % of the base signal during this time. Sensors constructed with other proteins that lacked the uranyl binding specificity of JG-A12 SLP showed a lower binding response. The phosphoprotein casein was used to further elucidate if the sequestering ability of JG-A12 SLP originated via a monodentate mechanism using phosphate groups or a bidentate mechanism involving both phosphate and carboxylate groups. This is because the JG-A12 SLP is similarly a highly phosphorylated protein.

Bovine serum albumin (BSA), a relatively stable and inert protein often used to block non specific analyte binding was similarly used as a control. There was virtually no response from the casein sensors which showed that in spite of a high degree of phosphorylation, the protein did not manage to bind a significant amount of uranyl. This supports the idea that the JG-A12 SLP was responsible for the specific  $\text{UO}_2^{2+}$  binding. BSA gave an intermediate response due to the non-specific electrostatic binding of  $\text{UO}_2^{2+}$  to the proteins negative surface charge. These two alternate protein sensors support the specific binding of JG-A12 SLP to uranyl in a bidentate manner.

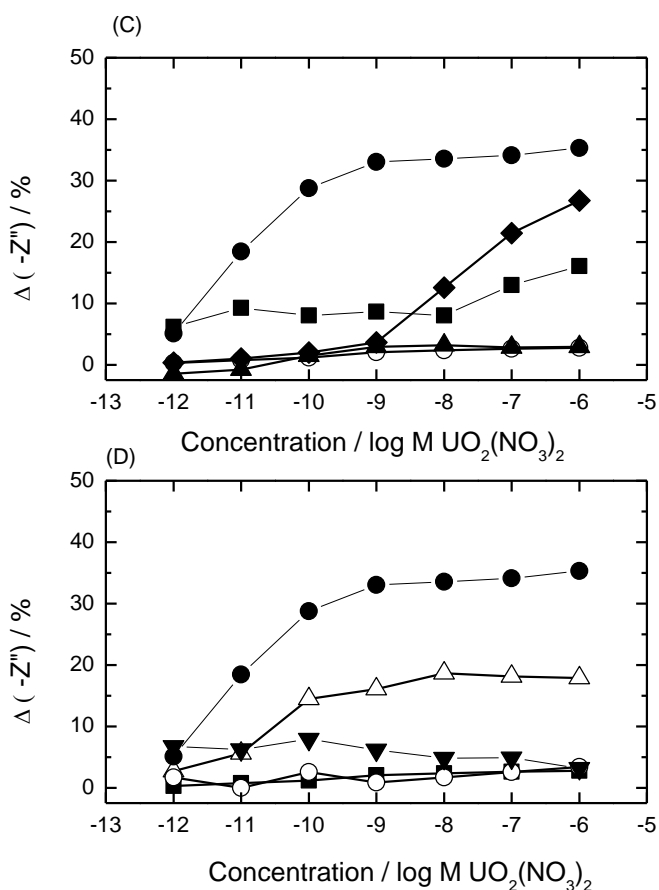


Figure 2-21 – Kinetic binding models of uranyl to JG-A12 electrode. (C) Modified SLP protein response to  $\text{UO}_2^{2+}$  (▲ both carboxylates and phosphates moieties blocked, ■ carboxylates only blocked, ◆ phosphates only blocked, ○ base signal drift over a six hour period, ● average uranyl response of SLP biosensor for comparison). (D) Effect of using non-specific proteins as the sensing agent. Biosensors were constructed and the response to  $\text{UO}_2^{2+}$  monitored (○ casein sensor response, △ BSA sensor response, ▼ BSA sensor response with carboxylates blocked, and ● average uranyl response of SLP biosensor for comparison). The percentage decrease in  $-Z''$  was calculated as previously. Sequential analyte injections were performed over a six hour period. (■ a control sensor with no analyte added showed only a 2% drift in base signal over the same period).

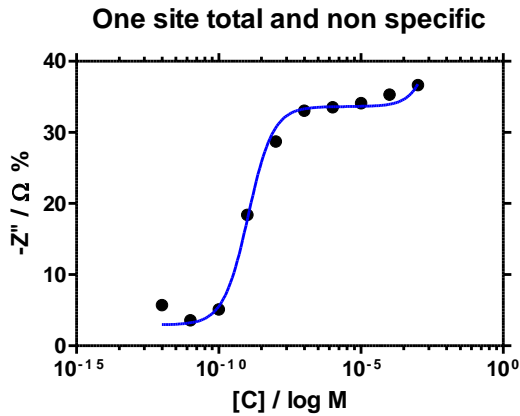
### 2.5.10.1. Kinetic binding analysis

Six kinetic models were fitted to the S-layer uranyl data, a range of those that were expected to be poor fit and potential matches to the binding mechanism. The two closest fit are displayed in Figure 2-22 and the models used in fitting shown in Equations 2-3 and 2-4.

$B_{max}$  is the maximum specific binding ( $-Z\%$ ). It is the specific binding extrapolated to very high concentrations of radioligand, so its value is almost always higher than any specific binding measured in experiments.  $K_d$  is the equilibrium binding constant in Moles, the concentration needed for half maximum binding under equilibrium conditions. NS is the slope of nonspecific binding in  $-Z\% M^{-1}$ .  $B_{maxHi}$  and  $B_{maxLo}$  are the maximum specific bindings to the two sites in the units  $-Z\%$ .  $Kd_{Hi}$  and  $Kd_{Lo}$  are the equilibrium binding constants, in the same units as X, the analyte concentration. It is the radioligand concentration needed to achieve a half-maximum binding at equilibrium. Fitted parameters for each model are summarised in Table 2-3. From experimental and literature interpretation, the fitting supports a two site binding model between phosphate and carboxylates, with a 50 % binding saturation ( $k_d$ ) between  $4.60E^{-8} M$  and  $7.98E^{-10} M$ .

Table 2-3 – Fitted binding kinetic parameters of SLP biosensor in response of uranyl. Two models were used, one site total and non-specific and two site total and non-specific.

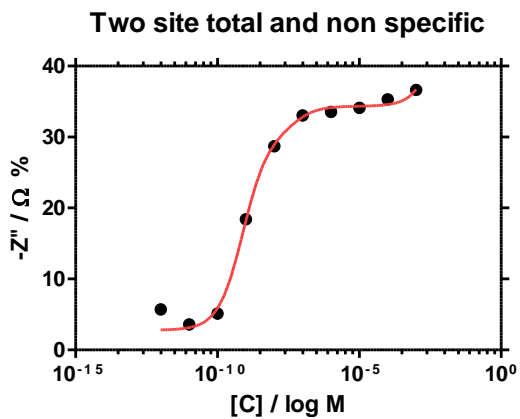
One site total and non-specific		Two site total and non-specific.	
Parameter	Value	Parameter	Value
$B_{max}$	$30.69 -Z\%$ ,	$kd_{Hi}$ and $Kd_{low}$	$>0$
$k_d$	$1.09E^{-9} M$	$B_{maxHi}$	$27.39 -Z\%$
NS	$3149 -Z\% M^{-1}$	$kd_{Hi}$	$7.98E^{-10} M$
		$B_{maxLow}$	$4.160 -Z\%$ ,
background	$2.94 -Z\%$ .	$kd_{Low}$	$4.60E^{-8} M$
		NS	$2371 -Z\% M^{-1}$
		background	$2.79 -Z\%$
		affinity ratio	57.63
		percent high affinity	86.82



$$Specific = B_{max} * \frac{X}{X + k_d}$$

$$Nonspecific = NS * X + Background$$

(2-3)



$$Specific1 = B_{maxHi} * \frac{X}{X + k_{dHi}}$$

$$Specific2 = B_{maxHi} * \frac{X}{X + k_{dLow}}$$

$$Nonspecific = NS * (X + Background)$$

(2-4)

Figure 2-22 – Kinetic fitting of SLP biosensor to increasing concentrations of uranyl. Of the two models used, one specific and two specific, the data shown supports a two site binding model.

### 2.5.11. Blocking of SLP phosphates and carboxy groups

Further supporting the EIS results that the SLP binding sites were chemically blocked (as detailed in Section 2.4.3.1) to inhibit analyte binding was confirmed by XPS analysis. This method analyses the ratio of carbon to gold within the few surfaces nanometres of the biosensor to determine chemical composition, shown in Figure 2-23.

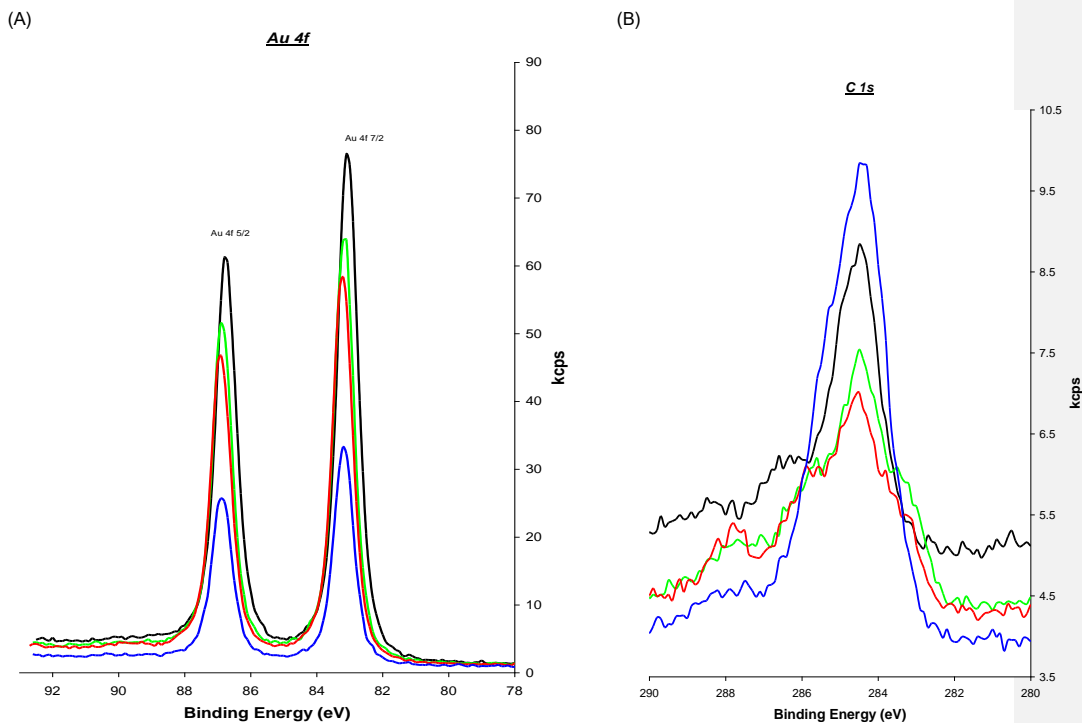


Figure 2-23 - A weak pair of peaks at 365 and 373 eV were observed and identified as Ag 3d3/2 and Ag 3d5/2 peaks. Detailed scans of the C 1s, the Au 4f were taken, baselines were fitted and the peak's areas compared to give relative atomic percentages, summarised in Table 2-4.

Table 2-4 - Gold and carbon XPS spectrum of electrodes that were either bare, coated with a functioning biosensor or a chemically blocked biosensor.

Sample	Ag3d5/2 %	Au 4f %	C 1s %
Bare P3 gold electrode	0.84	49.69	50.17
SLP biosensor 1	0.76	40.9	58.34
SLP biosensor 2	0.25	41.46	58.28
Chemically blocked biosensor	0.2	19.44	80.36

### **2.5.12. Life Time trials**

P3 or P4 4-ATP based sensors were stored in a variety of conditions. After 1 month of wet storage in PBS at room temperature or at 5 °C only 40 % remained functional. Of remaining electrodes after a 4 month period only one remained fully functional with the remainders dropping to only a 2-15 % response compared to newly made electrodes. Figure 2-24 shows the difference in signal stability and noise in (A) a newly made biosensor and (B) a 1 week old electrode stored in 10 mM PBS. As the S-layer proteins are stable at room temperature storage for over a year it was presumed the stability decrease was due to the linker molecule failure with the maleimide oxidation resulting in protein desorption or significant salt crystallisation from buffer storage observed in some SEM images.



## 2.6. Conclusion

It has been shown that by tethering protein layers to metal surfaces via bioconjugation it is possible to create a dense protein layer without denaturing the protein. Coating surfaces with proteins such as the JG-A12 SLP can create bio-functional surfaces that retain the *in vivo* functionality, which was successfully purified and sized as a 120 kDa monomer using HPLC and SDS-PAGE. While mSAMs create stable environments for a number of enzymes and proteins, this was not the case for JG-A12 SLP and a more direct bioconjugation procedure proved more effective. Biosensors were shown to respond to sub-nM levels of aqueous uranyl with this response inhibited by chemical modification of proposed binding sites. The response from surfaces coated with control proteins supported our contention that the binding specificity was conferred by the JG-A12 SLP. Moreover chemical modification of carboxy and phosphate groups on the SLP abrogates uranyl recognition, indicating that the previous suggested binding mechanism [87] was correct. This was confirmed by both EIS and XPS. The current biosensor detection limit is  $10^{-12}$ M. While a number of experiments were performed to  $10^{-15}$ M these are currently difficult to reproduce and highly sensitive to system noise. A limit of  $10^{-12}$ M and above has been reproducible across numerous protein and electrode batches. Surface interrogation using microscopy technique proved difficult because of the organic nature of the material, but qualitative data confirmed protein layer deposition. Two alternative successful tethering mechanisms, the 4-ATP and 4-MTP methods were shown to be stable, reproducible and remain conductivity, particularly of importance to the silane sinkers which without the new novel 4-MTP layer would form a bulk insulating surface layer. The biosensor was used on a new commercial batch of screen printed DropSens electrodes to transfer the system to a more scalable design. However, because of reference instability and poor resistance to cleaning methods they performed inferiorly to the P3/P4 electrodes.

Significant variation between otherwise reproducible sensor surfaces upon addition of the organic component is not uncommon, and is seen in many protein based ISFET (ion-sensitive field-effect transistors [101]. The current observed across the gating electrodes is very much influenced by the presence of a protein layer. The ions, initially present in the protein layer in a relatively high concentration, cause a local low resistance, thereby increasing the cut-off

frequency of the ISFET, analogous to ferricyanide ions diffusing to and from the electrode through the SLP layer.

Proteins adsorbing at a metal interface do not form a complete insulating layer and only cause relatively small capacitance changes. The capacitance changes are sensitive at low frequency, and 0.1 Hz was used as the optimum frequency to monitor binding. Adsorption of a protein layer at the surface has been shown to be observable as a function of capacitance as well as in interfacial potential.

A further reason for variation between sensor batches is that the protein coating may create micro chemical surroundings with a composition which deviates from the bulk electrolyte composition. This phenomena occurring will depend on the porosity of the adsorbed layer and species in the bulk analyte. These micro chemical environments can be observed with EIS as a lateral drift in the electron transfer resistance with time and can be accounted for by calibration [102] and is not a fatal problem for a working device.

The next stage would be to use the biosensor system in a bespoke microfluidic device which is currently being developed by colleagues in civil engineering here at the University of Leeds. Testing the device in synthetic groundwater systems and in the field would be the next logical steps of progression.

### **3 : Crown ethers – potential synthetic receptors for metal ions**

---

### 3.1 Chapter overview

Because of the lack of other available biological host proteins such as the JG-A12 protein, an alternative class of synthetic hosts, the crown ethers, were selected as potential hosts for chemosensing of analytes  $^{90}\text{Sr}^{2+}$  and  $^{137}\text{Cs}^+$ . A range of commercial crown ethers were identified and modified for specificity to  $^{90}\text{Sr}^{2+}$ . These hosts were then trialed as chemosensor hosts using EIS on hybrid mercury-ionic liquid electrodes or via SAMs on gold electrodes. No proportional quantification was achieved. A mass based detection system using frequency dampening as  $\text{Sr}^{2+}$  ions bound to a SAM bound crown ether host was demonstrated, but no satisfactory quantifiable method using EIS, stripping voltammetry or QCM was achieved. As a result, this approach was abandoned. The hierarchy of this chapter is shown in Figure 3-1.

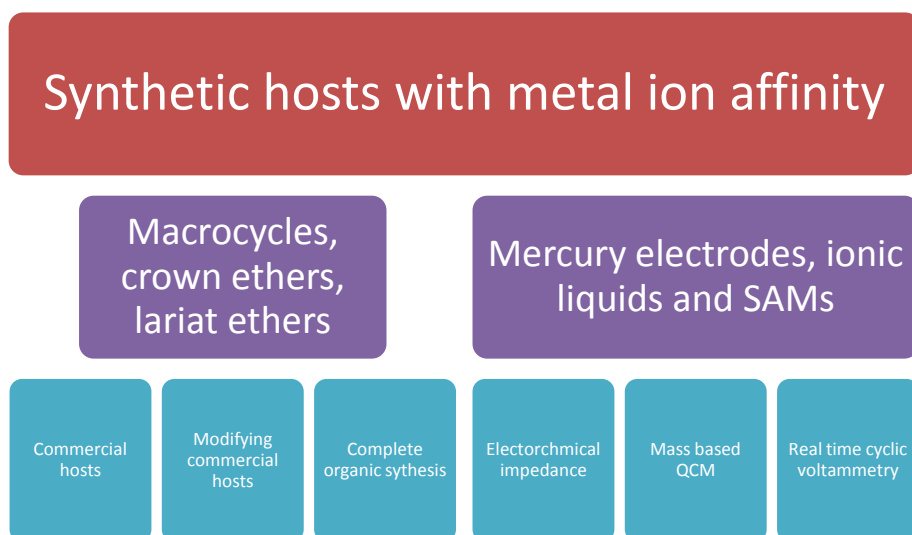


Figure 3-1 - Chapter three hierarchy outlining the methods used to use synthetic macrocycle hosts as potential components for chemosensors.

## 3.2 Introduction to macrocycles

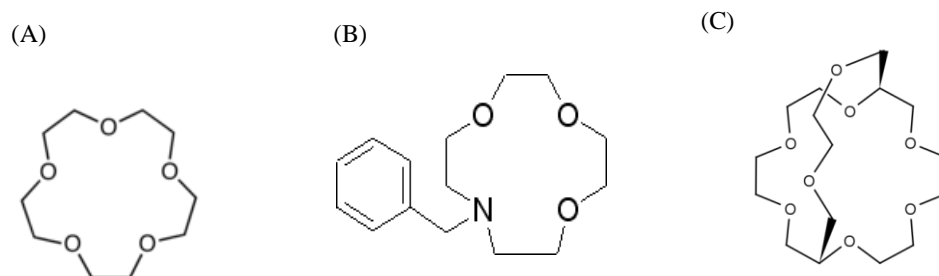


Figure 3-2 – Examples of the three broad macrocycle categories; crown ether, lariat ether cryptand / podand.

Macrocycles are by IUPAC definition ‘a cyclic macromolecule containing a ring of nine or more atoms with 3 or more potential donor atoms that can co-ordinate to a metal centre’[103]. Synthesis is frequently from monomer polymerisation, allowing control of the functional groups on the upper and lower rims, making these molecules particularly advantageous for metal chelation. Three broad classes of crown ether exist, as shown in Figure 3-2. The most basic crown ether is a cyclic crown (Figure 3-2 A) which is a two dimensional ring. The pore size is indicated by the nomenclature, for example, a 10-crown-5 ether corresponds to a crown of 10 carbon atoms with 5 donor oxygen atoms. Lariat ethers are crown ethers with a pivoting ‘podand’ side arm that allow a degree of three dimensional movement around the analyte (Figure 3-2 B). Dicyclohexano- 18-crown-6 (DC18C6) is a cyclic crown ether with a flexible rim in comparison to the identified caesium binders that function from a rigid circular arrangement of 6 co-coordinating crown-ether oxygens around the central metal cation. Synthetic podands however, are considered to have smaller stability constants and act as poorer ligands [104]. Natural podands however can have excellent binding abilities, such as polyether antibiotics (monsin and lasalocid), acting as naturally occurring membrane ion transporters [105]. The only supra-molecular structure that offers greater selectivity to lariat ethers are the cryptands (Figure 3-2 C). These are true three dimensional hosts resembling two crown ethers at perpendicular geometry, with the inner core offering chelation typically to one or two ions. These molecules have higher size selectivity and higher bonding affinity due to the lower entropic cost to binding (molecules are more rigid and cannot undergo significant conformational change like the lariat ethers) and often have a higher enthalpic gain from satisfaction of all inner core bonding sites [106]. One such

macrocyclic identified as binding strontium with high affinity is lariat dicyclohexano-18-crown-6 [107].

A summary of known ionic diameters and ether cores is shown in Table 3-1 as an indicator of size ranges. Noted however is the importance of dispersant compatibility, pH and polarity in terms of successful chelation, which is not just based on pore size comparison.

Table 3-1 - Comparison of a number of crown ethers with the ionic diameter of various metal cations [108].

Cation	Diameter of stated valency (Å)	Cation	Diameter of stated valency (Å)
Li <sup>+</sup>	1.36	Mg <sup>2+</sup>	1.44
Na <sup>+</sup>	1.90	Ca <sup>2+</sup>	2.20
K <sup>+</sup>	2.66	La <sup>3+</sup>	2.34
Cs <sup>+</sup>	3.38	Lu <sup>3+</sup>	2.00
Cu <sup>+</sup>	1.92	Zr <sup>4+</sup>	1.72
Ag <sup>+</sup>	2.52		

Crown Ether	Cavity Diameter (Å)
[12] crown - 4	1.20 - 1.50
[15] crown - 5	1.70 - 2.20
[18] crown - 6	2.60 - 3.20
[21] crown - 7	3.40 - 4.30

### 3.2.1 Therapeutics and analyte targeting

Therapeutic techniques have made advances particularly in the magnetic and nuclear resonance areas due to the need to target specific diagnostic and therapeutic agents. These agents include nucleic acids, proteins and enzymes, monoclonal antibodies and also specific cells and target receptors [109]. Chelation of radioactive ions is common in various medical imaging techniques. Delivery of lanthanide ions by use of co-ordination chemistry has significantly increased magnetic resonance imaging techniques [62]. These techniques initially focused on bioreceptor targeting. That is, identifying a receptor and designing how to target delivery to a specific location in the body. Loading of molecules (drugs, ions, genes etc) to deliver to the active site has often been the problem. Advances in the metal ion receptors have now caught up with the targeting mechanisms. In many cases these systems could be applied inversely. These hosts could be tethered to sensor designed surface and used to bind metal ions rather than deliver them. Thus, there is potential for small ion biosensing by applying hosts developed for medical imaging or remediation technologies. A range of synthetic metal ion receptors currently available is presented.

### 3.2.2 Hosts specific to the lanthanide series

Lanthanide ions act as hard acids, preferring hard base donors with polyamino carboxylate and phosphate ligands to successfully chelate with high co-ordination number acceptors [110]. One class of these are the bifunctional chelators. These are ligands that bear two different functional groups used to covalently attach the ligand to a targeting group. Often they are functional in aqueous media and react selectively with nucleophilic groups [62]. These receptors need to be thermodynamically and kinetically stable to bind and inhibit dissociation *in vivo* after sequestering of the toxic ion. The most common bifunctional chelators of this type in-use are the bis-anhydride of DOTA (1,4,7,10-tetraazacyclododecane- $N,N',N'',N'''$ -tetraacetic acid, Figure 3-3A) and DTPA (diethylene triamine pentaacetic acid, Figure 3-3B).

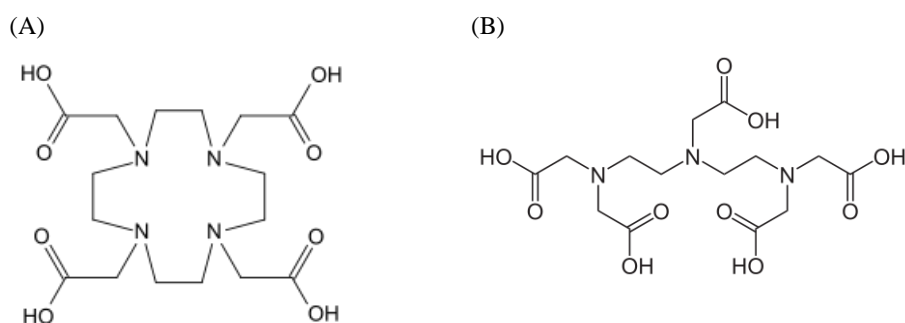
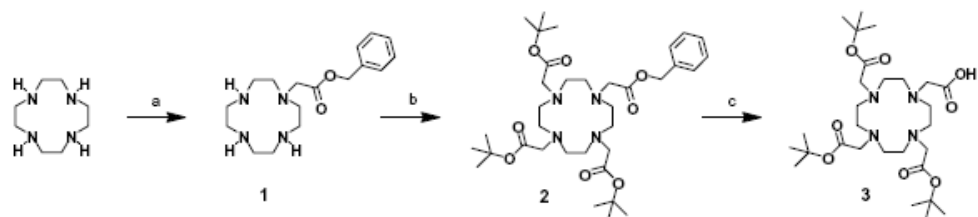


Figure 3-3 - Figure of bifunctional chelators (A) DOTA and (B) a derivative of DTPA, a linear octadentate polyaminocarboxylates that has been most studied to date [62].

The DOTA series are a more recently class of bifunctional chelators. While less stable than diethylene triamine pentaacetic acid (DTPA) derivatives (Figure 3-3), they have significantly increased metal binding capability [111] and have been used to target ions to a range of biological receptors. Human serum albumin (HSA) is a protein abundant in the blood plasma (~0.6 mM) and contains a number of hydrophobic cavities. Use of DOTA has been shown to deliver  $Gd^{3+}$  ions to HSA *in vivo*. The sequential synthesis of DOTA shown in Figure 3-4 A, and a range of HSA derivatives used is shown in Figure 3-4 B.

An area of research currently underway, is in designing bifunctional chelators, in which one arm binds to the chelator site, and the second to the host receptor. A substrate mimic for the enzyme carbonic anhydrase which normally binds zinc ions, was created using aryl sulphonamides. The substrate successfully bound to the enzyme's catalytic site inhibiting the enzyme, which was used to deliver a DTPA bound  $Gd^{3+}$  ion [112]. Combining these with oligonucleotide libraries allows powerful targeting methods to be developed. Inserting a gene sequence of a desirable protein into a viral DNA vector allows amplification of the corresponding sequence and replication of the desired protein. Attachment of this protein to a receptor molecule could be used for delivery to a specific bio receptor, or for biosensing at engineered surfaces. Rodriguez showed it was possible to create an engineered synthetic peptide that was then bound to the host complex Gd-DOTA via an amide linkage. This complex retained a moderate affinity for the corresponding site on protein GAL80, and successfully delivered the  $Gd^{3+}$  ion which was monitored in realtime by MRI [113].

(A)



(B)

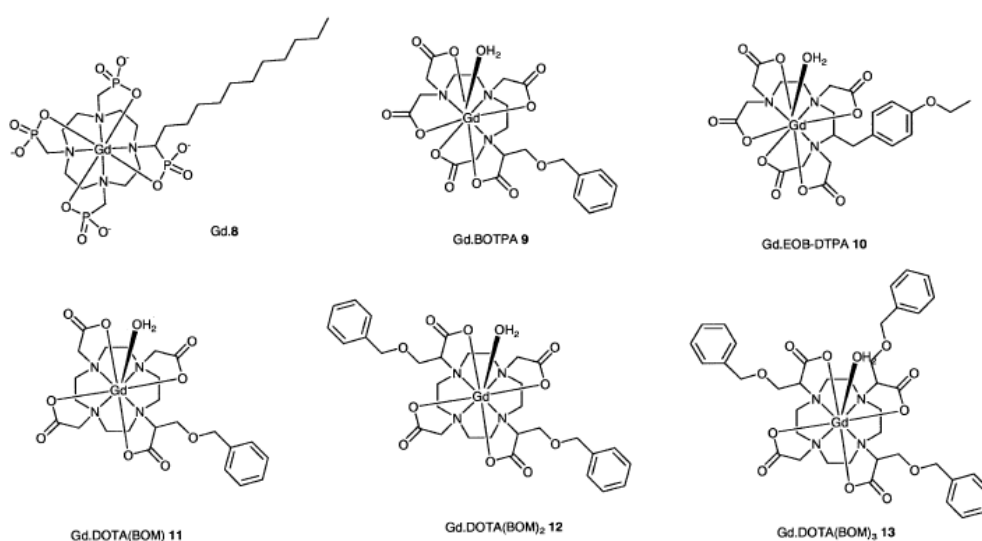


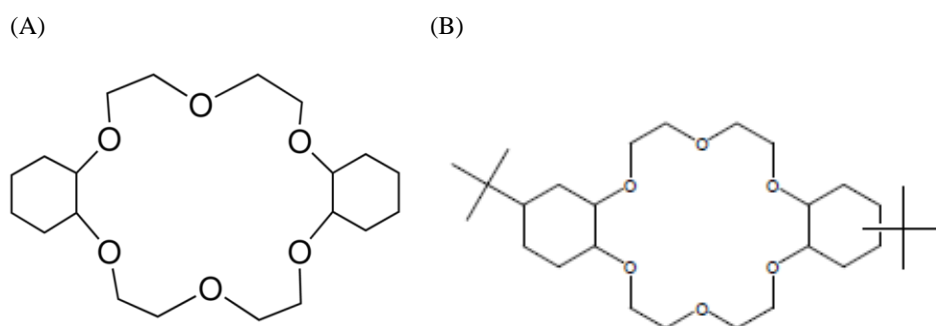
Figure 3-4 - Bifunctional chelators, serum albumin targeting vectors, enzyme and protein targeting. (A), Synthesis of bifunctional chelator 1,4,7,10-tetraazacyclododecane-N,N',N'',N'''-tetraacetic Acid (DOTA).Synthesis of tris-tBu-DOTA. Benzyl-bromoacetate, CHCl<sub>3</sub>, rt, 3 h 86% 2-tert-butyl bromoacetate, K<sub>2</sub>CO<sub>3</sub>, acetonitrile, rt, 2-5 h, 67 % 3Pd/C. H<sub>2</sub>, THF / MeOH 1:1, rt 2-8 h 71 % (Woods[62]). (B), BSA targeting derivatives that sequester and deliver gadolinium ions.

### 3.2.3 <sup>90</sup>Sr<sup>2+</sup> extraction in the nuclear industry

While a number of macrocycle hosts have been discussed based on therapeutic and medical technologies, they are also used significantly in bulk waste remediation, with solvent extraction in an acidic environment being an established technology.

For low level remediation it is important to first look at bulk remediation methods that are currently used in the nuclear industry, where parallels can be drawn and suitable chemical hosts identified. In solvent extraction, the analyte is in a miscible phase, ie aqueous, and the host molecule with desired specificity in a second immiscible phase, typically an organic solvent. By control of conditions such as pH, temperature, mixing rate and host, desired analytes can be extracted across the phase boundary while leaving other analytes in the aqueous phase.

Extraction in basic media, is a much more recent development than in acidic media. The SREX (strontium extraction process [114]) uses an expensive host, DtBuCH18C6 (Figure 3-5 B), but removes  $^{90}\text{Sr}^{2+}$  from high level waste (HLW) and aqueous media to strip strontium from organic media [115]. SREX methods offered higher selectivity and throughput with continuous processing possible and all liquid handling.



methyl-4-acyl-5-pyrazolone dispersed in benzyl alcohol. Moyer *et al* [117] showed that versatic acid and cleaning agent carbon tetrachloride was a viable strontium sorbent for strontium ions in high nitrate solutions [118]. While still used for small volume purification, these methods are not practical for large scale purification. One such host, calix[4]arene-bis(crown-6), shown in Figure 3-6, has excellent affinity for both  $^{90}\text{Sr}^{2+}$  and  $\text{Cs}^+$  ions but requires extensive chemical synthesis and there is currently no commercial source [119]. These sort of approaches to extraction have been superseded by emulsion and liquid membrane methods.

The lariat ether dicyclohexano-18-crown-6 (DC18C6), as the DC18C6[ $\text{Sr}^{2+}$ ] complex, bound  $\text{Sr}^{2+}$  in a 1:1 ratio. This complex could then bind to anions, such as nitrates and carboxylates in aqueous highly alkaline conditions (pH 11.2 [120]). It has been used as an extractant within several organic isoparaffinic hydrocarbon based systems [121] including kerosene, Span 80 (a polysorbate emulsifier) and D2EHPA (an organic extractant for metal ions) which itself has been used as an alkaline nuclear waste extractor, and the pseudo-emulsions LIX-79/n-heptane [122].

DC18C6 exists as five different stereoisomers based on the bonding of the cyclohexane rings (*cis* or *trans*) and the relationship of the two cyclohexane units (*syn* or *anti*). Two isomers *cis-syn-cis*- and *cis-anti-cis*-DC18C6 are easily obtained by the catalytic hydrogenation of dibenzo-18-crown-6 (DB18C6) [123], and are commercially available. The complexation and separation behaviour of these two isomers have been well established, as have their solid-state and solution structures.

(A)

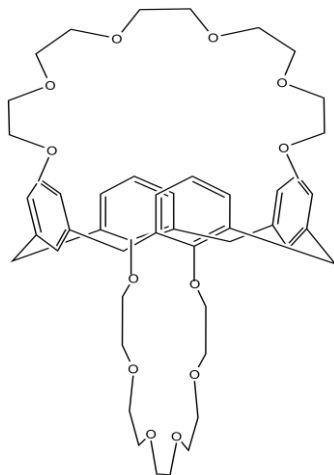


Figure 3-6 – Cryptand calix[4]arene-bis(crown-6), an excellent chelator for both strontium and caesium with a preference to the latter, is unusually water soluble [124] and able to hold two ions simultaneously stabilised by the phenol core and the upper and lower rings.

### 3.2.5 $^{137}\text{Cs}^+$ extraction in the nuclear industry

While an increasing number of extraction methods have been developed for bulk nuclear waste removal, in the 1980s practical extraction was still elusive due to poor selectivity and insufficient extraction efficiency of the chelators.

An application of caustic-side solvent extraction (CSSX) for the separation of  $\text{Cs}^+$  from legacy high level waste has had some success at US Department of Energy sites [125]. The need for concentrating high level wastes such as  $^{137}\text{Cs}$  is due to the cost and handling problems with decaying transuranic waste, and also to minimise disposal volume. The US Hanford site in Washington reported an accumulated stock of 55 million gallons of radioactive waste from defence related industries\ 15 % consisting of metal hydroxide sludge, with the bulk being ‘salt waste’ comprising  $\text{NaOH}$ ,  $\text{NaNO}_3$  and other soluble salts including  $^{90}\text{Sr}^{2+}$  and  $^{137}\text{Cs}^+$ . A number of early  $^{137}\text{Cs}$  extraction technologies were based on crystalline silico-titanate (CST) [126-128], cation exchange resins [129-131] and precipitation with tetraphenylborate, called the ‘in tank precipitation process’ [132-133]. Such methods were not possible until the mid 1990s until  $^{137}\text{Cs}^+$  selective hosts were identified that were able to remove  $^{137}\text{Cs}^+$  from a higher  $10^4$ - $10^6$  background concentration [134]. While industrial application of such synthetic chemical hosts was not used until the 1990s early caesium hosts identified had been documented more than a decade earlier [135].

Bis(tert-octylbenzo-crown-6 (BOBCalix6), a cryptand and a superior commercially available analogue calix[4]-bis-2,3-naphtho-crown-6 (CNC), is shown in Figure 3-7 B and has been used in such processes [136]. It should be noted that many similar analogues with high  $^{137}\text{Cs}^+$  selectivity all have 6 oxygens and a ring diameter of 4 phenol units.

The UNEX (UNiversal EXtraction) process is another process developed to remove  $\text{Sr}^{2+}$  and  $\text{Cs}^+$  ions after  $\text{UO}_2^{2+}$  removal. These cations interact with chlorinated cobalt dicarbollide and polyethylene glycol in a solution containing octyl(phenyl)-N, N-dibutyl carbamoylmethyl phosphine oxide (CMPO) in nitrobenzene [137]. Dibenzo-21-crown-7 (DB21C7) has also been shown to bind  $^{137}\text{Cs}^+$  from organic matrixes acetonitrile - dimethylsulfoxide (96.5:3.5, w/w) and nitromethane - dimethylsulfoxide (96.5:3.5, w/w) (Figure 3-7 A). Complexes of increasing stability observed were  $\text{Rb}^+ > \text{K}^+ > \text{Ba}^{2+} > \text{Tl}^+ > \text{Cs}^+ > \text{NH}_4^+ \approx \text{Pb}^{2+} > \text{Ag}^+ > \text{UO}_2^{2+} > \text{Hg}^{2+} > \text{Mg}^{2+} > \text{Na}^+$  [138].

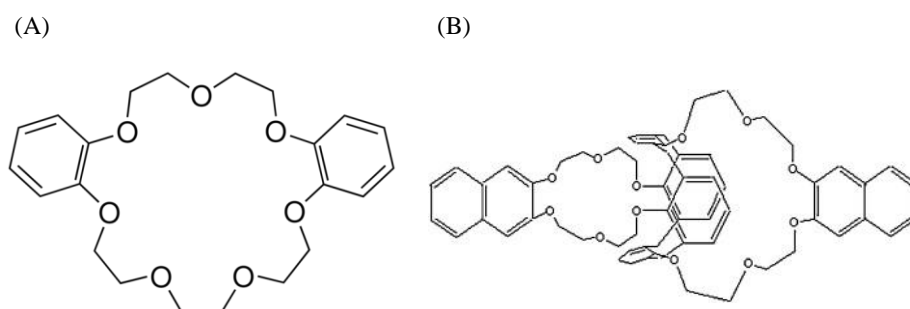


Figure 3-7 – Examples of crown ether discussed. (A) Dibenzo-21-crown-7 and cryptands and (B) calix[4]-bis-2,3-naphtho-crown-6 have high specificity for  $\text{Cs}^+$  extraction.

### 3.2.6 Uranium extraction and the nuclear industry

UREX (Uranium Recovery by Extraction) is a liquid-liquid phase process used to reprocess uranium, a similar process to (TRUEX) for plutonium enrichment developed in Russia and now common in the UK and France. Here, uranium is diluted in nitric acid, leaving  $\text{U}^{6+}$  and  $\text{Pu}^{4+}$ . Nitrates are removed from the aqueous phase typically by organic kerosene containing tributyl phosphate (TBP)[139].

By adding a second extraction agent, octyl(phenyl)-N, N-dibutyl carbamoylmethyl phosphine oxide (CMPO) in combination with tributylphosphate, (TBP), the PUREX process can be

turned into the **TRUEX (TRansUranic EXtraction)** process. TRUEX was invented in the USA by Argonne National Laboratory and is designed to remove the transuranic metals (Am/Cm) from waste.

The TRUEX process uses sequential nitric acid washes and organic heavy aromatic naphtha and octyl[phenyl]- N,N-diisobutylcarbamoylmethyl-phosphine CMPO extractants containing chelators diethylenetriaminepentaacetic acid (DTPA) hydrazine oxalate to remove elements Am, Cm, Pu, Np Ln, Y Tc and Zn [140].

### **3.2.7 Summary**

A range of macromolecular chelators that emerged from the fields of therapeutics, organic chemistry, solvent purification and the nuclear industry have been presented. Theoretically, from a perspective of donor groups and pore size, many hosts appear ideal for ion extractants. However, in practice, many fail at high or low pH, in complex contaminant mixtures, and exhibit poor stability over longer time periods or breakdown at elevated temperatures. As well as these factors, cost, availability and ease of synthesis effect the application of crown ethers.

## **3.3 Crown ethers and chemosensing**

Crown ethers are a relatively new integration with chemosensors. As of 2012, there are only around 300 publications to date on ScienceDirect compared to the 20,000 published on protein biosensing. The main mechanisms are either chromophore based or amperometric. In chromophore systems, binding of an ion to the crown ether either activates or quenches a fluorophore attached by a spacer arm. The alternative mechanism uses the crown ether similarly to the extraction methods discussed previously. The crown ether dispersed in an organic phase extracts the ion from an aqueous phase, transporting it to the working electrode where the ion undergoes a redox reaction.

### **3.3.1 Amperometric crown ether chemosensors**

Traditional mercury film electrodes are suitable for use with crown ethers and anodic stripping voltammetry (ASV) [141], with the advantage of analyte specificity endowed by the crown ether. However, because of toxicity issues, carbon paste seeded electrodes have been increasingly used. Desai [142] used four crown ethers. These were 18-crown-6, dibenzo-18-crown-6 (DB18C6), dicyclohexano-18-crown-6 and dibenzo-24-crown-8, out of which DB18C6 showed the greatest sensitivity for amperometric detection of pyridoxine hydrochloride. The crown ethers enhanced specificity can also allow small complex

molecule differentiation, such as in multivitamin pharmaceutical preparations. Thiamine hydrochloride, riboflavin, nicotinamide, para-aminobenzoic acid, cyanocobalamin could be differentiated by classification of their redox potential peaks that without the crown ether transporter would overlap giving a composite unidentifiable signal. Tetrathiafulvalene (TTF) based crown ethers that have been thiolated can be deposited from an acetonitrile solution into traditional mSAMs, as another potential sensor interface mechanism [143]. Importantly, they remained functional when switched to aqueous media, responding to  $\text{Li}^+$ ,  $\text{K}^+$ ,  $\text{Na}^+$ ,  $\text{Ba}^{2+}$  and  $\text{Ag}^+$  ions. Significantly this example shows that a single anchor point can be enough to tether crown ethers as opposed to linkage of every [n] ring and that the crown ethers can stack to form ion channels. An example of this tethering mechanism is shown in Figure 3-8 A where each phenol has a thiolated hydrocarbon tail that can bond to a gold substrate [144]. An alternative, Figure 3-8 B, is a non covalent linkage to the electrode such as SAM insertion via attachment of a hydrophobic tail [145].

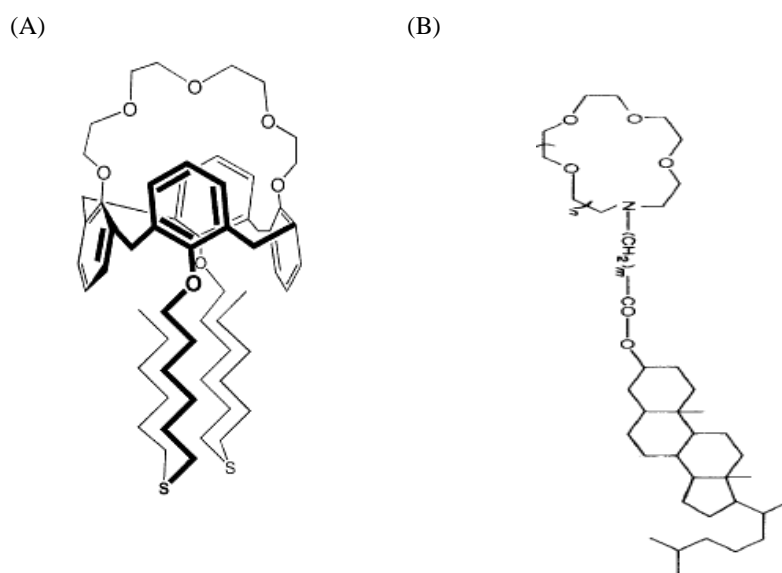


Figure 3-8 - Methods of tethering crown ethers to electrodes; (A), synthesis from monomers containing a functionalised spacer allowing orientated covalently linkage to a gold substrate, or (B), post synthesis modification of the crown ether such as adding a hydrophobic tail.

### 3.3.2 Chromogenic crown ether chemosensors

An ideal chromogenic host is one that upon analyte binding undergoes a colour change specific to the analyte bound. However, this is often not the case, with most chromophore ethers existing in an 'on' or 'off' state, producing a single colour change in analyte concentrations approaching milli molar (Figure 3-9). False negatives are likely if the host lacks specificity. However, if a known concentration of host molecule is known, by serial dilutions and calibration, a colour change can be used to give a rapid concentration based response. A range of aza crown ethers have been shown to do this in both organic and gaseous phases [146] but have also been shown to have poor specificity to  $K^+$  ions [103].

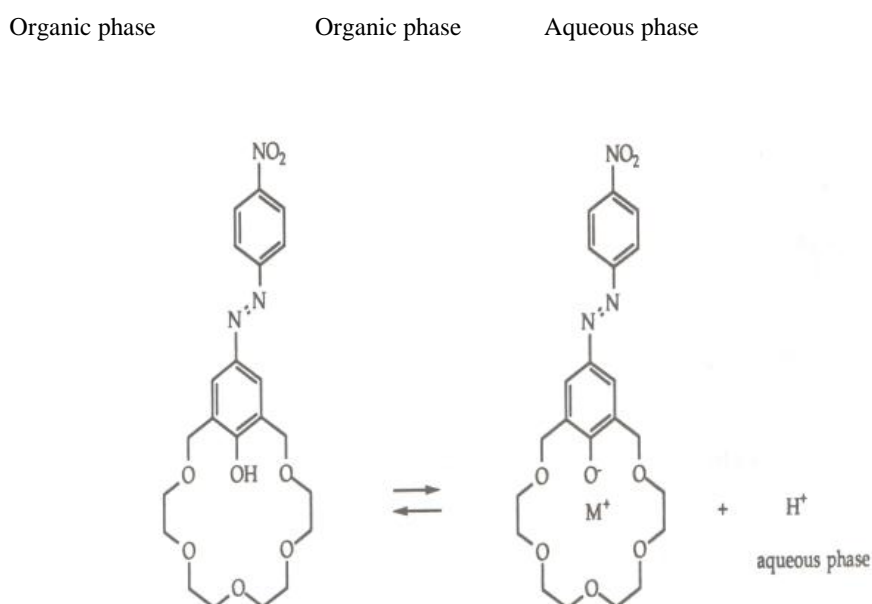


Figure 3-9 – Ionisable chromoionophores allow pH dependent switching between the bound 'off' state and the unbound 'on state' of the inner crown ether core.

Ionisable chromoionophores have greater specificity because of pH sensitive functional groups around the cavity. This effectively allows switching between 2 states attracting or repulsing analytes depending on protonation state [147] and also allowing recycling of the host molecule. Examples of chromoionophores that bind  $Li^+$  [147],  $Na^+$  [148],  $K^+$  [149] and

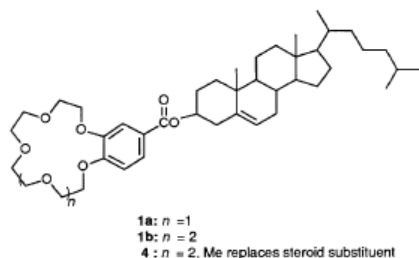
most of the alkali earth metal ions are known. However, sensors of this type typically work for analytes over the range of mM to M and would not be suitable for low level analyte detection.

### 3.3.3 Chiral crown ether chemosensors

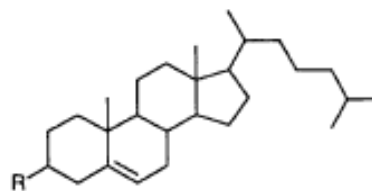
Chirality is a property regarding a molecule's structural characteristics. If it is impossible to superimpose itself on a mirror image, a molecule is deemed chiral and it has dissymmetry. Chirality is important for a range of organic chemistry and optical based phenomena, and thus is often important to differentiate between chiral molecules. In the past, the chiral recognition was estimated by indirect methods such as determination of association constants, membrane transport rates or reaction rates [150]. More recently a method of combining chiral (non symmetrical) crown ethers with chromogenic crown ethers using optically active amines [151] has been developed, therefore crown ethers have the power to couple enantio-selectively (allowing chemical reactions in which one chiral product is preferred) and enantiomer detection (differentiation of each of two stereoisomer molecules).

Figure 3-10 shows the chromogenic response of cholesterol steroidal crown compounds, a crown ether (A) modified to have cholesterol tail (B) and chirality. The response of the systems is believed to be due to the liquid nonanoate and cholesterol chloride dispersant, a room temperature liquid crystal (LC). Binding of analytes converts chemical signals to physical signals as the cholesteric LC acts as a nematic (chiral) helical structure with different layers of varying chirality altering the pitch distance over which  $360^\circ$  of phase change is observed [152]. Thus, as well as size and charge, crown ethers can also detect molecular chirality.

(A)



(B)



(C)

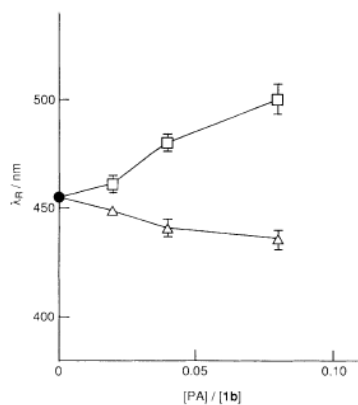


Figure 3-10 - Example of (A), a chromogenic steroidal crown compound, modified to have (B) a cholesterol tail attached. Upon addition of an alkali metal or ammonium cations the helical pitch of the formed liquid crystals changed resulting in a change in maximum absorbance wavelength shown in (C). A range of amine analyte compounds tested showed large  $\lambda_R$  difference between D- and L-isomers is observed for ammonium ions having bulky substituent's (such as phenyl and indolyl) [150].

### 3.3.4 Mass based crown ether chemosensors

Successful attempts have been made at binding cyclodextrin and small calixarene based hosts to a gold support layer using thiol bonding within a quartz crystal microbalance (QCM) system. Binding of the gaseous analyte tetrachloroethylene gave a large frequency dampening, signifying successful binding between the electronegative chlorine ions and the host electropositive aromatic rings [153]. However, this example is a special case as with many supramolecular systems. The tethering unit is the starting monomer of the molecule,

with the calixarene ring added in 6 to 8 steps unit by unit. Few calixarenes offer the possibility of post synthesis modification and those that do, care must be taken that this modification to add a tethering component does not affect the binding properties of the host [154].

### 3.3.5 Ionic liquids and chemosensors

Using an organic solvent aqueous gradient as described in traditional bulk remediation is both costly and highly toxic, leaving large amounts of radioactive chemical solvent that itself is toxic. One alternative is to encapsulate the desired host in a smaller volume, static reusable phase that still allows retention of the host, and only the desired analyte to travel the phase boundary and to the electrode for detection. One such encapsulation media for the chemoreceptors are ionic liquids.

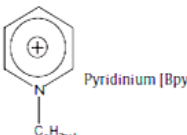
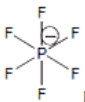
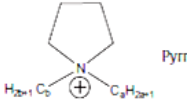
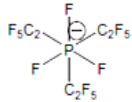
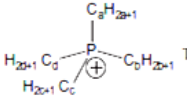
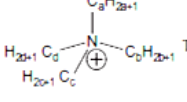
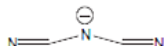
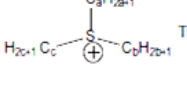
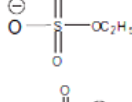
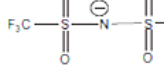
Room temperature ionic liquids (ionic liquid) are widely used in electrodeposition, electrosynthesis, electrocatalysis, chemical capacitor and lithium battery technologies. The earliest discovery was by Walden in 1914 [155] from reacting ethyl nitrate with alcoholic ammonia producing ethylammonium nitrate ( $C_2H_8N_2O_3$ ), an ionic liquid with a  $12\text{ }^\circ\text{C}$  melting point. Properties of ionic conductivity, solubility, usable potential window, viscosity and thermal stability can be tailored depending on the ions used and the application for which the ionic liquid is required. A summary of common salts that form ionic liquid below  $100^\circ\text{C}$  are listed in Table 3-2.

In combination with electrochemical sensors, ionic liquids have been used for cellulose film entrapment of enzymes [156], carbon nanotube enzyme composites on carbon and gold electrodes [157] and nanomaterial composites. An example of the latter is single-walled carbon nanotube gels that undergo cross linking because of the ionic liquid, which resulted in highly conductive polymers [158]. The ionic liquids used in this case were ([C4mim]Cl and 1-(2-hydroxypropyl)-3-methylimidazolium chloride, water soluble 1-butyl-3-methylimidazolium hexafluorophosphate ([bmim]PF<sub>6</sub>) and imidazolium salts respectively.

While not all ionic liquids are suitable for use in biocatalysis, enzymes have been shown to be typically stable in BF<sub>4</sub><sup>-</sup>, PF<sub>6</sub><sup>-</sup>, and NTf<sub>2</sub><sup>-</sup> anions [157]. This allows enzyme entrapment, retaining bioactivity for electrochemical interrogation. Similarly, 1-tetradecyl-3-methylimidazolium (TDMI-Tf<sub>2</sub>N) have been used for determination of rutin using the copper enzyme laccase from *Aspergillus oryzae*, with no decrease in enzyme activity observed [159].

Production of ionic liquid for sensing applications varies from the simple to the complex, with multiple washing and purification steps required. A number of carbon ionic liquid electrodes (Cionic liquidEs) have been formed using direct mixing. Maleki used graphite powder with ionic liquids together in an agate mortar and pestle, and formed the composite from mechanical grinding. The composite was then mixed with proteins and metallic nanoparticles for use as a glucose biosensor [160].

Table 3-2 – A summary of ionic liquid salts used for electrochemical biosensors [161].

Cations	Anions
 <p>Imidazolium [Bmim]<sup>+</sup></p>	 <p>Tetrafluoroborate [BF<sub>4</sub>]<sup>-</sup></p>
 <p>Pyridinium [Bpyr]<sup>+</sup></p>	 <p>Hexafluorophosphate [PF<sub>6</sub>]<sup>-</sup></p>
 <p>Pyrrolidinium [Bmpyr]<sup>+</sup></p>	 <p>Trifluorotris(pentafluoroethyl)phosphate [FAP]<sup>-</sup></p>
 <p>Tetraalkylphosphonium [P<sub>a,b,c,d</sub>]<sup>+</sup></p>	 <p>Thiocyanate [SCN]<sup>-</sup></p>
 <p>Tetraalkylammonium [N<sub>a,b,c,d</sub>]<sup>+</sup></p>	 <p>Dicyanamide [N(CN)<sub>2</sub>]<sup>-</sup></p>
 <p>Trialkylsulfonium [S<sub>a,b,c</sub>]<sup>+</sup></p>	 <p>Ethyl sulfate [EtSO<sub>4</sub>]<sup>-</sup></p>  <p>Bis(trifluoromethylsulfonyl)amide [NTf<sub>2</sub>]<sup>-</sup></p>

The ‘casting and rubbing’ method uses CNT-ionic liquid composite films and has frequently been used for making electrochemical biosensors. Films such as chitosan or polyvinyl alcohol are used to bind hosts such as hemoproteins [162]. Physical adsorption and sandwich

layer methods are similar to traditional immunoassays where immobilization of target antigen and antibody occurs on the surface of the Cionic liquidE. A secondary antibody labelled with a marker product such as horseradish peroxidase (HRP) binds specifically to the antigen sites producing a coloured product upon addition of O-aminophenol and H<sub>2</sub>O<sub>2</sub>. Ding [163] used such a method on a carbon paste electrode (CPE) consisting of room temperature ionic liquid (RTionic liquid) N-butylpyridinium hexafluorophosphate (BPPF<sub>6</sub>) and α -fetoprotein antibody.

## 3.4 Experimental

### 3.4.1 Experimental overview

Three approaches to crown ether chemosensing were taken; (i), direct insertion into a SAM on gold; (ii), intercalation into a SAM via a hydrophobic tail modification and (iii), mercury film electrodes using a crown ether seeded ionic liquid (Figure 3-11).

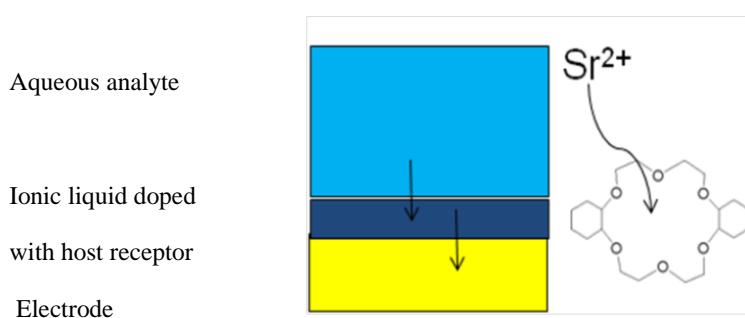


Figure 3-11 – Schematic of  $^{90}\text{Sr}^{2+}$  extraction using ionic liquids at an electrode interface. Ions in the aqueous phase are immiscible to the ionic liquid, similarly the hydrophobic crown ethers are immiscible to the aqueous phase. As a result selective ion transport only occurs across the interface as the host has specificity to the analyte.

After extensive literature review, the ionic liquid tri-1-butylmethylammonium bis((trifluoromethyl)sulfonyl)imide was selected as the most suitable for attempted  $^{90}\text{Sr}^{2+}$  and  $^{137}\text{Cs}^+$  sequestering. Chen and Hussey [164-166] used this ionic liquid for cyclic staircase voltammetry and mercury amalgam based CV for individual ion detection in noncomplex solutions. They state several assumptions used in their experimental design, and were used as the basis for chemosensing experiments. These assumptions are that although their experiments were performed in a nitrogen environment, they state the ionic liquid should still function in an oxygen environment, that the ionic liquid should have an interrogatable window down to -3.0 V, and finally that the ionic liquid should possess <0.1 % (w/w) water which should be achievable using vacuum treatment and heating.

### 3.4.2 Reagents

Cholesteryl chloroformate, 1-aza-18-crown-6, resorcinol, ethyl alcohol, methanol mercury(II) perchlorate, dimethylformamide, cholesteryl chloroformate 4-t-butylphenol, 37% formaldehyde solution, sodium hydroxide, phenyl ether, toluene, ethyl acetate, acetic acid, resorcinol, mercapto aldehyde, hydrochloric acid, 95% ethyl alcohol, methanol, sodium tetrathionite were from Sigma Aldrich. Carboxy 18C6, dicyclohexano-18-crown-6, aza-18-crown-6, triethylamine (Et<sub>3</sub>N) purchased from Acros organics. 2-iminothiolane (Traut's reagent), ethyl-3-(3-dimethylaminopropyl)carbodiimide (EDC/EDAC), n-hydroxysulfosuccinimide (sulfo-NHS) was purchased from Pierce. 2-Mercaptoethylamine-HCl was from ThermoScientific and mercapto acetaldehyde from Waterstone. Platinum and gold P3, P4 and P10 electrodes were sourced from Tyndall Institute, Cork.

### 3.4.3 Crown ether chemistry - modification of crown ether side arms

A range of commercially available crown ethers were either used as supplied or with side arm modification. Two crown ether synthesis methods, using acid catalysed one step synthesis were tested.

#### 3.4.3.1 Synthesis of N-(Cholesteryloxycarbonyl)aza-18-crown-6

The structure of the host molecule N-(Cholesteryloxycarbonyl)aza-18-crown-6 shown in Figure 3-12 was synthesised by reacting cholesteryl chloroformate with aza-18-crown-6.

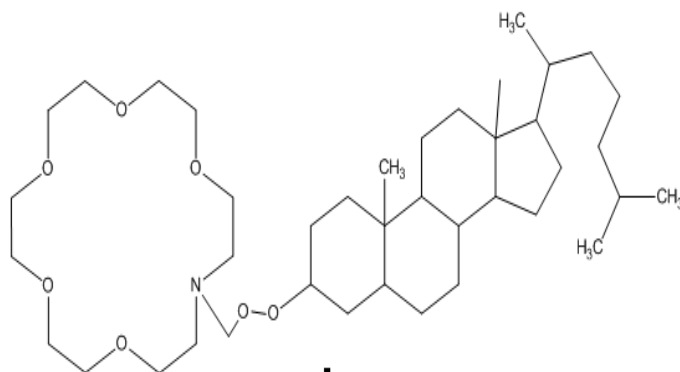


Figure 3-12 – Side arm modification of aza-18-crown-6 with hydrophobic cholesterol moiety. This allows the host to be inserted into SAMs via intercalation.

Aza-18-crown-6 from Acros (2.0 g, 8.0 mmol), was mixed with triethylamine (Et<sub>3</sub>N, 1.4 g, 14.0 mmol), dissolved in dimethylformamide (DMF, 50 mL) and heated to 90 °C. Cholesteryl chloroformate (3.6 g, 8.0 mmol) was added, and the temperature was maintained at 90 °C for 48 h. The mixture was cooled to room temperature, filtered, and concentrated in vacuo. Recrystallization from absolute EtOH resulted in pure N-(cholesteryloxycarbonyl)aza-18-crown-6 (Figure 3-12) (2.75 g, 52 % yield), a white solid.

### 3.4.3.2 Synthesis of 2-iminothiolane conjugated 4-Carboxybenzo-18-crown-6

Direct thiolation of amine containing crown ethers was achieved using 2-iminothiolane, to yield the target molecule shown in Figure 3-13. This molecule could be used to chemisorb to a gold substrate.

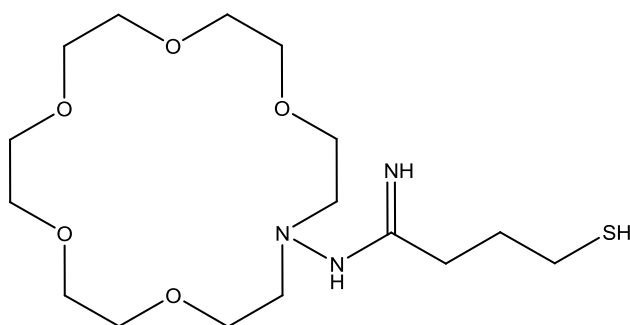


Figure 3-13 - 2-Iminothiolane modification of aza-18-crown-6 for direct conjugation to a gold substrate via the available thiol group.

2-Iminothiolane (also known as Traut's reagent) is a water soluble amine modifier reactive over the pH range 7 – 10. When reacted with an amine, its intrachain imidoester decyclises, forming a linear molecule with a free sulfhydryl group to thiol bond to a gold substrate.

2-iminothiolane conjugated 4-Carboxybenzo-18-crown-6 was prepared by dissolving a 10 mg/ml crown ether solution in to the non amine containing buffer, 50 mM PBS, pH 8. Traut's reagent was dissolved at 2 mg ml to give a 14.5 mM stock. To yield a ten fold molar excess of Traut's, 45.8 mL of Traut stock was added per ml of crown ether solution. This was reacted at room temperature for 1 h.

### 3.4.3.3 Separate attachment of 4-carboxybenzo-18-crown-6 to a 4-ATP SAM

Direct attachment of 4-carboxybenzo-18-crown-6 to an electrode with a predeposited 4-ATP SAM was done by conventional peptide bonding; the crown ether carboxylate to the SAM's free amine groups. A typical reaction used 10 mg/ml of 1-ethyl-3-(3-dimethylaminopropyl) carbodiimide plus 1mg/ml crown ether in 0.1 M MES buffer, pH 4.7, reacted for 4 h at room temperature.

### 3.4.3.4 Direct coupling of 4-carboxybenzo 18-crown-6 to a 4-ATP base layer

An alternative depositing method, rather than layering down the base layer and then the crown ether, was to react the linker and crown ether directly in solution, and then deposit onto the electrode (Figure 3-14). First thiol groups on 4-ATP that would otherwise react with EDC were reversibly blocked. EDC and sulfo-NHS were used to bind 4-ATP and 4-carboxybenzo 18-crown-6 via peptide bond formation.

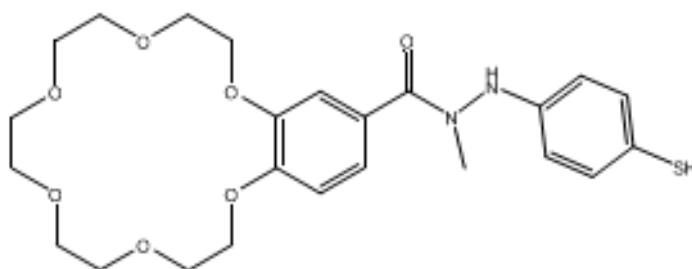


Figure 3-14 - Modified of 4-carboxybenzo-18-crown-6 to linker 4-ATP for chemisorptions onto a gold substrate.

### 3.4.3.5 Reversible blocking of sulfhydryl groups

4-ATP was dissolved in 10 mM PBS plus 1 mM EDTA to provide protection from catalysed oxidation. Sodium tetrathionate was added to a working concentration of 10mM and the mix reacted for 1 hour at room temperature. Excess sodium tetrathionate was removed by dialysis. This protected linker was then reacted with crown ether.

### 3.4.3.6 Reaction of crown-ether with linker

Carboxy-benzo-18-crown-6 was dissolved at 1-10 mg / ml in 0.1 M sodium phosphate pH 7.4 with 1 mM EDTA. 4-ATP was then added in a 10 M excess plus 5 mM sulfo-NHS and EDC to catalyse the condensation reaction. The mix was reacted for 2 h at room temperature. The products, 4-ATP-carboxy-benzo-18-crown-6 and unreacted components, were separated by gel filtration.

### 3.4.3.7 Reactivation of sulfhydryls

Removal of the sulfenylthiosulphate block was performed by adding a 300 fold excess of dithiothreitol (DTT) and incubation for 2 h at room temperature. The final product was then purified by gel filtration using monitoring at A280 nm to detect the aryl group. The linker modified crown ether with the reactivated thiol groups was then ready to be deposited onto a gold working electrode by chemisorption.

### 3.4.4 Crown ether synthesis

As well as modifying commercially available crown ethers a number of lariat ethers were synthesised.

#### 3.4.4.1 Synthesis of a hydrophobic tailed resorcinol crown ether for SAM insertion

A 4 x aromatic, 8 hydroxyl upper rim calixarene with 4 x C<sub>11</sub>H<sub>23</sub> hydrocarbon tails on the lower rim was synthesised for insertion into SAMs (Figure 3-15). This was performed by reacting an ethanol, HCL, resorcinol solution over an acetone-solid CO<sub>2</sub> bath with dodecyl aldehyde at -5 °C. After reaction, the solution was refluxed for 8 h at 80 °C to redisperse the precipitant. The solution was cooled to room temperature, Buchner filtered and washed with water to neutrality. Recrystallisation was performed using methanol, the resulting crystals dried under vacuum and stored with hygroscopic agents.

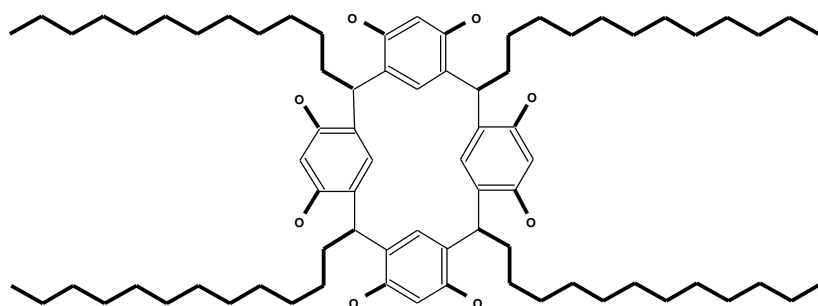


Figure 3-15 – Strontium resorcinol calixarene binder 2,c-8,c-14,c-20-tetraundecyl-4,6,10,12,16,18,22,24-octahydroxyresorc[4]arene, trivial name resorcinol calixarene. The tails are perpendicular to the central cavity.

Attempts were also made to synthesise an analogue of this host by replacing the dodecyl aldehyde tails with the short thiol containing compound mercaptoacetaldehyde. However, the refluxing stages using mercaptoacetaldehyde resulted in a viscous orange product suggesting a side reaction of the mercapto groups, and this synthesis was abandoned.

### 3.4.4.2 Attempted synthesis of caesium binder calix[4]resorcinarene

A 4 x phenolic resorcinarene containing a lower rim of four hydroxyls that has high specificity to  $\text{Cs}^+$  was attempted, shown in Figure 3-16. Although unsuccessful, the method has been shown to produce a relatively large amount of crown ether so the method is included [167].

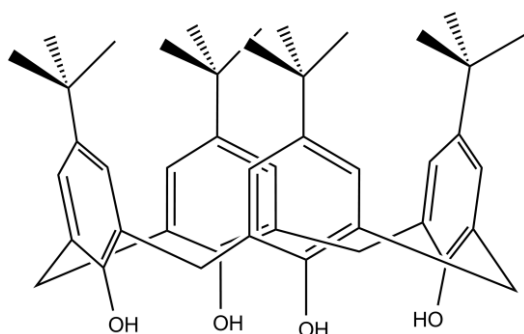


Figure 3-16 – Caesium binder pentacyclo [19.3.1.13,7.19,13.115,19] octacosal(25), 3,5,7 (28),9,11,13 (27),15,17,19(26),21,23-dodecaene-4,6,10,12,16,18,22,24-octol, trivial name calix[4]resorcinarene.

4-t-butylphenol, formaldehyde solution and sodium hydroxide were added to a nitrogen purged vessel under stirring. The solution was heated to 120 °C until a viscous mass was formed. The solution was cooled to room temperature and then phenyl ether and toluene added. The solution was reheated to 180 °C again allowing vapours to exit before 4 h refluxing with an Allihn condenser. After cooling to 60 °C ethyl acetate was added before cooling to room temperature before a final 1 h stirring. Crystals formed were filtered on a Buchner funnel under suction then triturated with acetic acid. A second filtration and wash with ethyl acetate was used prior to purification by dissolving and refluxing in 100 °C toluene. As this solution cooled the crystals that formed were filtered a third time and dried under vacuum.

This method from Parker [167] stated that due to entropic effects, regardless of the reaction time, only the desired macrocycles of 4 butylphenol moieties would form. However after multiple attempts, mass spectrometry showed significantly larger polymers forming, possibly due to contamination. As a result, synthesis of usable amounts of this crown ether was unsuccessful.

## 3.5 Analytical methods

### 3.5.1 Electrochemical Impedance Spectroscopy

Non aqueous EIS was performed use mercury coated platinum electrodes, against a silver wire pseudo reference and platinum counter. The system was interrogated using the redox probe ferrocenium and the oxidation peak observed at 0.22 V corresponding to the irreversible product ferrocene. Experiments were performed on an ECO CHEMIE Autolab Type II General Purpose Electrochemical System using GEPES and FRA software.

### 3.5.2 Quartz crystal microbalance

Micro gravimetry is a technique that relates frequency change of an oscillating surface to a change in mass as species absorb at the interface. A noncentrosymmetric quartz crystal is oscillated at an applied potential causing it to vibrate and resonate at a specific natural frequency. This phenomena is related by the Sauerbrey equation (Equation 3-1).

$$\Delta f = \frac{-2\Delta m f_0^2}{A\sqrt{\rho_q \mu_q}} = \frac{2f_0^2}{A\sqrt{\rho_q \mu_q}} \Delta m$$

(3-1)

Where  $f_0$  is the resonant frequency (Hz),  $\Delta f$  frequency change (Hz),  $\Delta m$  mass change (g),  $A$  crystal area (Area between electrodes,  $m^2$ ),  $\rho_q$  the density of quartz ( $\rho_q = 2.648 \text{ g/cm}^3$ ),  $\mu_q$  the shear modulus of quartz for AT-cut crystal ( $\mu_q = 2.947 \times 10^{11} \text{ g/cm.s}^2$ ,  $v_q$  the transverse wave velocity in quartz (m/s). As most of these parameters are material constants, a change of mass is, as an approximation, proportional to the observed change in frequency upon binding. It is noted that the Sauerbrey equation works under the assumption that rigid solids are binding at the interface, which is not true in the case of organic analytes and receptors.

### 3.5.3 Nuclear magnetic resonance

Nuclear magnetic resonance (NMR) is a phenomena where absorption of electromagnetic radiation occurs by a nucleus having a magnetic moment when in an external magnetic field. It is a powerful analytical technique for molecular analysis and was used to determine if crown ether modification was successful by confirming generation of new bonds during synthesis.

Aqueous samples were either synthesised directly in or transferred to deuterium oxide 99.9 atom % D, containing 0.05 % (w/v) 3-(trimethylsilyl)propionic-2,2,3,3-d4 acid sodium salt

(TMS) as reference. Non-aqueous samples were similarly prepared or transferred to chloroform-d, 99.8 % (Isotopic), containing 0.03 % (v/v) TMS reference. Samples were analysed in Norell 300 MHz tubes.

### 3.5.4 Mass Spectroscopy

Aqueous samples were prepared in deionised water to avoid salt contamination. Crown ethers modified in DMF underwent solvent evaporation and transfer to chloroform which formed aerosols at lower temperature and pressure. 50 µl of each sample was analysed by electrospray MALDI mass spectroscopy giving mass per charge ratios of molecules present in the solution.

## 3.6 Electrode preparation

### 3.6.1 Electroactive surface area calculation from piranha cleaning using the Cottrell equation

In addition to the 6 cleaning methods discussed for electrode preparation (see Chapter 2, 2.5.7.5) electrochemical analysis was used to interrogate the changes in electrode area from repeated piranha cleaning in response to electrode variability. This was performed by using the Cottrell equation to calculate the change in electroactive surface area of a bulk planar electrode (P3 or P4, but not P10) in relation to a change from the ferricyanide redox current (Equation 3-2).

$$a \propto \frac{\sqrt{2nAFCD}}{\sqrt{\pi}} \therefore A = \frac{-a}{2nFC\sqrt{\frac{D}{\pi}}} \quad (3-2)$$

where a = the gradient, n = no of electrons transferred, A = active area, F = Faraday's constant, 96485.3415 s A / mol, C = concentration of electroactive species, D =diffusion coefficient of said species.

Using the gradient of the oxidatative peak of a 10 mM ferricyanide redox couple, the average electrochemically active area of P3 electrode was calculated to be 0.0024 cm<sup>2</sup> (n = 10). Compared to the theoretical geometrical area 0.00785cm<sup>2</sup>, the active surface area was up to three times larger than predicted. This was a result of increased surface roughening from repeated piranha cleaning. Surface area increases between 1 and 10 times due to physical and chemical cleaning methods can account for the significant variation between electrode areas observed from multiple piranha cleanings.

### 3.6.2 Liquid metal electrodes

Because of the contamination and reproducibility problems highlighted in using bare metal electrodes and piranha cleaning, a technique developed in the laboratory of Professor A. Nelson, The Centre for Molecular Nanoscience (CMNS), University of Leeds [168], was adapted to the P3 and P10 electrodes. Mercury is the traditional electrode used in electrochemistry and is well defined. Being a liquid, surface tension and capillary forces create an atomically flat uniform surface, with electrode life spans extending beyond 6 months. The surfaces can often be 'self cleaned' and absorbed materials removed by holding the surface at negative potentials which debinds bound organics with no degradation of the mercury surface. These reasons still make mercury the best tool for electrochemistry in spite of its toxic properties.

To create static mercury electrodes on a solid platinum support, chronocoulometry is used to electroplate the electrode area. Aqueous  $\text{Hg}^{2+}$  ions from solution build up and deposit on an electrode held at a negative potential over time. The resulting droplets are stable and robust due to their electrostatically bound nature. Working out the electrode geometry and the radii of the hemisphere to be deposited on the P3 or P10 electrodes allows the number of mercury molecules and electrons required to create the desired electrode to be calculated.

#### 3.6.2.1 Calculations of electrical parameters for electroplating a mercury hemisphere on platinum P3 and P10 electrodes

The P10 electrodes are an array of thousands of micro spots to increase radial and enhance mass transport. The amount of mercury deposited on one of these systems can be calculated for one individual spot and simply multiplied to the total number of spots available. Figure 3-17 shows an electrode schematic of the P10 electrode arrays.

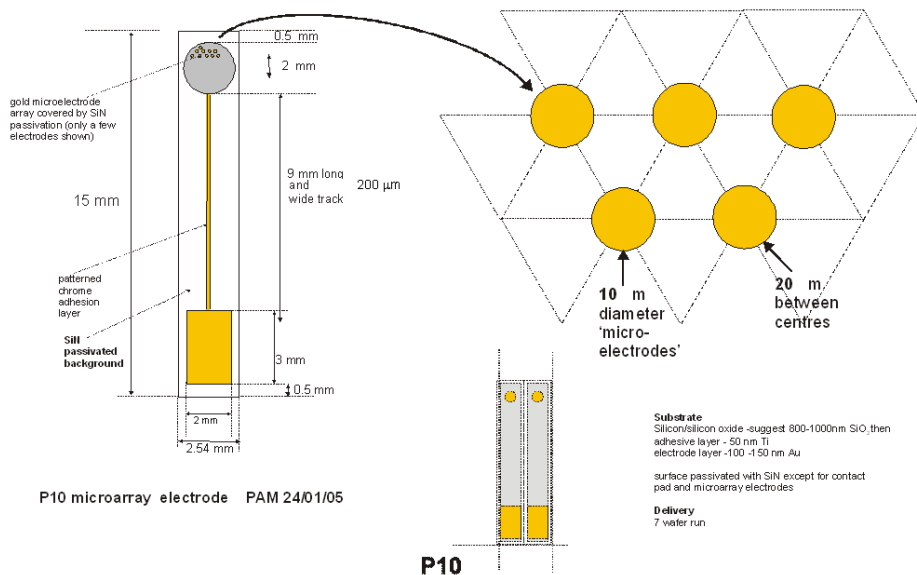


Figure 3-17 – Schematic of the P10 electrode exhibiting radial diffusion from an array of micro spots.

The geometrical volume of a hemisphere is first calculated and then the mass of mercury needed to create this. Since it is known that each mercury cation accepts 2 electrons, the charge transfer needed for chrono-coulometry can be calculated. A detailed derivation for P3, P4 and P10 electrode mercury electroplating is included in the appendix.

To deposit mercury onto the electrodes a solution of 50 mM  $\text{Hg}(\text{NO}_3)_2$  was dissolved in perchloric acid and deionised water as the working solution. The cell setup used a Pt P3, P4 or P10 working electrode (WE), a Pt counter electrode (crown ether) and a double junction Ag / AgCl reference electrode (RE). The chrono-coulometry module of Autolab GEPES software was used to control deposition. The applied potential and speed of deposition is limited to the interrogation window of platinum and also the stability range of the electrodes (too high a current on the micro arrays permanently burns off the surface coating). For deposition on macroscopic electrodes, a potential of +0.4 V with a cut off of -1 C was used instead of the theoretical -3.4 C in order to limit the experimental period (a -1.0 C deposition

takes between 2 and 4 h, therefore a -3.4 C electrode could take between 8 and 16 h). The P10 micro array deposition was more difficult to achieve reproducibly. A lower plating voltage of 0.1 V was used alongside the 0.4 V plating potential. However at 0.4 V, plating of -61.9 mC would have occurred within seconds. Because of the lower spot size and differences in surface tension if the electrodes were not immediately rinsed with deionised water the electroplated mercury would redissolve due to the perchloric acid.

### 3.6.3 Ionic liquid preparation

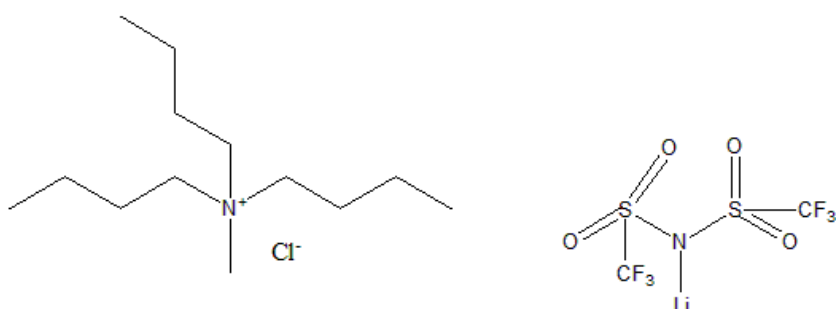


Figure 3-18 - Ionic liquid composed of tributylmethylammonium chloride ( $\text{Bu}_3\text{MeN}^+\text{Cl}^-$ ) and N-lithiotrifluoromethanesulfonimide ( $\text{Li}^+\text{Tf}_2\text{N}^-$ ).

The  $\text{Bu}_3\text{MeN}^+\text{Tf}_2\text{N}^-$  RTionic liquid were prepared by mixing an equimolarlar ratio of tributylmethylammonium chloride ( $\text{Bu}_3\text{MeN}^+\text{Cl}^-$ ) and n-lithiotrifluoromethanesulfonimide ( $\text{Li}^+\text{Tf}_2\text{N}^-$ ) in dry acetonitrile (MeCN), shown in Figure 3-18. This solution was stirred and refluxed at 80 °C for at least 3 d. As the reaction proceeded, fine white particles of LiCl precipitated from the solution. The solution was then evacuated to  $10^{-4}$  Torr at 100 °C in order to remove all traces of MeCN. After most of the MeCN was removed, the temperature was increased gradually to 120 °C and evacuation was continued until bubble formation ceased. The resulting hydrophobic ionic liquid was washed repeatedly with water to remove any unreacted starting materials and again evacuated to  $10^{-4}$  Torr at 100 °C for several days to remove traces of water. As reported by Sun [169], this evacuation procedure resulted in ionic liquid with a water content <0.1 % (w/w). A known mass of ionic liquid was coated onto mercury coated electrodes once seeded with crown ether.

### 3.6.4 SAMs on QCM electrodes for crown ether insertion

Self assembled monolayers (SAMs) are a molecular layer of molecules that mimic one leaflet of a cellular bilayer membrane. Although membrane proteins need a bilayer to insert into, smaller soluble proteins can be attached to a monolayer [170]. As they mimic the natural conditions of the cell proteins or peptides can often retain their functionality and remain active on such layers. There is a high entropic cost however to insert into a mono or bilayer. However, certain protein complexes, where the whole complex spans the membrane are stable. Previous work [94] has showed at low percentage ratios, stable mSAMs of, 16-Mercaptoundecanoic acid (MHDA) and the lipid 1,2-dipalmitoyl-*sn*-glycero-3-phosphoethanolamine-N-(cap biotinyl) (biotin-cap-DPPE) can form mSAMs.

All flow cell work was performed on a first generation flow cell designed by Dr Zachary Coldrick, SOMS, University of Leeds which consisted of a teflon rectangular body, input output flow ports passing a central circular cavity with an injection port, platinum counter electrode and miniature Ag/AgCl pseudo electrode entering the chamber from above.

To create a hydrophobic interior for the crown ether insertion, a SAM of 16-MHDA (Figure 3-19) were prepared by incubating cleaned electrodes in a 0.5 mM MHDA chloroform : ethanol solution for 5 h before rinsing with ethanol and dH<sub>2</sub>O to remove unbound excess MHDA. The chip was then ethanol rinsed and nitrogen dried before loading into the QCM crystal holder. The chamber was loaded with 10 mM PBS after 20 mins argon and continually pumped in a flow cell loop with 10 mM PBS. The capacitance component was nulled once a stable baseline was acquired prior to data logging using the hardware feedback response loop. Crown ether solutions and analytes were injected and flowed over the SAM surface, with insertion monitored as a dampening of frequency.

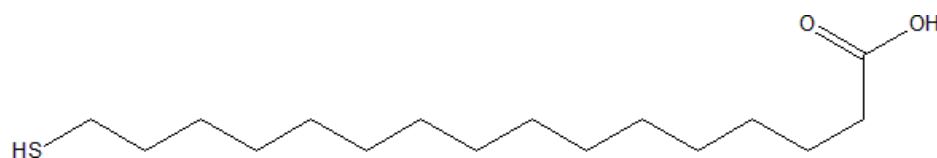


Figure 3-19 - 16-mercaptohexadecanoic used as the component of SAMs on gold for QCM interrogation and crown ether insertion.

### 3.6.5 SAMs of DOPC on HgPt electrodes

Mercury deposited platinum electrodes are able to support purely lipid SAMs, such as the dioleoyl lipids, a class of synthetic phosphatidylcholine (Figure 3-20). 1,2-dioleoyl-*sn*-glycero-3-phosphocholine (DOPC) which were deposited onto mercury electrodes using GEPES software, and interrogated in real time using SCOPE software. Layers were removed by using a cleaning potential of -3.0 V, and deposition at -0.5 V vs a Pt reference. A 40 Hz time base, 10 V channels and 2560 samples per scan was used.

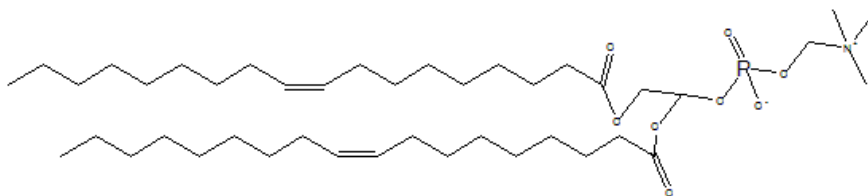


Figure 3-20 – Polar lipid DOPC used as a hydrophobic insertion layer on mercury coated platinum for crown ethers.

## 3.7 Results

### 3.7.1 Crown ether synthesis

Solution based reaction of Traut's reagent to aza-18-crown-6 (see section 3.4.3.4) showed a low product with only 12 % of the expected product. The bulk was protonated aza-18 crown 6.

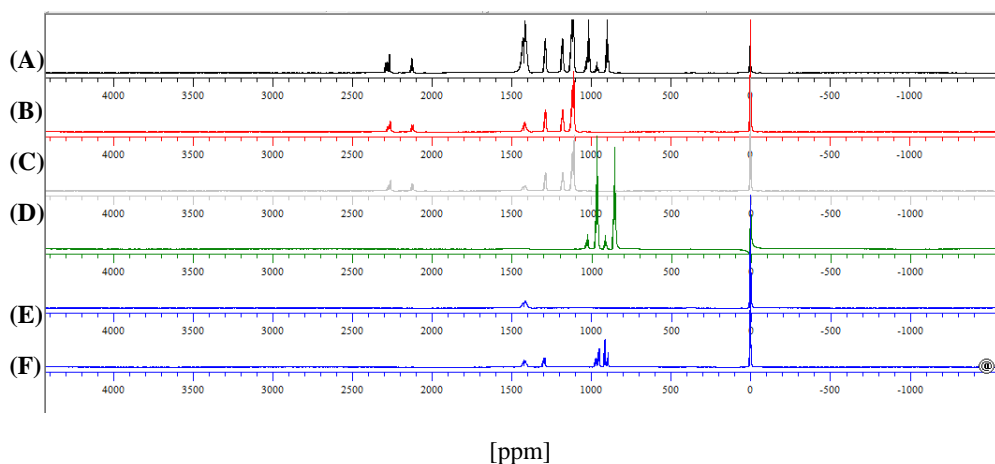


Figure 3-21 – NMR spectra of (A), successful linkage of 4-carboxybenzo 18-crown-6 to 2-MEA relative to the component molecule spectrum; (B) 4-carboxybenzo 18-crown-6, (C) 2-MEA/Traut's reagent, (D) triethylamine, (E) sodium tetrathionite and (F) sulfo-NHS. Samples used deuterium oxide 99.9 atom % D, containing 0.05 % 3-(trimethylsilyl)propionic-2,2,3,3-d4 acid, sodium salt, 300 Mhz tube.

Successful linkage of 4-carboxybenzo 18-crown-6 to Traut's reagent can be seen in Figure 3-21 A. Individual component molecules are shown in (B) 4-carboxybenzo 18-crown-6, (C) 2-MEA/Traut's reagent, (D) triethylamine, (E) sodium tetrathionite and (F) sulfo-NHS. Samples used deuterium oxide 99.9 atom % D, containing 0.05 % 3-(trimethylsilyl)propionic-2,2,3,3-d4 acid, sodium salt, 300 Mhz tube.

Similarly, successful synthesis of cholesterol aza-18-crown-6 (see section 3.4.3.1) is shown in Figure 3-22. The successful product (A) cholesterol aza-18-crown-6 is shown versus components (B) triethylamine, (C) cholesterol chloroformate and (D) aza 18-crown-6. Samples were analysed in chloroform-d, 99.8% (Isotopic) containing 0.03 % v/v TMS in 300 MHz tubes.

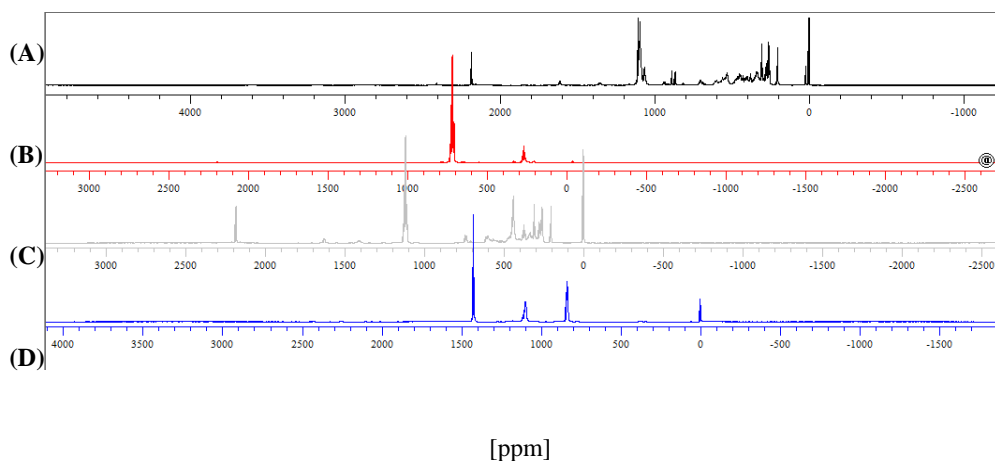


Figure 3-22 - NMR spectra of successfully synthesised cholesterol aza-18-crown-6 and the chemical components. (A), Cholesterol aza-18C6; (B), triethylamine; (C), cholesterol chloroformate; (D), aza-18-crown-6. Samples analysed in Chloroform-d, 99.8 % (Isotopic) containing 0.03 % (v/v) TMS, 300 MHz tube.

Mass spectrometry analysis of cholesterol tethered aza 18-crown-6 (Figure 3-23) showed (mass to charge ratios respectively); unreacted crown ether 264.18, triethylamine 102, DMF contamination from solvent transfer 74 and successful product 676.50.

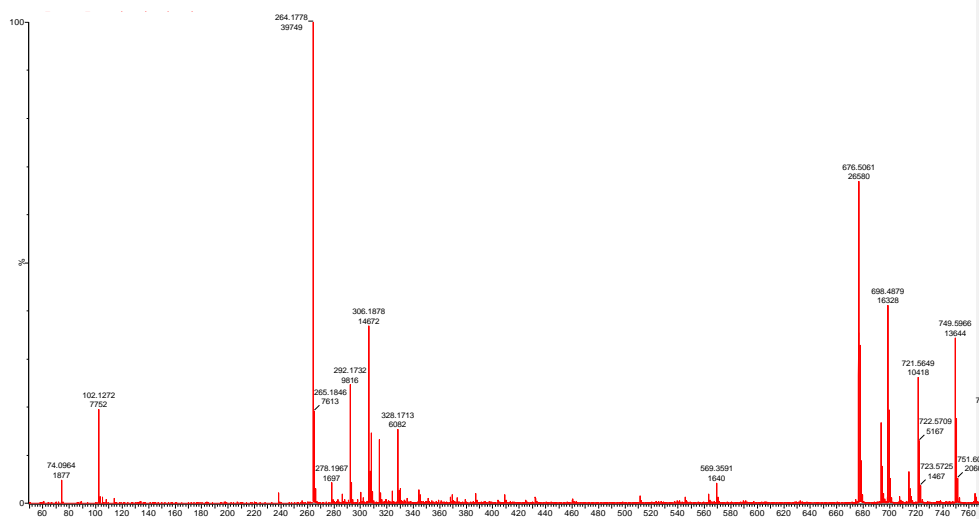


Figure 3-23 – Charge to mass spectrum graph showing confirmation of cholesterol tethered aza 18-crown-6 synthesis at Mw to charge ratio 676.

### 3.7.2 Direct tethering of crown ethers to electrodes via thiol bonding

In one method, direct assembly of crown ethers was performed by thiol chemisorption to gold electrodes. However, no significant change could be observed via impedance interrogation of assembled sensors with and without analyte. This was most likely because of two reasons. A protein such as an antibody with a mass of  $126,000 \text{ g}^{-1}\text{M}^{-1}$  is significant enough to create an observable change in impedimetric response. Compared to a 18-crown-6 ether molecule of  $264 \text{ g}^{-1}\text{M}^{-1}$ , a 500 x smaller mass, binding may simply have not resulted in a significant interfacial change. A crown ether typically only has one binding side between the oxygen rim and central core, or two in the case of calixarenes. Binding of ions to crown ethers occurs on such a small scale, with a small conformational change in structure that may not be observable by EIS at low concentrations. Secondly, orientation also limited the crown ethers interaction with the electrode. As crown ethers were lined perpendicular to the electrode rather than parallel, because of the orientation of the lariat side arms, this will have limited the change of capacitance observed. Confirmation of insertion into layers could be observed through chronoimpedance using 10 mM ferricyanide at 0.4 V. Time points every 15 min over 6 h repeatedly showed a capacitance ( $-Y''\omega$ ) increase from  $1.60 \mu\text{F cm}^2$  (a stable base value for an MHDA layer in buffer), from an initial drop to  $1.20 \mu\text{F cm}^2$ , signifying SAM reorientation after  $0.1 \mu\text{M}$  cholesterol addition. This stabilised as a cholesterol-MHDA mSAM with a capacitance of  $1.45 \mu\text{F cm}^2$  (normalised from a working area of  $0.00785 \text{ cm}^2$ ). Similar magnitudes were observed for insertion of cholesterol 18-crown-6, but no significant change was observed upon addition of strontium ions.

### 3.7.3 Optimisation of ionic liquid synthesis

Because direct linkage of crown ethers could not be detected due to steric restrictions and host distance from the electrode surface, dispersion in an ionic liquid allowed free diffusion of the host molecules to and from electrode. The host was then able to extract  $\text{Sr}^{2+}$  ions from the aqueous phase. The crown ethers in ionic liquid then should have transported the bound ions to a mercury-platinum electrode for reduction and quantification via an extrapolated current.

Table 3-3 shows the stages and mass yield of ionic liquid generated, from the reaction of tributylmethylammonium chloride ( $\text{Bu}_3\text{MeN}^+\text{Cl}^-$ ) and n-lithiotrifluoromethanesulfonimide ( $\text{Li}^+\text{Tf}_2\text{N}^-$ ) and the purification steps to produce ( $\text{Bu}_3\text{MeN}^+\text{Tf}_2\text{N}^-$ ). A starting reaction of 100 ml dry acetonitrile containing 1 M of each salt was weighed, and again after each step to determine yield of production. After 3 d refluxing, a significant mass loss occurred due to LiCl precipitation. Heating at  $120 \text{ }^\circ\text{C}$  to remove acetonitrile removed the bulk of the solvent down to around 50 % of the original mass. However, a significant amount of water was still

bound, and so a further 100 °C heating under vacuum was essential. Of the original 100 ml solution, only between 84 to 236 mg mass of ionic liquid was produced in initial batches. Reflux beyond 3 d increased yield to 1.27- 2.47 ml of ionic liquid. If stored under vacuum in a desiccator the ionic liquid could be stored for months, and recycled by heating under vacuum to remove any absorbed water.

Table 3-3 Determination of the inter batch amount of ionic liquid produced. Weighing after each solvent evaporation and washing step allows the amounts of liquid removed, precipitate extracted and final volume of ionic liquid to be determined.

Starting solution g/ ml	Mass solvent before evaporation	After solvent evaporation / g	ionic liquid after solvent evaporation / % starting weight	Weight after H <sub>2</sub> O wash and drying / g
0.467	17.516	0.34	63.56	17.26
0.463	18.191	1.046	54.77	18.16
0.459	19.47	2.146	53.27	19.29

Final ionic liquid mass / g	Mass loss from Li <sup>+</sup> and Cl precipitates / g	Final ionic liquid / ml (density conversation)
0.236	0.236	0.295
0.0840	0.256	0.105
1.02	0.0270	1.27
1.98	0.171	2.47

The ionic liquid could be seeded with 1 % (w/v) of solid scintillant PPO either in the acetonitrile stage after refluxing or directly into the final product. However, due to the ionic liquid viscosity, uniform mixing was a problem via this method. Incorporation of solid scintillants PPO and POPOP into the ionic liquid would allow direct scintillation counting of bound <sup>90</sup>Sr<sup>2+</sup> ions as an alternative to ASV quantification. However, POPOP appeared to undergo a chemical reaction with the ionic liquid resulting in a purple suspension. As a result only PPO was used as a solid scintillant to seed ionic liquids.

### 3.7.4 Non aqueous electrochemistry to determine transport ability of crown ether seeded ionic liquid

To maintain a  $< 0.1\%$  (w/v) water content of the ionic liquid, initial experiments used a non aqueous setup and alternative equipment arrangement, as well as redox probe. Aqueous salt electrodes such as Ag/AgCl cannot be used as the organic solvent used in solution, instead of water, would cause flocculation and block the glass frit. As a result, an alternative pseudo reference electrode was used. A pseudo reference is an electrode that does not have a constant well defined potential. Thus a known standard redox probe of known redox potential is used before and after the main experiments. In this case the probe ferrocenium, in acetonitrile solution, was used and the reduction peak around 0.22 V (see Figure 3-24) was used to confirm that the seeded ionic liquid could conduct a current from the solution, through the ionic liquid to the Hg-Pt electrode. Because of the poorer conductivity and IR drop occurring in non aqueous electrochemistry a broadening of the redox potentials is observed, as seen in Figure 3-24. To counteract this micro electrodes can be used which have a lower current density per electrode and can use much smaller currents are affected by this IR drop much less, returning the observed redox potentials closer to their expected potentials. Alternatively, a supporting electrolyte can be added to improve conductivity.

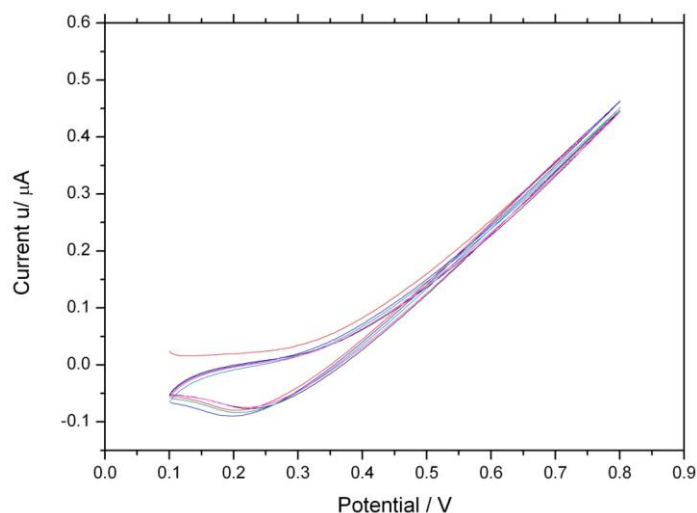


Figure 3-24 Oxidation of ferrocenium in acetonitrile to ferrocene around 0.2 V. This was used as the base signal to test Hg-Pt electrodes with fabricated pseudo AgAgCl reference electrodes. Performed using 10 mM ferrocene in acetonitrile solution at a scan rate of 50 mV/s.

If an offset drift is observed the corrected potential can be then applied to experimental data. A pseudo reference was made by anodising a silver wire encased inside a Vycor frit. Anodisation was achieved by using a 5 min incubation in HCl to create a surface silver chloride layer. Glassy carbon electrodes with mercury amalgam or the standard Pt-Hg macro and micro electrodes were coated with crown ether seeded ionic liquid.

A 50 ml chamber allowing working, reference and counter electrode insertion from the base was bespoke made. This allowed ionic liquid and sample to be coated onto the electrode from above before the environment was rapidly purged with argon to minimise the observed oxygen dift current.

Table 3-4 shows a summary of the expected redox reactions that would occur if traditional ASV were performed on contaminated ground water. Because of the complexity of the solution, individual analyte currents would overlap, and composite signals would make analyte differentiation and quantification impossible. This is why a seeded ionic liquid was used, in an attempt to introduce analyte specificity by transporting only the desired analyte to the electrode.

Table 3-4 – Collated standard redox potentials of a range of analytes expected in contaminated ground water (aqueous systems vs standard hydrogen electrode, +0.197 for Ag/AgCl/Sat. KCl) [45-46, 171].

Reaction	Standard electrode potential ( $E^\circ$ (V) vs SHE)
$\text{Li}^+ + e^- \rightleftharpoons \text{Li}(s)$	-3.04
$\text{Cs}^+ + e^- \rightleftharpoons \text{Cs}(s)$	
$\text{K}^+ + e^- \rightleftharpoons \text{K}(s)$	
$\text{Br}_2(l) + 2e^- \rightleftharpoons 2\text{Br}^-$	+1.07
$\text{Br}_2(aq) + 2e^- \rightleftharpoons 2\text{Br}^-$	+1.08

$\text{BrO}_3^- + 5\text{H}^+ + 4e^- \rightleftharpoons \text{HBrO}(aq) + 2\text{H}_2\text{O}$	+1.45
$\text{BrO}_4^- + 2\text{H}^+ + 2e^- \rightleftharpoons \text{BrO}_3^- + \text{H}_2\text{O}$	+1.85
$\text{Ca}^{2+} + 2e^- \rightleftharpoons \text{Ca}(s)$	
$\text{Na}^+ + e^- \rightleftharpoons \text{Na}(s)$	
$\text{Cr}^{3+} + e^- \rightleftharpoons \text{Cr}^{2+}$	
$\text{SO}_4^{2-} + 4\text{H}^+ + 2e^- \rightleftharpoons \text{SO}_2(aq) + 2\text{H}_2\text{O}$	+0.17
$\text{Sr}^{2+} + 2e^- \rightleftharpoons \text{Sr}(s)$	
$\text{Y}^{3+} + 3e^- \rightleftharpoons \text{Y}(s)$	
$\text{U}^{3+} + 3e^- \rightleftharpoons \text{U}(s)$	
$\text{U}^{4+} + e^- \rightleftharpoons \text{U}^{3+}$	
$\text{UO}_2^{2+} + e^- \rightleftharpoons \text{UO}_2^+$	+0.16
$\text{UO}_2^+ + 4\text{H}^+ + e^- \rightleftharpoons \text{U}^{4+} + 2\text{H}_2\text{O}$	+0.27
$\text{SiO}_2(s) + 4\text{H}^+ + 4e^- \rightleftharpoons \text{Si}(s) + 2\text{H}_2\text{O}$	
$2\text{H}_2\text{O} + 2e^- \rightleftharpoons \text{H}_2(g) + 2\text{OH}^-$	
$2\text{CO}_2(g) + 2\text{H}^+ + 2e^- \rightleftharpoons \text{HOOC-COOH}(aq)$ Oxalic acid also metal chelator	
$\text{O}_2(g) + \text{H}^+ + e^- \rightleftharpoons \text{HO}_2\cdot(aq)$	
$2\text{H}^+ + 2e^- \rightleftharpoons \text{H}_2(g)$	0
$\text{AgCl}(s) + e^- \rightleftharpoons \text{Ag}(s) + \text{Cl}^-$	+0.22

Even with deaeration a significant oxygen peak and drift was observed which interfered with observed analyte peaks. However, at high concentrations of analyte this should have not completely obstructed analyte reduction peaks. Analyte peaks that were detectable on mercury amalgam in aqueous solutions were not visible when the electrodes were coated with

ionic liquid. This suggests that the kinetics of transport through the liquid are slow and diffusion-dependent because of the high viscosity of the ionic liquid. Published diffusion coefficients for DCH18C6 • Sr<sup>2+</sup>  $2.1 \times 10^{-9} \text{ cm}^2 \text{ s}^{-1}$ , in the ionic liquid [165] would suggest a diffusion time of around  $2.1 \times 10^{-10} \text{ s}^{-1}$  to the electrode through an ionic liquid film of thickness one millimetre. The Koutecky-Levich [172] graphical representation uses the slope of a plot of the inverse of the limiting current versus the inverse of the square root of the electrode rotation speed. Analysis of redox currents in this way as a function of concentration allows diffusion coefficients to be calculated. This should be proportional to the diffusion coefficient and independent of rotating disc electrode speed, but will only work on single ion solutions. This does not appear to be accounted for by Chen [173]. Other problems were observed upon signal extrapolation. Lithium contamination from reacted ionic liquid biproducts was a common problem even with extensive washing steps. The ionic liquid, whilst hydrophobic, also showed signs of breakdown and water adsorption after continual use over several days. Recycling of the ionic liquid by re-drying under vacuum was possible but this would be useless in terms of a commercially viable sensor that would be required to analyse aqueous analytes over long periods of time. Also unmentioned in Chen's publications [169, 173-174] and of significant importance was that the inorganic forms of Sr<sup>2+</sup> and Cs<sup>+</sup> were insoluble in the ionic liquid. Because of these problems the ionic liquid approach was abandoned as a sensing method.

### **3.7.5 Ionic liquid retention of DC18C6 <sup>90</sup>Sr<sup>2+</sup> and <sup>90</sup>Y<sup>2+</sup>**

Because no quantifiable electrochemical signal using crown ether seeded electrodes could be observed via ASV, scintillation counting was used on incubated electrodes to determine if <sup>90</sup>Sr<sup>2+</sup> ions were successfully chelated and diffusing into the ionic liquid (Figure 3-25).

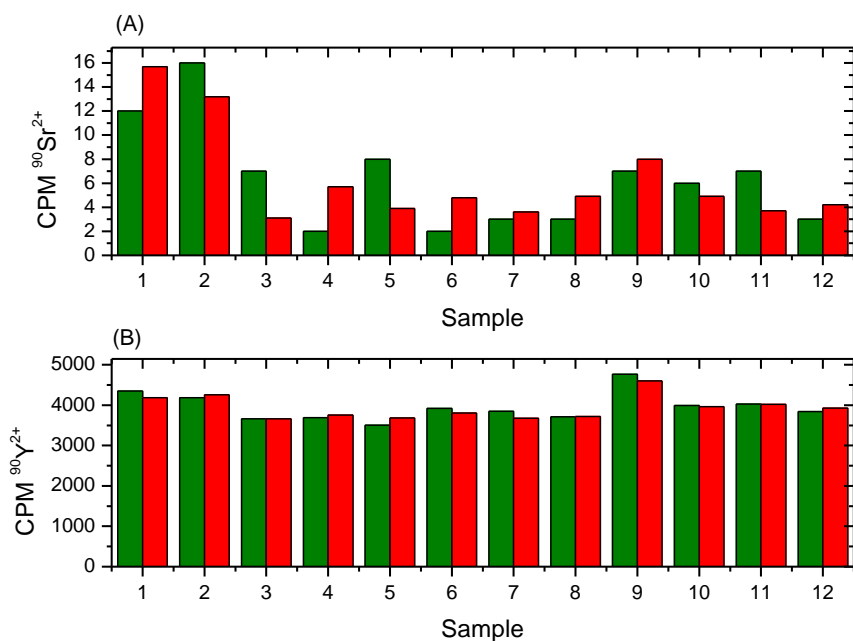


Figure 3-25 – Scintillation counting of DC18C6 ionic liquid coated HgPt electrodes that have chelated  $^{90}\text{Sr}^{2+}$  and  $^{90}\text{Y}^{2+}$  ions. Twelve samples under identical conditions but had the energy spectra differentiated to determine the amounts of each isotope bound simultaneously. Green bars are scintillation counting after 24 h, red bars the same samples counted after 48 h.

The amount of radionuclide bound across the twelve samples was consistent, but unfortunately the amount of  $^{90}\text{Sr}^{2+}$  bound was negligible (Figure 3-25 A). However, looking at the  $^{90}\text{Y}$  energy window spectrum a significant amount (38-47 %) of the original 10 kBq radioisotope in the incubation mix was bound  $^{90}\text{Y}^{2+}$  suggesting  $^{90}\text{Y}^{2+}$  was preferentially complexing with DC18-crown-6, this the reason why there was negligible strontium detected electrochemically, as the interrogation potentials used were that of strontium and not yttrium.

### 3.7.6 Mercury-platinum amalgam electrodes

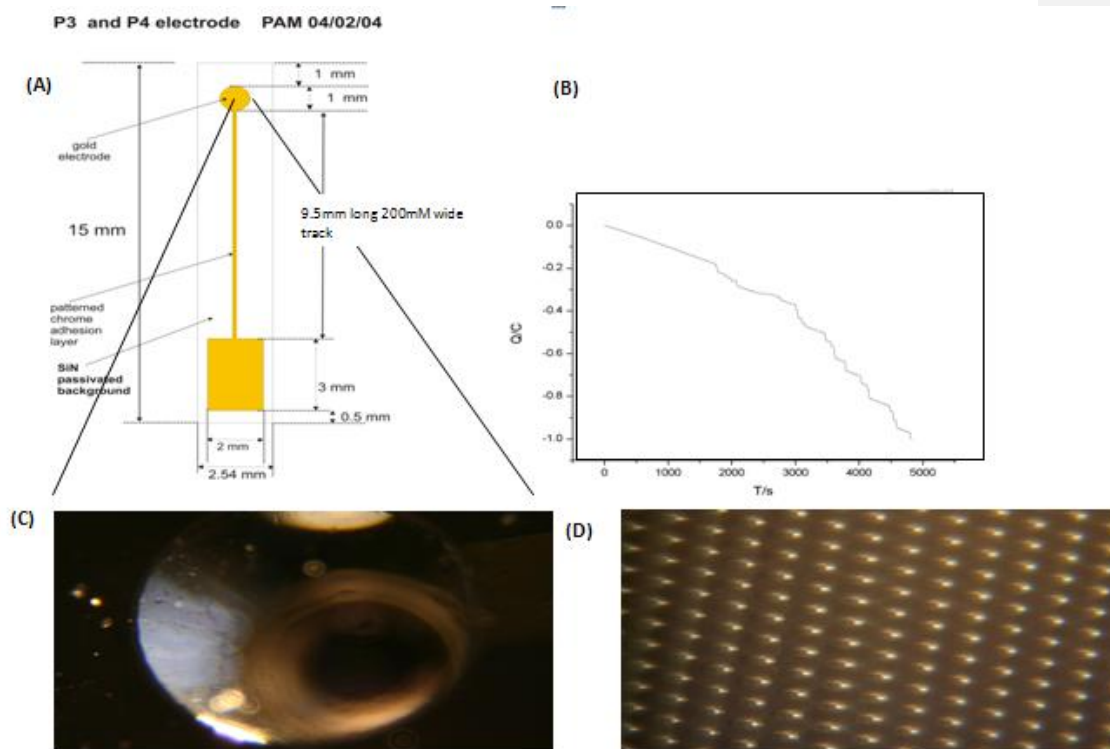


Figure 3-26 - (A), a schematic of the platinum and gold P4 electrodes used. (B), a platinum electrode under a held potential in mercuric nitrate solution undergoes amalgam plating. Deposition is monitored as the flow of charge with time. (C), successful platinum P4 Hg electroplating and (D) microscopically on a P10 microscopic array electrode.

Mercury was successfully deposited on to platinum macroscopic P3 / P4 electrodes (Figure 3-26 A and C) and also the P10 microscopic array electrodes (Figure 3-26 D). The macroscopic mercury electrodes were robust and allowed repeated use and were still stable after 8 months. Some poisoning of the electrodes occurred in a number of the metal ion ASV trials where the potential could not be raised high enough to strip adsorbed species before the electrodes broke down. The microscopic electrodes did give significantly higher responses due to radial diffusion. However, two main problems were encountered. Uniform production of the electrodes was problematic due to the plated mercury re-dissolving from the perchloric acid solution if not rapidly rinse after plated. Also, poisoning of the electrodes was a fatal problem. The bulk plated mercury droplets (P3/P4 electrodes) could withstand significantly lower conditioning potentials to clean the surfaces compared to the the smaller mercury

droplets of the P10 microarrays were stripped from the electrode surfaces. As a result, only P3 and P4 Hg coated electrodes were used for SAM deposition.

### **3.7.7 Crown ether insertion into SAMs on HgPt electrodes**

Because EIS and ASV methods failed to quantify the amount of  $^{90}\text{Sr}^{2+}$  ions chelated by the crown ethers, an alternative interrogation method using the HgPt electrodes and SAMs of MHDA or DOPC was performed.

#### **3.7.7.1 Static and flow cell deposition of DOPC monolayers on HgPt electrodes**

Both static and flow cell deposition of DOPC onto mercury electrodes was performed. Static deposition used physical dipping of an electrode through a 1 mg/ml DOPC in a 0.1 M KCl solution before application of a negative potential to orientate the absorbed molecules into an orientated SAM. Reproducibility of the layer formed was better by using deposition under negative potential in a flow cell system. For this process a bespoke flow cell [168] designed by Dr Zachary Coldrick, Centre for Molecular Nanoscience (CMNS), University of Leeds, was attached in a flow loop system to a 5 litre stock of 0.1 M KCl argon sparged buffer. Under flow and a very negative potential of -2.6 V, a DOPC solution was introduced into the flow cell injection port. This deposition potential was stopped as the deposition peaks appeared and potentials switched to the interrogation profile. The interrogation profiles used were -0.2 V to -1.2 V, -0.2 V to -1.4 V, -0.2 V to -1.6 V, -0.2 V to -1.8 V, -0.2 V to -2.0 V, each at a scan rate of 50 m V/s. An overlay of the resulting lipid conformational changes is shown in Figure 3-27.

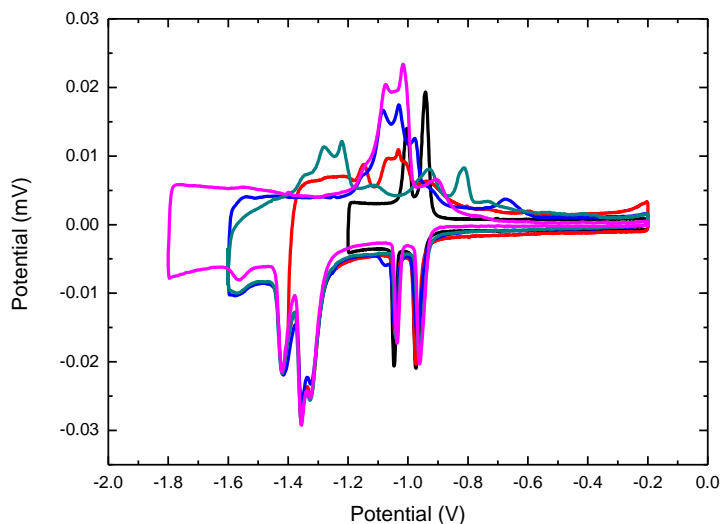


Figure 3-27 - Successful DOPC deposition on to HgPt electrodes. Rapid real time cyclic voltammetry shows peaks corresponding to SAM poration, reorientation, desorption and resorption. The upper peaks correspond to solution DOPC diffusing and desorbing from the electrode surface.

The peaks observed for the DOPC lipid phase transitions (Figure 3-27) have been studied in detail and have been shown to correspond to different states of the absorbed SAM [39]. Three known capacitance-potential peaks of DOPC in electric fields have been extensively studied. The first at 0.94 V corresponds to an initial conformational change of the monolayer, a field induced change in orientation of the polar heads of the DOPC lipid [175] and this one was selected to monitor crown ether complex insertion. The 3 known capacitance peaks are characterised at -0.94 V corresponding to a lipid conformational change, a phase transition at -1.0 V [175] and the onset of poration and desorption at -1.25 V. Incremental increase of potential (scan ranges from 0.2 V to 1.2, 1.4, 1.6, 1.8V respectively) showed lipid reorientation in realtime. Introducing a planar molecule such as the crown ether that can insert into the DOPC SAM layer was monitored in real time by changes in the observed cyclic voltammogram shown in Figure 3-27.

### 3.7.7.2 Effect of carboxy-benzo 18-crown-6 on a DOPC monolayer

To determine if the DOPC reorientation peaks were influenced by DCH18C6, sequential injections of increasing crown ether concentrations were injected into the flow cell and the interactions with an assembled DOPC SAM monitored. The natural DOPC trace (black

lines) compared to the disrupted state as a result of insertion (red lines) are shown after 10 min interaction (Figure 3-28).

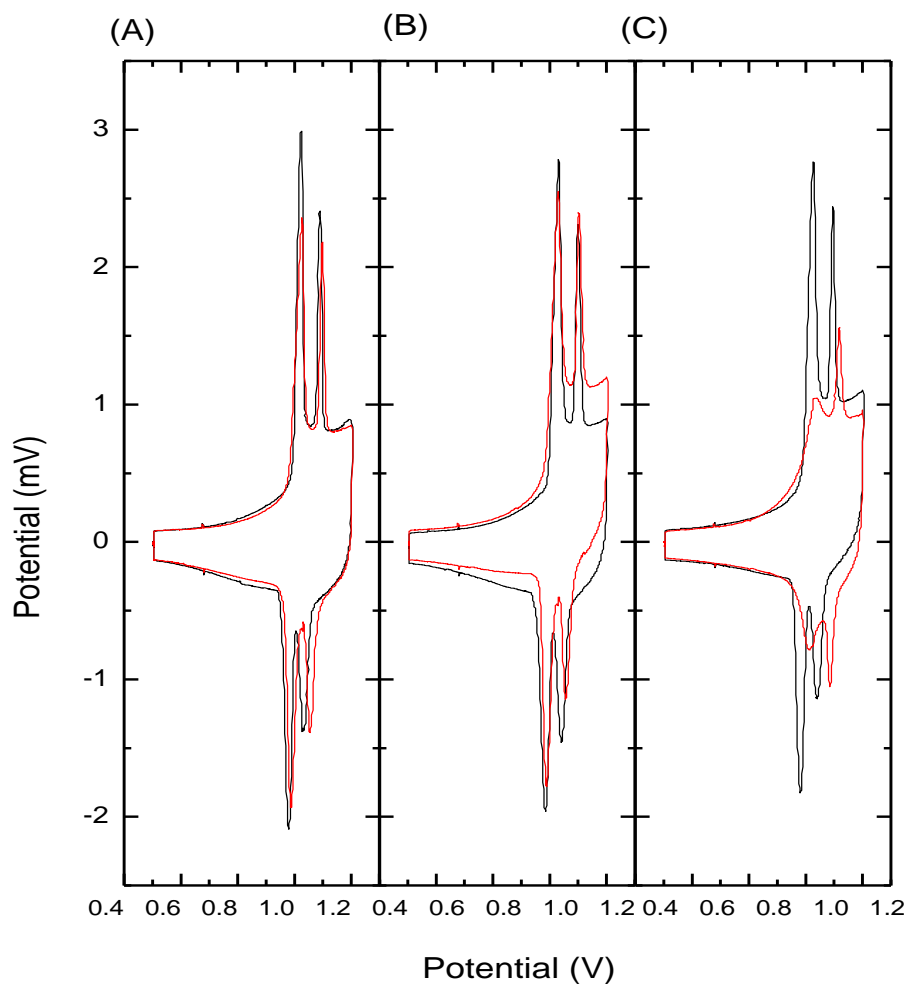


Figure 3-28 - Real-time cyclic voltammetry of 4-carboxy-benzo-18-crown-6 interaction with DOPC SAM on a Hg-Pt electrode. — Base line of DOPC and — recovery after 10 min interaction with (A) 10 nM, (B) 10  $\mu$ M and (C) 10 mM of carboxy-benzo-18-crown-6- $\text{Sr}^{2+}$ .

Increasing concentrations of 4-carboxybenzo-18-crown-6 were injected into the flow cell from nano to milli molar concentrations onto a DOPC-HGPT electrode and the reorientation and shift in peaks monitored. Beyond micromolar amounts of crown ether instantaneous

decrease and shifts in the lipid peaks were observed (Figure 3-28 A -C). A decrease of the conformational change and phase change peaks suggests crown ether insertion and disruption of the assembled SAM. A shift of the peaks to more negative potentials (red traces) suggests that the crown ether was disrupting the lipid domains, causing them to respond at only more negative potentials. Scans every minute for 5 mins allowed the reorientation and recovery of the SAMs to be observed. All concentrations show an amount of crown ether was successfully retained by the SAM by the peak offset (10-20 mV). Up to millimolar amounts of crown ether showed over 90 % recovery of the initial peak potential. At high crown ether concentration, the DOPC peaks are almost completely displaced with minimal recovery with time, suggesting significant displacement of the lipid layer by crown ether.

To determine if the DOPC reorientation peaks could be used as a real time detection mechanism for the chelated  $\text{DCH18C6} \cdot \text{Sr}^{2+}$  complex, sequential injections of increasing concentrations of ion-crown ether were injected into the flow cell and the interactions with an assembled DOPC SAM monitored, shown in Figure 3-29.

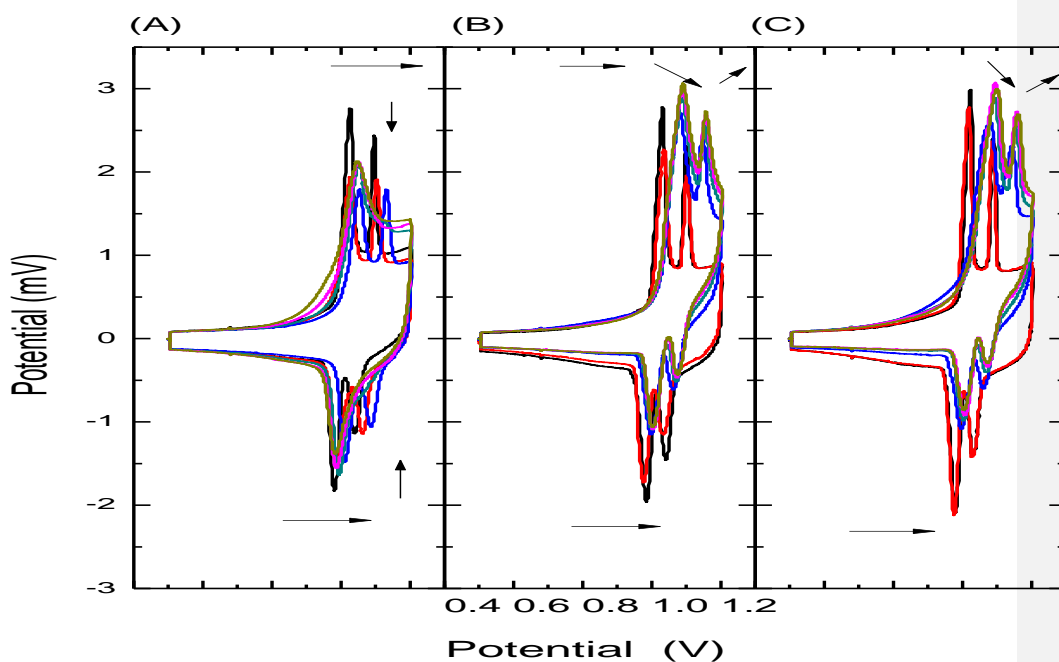


Figure 3-29 - Real time rapid CV of DOPC SAM recovery with time from increasing concentrations of crown ether. — DOPC base line; interaction with crown ether after — 1 min; — 2mins; — 3 mins; — 4 mins; — 5 mins. (A), 10 nM; (B), 10  $\mu$ M, (C), 10 mM. At low concentrations peak recovery shows host elution, while at high concentrations permanent displacement and reorientation of the SAM occur. Arrows indicate the directional shift of the peaks with time. Resorption peaks show a negative shift, decrease and then broadening and recovery at low concentrations suggesting crown ether layer formation in lipid.

Addition of  $\text{Sr}^{2+}$  either directly by mixing with with the host molecule, or flowed over a SAM-crown ether layer was used to determine if peak changes, specifically the -0.94 V lipid conformational change peak, and the - 1.0 V phase transition at peak, could be used for analyte quantification (Figure 3-29). Direct reduction of  $\text{Sr}^{2+}$  ions occurs at -2.89 V (vs H electrode [45]). Such an anodic potential would completely remove the adsorbed DOPC and thus could not be used with ASV. As a result, ratios of analyte:host were preincubated or flow injected in (1000:1, 100:1 10:1 and 1:1) ratios. No reproducible shift in peak potential between host and host analyte complex could be observed as the potentials are sensitive to oxygen and reference drift. Initial scans that showed a negative potential drift upon addition of  $\text{DCH18C6} \cdot \text{Sr}^{2+}$ . However, injection of a competitor chelator, chloranilic acid to remove bound  $\text{Sr}^{2+}$  did not result in a return of the DOPC crown ether peaks. As expected, by

increasing the scan rate whilst increasing the rate of DOPC recovery, the amount of crown ether displaced from the electrode was not affected. As a result rapid CV could not be used as a sensing mechanism for  $\text{Sr}^{2+}$  but did show crown ethers adsorb at a mercury film interface causing permanent disruption of a DOPC SAM. This approach showed an amount of crown ether permanently electrostatically bound to the Hg surface while a proportion was displaced and eluted.

Figure 3-30 shows the lateral potential deviations, if a shift in the potential the phenomena occurred at as a result of crown ether insertion (A) and (C). (B) and (D), correspond to a shift in peak height which shows if a change in potential across the electrode surface occurred as a result of crown ether insertion signifying disruption and poration of the SAM layer visible as a potential drop.

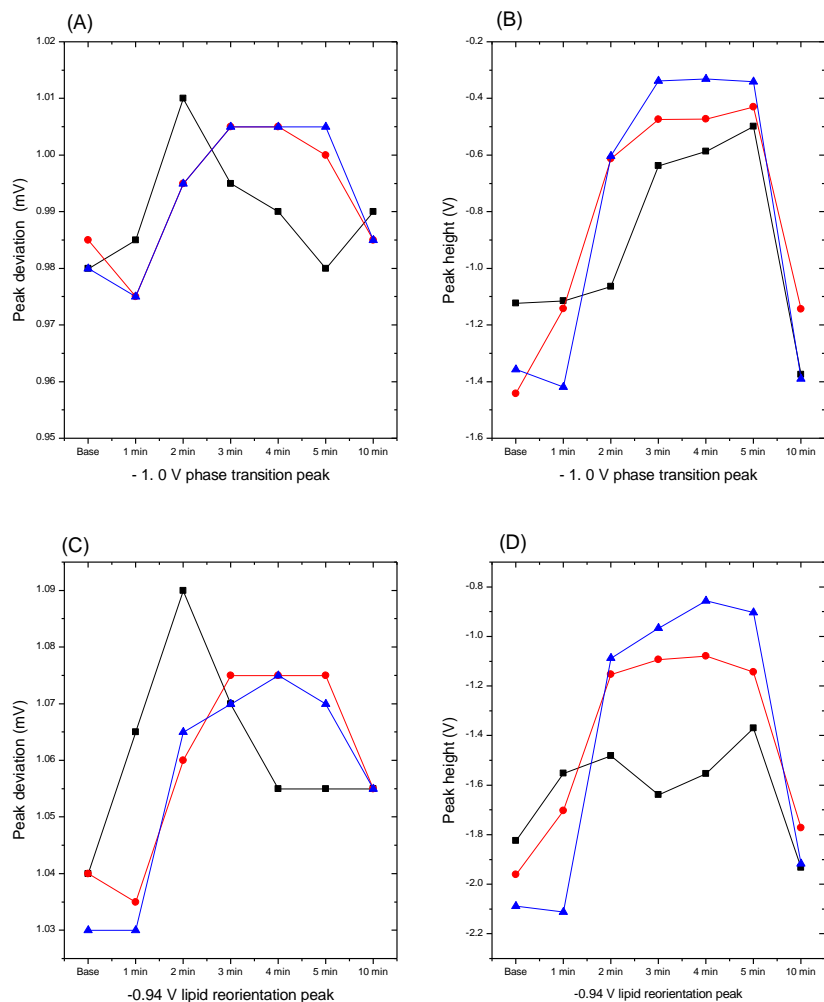


Figure 3-30 – The changes in potential or current of realtime cyclic voltammetry scans monitoring the host-lipid interaction at a Hg-Pt electrode. Effect of crown ether insertion on the characteristic known DOPC -0.94 V lipid reorientation peak, and -1.0 V phase transformation peaks. Symbols correspond to ■ 10mM, ● 10 μM or ▲ 10 nM crown ether injected. (A) and (B) show deviations in the -0.94 reorientation peak corresponding to deviation in the optimum reorientation potential. (C) and (D) correspond to the -1.0 V phase transition, showing potential diaviations from the preferred potential as a resulted of lipid-host molecule interactions and disruption of the SAM layer.

The deviation in the phase transition peak (Figure 3-30 A) showed an increasing negative shift of up to 1.01 mV at all concentrations of crown ether within the first 2 min of crown ether interaction suggesting insertion of crown ether and disruption of the SAM due to the more negative potentials needed to onset the lipid reorientation phase. After 10 min there was almost complete recovery suggesting a stable reorientation of lipid domains and crown ether was achieved.

The deviation in the reorientation peak (Figure 3-30 C) shows a far more significant and rapid shift to more negative potentials before insertion resulting from electrostatic interactions between the negative DOPC head groups and crown ether. Recovery also occurs over the next 10 min but at a slower rate and showed permanent deformation of the SAM, supporting the theory of stable crown ether head group interactions.

Changes in peak height signified changes in potential across the electrode interface as a result of significant changes in the SAM structure or porosity. The clearest linear response was observed at all three crown ether concentrations, looking at the reorientation peak (Figure 3-30 B) where a peak height reduction of over 1 mV occurred within the first 2 min and continued beyond 5 min. This supports the theory of rapid crown ether insertion into the hydrophobic cavity made available by the SAM to minimise solvent-crown ether interactions.

A similar trend is observed in the peak height change for the reorientation peak (Figure 3-30 D), the exception at millimolar concentration, where the disruption in SAM interfacial changes saturates at 2 min interaction before a further change beyond 4 min. This suggests a two stage process was occurring. Again, only partial recovery was observed after 10 min suggesting permanent crown ether sorption and SAM hindrance by crown ether occurred. While a number of interesting molecular phenomena were observable in realtime with this technique, as the response was not linear or analyte dependant, it would not currently be suitable for a sensing device.

### **3.7.7.3 Insertion of free cholesterol and cholesterol aza-18-crown-6 insertion into an MHDA SAM**

Both free cholesterol and cholesterol tethered aza18C6 could be seen to insert into MHDA layers on gold as a tethering mechanism. This was observed as a frequency dampening of an oscillating AT cut gold QCM chip with a predeposited SAM from a 24 h incubation of 1 mg/ml MHDA. Noise and density gradient changes can appear as different solvents mix, giving an apparent false mass change.

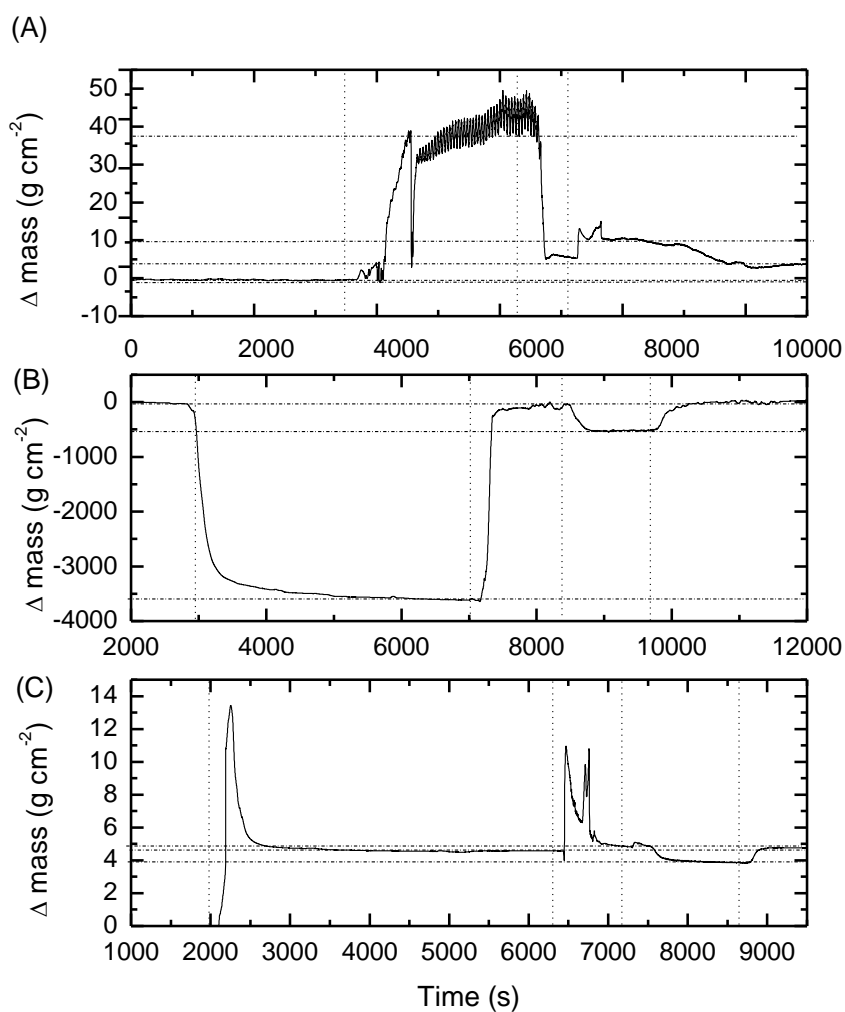


Figure 3-31 – QCM measurements were made on Mactek 1 inch At cut crystals coated with a gold electrode. Fundamental frequency was around 6 MHz and  $\Delta f$  was converted to  $\Delta$  mass using Mactek software. The following additions were made (A), 3 mg / ml free cholesterol; (B), cholesterol aza-18-crown-6 (10 mg/ml in EtOH); (C), attempted cholesterol aza-18-crown-6 insertion (10 mg/ml in EtOH in 10 % (v/v) chloroform) which resulted in stripping of the MHDA base SAM.

As a result strict washes and buffer changes were made after each addition to account for the frequency fluxes caused by the small percentages of organic solvents used to disperse hydrophobic hosts. Figure 3-31 shows masses calculated using Sauerbrey's equation in response to crown ether insertion or analyte binding.

In compliment to the real time CV interactions of crown ethers with SAM layers, binding interactions and insertions were monitored as a function of frequency dampening, and extrapolated to a  $\Delta$  of interfacial mass (Figure 3-31). Before the cholesterol modified crown ether was used, it was confirmed that the free form of cholesterol inserted into an MHDA SAM (Figure 3-31 A). A sequential change from aqueous MOPS buffer to 1 mM synthetic cholesterol in methanol resulted in a 'falsepositive', a solvent gradient flux mass increase to  $46.0 \mu\text{gcm}^2$ . Only after a second MOPS wash which stabilised the signal gave the true  $\Delta$  mass of  $3.987 \mu\text{gcm}^2$ . A final base corrected average of  $\Delta$  mass of  $3.574 \mu\text{gcm}^2$  mass increase was observed from the  $50 \mu\text{l}$  injection of 1 mM cholesterol. Similar magnitudes of mass change were observed from cholesterol dispersed in PBS and pure ethanol.

Figure 3-31 B shows successful insertion of cholesterol tethered aza -18-crown-6 from a  $100 \mu\text{l}$  injection of 10 mg/ml crown ether, observed as mass increase of  $4.56 \mu\text{gcm}^2$ . This increased to  $4.87 \mu\text{gcm}^2$  during a buffer wash. A switch to a  $\text{Sr}(\text{NO}_3)_2$  solution momentary increased the frequency dampening, but stabilised at a  $\Delta$  mass of  $3.93 \mu\text{gcm}^2$ . After a MOPS buffer wash to remove unbound analyte, the true  $\Delta$  mass stabilised at  $4.76 \mu\text{gcm}^2$  which showed an increase of  $0.2 \mu\text{gcm}^2$  from bound  $\text{Sr}^{2+}$  ions. Repeat of this experiment showed successful crown ether insertion, but destabilisation of the signal upon  $\text{Sr}^{2+}$  addition. A significant increase in noise was also observed. The likely cause of noise was because analyte binding was increasing the host hydrophilicity, which was still counteracted by the dominating hydrophobic insertion forces between cholesterol and MHDA molecules. This sudden instability and the Sauerbrey equations incompatibility with non rigid molecules are the likely cause of the observed noise and signal instability. These results support the conclusion that  $\text{Sr}^{2+}$  binding to the crown ether occurred, but could not be quantified accurately. Further experimentation using D-QCM would be needed to develop this approach.

A range of organic solvents were used to attempt to increase the amount of crown ether loaded into the MHDA SAM. Acetone, ethanol and methanol were found suitable to dissolve many of the crown ethers. However, whilst efficient at solvating the crown ether, DMSO and

chloroform resulted in removal of the SAM layer completely (Figure 3-24 C), where the starting mass is equal to the final mass.

#### 3.7.7.4 $\text{Sr}^{2+}$ binding by resorcalix[4]arene inserted into MHDA SAMs

An 1:10 (v/v) acetonitrile ethanol solution was polar enough to dissolve the host resorcalix[4]arene and deliver the crown ether to the SAM without stripping the SAM. Flow of host molecule over a prepared MHDA layer showed successful and stable insertion of resorcalix[4]arene (Figure 3-32).

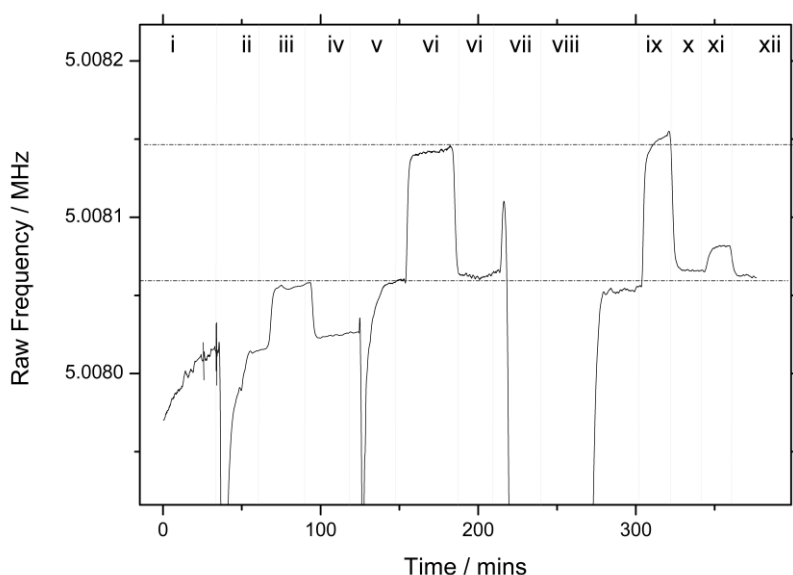


Figure 3-32 - Insertion of resorcalix[4]arene into a MHDA SAM. Figure numerals indicate solutions flowed over the gold SAM coated surface; (i)  $\text{dH}_2\text{O}$ ; (ii), ethanol; (iii), 10 mg resorcalix[4]arene in 10:1 (v/v) ethanol : acetone; (iv), ethanol; (v),  $\text{dH}_2\text{O}$ ; (vi), 1 mM  $\text{Sr}(\text{NO}_3)_2$ ; (vii),  $\text{dH}_2\text{O}$ ; (viii), 1 mM EDTA; (ix), 1 mM  $\text{Sr}(\text{NO}_3)_2$ ; (x),  $\text{dH}_2\text{O}$ ; (xi), 1 mM EDTA; (xii),  $\text{dH}_2\text{O}$ .

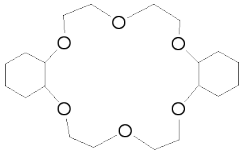
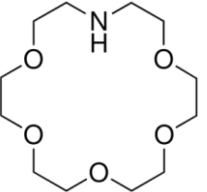
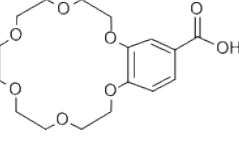
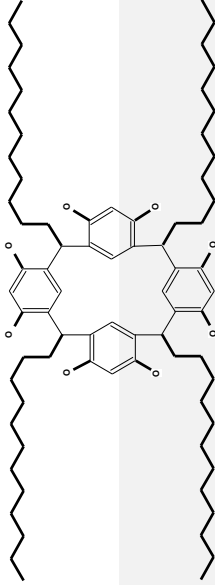
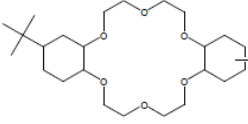
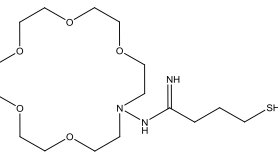
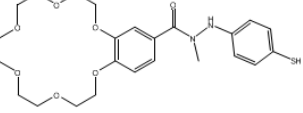
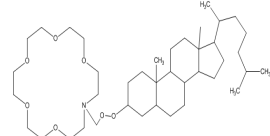
Insertion of resorcalix[4]arene was observed as a frequency increase from steps (ii) to (v). After this event, a frequency increase and false apparent mass decrease is observed, a result of switching through a mild organic solvent wash to remove unbound host, and switching to aqueous solvents. However, a repeatable mass decrease upon 1 mM  $\text{Sr}(\text{NO}_3)_2$  addition was observed in steps vi and ix, which could be reversed by addition of the chelator EDTA, which

removed  $\text{Sr}^{2+}$  ions from the resorc[4]alixare. This behaviour supports the theory that  $\text{Sr}^{2+}$  ions are binding to the surface, but a frequency increase, rather than decrease occurred. The proposed reason for this is similar to the problems observed with the insertion of cholesterol aza-18-crown-6 (as discussed in section 3.7.7.3). The hydrophobic tails of resorcalix[4]arene insert into the SAM but are not covalently bound to the gold substrate, and as a result the molecule does not oscillate with the SAM. Binding of  $\text{Sr}^{2+}$  ions increased hydrophilicity of the receptor molecule, and may in fact resulted in the molecule moving partially back into the solvent, and away from the substrate. This resulted in the observed frequency increase, rather than the expected decrease. This affect was reproducible, but not proportional to dilutions of  $\text{Sr}^{2+}$ . As a result, because no calibration could be made, the system was abandoned as a sensing procedure.

### 3.8 Conclusion

After the success of using surface layer proteins as a specific receptor for a functioning uranyl biosensor, an alternative approach was needed for other analytes due to the lack of binding proteins with specificity to  $\text{Cs}^+$  or  $\text{Sr}^{2+}$ . Because of this, a number of synthetic hosts identified from literature with desired specificities were either obtained commercially or used as supplied, chemically modified or synthesised for specific functionality. These were combined with techniques including EIS, real time rapid CV, scintillation counting and QCM. The range of hosts molecules are summarised in Table 3-5. Use of rapid cyclic voltammetry on HgPt electrodes showed their interaction, adsorption and displacement via SAMs in real time. The crown ether were shown to adsorb hydrophobically to the electrode. While macrocycle-surface interactions could be observed, no proportional and reproducible signal could be observed to the addition of  $\text{Sr}^{2+}$ . Similarly, attempts to use these hosts at electrode interfaces with EIS was unsuccessful. The failure was most likely due to the orientation of crown ethers perpendicular to the interface from the angles imposed by the lariat side arms. This coupled with minimal conformational change upon analyte binding, resulted in interfacial changes that could not be detected. The use of ionic liquid masked the desired  $\text{Sr}^{2+}$  and  $\text{Cs}^+$  peaks expected in mercury ASV experiments. The possibility that the ions were not being transported by the layer was ruled out by scintillation counting of the radioisotope ions which confirmed a small, but reproducible sorption of  $^{90}\text{Sr}^{2+}$ , but a significantly higher degree of specificity for  $^{90}\text{Y}^{2+}$  not previously reported. Problems with ionic liquid breakdown due to water incorporation and slow ion transport through the ionic liquid without the use of a rotating disk electrode resulted in this approach being abandoned.

Table 3-5 – Summary table of macrocycle molecules and subsequent successful modifications used in this chapter.

Dicyclohexano-18-crown-6 and derivatives	Aza -18-crown-6 and modified forms	Carboxybenzo 18-crown-6 and modified forms	Synthesised crown ethers
			
Dicyclohexano-18-crown-6	Aza -18-crown-6, (1,4,7,10,13-pentaoxa -16-aza- cyclo octadecane)	Carboxybenzo 18-crown-6	
			
tert butyl dicyclohexano 18 crown 6	4-Imino-4-(1,4,7,10,13-pentaoxa-16-aza-cyclooctadec-16-yl)-butane-1-thiol	6,7,9,10,12,13,15,16,18,19-decahydro-5,8,11,14,17,20-hexaoxa-benzocyclooctadecene-2-carboxylic acid N'-(4-mercapto-phenyl)-N-methyl-hydrazide	2,c-8,c-14,c-20-tetraundecyl-4,6,10,12,16,18,22,24-octahydroxyresorc[4]arene
	16-[17-(1,5-Dimethyl-hexyl)-10,13-dimethyl-hexadecahydro-cyclopenta[a]phenanthren-3-ylperoxymethyl]-1,4,7,10,13-pentaoxa-16-aza-cyclooctadecane		

Insertion of crown ethers into SAMs was observed as a frequency dampening effect on lipid coated gold QCM chips. Addition of analyte to cholesterol tethered crown ethers caused signal destabilisation due to significant disruption of the SAM by cholesterol reorientation. The resorcinol calixarene with its 4 hydrophobic chains similarly inserted into MHDA SAMs, but upon  $\text{Sr}^{2+}$  addition, an apparent decrease of mass was observed. This apparent mass decrease could be cycled with addition of a chelator and more  $\text{Sr}^{2+}$ . The cause for this was theorised due to an increase in hydrophilicity of the polar crown head group and partial removal from the SAM layer. Attempts to synthesise a similar host by replacing the dodecyl aldehyde tails with a shorter moiety that would enable covalent linkage to the gold substrate to eliminate this problem was attempted, but synthesis was unsuccessful. An 'on' or 'off' strontium binding system was shown, but this was not sensitive enough to create a usable calibration curve against known  $\text{Sr}^{2+}$  concentrations.

## **4 : Functionalised nanoparticles for chelation of radionuclides**

---

## 4.1 Chapter overview

Because of the problems detecting ions using chemosensing hosts as detailed in Chapter 3, an alternative strategy was instigated whereby enhanced chelator surfaces in the form of functionalised particles would be combined with radionuclide speciation via scintillation or gamma counting. Because metallic particles are coloured and interfere with scintillation counting, biosilica was chosen as an optically transparent, robust material for functionalising with a range of simple chelator groups. The particles created had a superior capacity to commercial resins and were able to bind a significant amount of  $^{90}\text{Sr}^{2+}$ , but all systems struggled to bind significant amounts of  $^{137}\text{Cs}^+$ . Low level radioisotope concentrations modelled on Sellafield SGW were detected with a 1 h incubation time and 2 h counting profiles. The overall hierarchy of this chapter is shown in Figure 4.1.

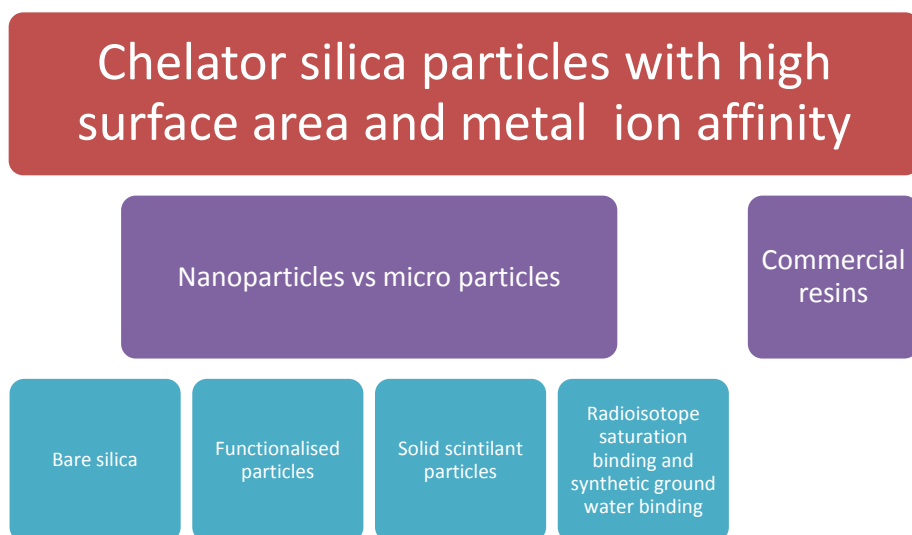


Figure 4-1 - Chapter four hierarchy outlining the methods used to create chelator particles with a high specificity particularly to  $^{90}\text{Sr}^{2+}$  with greater binding capacity than a number of commercial resins and functionalised nanofibres.

## 4.2 Functionalised nanoparticles

While there is no international definition of a nanoparticle, the UK PAS (Publicly Available Specification, British Standards Institution) [176] in broad terms defines a nanoparticle as a particle that has at least one dimension of less than 100 nm. Because of their high surface area to volume ratio they often exhibit unusual optical, chemical and physical properties when compared to the bulk materials [177]. Metallic, polymeric, organic and inorganic

particles are the most frequently used types of nanoparticle. Because metallic particles exhibit strong colour properties that interfere with scintillating counting, a system of optically transparent functionalised silica particles was developed.

### 4.3 Functionalised silanes

One useful class of silanes has a central Si atom bonded to an alkyl linker arm  $(CH_2)_n$  plus the functional or reactive group (Figure 4-2). The most common groups around the central Si atom are methoxy (alkyl H-C chain linked to an O); alkoxy, or ethyl ether, the ethoxyl silanes which can be hydrolysed to leave the reactive S-OH silanol groups. These groups condense to form covalent bonds on hydroxyl coated surfaces.

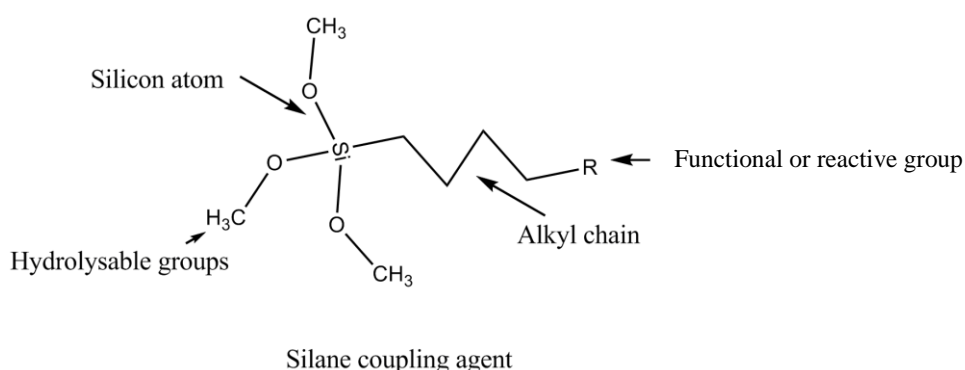


Figure 4-2 - The basic schematic of a bioconjugatable, hydrolysable silane used to nucleate the silica particles. The most common unfunctionalised forms are TEOS (tetraethyl orthosilicate) or TMOS (tetramethyl orthosilicate). R can be a wide range of groups but is most commonly an amine or thiol.

The side arms of the silane can allow a versatile range of organo-reactive or organo-functionalisation. Functionalised compounds that are commercially available include amino, aldehydes, epoxy, alcohols, carboxylic acid, esters and thiol silanes [178].

## 4.4 Silanol condensation theory

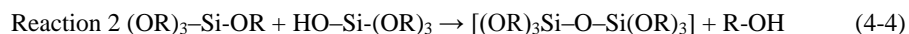
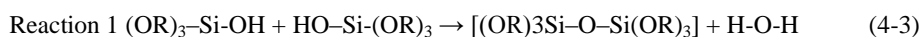
The effect of hydrolysis on a silane is liberation of the side arms revealing a hydroxyl group (Equation 4-1). In the case of TEOS, the R is the alkyl group C<sub>2</sub>H<sub>5</sub>.



Complete hydrolysis can replace all 4 groups (Equation 4-2):



Partially hydrolysed silanes condense to form siloxane (Si-O-Si) bonds, resulting in the release of water (Equation 4-3), allowing three dimensional growth as the reactive silanols, R-OH, cross react and condense (Equation 4-4), in this case C<sub>2</sub>H<sub>5</sub>, alcohol:



A range of functionalised silanes are also available where typically one of the 4 alkoxy groups is replaced by a Si-C bonded functional group, e.g in 3 aminopropyl trimethoxysilane (APTES) there are 3 ethoxy groups, which can still be hydrolysed and the aminopropyl which can not. The condensation of APTES leaves pendant aminopropyl groups available for further reaction. When combined with a nucleating agent, growth occurs in three dimensions resulting in particle nucleation. If no nucleating agent is present, two dimensional growth occurs allowing the coating of surfaces, an example shown in Figure 4-3 where two dimensional growth of APTES occurs on a planar bulk surface. This idea is explored in detail in Chapter 5.

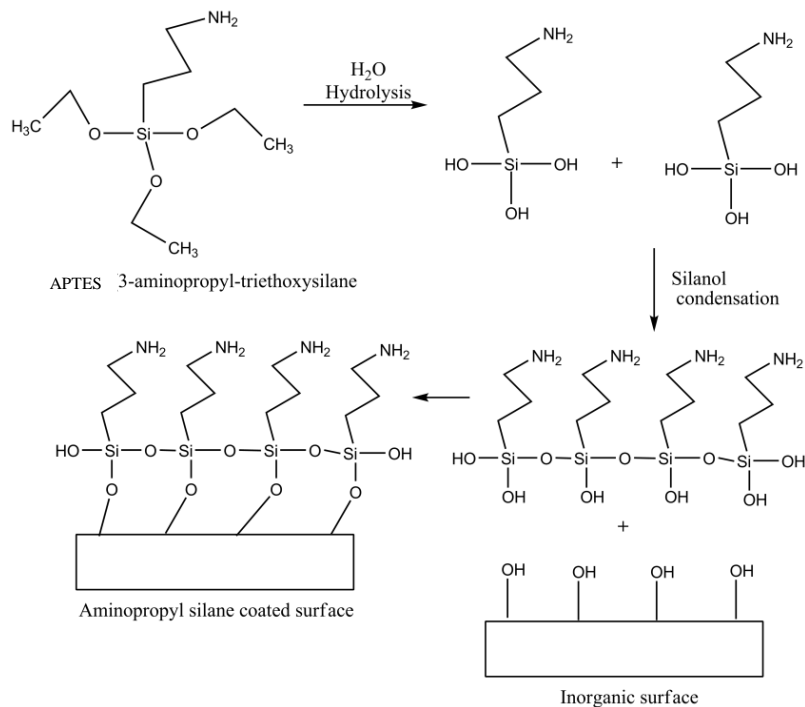


Figure 4-3 - APTS condensation onto hydroxyl surface via silanol bond formation. This method allows large surface areas to be coated on hydroxyl coated surfaces (glass, silica, metal oxides, etc) with a wide range of functionalities.

## 4.5 Silica nanoparticles

A vast area of nano, micro and micelle particle engineering is based on emulsion processes, the stabilisation of a liquid in liquid suspension of two or more immiscible substances as a colloidal suspension. Condensation of silanols inside the encapsulated water-in-oil (W/O) emulsion sites; known as the sol gel method can be catalysed either by  $NH_3$  or  $HCl$  [179]. The emulsion droplets act as a size template and restrict the nucleation size of the silica particles to the stabilised drop size. They are however limited to broad polydisperse systems. Emulsions themselves are a huge industry where particle engineering aims to create monodisperse suspensions. Producing monodispersity requires precise chemical engineering with dedicated engineered rigs, emulsifiers and sonicators. Developing such a system would be a complete project in itself, which is why an alternative method using a modified classical Stober 'seed and growth' method was used, comprising of an ammonia, ethanol water solution mixed with tetramethyl orthosilicate (TEOS). Particle size distributions were improved by control of the growth conditions i.e temperature, pH and choice of solvent.

## 4.6 Bifunctional silica particles

Functionalised silica particles have a broad application base and have been used for shielding metallic nanoparticles (Al/Zn) and corrosion resistance [180], encapsulation of fluorescent dyes [181] as well as drug encapsulation [182]. Recent advances in dye encapsulation have had huge effects on the application of commercial dyes. A significant drawback of optical systems is that the chemical dye used is sensitive to pH, oxidation, photo-degradation and quenching. Research dyes have extensive chemical modification or protection to slow hydrolysis and breakdown of the dye, with costs reaching hundreds of pounds per milligram. The ability to encapsulate cheap water miscible or even immiscible dyes that cost pounds per gram is particularly advantageous. This encapsulation method is allowing a number of traditional dyes to be dispersed with none of the former limitations, and is causing a resurgence in dye based fluorescence. This was previously believed to be moving towards quantum dot based fluorescence. Quantum dots are group III-V composite semiconductor particles that emit photons of a desired engineered band gap energy with a brightness that can be more than one hundred times brighter than chemical dyes [183]. While originally believed to be the future of optical based systems, their problems of high toxicity and molecular blinking from single photon emission has meant that practical applications have not lived up to their initial promise. Silica particles containing fluorescent cores have recently been shown to be brighter than quantum dots because the delocalisation and emission of multiple photons does not suffer from the molecular blinking. Such particles are created in two stage processes. First, the anhydrous and condensation of tetraethylorthosilicate (TEOS) with a dye such as fluorescein isothiocyanate (FITC) creates intensely bright silica particle cores. A second step disperses these cores that are now protected from hydrolysis and chemical bleaching in aqueous media.

Size control depends on a wide range of variables but the dominating factors are silane concentration, temperature, nucleation time, feeding time and solvent. Salt concentrations significantly alter the particles' double layer and dramatically alter stability and size. NaCl reduces repulsion between condensed colloidal species and was showed to reduce particle size rather than the expected charge screening and aggregation of particles [184]. Surfactants as well as charged species are frequently used to stabilise dispersions. These can bond covalently or act via chemisorptions. For example octadecyl and other hydrocarbon surfactants adsorb onto silica particles stabilising them and allowing dispersion in strong

organic solvents with which they are not normally miscible. Combining this with index (mis)matching (e.g. chloroform, hexadecane, solvents of refractive index significantly different to that of silica) allows direct particle visualisation via microscopy that is not normally possible [185]. There are however a number of contradictory publications regarding silica particles and stabilisation; with claims of the surfactant SDS both increasing aggregation [185], and inhibiting nucleation altogether [186]. This is because many systems use multiple nucleating agents, stabilisers, salts and surfactants and it is impossible to determine experimentally the effect of each component. As a result, particles were grown from two basic protocols without salts or surfactants for enhanced control over the particles produced.

#### 4.7 Nanoparticle dispersity

Accurate growth of monodisperse nanoparticles is often a very difficult process requiring strict monitoring and control of the growth environment temperature, pH, and silane concentrations. Without these controls entropic constraints lead to polydisperse particle systems. Colloidal particle dispersity can be measured as a size distribution index (U), shown in Equation 4-5. The lower the U value, the more monodisperse the sample. Monodispersity calls for  $U < 1.05$  [184].

$$U = \frac{D_w \text{ weight average particle size}}{D_n \text{ number average particle size}} \quad D_n = \frac{n \sum n_i D_i}{\sum n_i} \quad D_w = \frac{n \sum n_i D_i^4}{\sum n_i D_i^3} \quad (4-5)$$

where  $D_n$  is the average particle size, U the size distribution index of silica particles,  $D_i$  the diameter gained by measuring  $n_i$  particles (about 100) for each sample using SEM,  $D_n$  is the number average particle size, and  $D_w$  is the weight average particle size.

Mixing of components is extremely important in influencing particle formation kinetics, size distribution and morphology [187]. Ideally, rapid nucleation is followed by a slow growth phase during which the particles are stabilised against collisional aggregation. Steric surfactant stabilisers can be used at this stage but are costly, available in limited quantities and only useful in liquid phase growth [188]. Size fractionation by centrifugation allows more monodisperse fractions to be fractionated from polydisperse systems [187], but is not suitable for bulk synthesis. While a number of electrostatic controlled processes are available for monodisperse gaseous particle growth, aqueous phase growth has problems of container

interactions and aggregation. Because gaseous phase growth was not an option, a range of experiments controlling liquid phase growth with temperature, silane concentration, heating and mixing effects were performed to optimise silica particle growth. Polypropylene growth vessels particularly improved growth and minimised surface condensation which occurs significantly in glassware.

#### **4.8 Long term stability of nanoparticles**

Physical instability due to aggregation, particle fusion and chemical instability due to hydrolysis or chemical reactivity are barriers to nanoparticle stability in solution. To improve stability, the solvent of such colloidal suspensions is removed. The most common method to accomplish this is freeze drying, also known as lyophilisation. This is where water is removed from a frozen sample by sublimation under vacuum. The process generates desiccation stresses on the particles so stabilisers are usually added which can increase shelf life up to several years [189].

Sedimentation of sub-micron particles by gravitational forces is usually not a problem because of the counter forces of mixing from diffusion, convection and Brownian motion. Brownian forces dominate and keep the particles suspended. Addition of active molecules can induce particle agglomeration by displacing surface stabilisers. High molecular weight stabilisers can cause bridging flocculation when the free end of lengthy stabilisers adsorb onto adjacent nanoparticles, drawing them together. Charge stabilised particles can aggregate due to charged species adsorption in the electrical double layer. While extensive reviews are available for polymeric and organic drying of particles [190], to date, the only reported method of long term silica particle storage is by freezing. A first stage 30 min -80 °C freeze is followed by a primary drying stage which held the particles at -40 °C under 0.05 mbar pressure for 48 h, followed by a second drying phase at -20 °C, 0.01 mbar for 96 h [191]. Based on this protocol, a storage method was designed using an Anderman vacuum oven and a VirTis Vantage freeze dryer.

## 4.9 Experimental

### 4.9.1 Experimental overview

A range of optically inert biosilica nano and microparticles were grown using either direct nucleation (Section 4.11.1) or prehydrolysis (Section 4.11.2) methods. These were then functionalised with a range of chemical groups. Growth and functionality was confirmed by electron microscopy, FTIR and PCS. Potential chelator particles were used in scintillation counting experiments to determine saturation binding capacities for  $^{90}\text{Sr}^{2+}$  and  $^{137}\text{Cs}^{+}$  ions.

### 4.9.2 Reagents

Tetramethyl orthosilicate (TMOS), tetraethyl orthosilicate (TEOS); 3-(trimethoxysilyl)propyl methacrylate (methacrylate silane), 3-(triethoxysilyl)propyl isocyanate (isocyanate silane), (3-mercaptopropyl)trimethoxysilane (mercapto silane) were obtained from Sigma Aldrich. O-(Propargyloxy)-N-(triethoxysilylpropyl)urethane (alkyne silane) was bought from ABCR. 3-aminopropyltriethoxysilane (APTS, amino silane) was sourced from Across Organics. 3-[(trimethoxysilyl)propyl]ethylenediaminetriacetic acid (EDTA silane and triethoxysilylpropylmaleamic acid (carboxylate silane) were sourced from Silar Laboratories. Sodium borohydride, agarose fluorescein isothiocyanate, ferrocenecarboxyaldehyde were from Sigma Aldrich. Silanes will be subsequently referred to by their acronyms. All the abbreviations refer to the trimethoxy- or triethoxy- forms.

Scintillants and their sources were anthracene (Aldrich), 1,4-bis(5-phenyloxazol-2-yl) benzene (POPOP) (Sigma), 2,5-Diphenyloxazole (PPO) (Sigma), 1,1,4,4-tetraphenyl-1,3-butadiene (TPB) (Across Organics), polyethylene glycol p-(1,1,3,3-tetramethylbutyl)-phenyl ether (Triton X-100) (Sigma), p-terphenyl (Aldrich), methylstyrene/vinyl toluene (Aldrich). Ammonium hydroxide solution, ferrocenecarboxyaldehyde, ethylenediamine, sodium borohydride were from Sigma Aldrich. All other solvents and acids were sourced from Fisher Scientific unless otherwise stated.

## **4.10 Analytical methods**

### **4.10.1 Photon correlation spectroscopy of nanoparticles**

A Malvern Instruments Zetasizer Nano ZS calibrated to appropriate solvents, densities and refractive indexes was used to determine nanoparticle size distributions using 1 ml sample volumes at room temperature.

### **4.10.2 Field emission gun tunnelling electron microscopy of silica particles**

A drop of ethanol dispersed particles were dropped onto a copper-carbon grid and dried at room temperature. Imaging was performed on an FEI Tecnai TF20 200 kV FEG TEM fitted with a Gatan sc600 CCD camera and an Oxford Instruments 80 mm<sup>2</sup> X-max SDD EDX detector running INCA software.

### **4.10.3 Fourier transform infrared spectroscopy**

All FTIR regardless of sample preparation was performed on a liquid N<sub>2</sub> PerkinElmer Spectrum 100 FTIR Spectrometer. A scan range of 4000 to 750 cm<sup>-1</sup>, resolution 1 cm<sup>-1</sup> and scan averages of n = 30 per point was used. 3 regions per sample were compared for peak uniformity.

For determination of nanoparticle functionality, strictly anhydrous preparations were needed. Best spectra were obtained using ATR (Attenuated total reflectance)-FTIR. Particles were vacuum dried overnight, and homogenised into warm desiccated KBr. Samples were transferred to a Specac pellet die evacuated for three minutes and placed inside a Specac hydraulic press and compressed under high pressure (minimum of 5 tonnes) for 3 minutes. The resulting crystals were stored under desiccation until ready to be analysed.

If a sloping base was observed indicating infra red beam scattering from improper sample preparation, the sample was not used. Proper solvent drying was confirmed by the absence of broad absorption bands corresponding to ethanol contamination (2800 – 3600, 1200 – 1300, 1260 -1500 and below 900 cm<sup>-1</sup>). Other absorption bands used for quality control are summarised in Table 4-1 [192]. Known ATR-FTIR artificial bands were eliminated by cleaning the probe between samples. Christiansen effect absorption (light scattering from particles of equal size to the infrared wavelength) was minimised by a strict grinding duration.

Table 4-1 - A summary table of potential spurious bands that frequently are seen from poor sample preparation, sampling technique or other phenomena.

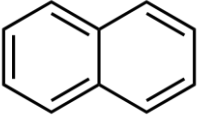
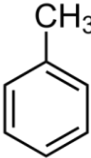
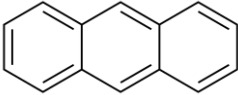
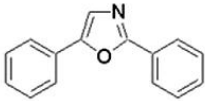
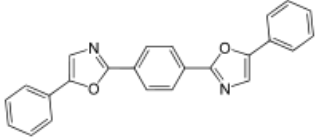
Wavenumber (cm <sup>-1</sup> )	Compound [192] and [24]
2800-3600 1200 -1300 1260 – 1500 Below 900	EtOH contamination (improper drying)
1590	Gaseous CO <sub>2</sub> forming carbonates

#### 4.10.4 Accurate determination of nanoparticle chelation

Attempts were made to develop a procedure to accurately determine the amounts of radionuclide bound by the functionalised nanoparticles from solution. It was essential to differentiate the signal from bound and unbound radioligand.

The main approach was to utilise functionalised NP to bind radioligand, then recover these by centrifugation and quantify the radionuclides by scintillation counting. A range of organic scintillants was investigated for use in scintillation cocktails, summarised in Table 4-2, including the commercial scintillation cocktail Emulsi Safe.

Table 4-2 - Organic molecules used as scintillants for beta radiation.

Name	Chemical structure
Naphthalene	
Toluene	
Anthracene	
Xylene	
2,5-Diphenyloxazole (PPO)	
1,4-bis(5-phenyloxazol-2-yl) benzene (POPOP)	

#### 4.10.5 Centrifuge assays for $^{90}\text{Sr}^{2+}$ and $^{137}\text{Cs}^+$ binding

In order to assess the binding capacity of functionalised NPs a centrifugal binding assay was used [193] (Figure 4-4 A). In order that the three layers retained their integrity, the approximate density mix of gradient oils dinonyl phthalate / dibutyl phthalate had to be determined.

A centrifugation assay was designed using a gradient of 100  $\mu$ l 1 M sucrose, a 200  $\mu$ l hydrophobic oil layer and 100  $\mu$ l sample containing radioisotope of a known concentration incubated with a predetermined mass of particles. In this way only bound analyte will be able to pass the oil layer. Background radiation was subtracted using blanks and physisorbed analyte accounted for by subtracting the amount bound on unfunctionalised TEOS particles. Thus the remaining signal is due to the binding capacity of the particles. Increasing ratios of the oils showed that a 80  $\mu$ l : 20  $\mu$ l or greater ratio of dinonyl phthalate to dibutyl phthalate was dense enough to retain unbound radioisotope and the aqueous phase in the upper tube segment even after a 1 min 13,000 RPM centrifugation (Figure 4-4 B).

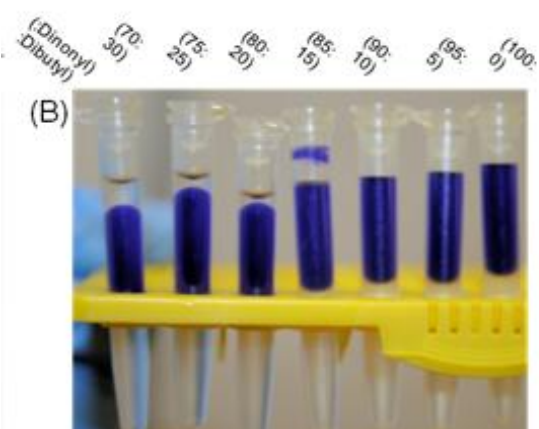
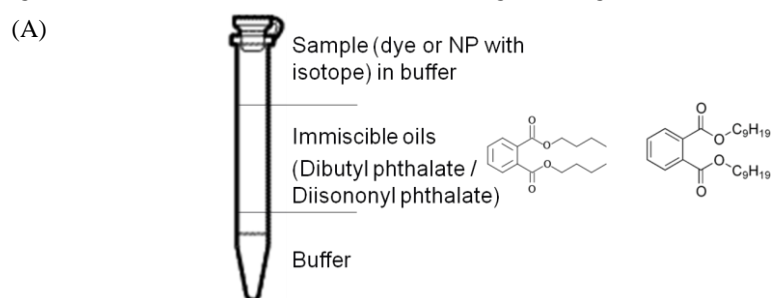
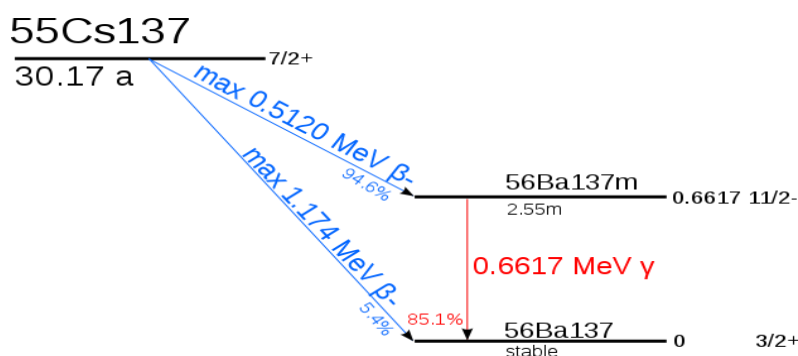


Figure 4-4 – (A), Cartoon of centrifugation assay which used an aqueous : oil : aqueous gradient to separate bound and unbound analyte from the NPs. Increasing ratios of oils (dinonyl phthalate to dibutyl phthalate) with a sample dye added. (B) After 1 min centrifugation at 13,000 RPM, an 80  $\mu$ l : 20  $\mu$ l ratio of dinonyl phthalate to dibutyl phthalate was found to be the optimum condition.

#### 4.10.6 Gamma radiation of $^{137}\text{Cs}^+$

Samples were typically counted for 30 min per tube. A counting profile used two windows defined as region A: 15-50 keV, corresponding to the X-ray peak that occurs as a 30 keV emission, the Ba K-alpha peak, and region B: 51-1000 keV, corresponding to the gamma higher energy emission at 600 keV (Figure 4-5). 95 % of  $^{137}\text{Cs}^+$  decays to  $^{137\text{m}}\text{Ba}$ , the gamma emitter, the other 5 % decaying to  $^{137}\text{Ba}$ , the stable isotope.

(A)



(B)

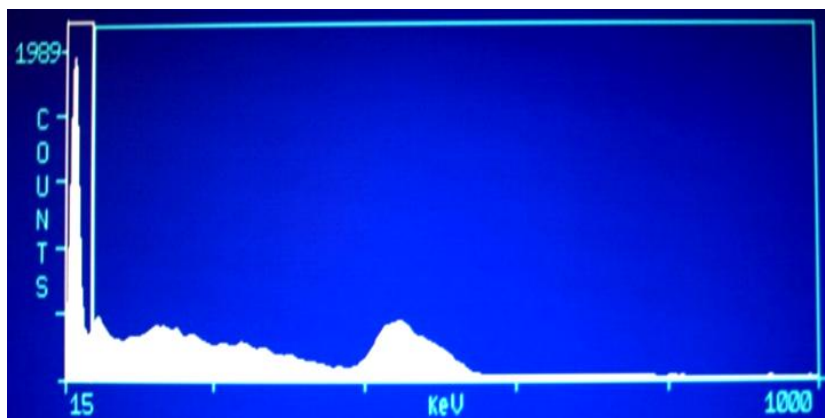


Figure 4-5 – (A) Theoretical and (B) a screenshot of the experimentally observed emission peaks as  $^{137}\text{Cs}$  decays either to  $^{137\text{m}}\text{Ba}$ , then  $^{137}\text{Ba}$  emitting a  $\gamma$  emission, or directly to  $^{137}\text{Ba}$  via  $\beta$  emission. The 30 keV emissions (boxed peak) was used to identify  $^{137}\text{Cs}$  decay.

#### 4.10.7 Beta counting of $^{90}\text{Sr}^{2+}$

$^{90}\text{Sr}^{2+}$  decays via beta emission. As a result beta counting was used to quantify the amounts of  $^{90}\text{Sr}^{2+}$ . Figure 4-6 shows the possible  $^{90}\text{Sr}^{2+}$  decay emissions. While 3 beta emissions are possible, experimentally one main peak <18 keV corresponding to the low level  $^{90}\text{Sr}^{2+}$  beta emissions was detected and used for quantification. Counting windows defined were A: 0-18.6 keV, B: 18.6-200 keV, C: 200-2000 keV).

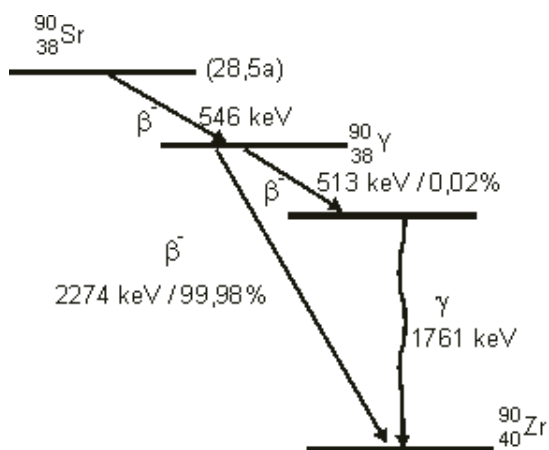


Figure 4-6 – Theoretical decay emission routes for  $^{90}\text{Sr}^{2+}$  via a high energy beta emission decaying to  $^{90}\text{Y}$ , then a further high energy beta emission, or a further low energy beta and gamma emission to the stable form  $^{90}\text{Zr}$ .

### 4.11 Methods

#### 4.11.1 Direct nucleation of silica nanoparticles

A method based on Achatz [194] combined with a modified Stober method [186] for a one step simultaneous growth and functionalisation of silica cores was used. In a typical experiment a functionalised silane e.g. aminosilane (21.4 mg, 0.12 mM) was added to 0.4 ml anhydrous dispersant (EtOH, MeOH, acetone or DMF) containing 200  $\mu\text{l}$  28 % ammonium hydroxide. Separately prepared TEOS (0.476 ml, 2 mM) in 50 ml of the same solvent was hydrolysed in 28% (w/v) ammonium hydroxide solution (1.76 ml). 1 ml of aminosilane solution was added to the TEOS solution, and reacted for 4 h at a controlled temperature ( $\pm$

0.5 °C). Silica nanoparticles were collected by centrifugation at 3,600 RPM or recovered with a 30 kD cut off centrifugal filter. Particles were washed in ethanol twice and then in 5% (v/v) ammonium hydroxide before storage in this solution.

#### **4.11.2 Prehydrolysis nucleation of silica nanoparticles**

A method used recently by Lee [185] used prehydrolysis of silane components and functional monomers to significantly reduce particle size distribution. This was by minimising rapid hydrolysis which results in rapid localised pH changes. If this occurs, localised environmental pH changes result in multiple nucleation sites and uncontrolled growth. A typical protocol used two types of ethanol solutions with identical volumes (25 ml), denoted as solution I and solution II, which were prepared separately. Solution I consisted of NH<sub>4</sub>OH (1.0 M NH<sub>3</sub>), and H<sub>2</sub>O. Solution II contained 2.216 ml TEOS (0.4 M) and any further by e.g. FITC or modified ferrocene. These solutions were mixed together either by diffusion or using a shaker for 3 h. After the reaction, the samples were centrifuged at 3,600 RPM for 10 min to collect the silica particles. The collected particles were washed with ethanol by centrifugation and decantation several times in order to remove unreacted components.

#### **4.11.3 Fabrication of mercapto-and sulphonate- silica particles**

A 50 ml batch of silica core particles was prepared by the prehydrolysis method. 100 µl of mercaptosilane was added and reacted for a further 2 h, without stirring. Purification was as previously described. Mercaptoparticles showed the narrowest Gaussian size distribution and were the best for controlled growth. Unless otherwise stated other functionalities were produced in this method.

Sulfonate particles were then prepared using a 2 stage oxidation of mercapto-silica particles. Mercapto-silica particles were dried under vacuum ( $< 10^{-2}$  bar) overnight then redispersed in 14 ml 35 % (v/v) H<sub>2</sub>O<sub>2</sub> plus 50 ml methanol, stirred for 24 h. These were then washed and resuspended in 0.1 M H<sub>2</sub>SO<sub>4</sub> and stirred for a further 4 h before another H<sub>2</sub>O wash and resuspension.

##### **4.11.3.1 Surface quantification of thiols on mercaptoparticles**

Ellman's reagent was used to quantify the surface density of available thiols on mercapto particles. For this a 1 ml 0.5 M mercapto silane stock (93 µl to 907 µl H<sub>2</sub>O) was used. Of this stock 2.05, 0.64, 1.23, 0.82, 0.41 µl was added to reaction buffer (Tris HCl pH 8) to

make a total assay volume of 205  $\mu\text{l}$  (working concentrations 1 to 5 mM) concentrations a 41 times dilution. 5  $\mu\text{l}$  of samples (known or nanoparticles) was added, incubated for 5 minutes and the absorbance of the generated NTB<sup>2-</sup> at 412 nm recorded. Unlike the problems observed with amine dyes (which were unable to generate a linear response on amine particles), a coloured product is only generated upon reaction with free sulfhydryls and doesn't require subsequent purification.

#### **4.11.4 EDTA silica particles**

EDTA coated particles were prepared as 4.11.3 except a 60 % (v/v) solution was needed to hydrolyse the EDTA silane. Control over temperature and silane ratios was needed to inhibit uncontrollable polymerisation and hydrogel formation.

#### **4.11.5 Dye core particles.**

Fluorescent dye core particles were made as an indicator of successful nanoparticle growth before particles could be sized and confirmed via PCS. This was performed by reacting the dye fluorescein isothiocyanate (FITC), whose isothiocyanate ( $-\text{N}=\text{C}=\text{S}$ ) was reacted with amine functionalised particles. The excitation and emission spectrum peak wavelengths for the tethered fluorescein dye were approximately 495 nm and 521 nm. Normally fluorescein hydrolysed and photo bleached within a few days. However, a modification step that coated the FITC silica particles with a further TEOS or TMOS, created a protective outer silica layer protecting the dye molecules from aqueous contact. Particles stored in ambient light were still functional months later.

A summary of the different silica functionalised particles synthesised is shown in Figure 4-7.

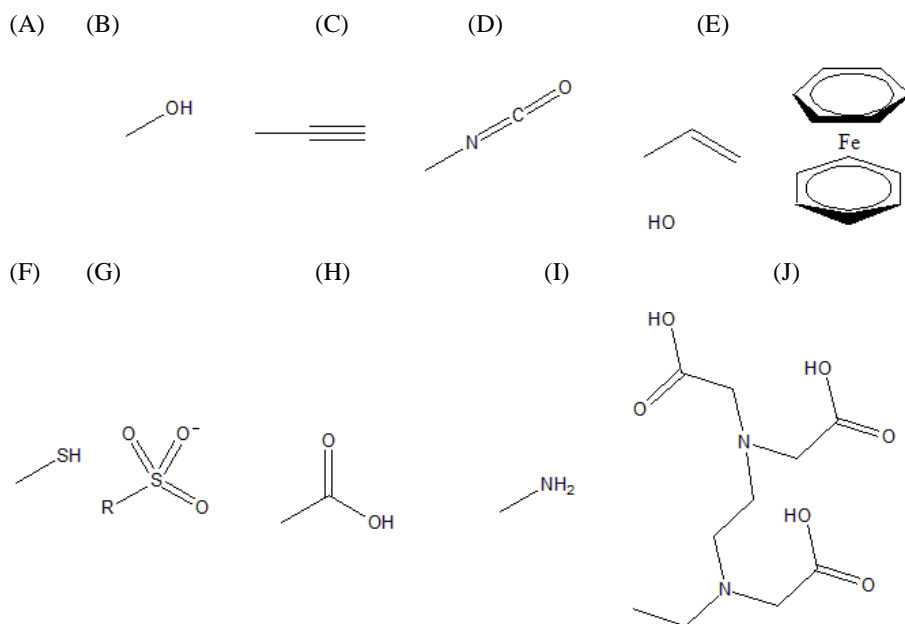


Figure 4-7 - Summary of the functional groups on modified silica particles. Basic hydroxyl groups (A) were modified to (B) alkyne, (C) isocyanate, (D) methacrylate, (E) ferrocene, (F) mercapto, (G) sulfonate, (H) carboxylic acid, (I) amine or (J) EDTA functionality.

#### 4.11.6 Nanoparticle and scintillant seeded agarose gels

In order to utilise the chelators functionalised NP for  $^{90}\text{Sr}^{2+}$  and  $^{137}\text{Cs}^+$  capture, for ease of use they had to be immobilised in some way. Agarose gels which are relatively porous are hydrophilic, and were investigated for this purpose.

Nanoparticles were dried overnight and then ground with mortar and pestle. These were rapidly dispersed in agarose gels that were prepared at 1 % (w/v) above 60 °C. One millilitre or liquid gel was added to a glass scintillation vial and rotated on a roller-mixer for 30 min. As the temperature cooled below 60 °C the gel solidified creating an NP seeded film.

To seed with scintillant, organic dispersants were needed that were able to solubilise these highly hydrophobic molecules. However, agarose proved to be soluble in the mildest organic solvents including DMSO, acetone and methanol. As a result, most scintillants were dispersed in glacial acetic acid rather than pure organic solvent. Glacial acetic acid spiked with 10% (v/v) methanol or DMSO increased solubility without removing the agarose layer.

This was performed by incubating the coated vials on rollers first in 1.5 ml glacial acetic acid for 30 min to remove adsorbed water and increase gel hydrophobicity. 0.5ml of saturated scintillant for 45 mins and finally 5 ml of H<sub>2</sub>O was used to physisorb surface bound scintillant while flocculating free bulk scintillant.

#### 4.11.7 Commercial functionalised resins

To compare binding efficiencies, a number of commercial cation binding resins were obtained (Table 4-3), and used without without further modification, other than a protonation wash prior to incubation with radioisotope.

Table 4-3 - Commercial resins compared.

Resin	Type	Matrix	Functionality
DOWEX MARATHON C	Strong Cation Acid	Styrene-DVB, Gel	Sulfonic acid
DOWEX HCR-W2	Strong Cation Acid	Styrene-DVB, Gel	Sulfonic acid
DOWEX MAC-3 LB	Weak Cation Acid	Polyacrylic, Macroporous	Carboxylic acid
AMBERLITE™ IRC748	Weak Cation Acid	Macroreticular	Iminodiacetic
BIORAD Ag50W	Strong cation	Styrene	Sulfonic acid
BIORAD Biobeads	Neutral	Polystyrene	Neutral
AMBERLITE™ IRC758	Weak Cation Acid	Macroreticular	Iminodiacetic

## 4.12 Results and Discussion

### 4.12.1 Synthesis of silica particles

#### 4.12.1.1 Particles and mass yield

TEMOS in ethanol nucleated nanoparticles were grown for set periods of time with physical agitation before halting the reaction via centrifugation at 3600 RPM and a minimum of two solvent exchanges to remove unreacted components. The resulting masses of particles was dried overnight at 120 °C and weighed. The resulting masses of NP generated as a function of time are summarised in Table 4-4. Up to 5 h the particles nucleated and grew to the optimum yield.

Although results were somewhat variable at 8 h due to surface nucleation and vessel coating, 24 h would generate the most mass. At this stage, bulk aggregates rather than particles were formed, and as a result 5 h was deemed the maximum nucleation time.

Table 4-4 – Dried mass yield of 40 °C nucleated functionalised silica, which resulted in particles, surface coatings and bulk aggregates. The average mass of particles in mg is given (n =3).

Functionality	Nucleation time / h			
	2	5	8	12
Amine	45.1	148.3	52.9	184.5
EDTA	14.3	120.9	17.0	90.2
Methacrylate	52.3	84.2	37.7	71.0
Sulfonic acid	6.6	156.8	93.6	114.6

A reaction continued beyond this period showed a second nucleation and growth phase either as surface coating of the reaction vessel became unfavourable, or as the number of nucleation sites became too large and silica surface coatings desorbed into solution. By this point bulk aggregates rather than particles were observed, of the size scale of millimetres to centimetres.

#### 4.12.1.2 The critical silane concentration limit

All self assembling molecules have an aggregation activation concentration. Below this value monomers are preferred. At this concentration and above the entropic loss is counteracted by an enthalpic gain. Thus, increasing nanoparticle yield must be balanced with the constraints of growth. While a number of factors discussed increased nanoparticle size

polydispersity, it was observed that keeping silane concentrations below 0.2 M significantly improved particle size distributions. Beyond this concentration, broader size ranges and multiple bi- and tri- Gaussian size distributions were observed or bulk aggregation occurred.

#### 4.12.1.3 Effects of solvent and purification regime

Temperature control within  $\pm 0.5$  °C caused significant improvement in particle growth uniformity. A range of elevated temperatures were used to attempt to increase yields over shorter production times. Beyond 60 °C, slight surface layer coatings were produced, while at 85 °C silanes rapidly come out of the liquid phase and generated bulk silanised layers. This occurred even in resistant polypropylene vessels where liquid-particle nucleation was found to be entropically more favourable, however, for the narrowest size distribution, it was found that the best method was to use low water ratios grown at room temperature over many hours. Slow nucleation via Brownian motion is preferable to accelerated aggregation from elevated heat. Figure 4-8 A shows room temperature based reaction of 5 % (v/v) TEMOS with 100  $\mu$ l aminosilane, 3 % (v/v) dH<sub>2</sub>O in ethanol, pH 5. For the first 8 h of reaction a 40 nm increase in average particle size was observed. Beyond 8 h, the particle size increased dramatically as the size distribution indicates. Beyond 24 h particle sizes reached the micron range.

The effect of nucleation solvent also played an important role in particle growth. Silanes are initially insoluble in water until they diffuse, contact a water molecule and hydrolyse. Therefore the rate of phase transition is influenced by silane-solvent interactions (polarity, hydrogen bonding, Van der Waals interactions) and these have an important role on particle growth. Figure 4-8 B shows reactions based on 5 % (v/v) silane in a range of solvents, including methanol, ethanol, DMS, DMSO, acetone, and pure water, with 3 % (v/v) H<sub>2</sub>O added. The average sizes for particles grown in these solvents were; DMSO (CH<sub>3</sub>-SO)-CH<sub>3</sub>,  $\delta$ P 18.4) one of the most polar aprotic solvents, showed the most rapid bulk aggregation, and as a result very variable particle sizes (8933.0  $\pm$  17596.6 nm 5518.2  $\pm$  9658.7 nm).

Protic solvents, methanol (CH<sub>3</sub>-OH) averaged 104.152  $\pm$  28.51 nm and 17.32  $\pm$  4.59 nm. These were the smallest particles with the narrowest size distribution. Water (H-O-H), averaged 202.82  $\pm$  11.04 nm and 132.46  $\pm$  1.88 nm. The reason for narrower size distributions is due to the ease of rapid transition from insoluble to soluble phases and a slow growth process. Acetone (CH<sub>3</sub>-CO)-CH<sub>3</sub>, whilst having a polarity rating between methanol

and water ( $\delta P$  for acetone is 10.4 vs 8.8 for methanol and 12.3 for water [195]) surprisingly, resulted in significantly larger and more polydisperse particles ( $3521.2 \pm 296.9$  nm and  $4831 \pm 2020.7$ ). Rapid nucleation and similar growth to particles grown in DMSO was observed suggesting that the highly polar carbonyl oxygens were driving aggregation.

As these data are at the upper limits of the sizing machine range they must however be treated with caution. The reason for the bulk aggregates may have been increased aggregation at the silane-solvent interface, resulting in a more rapid silane-silane interaction, and silanol condensation rather than solvent dispersion.

Although DMS ( $C_2H_6S$ ) also caused particle growth, it was difficult to work with, being an aggressive solvent, and its use was abandoned.

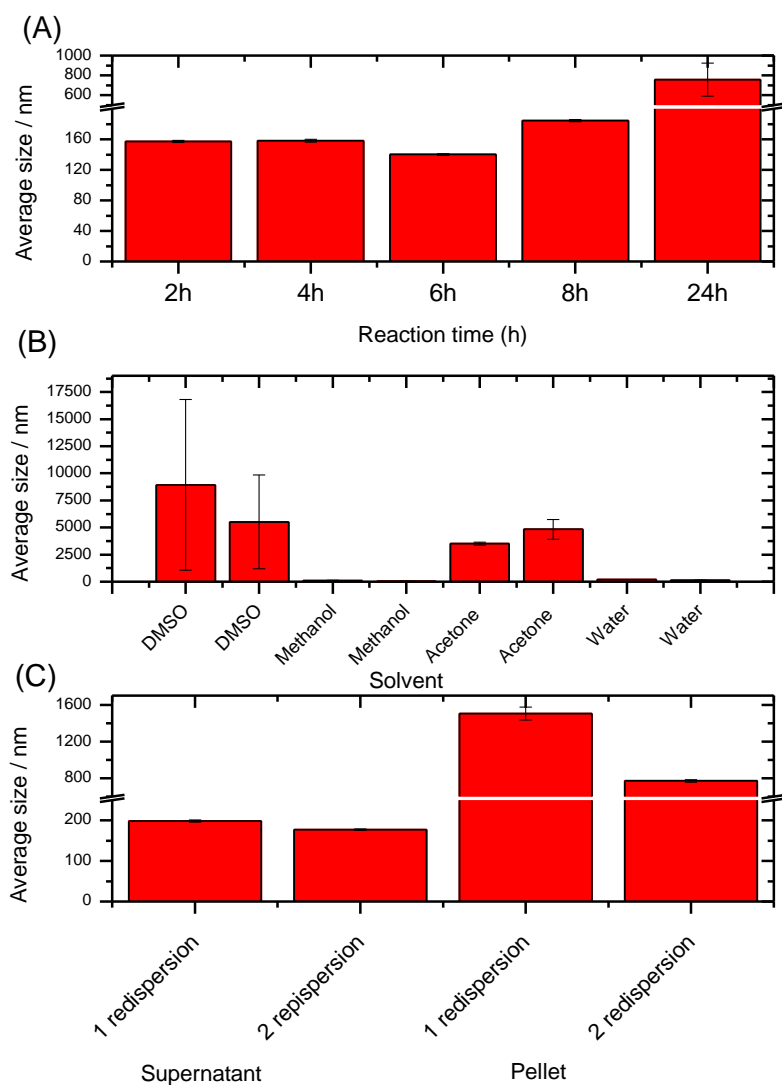


Figure 4-8 - Silica nanoparticle nucleation as a function of parameter. The reaction solution contained 5 % (v/v) TEMOS, 100  $\mu$ l APTS, 3 % (v/v) H<sub>2</sub>O in ethanol. (A), Improved narrower size distribution of amino nanoparticle growth was shown using a controlled temperature Huber water bath at 20 °C  $\pm$  0.5 °C. (n = 3). (B), Dependence of silica nucleation on dispersion solvent (2 independent batches, n = 3 in each). (C), Effects on stability of nanoparticle from purification and solvent redispersion (n = 3).

To halt particle growth, solutions were diluted in a 1:4 ratio into fresh solvent, centrifuged down and the particle mass in pellet and supernatant compared, after drying down, in size (Figure 4-8 C). Particle suspensions with only one wash showed significant aggregation. This was reduced if two solvent washes were used, which significantly reduced the size of particles found in the pellet. Particles that remained in the supernatant after centrifugation, too light to sediment, appeared stable for several days and did not undergo further nucleation if used rapidly. As a result, to ensure minimal further aggregation typically 3 decanting and redispersion steps were used to purify particles before storage for longer periods.

#### **4.12.1.4 Effect of pH on silica nucleation**

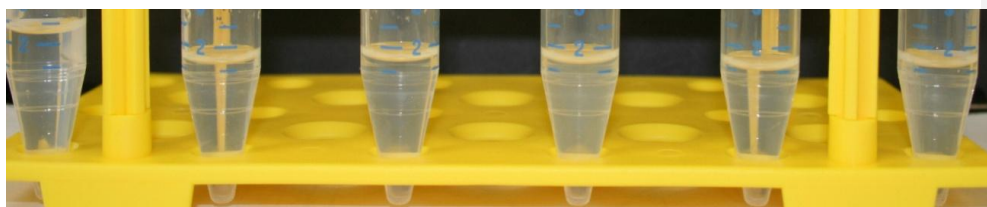
Initial experiments were particles nucleated at pH 7. However problems occurred with the sulfonate and EDTA silanes due to phase separations between silane and solvent. Figure 4-9 shows that a change in pH while maintaining all other factors constant significantly altered the amount and form of silica particles nucleated. At highly alkaline pH (> pH 9) bulk aggregation and sedimentation occurred, whilst between pH 4 and 7 a white translucent solution was nucleated showing particle formation. Below pH 4 opacity, was minimal, indicating little nucleation.

When silica particles were functionalised with EDTA (Figure 4-10) at highly alkaline pH (> pH 9) large white aggregates sedimented. Beyond pH 10 the bulk solution flocculated with large aggregates settling in solution. Similarly to the mercapto silica particles, at increasing acidity the rate of hydrolysis and nucleation is reduced, but between pH 3 and 8 a stable silica sol was formed without bulk aggregation.

Overall this comparison shows that although the optimum growth conditions varied with the functionalised silanes used, somewhere between pH 3 and 8 was generally suitable for all. Generally, nucleation was enhanced at the higher end of the pH range.

Further treatment to cause silanol stabilisation ('calcination') could be achieved by 15 min firing at 110 °C [196].

(A) pH 1            2            3            4            7            8



(B) pH 9                    10                    11                    12

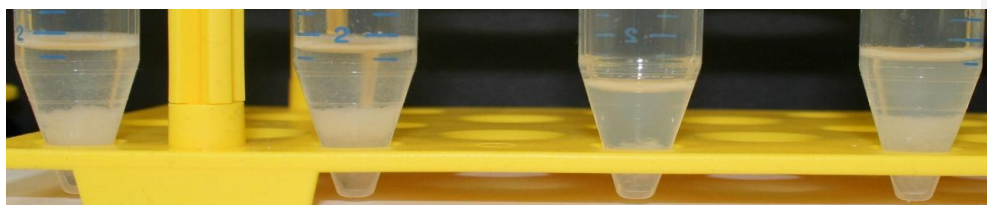
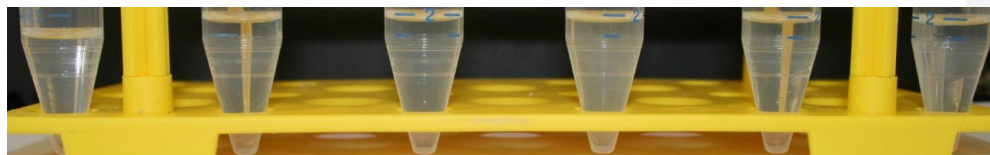


Figure 4-9 - Image of mercapto silica nanoparticles, 20 h nucleation of TEOS at room temperature on a Stuart gyro-shaker, speed 8, as a function of pH.

(A) pH 1            2            3            4            7            8



(B) pH 9                    10                    11                    12

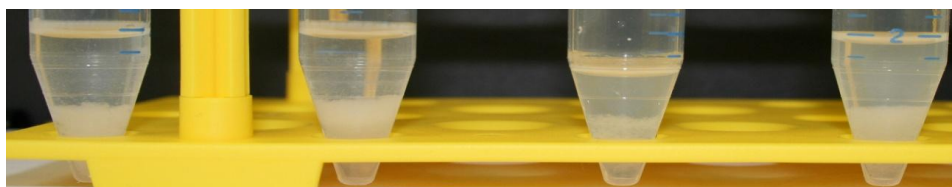


Figure 4-10 - Image of EDTA silica particles nucleated at different pH. Particles were grown from a 20 h nucleation of TEOS at room temperature on a Stuart gyro-shaker speed 8.

#### 4.12.2 EDTA silane hydrolysis and condensation

The silane 3-[(trimethoxysilyl)propyl]ethylenediaminetriacetic acid being an alkoxy silane was expected to behave similarly to the other functionalised silanes used. However the compound was supplied as 40 % (w/v) in water, which are conditions under which most alkoxy silanes would have completely hydrolysed and bulk polymerised. A similar protocol to the one reported in this thesis [197] to functionalise carbon-silica particles with EDTA-silane proposed direct hydrolysis and condensation, for use as a MALDI-mass spectrometry reference, as does a method to silanise graphene with EDTA functionality and a redox species [198]-[199]. Under acidic conditions, Tien [199] suggested that the hydrolysis rate of TEOS and EDTA silane is decreased by substituents which increase steric crowding around the central silicon atom. Electron-donating substituents, which help counteract the increasing positive charges and protonation, should increase the hydrolysis rate but to a lesser extent, because the silicon acquires little charge in the transition state.

Extensive optimisation was needed because of the different rates of hydrolysis. Phase separation and sedimentation occurred between EDTA-silane and TEMOS, most likely due to localised pH shifts which occurred if the EDTA-component was not prehydrolysed and then added to prenucleated silica cores. A 45 % (v/v) of H<sub>2</sub>O to EDTA silane at pH 5 resulted in a significantly slower hydrolysis rate compared to other silanes, but ensured activation with minimal self condensation before addition to pre-grown silica cores. This resulted in EDTA functionalised silica particles with minimal aggregation.

#### 4.12.3 Synthesis of functionalised nanoparticles using a two step prehydrolysed silane method

Particles that were grown from separate pre-hydrolysed solutions; one ammonia solution which contained functional monomer, and a second with hydrolysed TEOS that were then combined created distinctly different particles compared to direct mixing and Stober method nucleation. Particles produced via this method were significantly smaller and more consistently uniform, with a narrower size distribution. Why should prehydrolysing the functional silane that condenses onto the surface of prenucleated silica cores so radically alter the observed size distribution? If a single molecular layer of functional silane is deposited, the size increase would be on the scale of Å. A single molecule deep layer is unlikely, and a functionalised mesh layer formed, accounting for this increase in particle diameter.

Simultaneous nucleation and hydrolysis of the silica cores and functional monomers causes significant localised changes in pH and solvent polarity. It is also important to note that each functional monomer hydrolyses at a different rate, directly affecting the core growth rate and stability. Early experiments that used between 0.1 – 1 : 1 molar ratio of functional monomer to TEOS indeed showed significant aggregation and sedimentation. Simply adding excess functional monomer which can be removed by centrifugation or decanting is not an option, as second nucleation sites and polydisperse particles form with excess silane. Generally, particles grown with the two step silane prehydrolysis method using a 0.5 % (v/v) functional monomer to TEOS ratio created more stable particles of white translucent sol suspension.

Adding an excess of functional monomer frequently resulted in continual unstoppable nucleation and formed bulk solid gels. EDTA silane in particular was difficult to incorporate onto particles. Initially, solutions formed integrated networks of polymers or solid gels, possibly due to inter carboxylic interactions between adjacent particles similar to the effect of bridging flocculation.

#### **4.12.4 Effects of varying solution component on nanoparticle growth**

The effect of varying silane, water and ammonia were systematically examined by keeping any two of these constant whilst varying the third.

Figure 4-11 A shows that ammonia, the nucleation initiator, did not significantly alter the size distribution of nanoparticles observed, with particles averaging between  $353.6 \pm 227$  nm and  $559.88 \pm 299$  nm. However, beyond 6 % H<sub>2</sub>O (Figure 4-11 B) the polydispersity of particles increased significantly and particle size increased beyond 4  $\mu$ m, with a standard error of similar magnitude presumed due to the increased rate of hydrolysis. Up to 8 % (v/v) silane, particle sizes ranged up to around 8 were seen. However, beyond this, bulk flocculation occurred (Figure 4-11 C). From these experiments, optimum conditions were found to be room temperature nucleation, using 5 % (v/v) H<sub>2</sub>O, no more than 2 % (v/v) silane, a constant 2 % (v/v) ammonium hydroxide, nucleated in ethanol at pH 5.

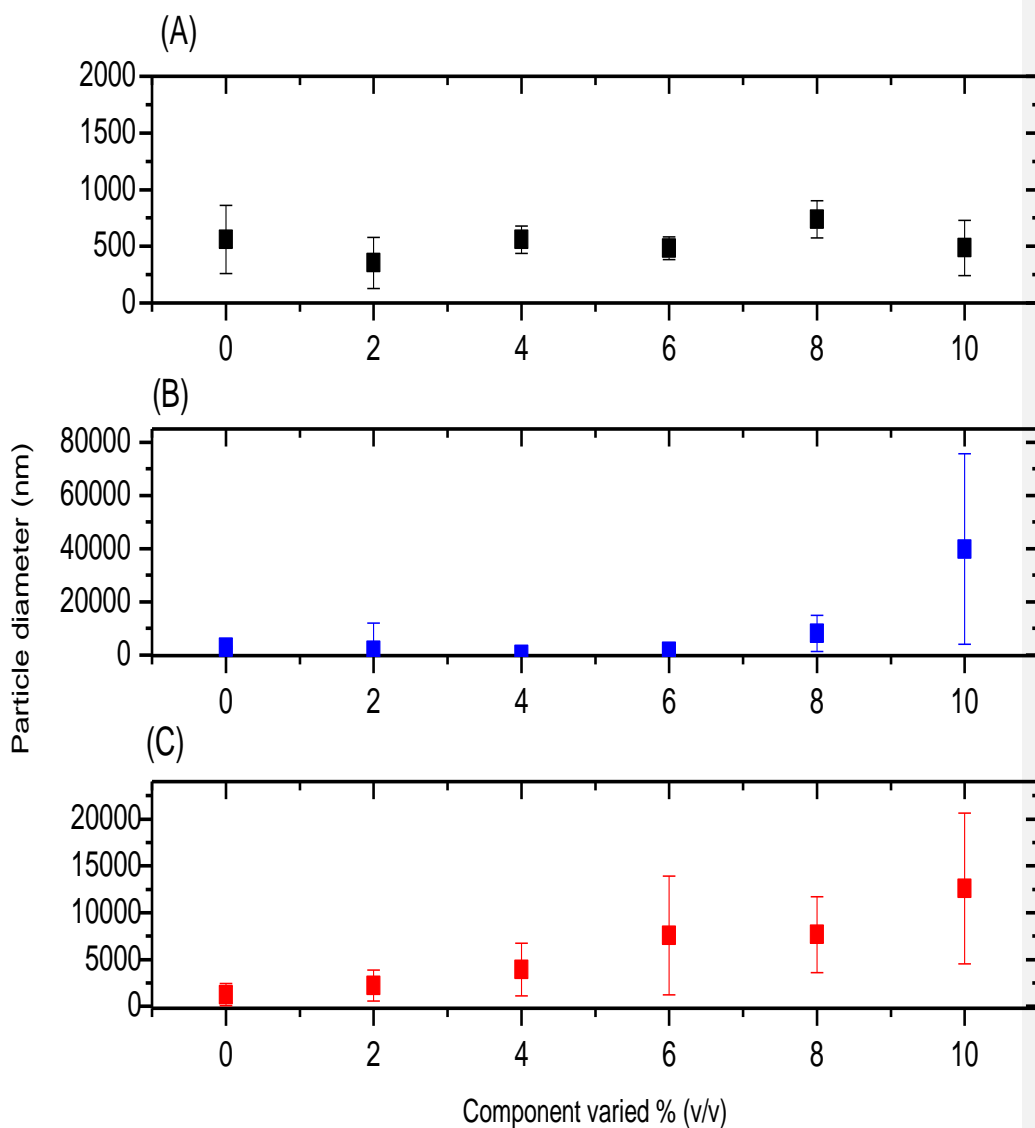


Figure 4-11 – Nanoparticle growth at RT as a function of solution components. Components varied were (A), ammonia; (B), water; and (C), amino silane varied as a % (v/v) ratio of the total volume. (D) shows as overlay comparison of the 3 variables. Constant parameters used were 5 % (v/v) ammonia, 5 % (v/v) water or 2 % (v/v) silane. ( $n=3 \pm S.D$ ).

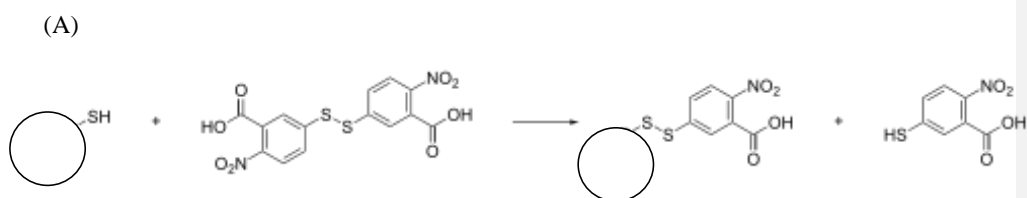
## 4.13 Particle characterisation

### 4.13.1 Sulfhydryl quantification with Ellman's reagent

Ellman's reagent was used to quantify the surface density of available thiols on mercapto particles. Absorbance of known standards were used to plot a calibration curve (Figure 4-12). The reaction scheme is shown in Figure 4-12A; reaction of DNTB releases the yellow 2-nitro-5-thiobenzoate (NTB<sup>-</sup>) anion, which adsorbs strongly at 412 nm. (B) shows calibration against the standard 3-mercapto propyltrimethoxy silane. Using this procedure, silica particles formed using 3-mercapto propyltrimethoxy silane were used to calculate 11 – 15 mM thiol groups per g of particle mass (Table 4-4).

Table 4-4 shows the accessible mercapto groups per mass of nanoparticle. This may include internal mercapto groups as organic silica is porous. The optimised prehydrolysis method yielded 11.19 to 14.74 mM -SH g<sup>-1</sup> NP.

Sample	412nm	Corrected A@412nm	Calibration estimate mercapto (mM -SH)	Nanoparticle mass / g	mM -SH g <sup>-1</sup> NP
1	0.186	0.1802	0.260	0.02323	11.19
2	0.355	0.3492	0.402	0.02723	14.74



(B)

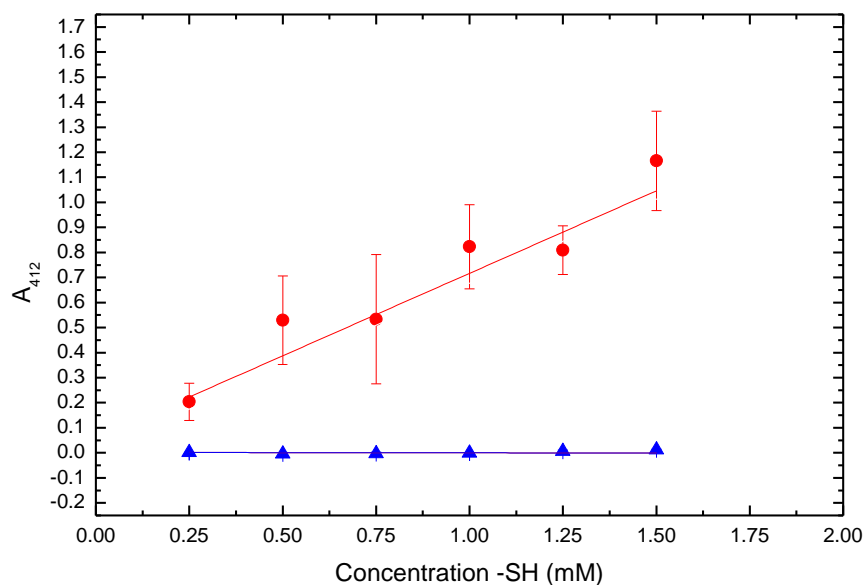


Figure 4-12 - (A), Available thiols on the nanoparticle surface react with and cleave the DNTB disulfide bond to give 2-nitro-5-thiobenzoate (NTB<sup>-</sup>), which ionizes to the NTB<sup>2-</sup> dianion, a yellow product that adsorbs at 412 nm in a 1:1 stoichiometry reaction. (B), Calibration curve from UV- visible spectroscopy for thiol quantification on mercapto silica particles using Ellman's reagent. Symbols:  $\blacktriangle$ , Control of unfunctionalised silica particles showing no reaction to Ellman's reagent;  $\bullet$ , calibration curve from dilutions of known mercaptosilane concentrations used to estimate the surface thiols present on mercapto nanoparticles.

#### **4.13.2 FEG TEM and EDX surface analysis of functionalised silica nanoparticles**

Core silica TEOS particles, nucleated using the optimised prehydrolysis method, were found to have narrower Gaussian size distributions than the one step Stober method. Photon correlation spectroscopy (PCS) sizing of particles (n=5), (Figure 4-13 A) showed an average particle size of 127.3 nm. EDX elemental analysis (Figure 4-13 B) showed significant amount of Si and O as expected. Cu peaks seen were a result of the sample support stubs. Similar size ranges were visually confirmed by sizing point regions of particle dispersions on dried samples using TEM. Figure 4-13 C and 4-13 D shows spherical aggregates of crystalline silica.

Further modification with a functional silane (EDTA) was then performed to compare any significant changes in particle morphology and size.

PCS sizing (Figure 4-14 A) showed an average of 35 nm, comparable to visual TEM sizes (Figure 4-14 C and D), with EDX analysis showing the presence of Si, O and Cu (Figure 4-14 B).

While particle size did not significantly increase under controlled prehydrolysis and deposition of the functional monomer, the surface morphology clearly changed, as seen in Figure 4-14 C and D. TEM analysis confirmed particles were stable over two months, as little aggregation of EDTA particles that were made using the prehydrolysis method was observed.

However, the EDTA particles appeared much more electron dense (Figure 4-14 C and D). This was most likely due to chelation of  $\text{Cu}^{2+}$  from the copper support stubs by the EDTA groups.

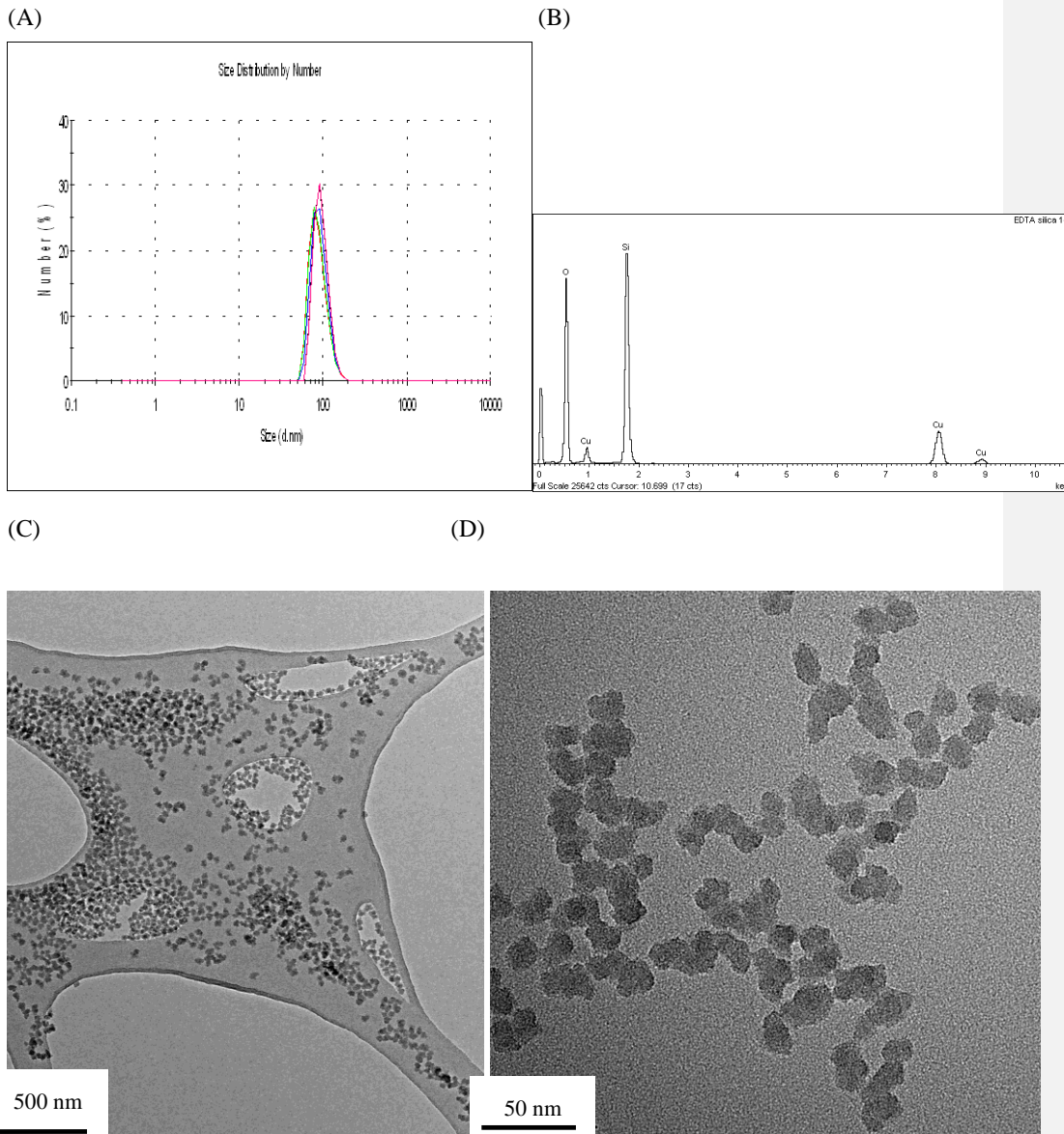


Figure 4-13 Figure of bare TEOS silica particles. (A) Photon correlation spectroscopy sizing ( $n = 5$ ), average size = 127.3 nm, S.E.M = 0.171 (B) EDX elemental analysis shows silicon, oxygen and copper (C) and (D) TEM images of dried particles on a carbon substrate.

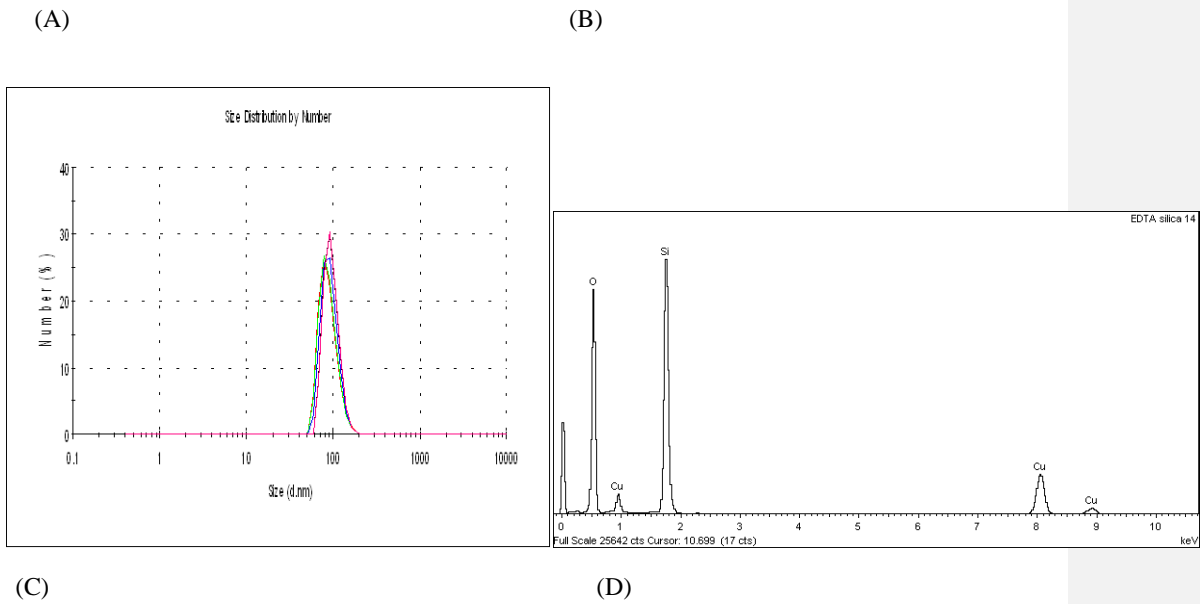


Figure 4-14 – Figure of EDTA functionalised particles, prehydrolysis method, 4 h RT nucleation, 2 centrifugation steps. Photon correlation spectroscopy sizing of 1 week old particles ( $n = 5$ ) = 109.2 nm, S.E.M = 0.286. TEM images of 5 week old particles. EDX elemental analysis shows silicon, oxygen and copper.

### 4.13.3 Confirmation of nanoparticle functionalisation by FTIR

Basic particle functionality was confirmed by Fourier transform infrared spectroscopy (FTIR) by first analysing the bare silica particle spectra and identifying adsorption peaks and then identifying new peaks after functionalisation.

Particles dried onto support substrates or prepared in anhydrous solvent dispersions yielded poor spectra masked by water adsorption peaks. As a result all particle analysis was performed using a solid KBr support matrix. Figures 4-15 and 4-16 show absorption peaks observed using FTIR. The spectra were used to identify successful functionalities condensed onto the TEOS particles. In addition attenuated total reflectance Fourier transform infrared spectroscopy (ATR-FTIR) was used for finer resolution in the fingerprint region (700–500  $\text{cm}^{-1}$ ). Scans used a range of 4000 to 750  $\text{cm}^{-1}$ , a resolution of 1 $\text{cm}^{-1}$  and with 30 spectra averaged. Summaries of spectra specific peaks to the desired functionalities are shown in Tables 4-4 to 4-9.

TEOS unfunctionalised core particles were analysed as the base model. General silica peaks observed corresponded to H-bond hydrolysis (Si-OH, CO-OH and H<sub>2</sub>O) at 3390  $\text{cm}^{-1}$ , weaker non-hydrogen bonded silanols appeared at 3738  $\text{cm}^{-1}$  [200]. Bulk water absorbance was observed at 3452  $\text{cm}^{-1}$  if samples were improperly dried. General silica peaks, single silanols and vicinal silanols occurred at 3747  $\text{cm}^{-1}$  and 3660  $\text{cm}^{-1}$ , and a general broad peak between 3000–4000  $\text{cm}^{-1}$  [201] were observed in all particles. The recurring peak in all scans around 1590  $\text{cm}^{-1}$  and 1410  $\text{cm}^{-1}$  is atmospheric CO<sub>2</sub> [199] and is commonly seen in most FTIR. Additional peaks in subsequent particles corresponded to successful functionalisation.

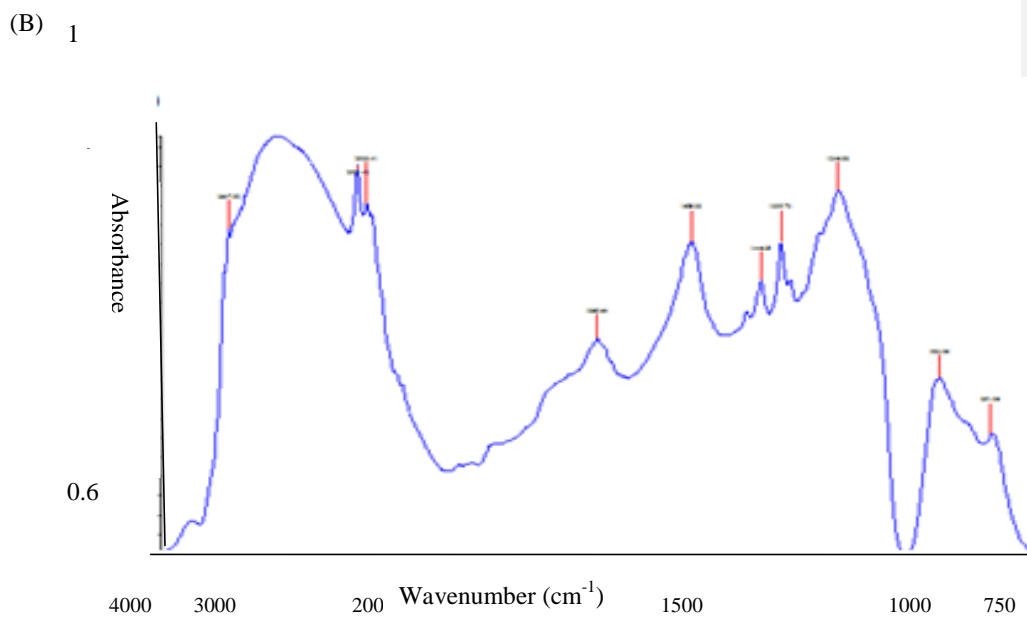
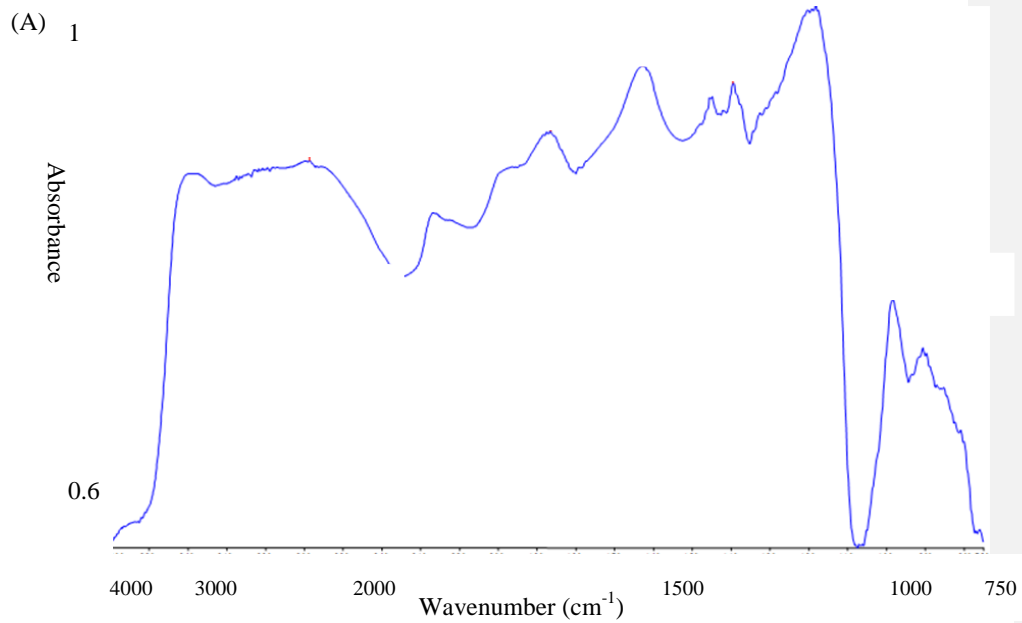


Figure 4-15 – FTIR spectra of functionalised nanoparticles dispersed in a KBr matrix. Particle functionalities were; (A), carboxylic acid; (B), EDTA, condensed onto TEOS particles.

Carboxylic acid (Figure 4-15 A) and EDTA particles (Figure 4-15 B) shared a peak at  $1724\text{ cm}^{-1}$  and a broader region  $2800 - 3000\text{ cm}^{-1}$  that corresponds to stretching of the acid C=O and  $\text{CH}_2$  arms respectively. C=O is also reported at  $1580\text{ cm}^{-1}$  which also corresponds to absorbed  $\text{H}_3\text{O}^+$  hydronium ions [202]. The  $1780\text{ cm}^{-1}$  peak can drift depending on the acid conjugate by around  $80\text{ cm}^{-1}$  as shown in butanoic acid spectra [202]. An overlap of EDTA and silanol peaks caused the broad absorbance observed;  $1634\text{ cm}^{-1}$  is again  $-\text{OH}$  vibration but also an indication of absorbed water on to the carboxyl. The  $1480\text{ cm}^{-1}$  and  $1395\text{ cm}^{-1}$  peaks correspond to  $-\text{COO}^-$  stretching. Tien [199] suggested peaks  $1332\text{ cm}^{-1}$  and  $712\text{ cm}^{-1}$  occurring on EDTA sol gel material corresponded to the EDTA silica molecule. The  $1330\text{ cm}^{-1}$  peak occurs in functionalised silica particles while the closest lower peak was seen at  $861\text{ cm}^{-1}$  ( $1395\text{ cm}^{-1}$  and  $906\text{ cm}^{-1}$  respectively in carboxylic acid particles). The EDTA  $2980\text{ cm}^{-1}$  and carboxylic acid  $2973\text{ cm}^{-1}$  peaks correspond to  $-\text{CH}_3$  stretching with an overlap at around  $2880\text{ cm}^{-1}$  with  $\text{CH}_2$  stretching. Smaller and just visible peaks between  $1500\text{ cm}^{-1}$  to  $1735\text{ cm}^{-1}$  ( $1266\text{ cm}^{-1}$ ,  $1395\text{ cm}^{-1}$ ,  $1409\text{ cm}^{-1}$ ) correspond to the chelator arm  $\text{N}(\text{CH}-\text{COOH})_2$  [203].

The first method of direct condensation using sulfonate trimethoxysilane to directly grow sulfonic acid particles failed, with spectra observed corresponding to those of the bare TEOS particles. This suggested the silane hadn't hydrolysed and condensed onto particles. Instead binding the sulfonic acid containing amino acid taurine, via its free amine side arm, to carboxylic acid particles was attempted and success confirmed by available spectra, where 20 of the 23 expected peaks observed between  $700$  to  $1600\text{ cm}^{-1}$  were present [204].

An alternative approach involving the two step oxidation of thiol particles to sulfonates (see section 4.11.13) also revealed new peaks that were not obtained in FTIR spectra from the starting mercapto particles.

The two step oxidation route to convert mercapto particles to sulfonic acid moieties showed new peaks corresponding to the sulfonic acid group not present in the mercapto particle spectra (Figure 4-16 A), which are summarised in Table 4-9.

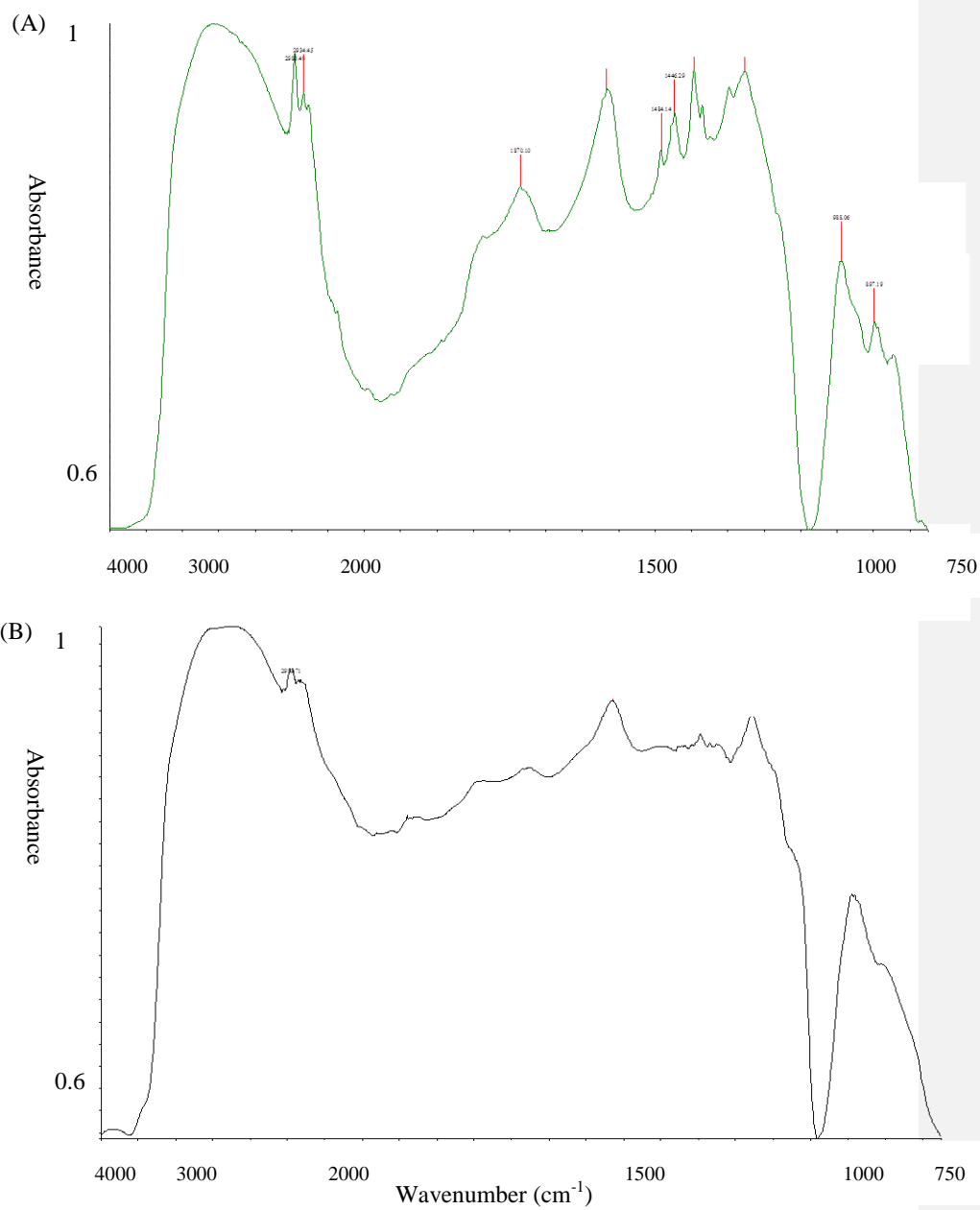


Figure 4-16 – FTIR spectra of functionalised nanoparticles dispersed in a KBr matrix. (A) mercapto and (B) amine groups condensed onto tetraethyl orthosilicate particles.

#### **4.13.4 Nanoparticles seeded with scintillant and embedded in agarose gels**

It would be advantageous to combine a solid scintillant onto the functionalised particles along with the chelator groups to allow direct use in scintillation counting. This would remove the need for large volumes of scintillation cocktail that would result in quantities of organic solvent and radioactive waste.

To do this, a known dried mass of particles, basic TEOS particles and EDTA, carboxylic acid, amine or mercapto functionality was dispersed in agarose along with a solid scintillant; POPOP, methyl styrene or Triton X-100. This was to create a solid state scintillation matrix that could both bind and convert analyte detection to a usable signal, thereby negating the need for scintillation fluid. These seeded matrixes were coated on glass vials or inside glass capillaries, a radioactive analyte flowed over the surfaces and the isotope bound quantified.

Of the 5 particles TEOS, EDTA, carboxylic acid, amine, with 3 scintillants, plus an agarose only control with and without scintillants, 24 conditions were used. Scintillation counts from 1 h flows of a 10 ml 20 kBq  $^{90}\text{Sr}^{2+}$  stock showed surprisingly poor binding; counts ranged from 0.6 to 3.4 % of the stock concentration. The counts were significantly less than for free nanoparticles and frequently the agarose gel only controls only controls showed higher counts (1.1 – 3.4 % of analyte bound). This suggested that with time the nanoparticles were desorbing and being flushed from the gel and capillary tubing and the signal detected was from a small amount of physisorbed radioisotope and scintillant that remained. Frequently the entire gel desorbed from the glass capillary and was lost as there was no covalent linkage between gel and surface. While this showed that solid scintillant surfaces have potential, the nanoparticles were not compatible with an agarose matrix. Thiol seeded gels were one exception, with physisorbed corrected counts bound between 8.5 - 9.2 % of the total radionuclide stock for POPOP and methyl styrene scintillant loaded samples.

#### **4.13.5 ATR-FTIR of bifunctional solid scintillant chelator particles**

Scintillant depositing during the particle growth phase was inconsistent because attachment of the scintillant to the TEOS particles was based on electrostatics. Because of this an alternative method of co-condensing the silane, trimethoxyphenylsilane with the chosen chelator groups was devised, to act as a close proximity scintillant for  $\beta$  emitter quantification. Bifunctional micro particles were created by the simultaneous deposition of 30 min prehydrolysed solutions of phenyl trimethoxyylsilane and a second functionality at varying ratios using the prehydrolysis method; see schematic Figure 4-17. In subsequent

ATR-FTIR spectra, bare silica particle spectra (Figure 4-18) are shown in black, silica trimethoxyphenylsilane in blue, and the bifunctional silica-scintillant-chelator particle spectra shown in red. Bracketed peaks correspond to broad regions published for functional groups regions, the unbracketed peaks are the corresponding peaks identified to fit these.

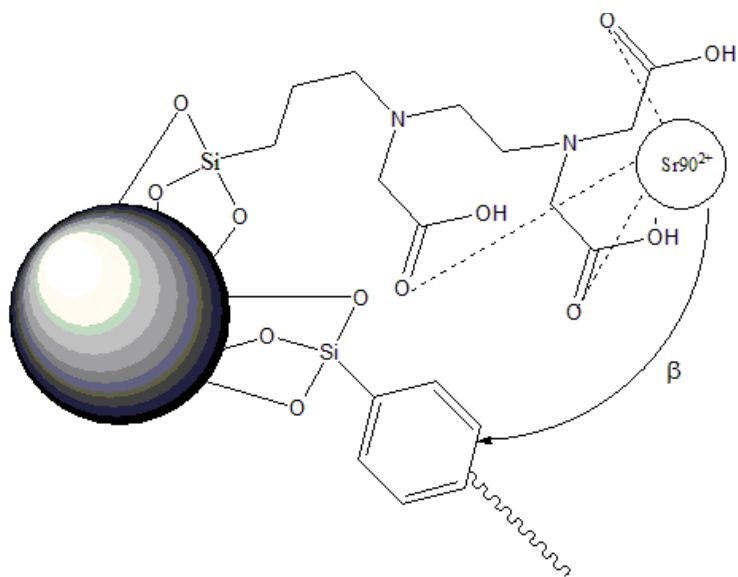


Figure 4-17 – Schematic of solid scintillant EDTA/phenyl functionalised chelator particles. Upon the EDTA arms chelating a  $^{90}\text{Sr}^{2+}$  ion, an emitted  $\beta$  particle excites phenyl groups in close proximity which emit a photon of light during de-excitation allowing scintillation counting without traditional scintillation cocktails.

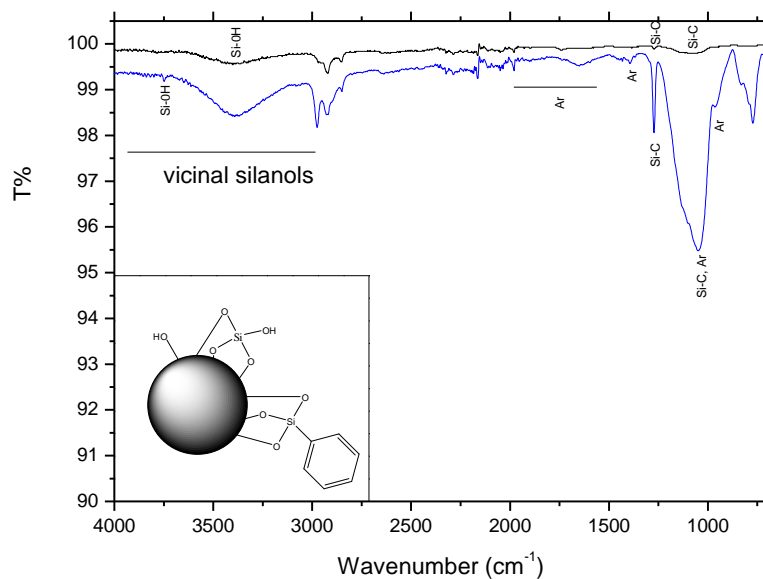


Figure 4-18 – ATR-FTIR transmission spectra of functionalised particles. Lines correspond to: (—) TEOS unfunctionalised particles, (—) TEOS particles with solid scintillant trimethoxyphenylsilane. Inset a schematic of particle structure shown in Figure 4-17.

Table 4-5 - ATR-FTIR summary for unfunctionalised TEOS silica particles, and general troughs common in all particles.

Wavenumber (cm <sup>-1</sup> )	Functional group	Reference
3390	Si-OH H <sub>2</sub> O	[200]
3738	Si-OH	[200]
3452	H <sub>2</sub> O	[200]
3000 – 4000 (3747 , 3660)	silanols, vicinal silanols	[201]
1590	CO <sub>2</sub>	[199]
1249	Si – C stretching	[205]
1108	Si – O stretching	[205]

Table 4-6 - ATR-FTIR summary for trimethyl(phenyl)silane functionalised TEOS silica particles, common to all bifunctional particle spectra.

Wavenumber (cm <sup>-1</sup> )	Functional group	Reference
1430	Ar,	[192]
1100	Ar, Si-C overlap	[192]
1030	Ar, Si-C overlap	[192]
1000	Ar	[192]
1697,1533 (1660 – 2000)	Ar, 2 unique peaks used as identifier	[192]

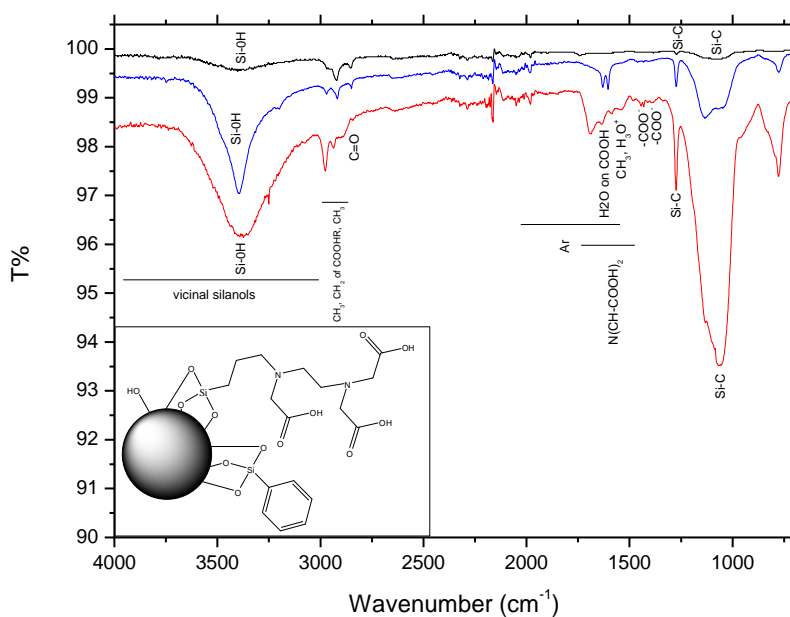


Figure 4-19 – ATR-FTIR transmission spectra of functionalised particles. Lines correspond to: (—) TEOS unfunctionalised particles, (—) TEOS particles with trimethoxyphenylsilane and a chelator functionality, (—) TEOS particles with EDTA functional group only. Inset a schematic of particle structure shown in Figure 4-17.

Table 4-7 - FTIR summary for triethoxysilylpropylmaleamic acid functionalised TEOS silica particles.

Wavenumber (cm <sup>-1</sup> )	Functional group	Reference
1724	carboxylic acids	[202]
2800 -3000	C=O and CH <sub>2</sub>	[202]
1580	C=O, H <sub>3</sub> O <sup>+</sup>	[202]
1634	H <sub>2</sub> O on COOH	[199]
1480 and 1395	-COO <sup>-</sup> stretching	[199]
1395 and 906	SI-OH in Carboxylic particles	[199]
2973	Carboxylic acid -CH <sub>3</sub> CH <sub>2</sub> stretching	[199]

Table 4-8 - ATR-FTIR summary for 3-[(Trimethoxysilyl)propyl] ethylenediaminetriacetic acid functionalised TEOS silica particles.

Wavenumber (cm <sup>-1</sup> )	Functional group	Reference
1724	carboxylic acids stretching	[202]
2800 -3000	C=O and CH <sub>2</sub>	[202]
1580	C=O, H <sub>3</sub> O <sup>+</sup>	[202]
1634	H <sub>2</sub> O on COOH	[199]
1480 and 1395	-COO <sup>-</sup> stretching	[199]
1332 and 712	Inter COOH interactions (sol gel)	[199]
2980	EDTA -CH <sub>3</sub> CH <sub>2</sub> stretching	[203]
2973	Carboxylic acid -CH <sub>3</sub> CH <sub>2</sub> stretching	[203]
(1500 to 1735) 1266, 1395, 1409	N(CH-COOH) <sub>2</sub>	[203]

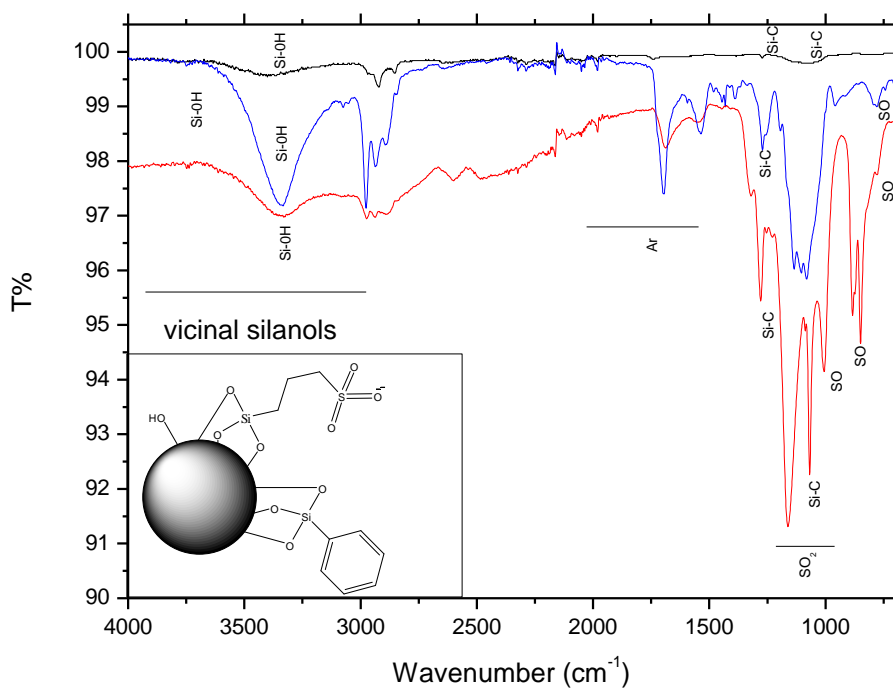


Figure 4-20 – ATR-FTIR transmission spectra of functionalised particles. Lines correspond to: (—) TEOS unfunctionalised particles, (—) TEOS particles with trimethoxyphenylsilane and a chelator functionality, (—) TEOS particles with functional sulfonic acid group only. Inset a schematic of particle structure shown in Figure 4-17.

Table 4-9 - ATR-FTIR summary for sulfonic acid functionalised TEOS silica particles.

Wavenumber (cm <sup>-1</sup> )	Functional group	Reference
large broad peak at 1129 with a small shoulder at 1056 overlaps Si-O	Sulfate (from sulfuric acid)	[205]
(1140 – 1260)	-SO <sub>2</sub> O <sup>-</sup> SO <sub>2</sub> symmetrical stretching	[192]
(790-830)	SO stretching	[192]
<i>Expected</i> (860 – 1020)	a asymmetrical SO stretching	[192]



Table 4-10 – ATR-FTIR summary for 3-mercaptopropyltrimethoxysilane functionalised TEOS silica particles.

Wavenumber (cm <sup>-1</sup> )	Functional group	Reference
1006-1010	C <sub>2</sub> H <sub>5</sub> propyl group attached to the silicon atom after hydrolysis, overlap with broad Si-OH peaks	[206]
2561	S-H stretch	[207]
2156 2543	Si - C Si - O stretch	[205]
2555 (2850–2930)	S-H stretching vibration aliphatic C-H stretching of the propyl / methylethyl groups (linear 3 carbon-R)	[208]

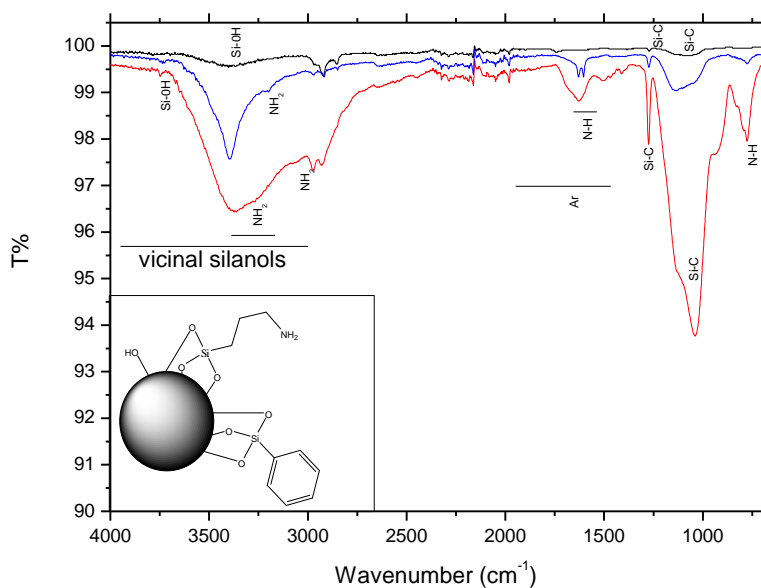


Figure 4-22 – ATR-FTIR transmission spectra of functionalised particles. Lines correspond to: (—) TEOS unfunctionalised particles, (—) TEOS particles with trimethoxyphenylsilane and a chelator functionality, (—) TEOS particles with functional amine group only. Inset a schematic of particle structure shown in Figure 4-17.

Table 4-11 – ATR-FTIR summary for aminopropyltrimethoxysilane functionalised TEOS silica particles.

Wavenumber (cm <sup>-1</sup> )	Functional group	Reference
3450 -3160	Solid state primary aliphatic amines	[192]
960 1390	More frequent in 40°C samples unhydrolysed ethoxy groups. Low concentrations silane not observed	[206]
779, 826 (895-650)	Additional N-H bonding observed due to disk compression	[192]
1643	NH <sub>2</sub> scissoring	[207]
3269 3207 (3550 – 3250)	N-H asymmetric and symmetric vibrations	
3368 and 3298	-NH <sub>2</sub> stretches	[207]
1601, 1608,1620 (1650 – 1580)	N-H deformation vibrations	[17]

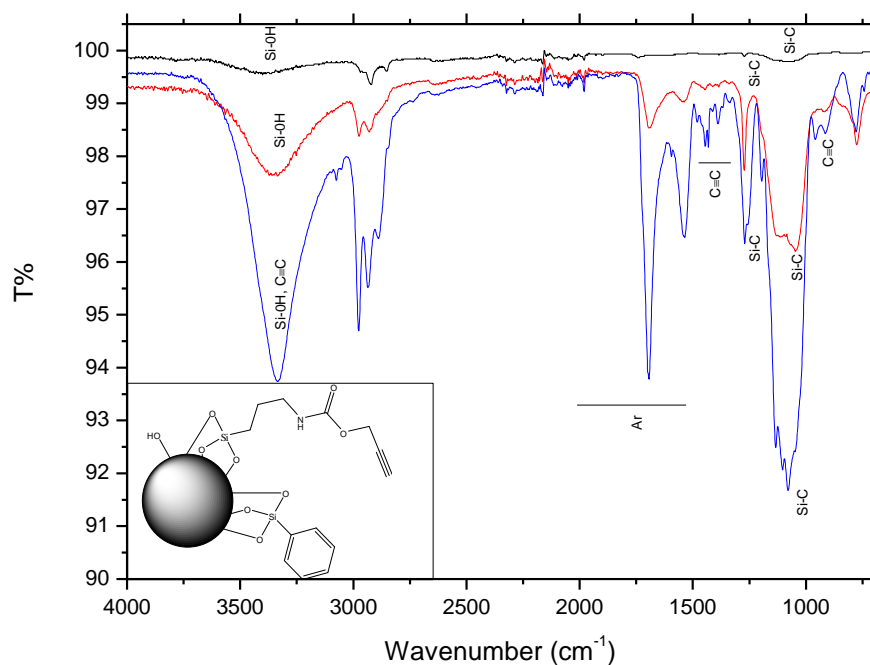


Figure 4-23 – ATR-FTIR transmission spectra of functionalised particles. Lines correspond to: (—) TEOS unfunctionalised particles, (—) TEOS particles with trimethoxyphenylsilane and a chelator functionality, (—) TEOS particles with functional alkyne group only. Inset a schematic of particle structure shown in Figure 4-17.

Table 4-12 – ATR-FTIR summary for (O-(propargyloxy)-N-(triethoxysilylpropyl)urethane functionalised TEOS silica particles.

Wavenumber (cm <sup>-1</sup> )	Functional group	Reference
3300	C≡C overlaps Si-OH	[207]
1220 - 1380	C≡C overtone	[17]
950	C≡C m-w	[17]
906	C≡C m-s	
770	C≡C m-s	

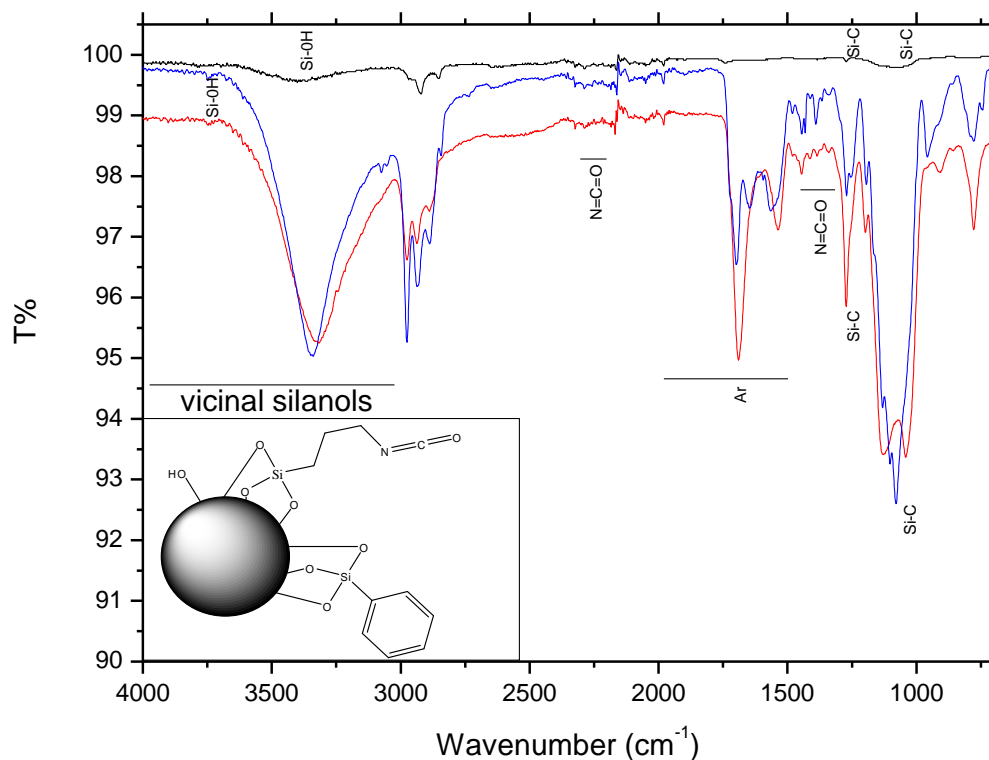


Figure 4-24 – ATR-FTIR transmission spectra of functionalised particles. Lines correspond to: (—) TEOS unfunctionalised particles, (—) TEOS particles with trimethoxyphenylsilane and a chelator functionality, (—) TEOS particles with functional isocyanate group only. Inset a schematic of particle structure shown in Figure 4-17.

Table 4-13 – ATR-FTIR summary for 3-Isocyanatopropyltriethoxysilane functionalised TEOS silica particles.

Wavenumber (cm <sup>-1</sup> )	Functional group	Reference
1360-1445	N=C=O symmetrical stretching present	[192]
2200 -2300	N=C=O asymmetrical stretching not present	[192]

#### 4.13.6 Radioisotope saturation binding of particles and scintillation counting

The optimised density oil layer used within the centrifugal binding assay (see section 4.10.5) allowed samples of nanoparticles to be incubated with radionuclide and then centrifuged to separate the bound and unbound radionuclide. A 50  $\mu\text{l}$  aqueous redispersion of dried nanoparticles was added to 50  $\mu\text{l}$  of radioisotope, incubated for 1 h at room temperature then sedimented to determine the amounts bound.

Figure 4-25 A shows nanoparticles incubated with 20 kBq radionuclide stock of  $^{90}\text{Sr}^{2+}$  and the amounts chelated by the nanoparticles (green bars), and the unbound radioisotope measured (red bars). The minor variation in stock activities around 20 kBq shows there is a degree of variation, with standard deviations between 10 and 12 % resulting from pipetting and transferral error. However, because the isotope count used was around 25 % above the maximum saturation of the best chelator particles (EDTA particles managed to bind 10,900 Bq to 12,400 Bq) this will not have affected the accuracy of binding experiments. All samples were corrected and had background nonspecific bound isotope removed by subtracting the CPM bound by bare silica particles. This was then used to calculate the total mass of analyte bound from calibration against a stock of known activity.

Bare silica particles bound minimal  $^{90}\text{Sr}^{2+}$  radionuclide at acidic and alkaline pH (29 to 300 Bq). Carboxylic acid particles were expected to bind more significantly more activity. The intermolecule spacing may have resulted in each COOH acting independently rather than in a bidentate fashion, and as a result not resulting in significant chelation. Of the four types of particles, amine and EDTA particles bound a significant proportion of the radioisotope. As a function of pH, (Figure 4-25 B) both particles performed excellently between neutral (pH 7) to highly alkaline (pH 11) with EDTA particles binding a total average activity of 10972 Bq and 12393 Bq; amine particles binding 11835 Bq and 10946 Bq at these pHs respectively.

Figure 4-25 C shows the total saturated binding showing that the binding capacity between batches of particles is consistent and reproducible ( $n=3$ ,  $\pm$  S.D).

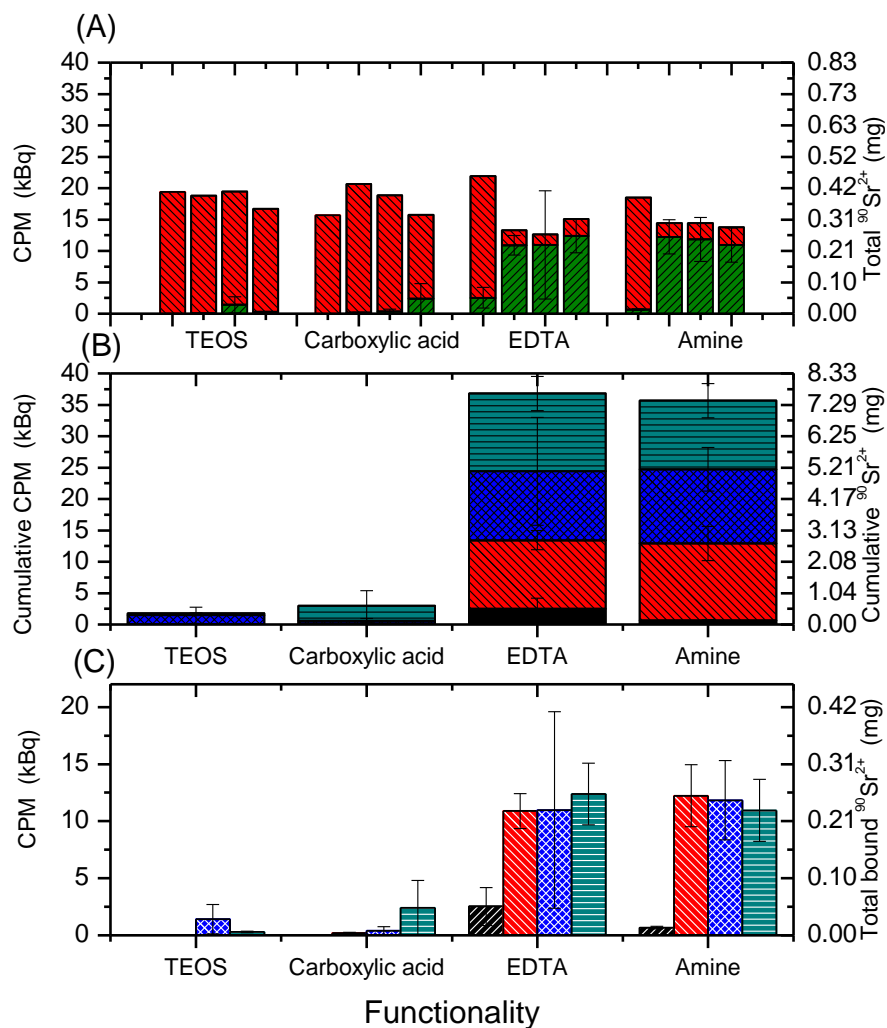


Figure 4-25 – Functionalised chelator nanoparticles and sequestering ability for aqueous  $^{90}\text{Sr}^{2+}$ . (A) Ratios of isotope remaining in the upper tube segment unbound (red) and isotope chelated by the nanoparticles (green) to show reproducibility between samples. (B) Relative CPM and mass of  $^{90}\text{Sr}^{2+}$  bound as a function of pH; green, pH 11; blue, pH 7; red, pH 2; black, pH 1. (C) Total bound  $^{90}\text{Sr}^{2+}$  as a function of pH; black, pH 1; red, pH 2; blue, pH 7; green, pH 11.

Using the mass of nanoparticles used and the known isotope specific activity, the mass of strontium bound per unit mass of nanoparticles was determined, summarised in Table 4-14. It can be seen from the TEOS samples  $^{90}\text{Sr}^{2+}$  is adsorbed to the surface hydroxyls or hydrophobically into the particle interior. The weak cation exchanger carboxylic acid bound a less than 1 % mass ratio and only functioned effectively at high alkaline pH. As contaminated ground water samples are expected as slightly acidic (~pH 5) they would not be a suitable chelator. Between the functional pH range of EDTA (pH 2 – 11) EDTA particles bound 50 % of their own mass, an impressive loading capacity. Surprisingly, amines too while in protonated form, bound a high amount of  $^{90}\text{Sr}^{2+}$  ions, between 10 and 45 % their own mass.

Table 4-14 – Functionalised NP and  $^{90}\text{Sr}^{2+}$  saturation, normalised per mass of particles ( $\mu\text{g}^{-1}$   $^{90}\text{Sr}^{2+}$  bound per  $\mu\text{g}^{-1}$  NP).

$\mu\text{g } ^{90}\text{Sr}^{2+}$ bound $\mu\text{g}^{-1}$ NP	Mass of $^{90}\text{Sr}^{2+}$ bound				Mass of NP / $\mu\text{g}$
	pH 1	pH 2	pH 7	pH 11	
TEOS	0.001	0.000	0.001	0.001	900
Carboxylic acid	0.000	0.000	0.005	0.002	745
EDTA	0.105	0.069	0.449	0.063	505
Amine	0.025	0.005	0.451	0.100	565

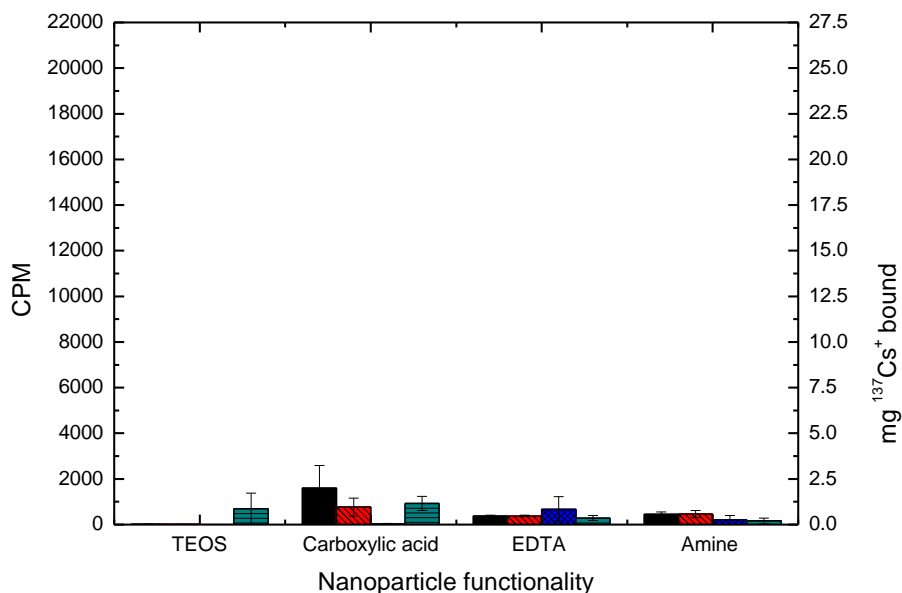


Figure 4-26 - Functionalised chelator nanoparticles and sequestering ability to aqueous <sup>137</sup>Cs<sup>+</sup> ions. Bars correspond to pH used; black, pH 1; red, pH 2; blue, pH 7; green, pH 11.

Experiments under identical conditions performed to bind <sup>137</sup>Cs<sup>+</sup> ions are summarised in Figure 4-26. As can be seen, all particles performed poorly compared to <sup>90</sup>Sr<sup>2+</sup> binding. A greater variation was seen between batches of bare silica particles and the carboxylic particles. EDTA particles bound an average of 199.7 Bq and 166.0 Bq and amine batches an average 32.0 Bq and 925.4 Bq at pH 7 and pH 11 respectively.

EDTA and amine particles were able to bind 13 times more <sup>90</sup>Sr<sup>2+</sup> than that <sup>137</sup>Cs<sup>+</sup>. An explanation for this can be seen from the ions valency. The divalent ions <sup>90</sup>Sr<sup>2+</sup> would be expected to form stronger complexes than mono valent <sup>137</sup>Cs<sup>+</sup> ions. How well each functional group can chelate is also dependent on ion and pH. A summary of pKa values for each functional group is shown in Table 4-15.

Table 4-15 – Summary table of theoretical pK<sub>a</sub> values of functional groups used on functionalised nanoparticles.

Functionality	Chemical groups	pK <sub>a</sub> [82, 209-210] [18]
Silanols	-OH ⇌ -O <sup>-</sup>	Varies 3.5 -4. 6 6.2 – 6.8
Carboxylic acid	R—COOH ⇌ R-COO <sup>-</sup>	pKa 5
EDTA	C <sub>10</sub> H <sub>16</sub> N <sub>2</sub> O <sub>8</sub>	H <sub>4</sub> = 2.07 H <sub>3</sub> = 2.75 H <sub>2</sub> = 6.24 H <sub>1</sub> = 10.34
Amine	-NH <sub>2</sub> ⇌ NH <sub>3</sub> <sup>+</sup>	9.5
Sulfonate	SO <sub>2</sub> -OH ⇌ SO-O <sup>-</sup>	1.6

The pK<sub>a</sub> is the point at which 50 % of groups are in the protonated form. At one pH above or below the pK<sub>a</sub> 90 % of the functional groups are in their deprotonated or protonated state respectively. The chosen pH range (pH 1, 2, 7, 11) of experiments corresponds to the different protonation states become protonated, introducing electrostatic repulsion and loss of chelating ability. Minimal binding of silanols (TEOS particles below pH 7) is expected due to protonation. Some binding of carboxylic acid particles would be expected above pH 6 (pK<sub>a</sub> - 5) but only bound significant amounts of <sup>90</sup>Sr<sup>2+</sup> in strongly alkaline environments. EDTA's 4 protonation states show that enough functional chelating groups are still available until as low as pH 1 where binding fails. Amine particles surprisingly were able to bind large amounts of <sup>90</sup>Sr<sup>2+</sup> well beyond its theoretical limit of pH 8.5 (pK<sub>a</sub> 9.5).

Thus the functional pH ranges of each molecule have been identified, the difference in binding is due to the nature of the analyte, <sup>90</sup>Sr<sup>2+</sup> and <sup>137</sup>Cs<sup>+</sup> and not the host molecule. The nanoparticles work well as chelators for divalent ions such as <sup>90</sup>Sr<sup>2+</sup> due to the higher charge valency but not as well for monovalent species such as <sup>137</sup>Cs<sup>+</sup>.

#### 4.13.7 Particle stability

If particles were used within several days, EtOH storage was suitable. Beyond several weeks particles showed signs of aggregation and sedimentation. Freeze drying was also used but particles often aggregated significantly.

Electrical double layer theory was discussed in Chapter 1. Double layers in colloids are formed by potential determining ions, and natural surface charge on a particle. Both vary dependent on the surrounding electrolyte. Thus nanoparticle stability is controlled by the supporting electrolyte. Silica colloids are known to exhibit Janus characteristics, and are able to form both positive and negatively charged suspensions. Under usual circumstances silica normally exhibits a negative double layer [211].

Silica particles appeared stable in phosphate buffer ( $\text{H}_3\text{PO}_4$ ) at pH 7 for up to a week. They are also known to be stable in borate ( $\text{BO}_3^{3-}$ ) buffers at alkaline pH 9-10 [212]. At alkaline pH phosphates form up to trivalent anions. The Schulze-Hardy rule states that particle flocculation is determined by valency, rather than the type of ions, that have opposite charge to the particle. The higher the opposing charge valency the higher the flocculating power, and thus the lower the flocculating concentration of salt required. This is known as the Hofmeister series, or lyotropic series. Positive cations for negative sols follows the series  $\text{Cs}^+ > \text{Rb}^+ > \text{NH}_4^+ > \text{K}^+ > \text{Na}^+ > \text{Li}^+$ , while anions for positive sols follows  $\text{F}^- > \text{Cl}^- > \text{Br}^- > \text{NO}_3^- > \text{I}^- > \text{CNS}^-$  [211]. Double layer repulsion stabilises particles, counteracted by Van der Waals attraction. Compression of a particle's double layer with high valency counter ions such as  $\text{CO}_2^{3-}$  resulted in rapid flocculation.

#### 4.13.8 Bifunctional particles

Bifunctional particles were created by the simultaneous deposition of prehydrolysed solutions of phenyl trimethoxysilane and a second functionality at varying ratios. While the functionality was confirmed by ATR-FTIR (Section 4.13.5) it was important to determine if adding multiple silanes, the phenyl silane used as a solid scintillant, resulted in secondary particle nucleation or particle aggregation affects. To investigate this, bare silica particles, phenyl only functionalised particles and functional monomer only particle were compared to particles nucleated simultaneously with increasing volumes of both silane. The effects of particle size distributions are shown in Figure 4-27.

Condensation was allowed for 24 h and then the supernatant solution analysed using PCS. Because each silane reacts at a different rate there were visible differences in solutions within minutes of the reaction starting. Amine solutions showed significant rapid condensation and in some cases bulk aggregation within the first 30 min. EDTA solutions only partially hydrolysed,, with the insoluble phase sedimenting out resulting in partial bulk gelation. Whilst mercapto and isocyanate phenyl solutions appeared to undergo rapid hydrolysis and complete dispersion upon addition to the silica-ethanol solutions, the alkyne silane exhibited super hydrophobicity and was only dispersed when added to ethanol.

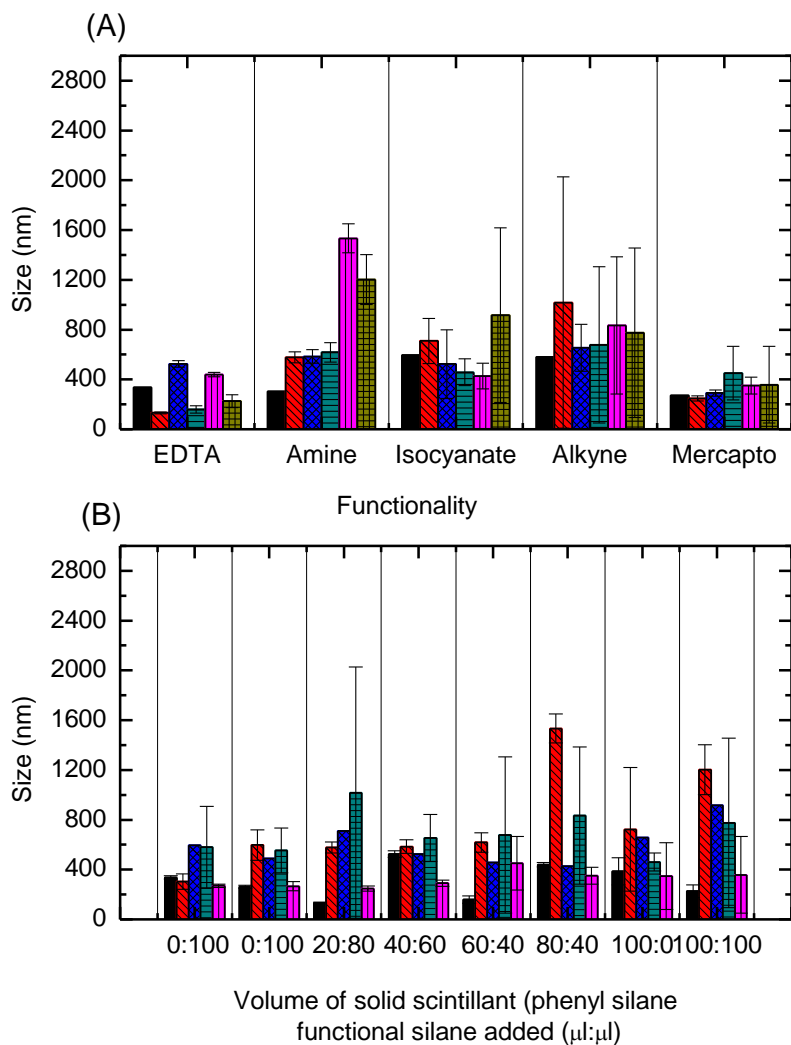


Figure 4-27 - Co-condensation of two functional silanes onto precursor silica particles (4 h growth, 24 h condensation). (A) Particle size distribution as a function of functional monomer varied. Amounts of phenyl silane and functional monomer added, in ml, were; 0 μl:100 μl (no phenyl silane, functional monomer only); black, 20 μl:80 μl; red, 40 μl:60 μl; blue, 60 μl:40 μl; green, 80 μl:20 μl; purple 100 μl:0 μl (phenyl silane only, no functional monomer). (B) Particle size distribution as a function of the two functional silane volumes used. Bars correspond to functionalised silane used; black, EDTA; red, amine; blue, isocyanate; alkyne, green; purple, mercapto silane. 400 sizing scans were obtained from the 5 silanes combined with 6 ratios of silanes, (n = 10 per average).

No general trend was observed for increasing the ratio of phenyl silane to functional monomer (Figure 4-27 A) other than that pure phenyl trimethoxyethylsilane particles compared to pure functional silane particles resulted in smaller particles (200 to 800 nm) with smaller size distributions. The mean particle size is not affected as most silica nucleation will have halted by this point, with the functional silanes only condensing onto the already grown particles. The degree of aggregation caused by this does however vary between functional monomers.

This varying rate of silane hydrolysis and condensation clearly influenced inter particle aggregation and the particle polydispersity observed (Figure 4-27 B). EDTA particles visibly showed aggregation and sedimentation. The particles stable in the supernatant however were of a narrow size distribution, around 400 nm. Beyond 60  $\mu$ l:40  $\mu$ l (phenyl silane and functional monomer) volumes of silane, sol gel formation did not occur, and solution opacity increased beyond a 20  $\mu$ l:80  $\mu$ l ratio with increasing phenyl trimethoxyethylsilane.

In spite of the rapid aminosilane condensation, particle size ranges were narrow until beyond a 60  $\mu$ l:40  $\mu$ l ratio, which resulted in a large degree of aggregation and broader size ranges were seen, with these samples ranging from 590 nm to 1600 nm.

As also observed by TEM (section 4.13.2), alkyne nanoparticles formed clear bimodal size distributions with around 20 % of particles observed less than 10 nm and a fraction greater than 1000 nm. Mercapto particles again showed the most narrow size distribution, generally being between 240 and 360 nm.

#### **4.13.9 Bifunctional particles and scintillation binding**

Functionalised chelator particles without the phenyl silane solid scintillant, tested under saturation conditions counted in Emulsi Safe scintillation fluid, were summarised in section 4.14.7. These bound between 10 -12,000 CPM for amine and EDTA particles, but under 2000 CPM for the carboxylic acid particles. The bifunctional chelator particles were also tested under the same conditions as saturation binding except no scintillation cocktail was added for counting experiments. In this case, scintillation events were counted from  $^{90}\text{Sr}^{2+}$   $\beta$  emissions interacting with the phenyl scintillants in close proximity (Figure 4-28).

The CPM values observed for the solid scintillant particles were significantly less than for Emulsi Safe fluid scintillation counting. This was because of the higher density of scintillant molecules in the Emulsi Safe fluid, which saturated the radioisotopes generating a higher scintillation yield. Because all phenyl solid scintillant particles produced a similar magnitude of counts it suggests that the available phenyl groups have reached maximum scintillation ability regardless of the amount of radioisotope bound. In present form the

system would only be suitable for high level counting. However, these particles show that solid scintillant chelators particles are possible, without the need for scintillation fluid and could be improved by finding a better scintillant or increasing the scintillant density per particle.

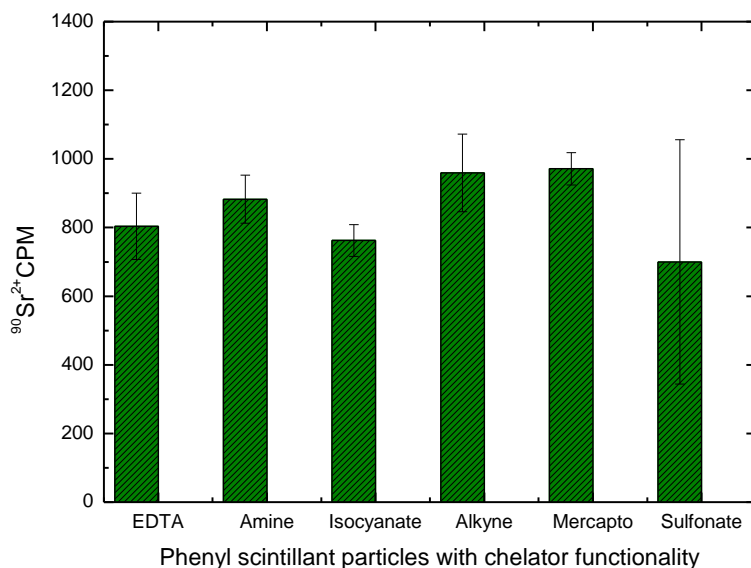


Figure 4-28 –Ability of bifunctional scintillant chelator particles to detect  $^{90}\text{Sr}^{2+}$  ions without scintillation cocktail. Particles comprising of phenyl functionalised silica, and a chelators group (EDTA, amine, isocyanate, alkyne, mercapto or sulfonate) were tested under saturation conditions with  $^{90}\text{Sr}^{2+}$  solutions (20 kBq) and counted without traditional scintillation cocktail.

#### 4.14 Commercial resins binding of $^{90}\text{Sr}^{2+}$ and $^{137}\text{Cs}^+$

The range of commercial resins were tested under the same conditions. A known mass of resin was incubated with radionuclide for 1 h at pH 1 or pH 7, and the amount of radionuclide bound determined by scintillation counting in Emulsi Safe. The binding data for four commercial cation binding resins is shown in Figure 4-29.

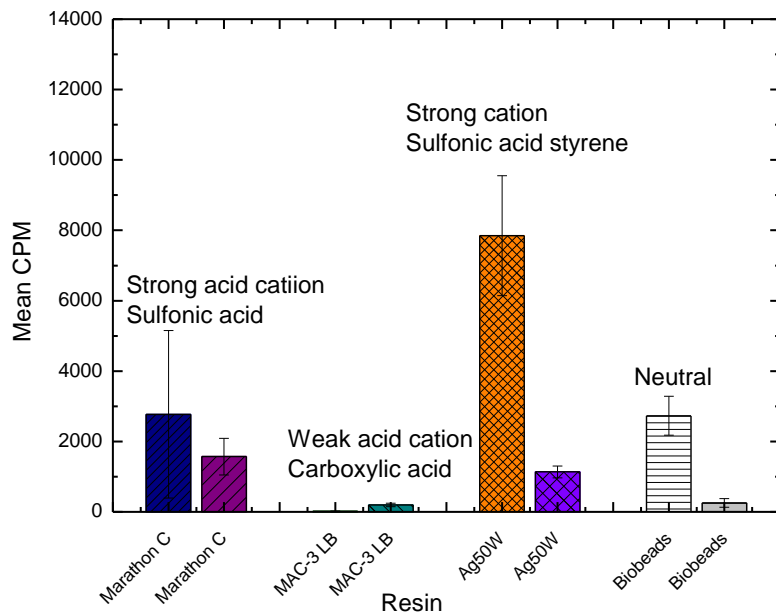


Figure 4-29 - Radioisotope saturation binding experiments of  $^{90}\text{Sr}^{2+}$  using a range of weak and strong cation resins. After 1 h with shaking, the resins were recovered by centrifugation, and added to 5 ml of scintillation fluid. In each case, the left bar shows data from media at pH 7 whilst the right hand bars show media at pH 1.

The saturation amounts of radionuclide bound is shown in Figure 4-29. Weak cation exchangers (carboxylic acid,  $\text{pK}_a$  5) are expected to be pH dependent and fail at highly acidic pH due to protonation interfering with chelation. Strong cation binders, (sulfonic acids  $\text{pK}_a$  1.5) are essentially pH independent and should theoretically have bound across the experimental range used. However, experimentally all strong cation binders (Marathon C, Ag50W) performed poorly at low pH as did weak binders (MAC-3LB, Biobeads). Marathon C, Ag50W and Biobeads showed a 45 %, 85 % and 91 % increase in analyte binding at optimum pH 7, compared to fully protonated states. The data are also presented in Table 4-16 where the final column shows the mass of analyte bound per mass unit of resin. The highest capacity binders Marathon C and Ag50W were able to bind 0.0566  $\mu\text{g}$  and 0.01528  $\mu\text{g}$   $^{90}\text{Sr}^{2+}$  per  $\mu\text{g}$  resin respectively, at optimum pH dropping to 0.0320  $\mu\text{g}$  and 0.00221  $\mu\text{g}$   $^{90}\text{Sr}^{2+}$  per  $\mu\text{g}$  resin in their protonated forms.

Table 4-16 – Commercial resin saturation binding of  $^{90}\text{Sr}^{2+}$ . Mass of analyte bound per mass of resin calculated at each pH. Mean data are shown, n = 3.

Resin	Mean CPM	SEM	mass of analyte bound ( mg)	$\mu\text{g}$ resin per $\mu\text{g}$ analyte bound
Marathon C (pH 7)	2772	2377	0.05775	0.00566
Marathon C (pH 1)	1569	523	0.03269	0.00320
MAC-3 LB (pH 7)	13	9	0.00027	0.00003
MAC-3 LB (pH 1)	199	49	0.00415	0.00040
Ag50W (pH 7)	7848	1704	0.16351	0.01528
Ag50W (pH 1)	1136	170	0.02367	0.00221
Biobeads (pH 7)	2732	553	0.05691	0.01498
Biobeads (pH 1)	257	122	0.00535	0.00141

A comparison of the new functionalised chelator nanoparticles compared to commercial resins is shown in Table 4-17. On mass ratio bound, amine and EDTA particles could bind 44-45 % their own mass compared to 5.6 % and 1.5 % for the strongest commercial resins Marathon C, Ag50W. The higher surface area to bulk ratio clearly shows that the higher density of available chelating groups on the nanoparticles gave a significantly enhanced binding capacity for divalent cations.

Table 4-17- Comparison of normalised  $^{90}\text{Sr}^{2+}$  saturation binding data at pH 1 and pH 7 for the four chelator nanoparticles and four commercially available resins ( $\mu\text{g}$   $^{90}\text{Sr}^{2+}$  bound per  $\mu\text{g}^{-1}$  NP ).

Functionality	pH 1	pH 7
TEOS	0.00100	0.00100
Carboxylic acid	0.00000	0.00500
EDTA	0.10500	0.44900
Amine	0.02500	0.45100
Marathon C	0.00320	0.00566
MAC-3 LB	0.00040	0.00003
Ag50W	0.00221	0.01528
Biobeads	0.00141	0.01498

#### 4.14.1 Commercial resins and $^{137}\text{Cs}^+$ binding

The six commercial resins used to bind  $^{137}\text{Cs}^+$  ions showed narrower variation in performance, with averages ranging between 9759 and 13431 CPM (Figure 4-30). At neutral pH the resins were far superior to the functionalised nanoparticles. With the exception of resin Ag 50wx2, the resins were typically only able to bind 19 – 24 % of their own mass in analyte, summarised in Table 4-18.

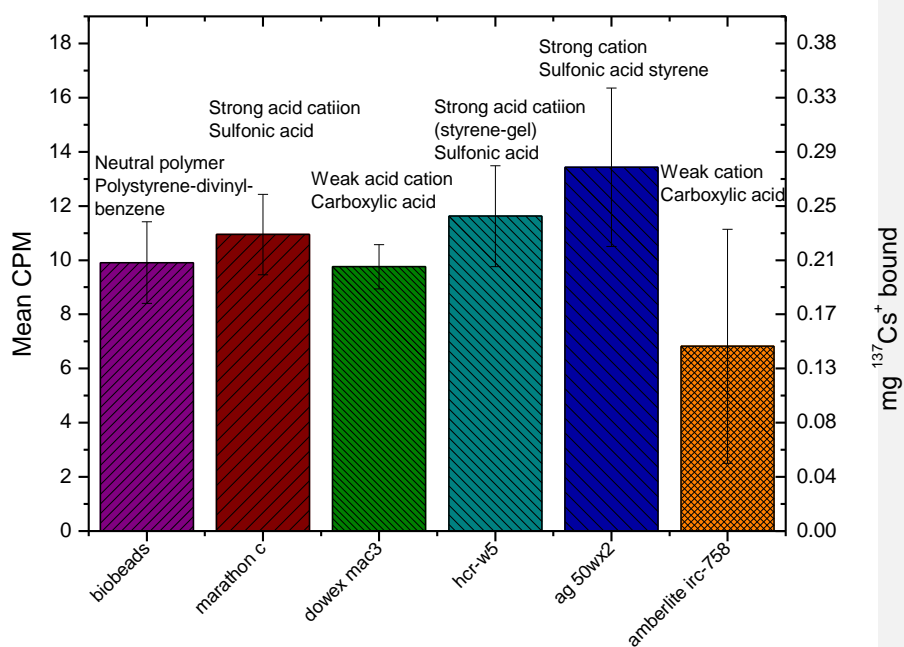


Figure 4-30 – Saturation binding ability of six commercial resins to high concentrations of  $^{137}\text{Cs}^+$  ions. Mass of ions extrapolated from calibrated radioisotope stock shown on the right axis.

Table 4-18 – Table of normalised  $^{137}\text{Cs}^+$  binding saturation data for commercial resins. Figures normalised showing  $\mu\text{g } ^{137}\text{Cs}^+$  bound  $\mu\text{g}^{-1}$  resin.

Resin	Mean CPM	Mass of resin per tube (mg)	Amount of $^{137}\text{Cs}^+$ bound (mg)	$\mu\text{g resin per } \mu\text{g } ^{137}\text{Cs}^+$ bound
Biobeads	9907.5	0.855	0.206	0.24141
Sephadex marathon c	10945.7	1.170	0.228	0.19490
Dowex mac3	9758.7	0.605	0.203	0.33605
Ion exchange hcr-w5	11623.4	1.110	0.242	0.21816
Ag 50wx2	13431.2	0.485	0.280	0.57694
Amberlite irc-758	6825.0	0.665	0.142	0.21382

#### 4.14.2 Performance in synthetic groundwater with low level radionuclide contamination

The previous experiments in buffer do not account for the interferants and competing species for chelation present in the real analyte matrix, i.e groundwater. As a result, all resins and functionalised nanoparticles were incubated in synthetic ground water spiked with low level  $^{90}\text{Sr}^{2+}/^{137}\text{Cs}^+$  contamination levels typical of Sellafield groundwater – 1 kBq  $^{90}\text{Sr}^{2+}$  and 0.1 kBq  $^{137}\text{Cs}^+$  (discussed in Chapter 1). 1 h incubations were allowed with 50  $\mu\text{l}$  samples which were then scintillation counted. The data are shown in Figure 4-31.

All experiments to quantify  $^{137}\text{Cs}^+$  were below the detection limits of the Wallac Cobra  $\gamma$  counter. As a result, for a practical sensing device an accumulation system with analyte continually flowing over chelators would be needed until the amount accumulated is within the machine limits.  $^{90}\text{Sr}^{2+}$  beta counting was however within detection limits.

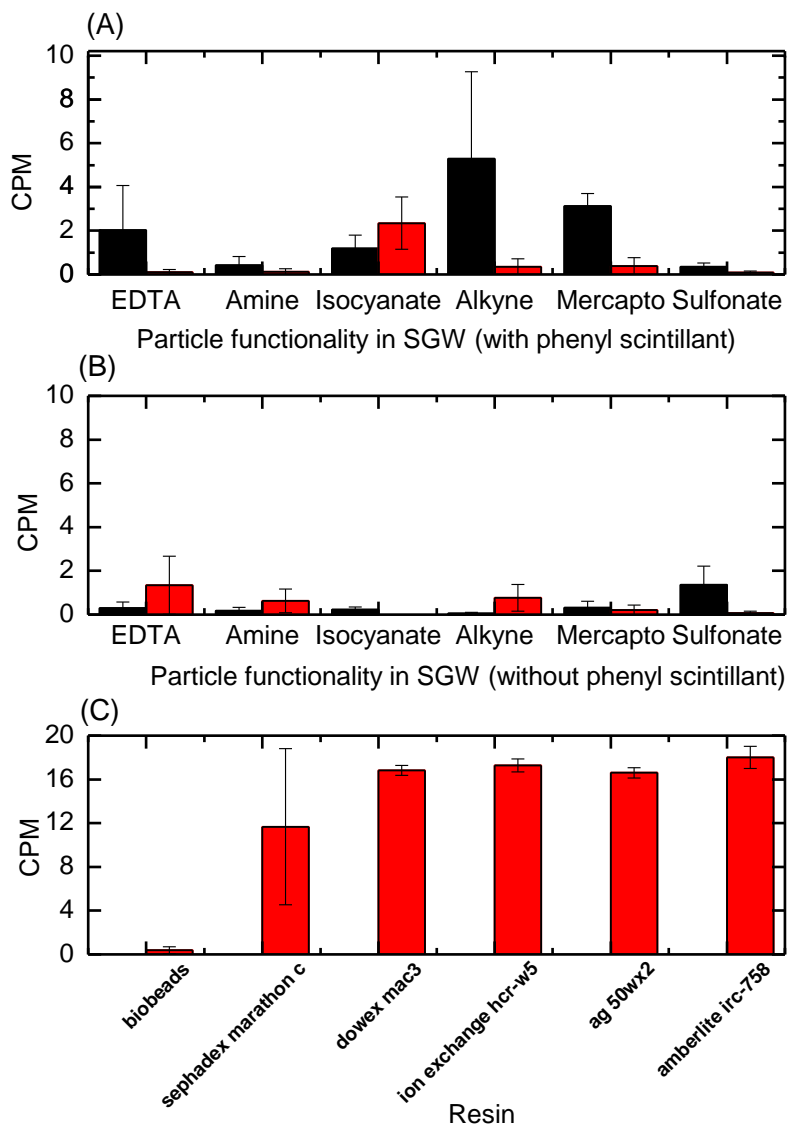


Figure 4-31 – Chelating ability of functionalised silica particles. (A), phenyl scintillant particles; (B), chelator only particles without scintillant; (C), commercial resins. A known mass of particles or resin was incubated in 50uL of synthetic groundwater. Levels of  $^{90}\text{Sr}^{2+}$  and  $^{137}\text{Cs}^+$  were chosen on the basis of typical activities around Sellafield. Black bars correspond to samples counted with Emulsi safe scintillation cocktail, red bars without.

Because of the low radioisotope concentrations of  $^{90}\text{Sr}^{2+}$  and  $^{137}\text{Cs}^+$  present and the lower scintillation yield of the phenyl silane it was not possible to accurately determine the amount of analyte bound. Figures 4-31 A and B show particles counted with (red bars) and without Emulsi Safe scintillation cocktail (black bars) to determine if there was a significant difference between the scintillation methods at such low level analytes. While both methods bound small levels of analyte (< 6 CPM and < 2 CPM) the levels bound with the phenyl scintillant particles were within the standard deviation. As a result at low levels, the Emulsi Safe counting method was more reproducible with narrower variation between samples. For the scintillant nanoparticles to be used for low level contamination detection a sorption system with larger volumes of analyte flowing over the particles, chelating higher concentrations to within detectable levels would be needed. The commercial resins consistently managed to bind a higher level of radionuclide (12 -17 CPM). From previous experiments, the higher levels bound by the resins are likely due to  $^{137}\text{Cs}^+$  chelation and the amounts bound by the NP due to  $^{90}\text{Sr}^{2+}$ . This could not be confirmed because the amounts were below the sensitivity limits of the Wallac  $\gamma$  counter.

#### 4.15 Conclusion

A range of silica nanoparticles were grown based on a controlled pH dependent hydrolysis of low percentage (v/v) methoxy silanes. Optimal conditions used ammonium hydroxide nucleation using less than 5 % water allowed a controlled reaction rate to create particles of a uniform size confirmed by SEM, TEM and PCS. It was shown possible to use a range of organic solvents, ethanol, methanol or acetone for particle growth which have low boiling points for solvent transfer, and importantly, low toxicity. Heating with a controlled water bath at 40 °C was shown to produce micron size particles large enough for sedimentation at low g forces. Reaction of these core TEOS or TEMOS particles with further bioconjugatable silanes allowed a range of bespoke chemical functionalities to be added as the conjugates hydrolyse and couple directly to the core particle silanols. While it has been shown in literature already that amino [213] and mercapto [214] functionalisation was possible, a range of other silanes were used. Only the sulfonate silane failed, as it appeared not to hydrolyse. As sulfonates are a powerful pH independent cation chelator [82] an alternative was developed using oxidation of precursor mercapto-particles.

Significant variation in particle size dispersity of core silica particles and the functionalised forms was only observed with (O-(propargyloxy)-N-(triethoxysilylpropyl)urethane) alkyne particles, which have potential use for a range of high yield click chemistry based modification [215]. These methods have great potential for bulk scalable production of functional particles.

The functionalised particles were subject to various characterisation procedures, however the key approach was ATR-FTIR analysis in KBr anhydrous matrixes which allowed functionalisation to be confirmed.

Of the functionalities created, candidate chelating particles (amine, carboxylate, mercapto and sulfonates) were used in radionuclide binding experiments. The saturation of binding as a function of pH was determined, and normalised per mass of particle. The same observations were applied on four commercially available cation binding resins and it was shown that the functionalised EDTA and amine nanoparticles, compared to an equal mass of the best commercial resins, were able to bind up to 45 % more  $^{90}\text{Sr}^{2+}$ . Nanoparticles performed significantly better than the commercial resins at chelating  $^{90}\text{Sr}^{2+}$  but not  $^{137}\text{Cs}^+$ . Bifunctional scintillant chelator particles were shown to directly measure radionuclides present at high level  $\beta$  contamination, but at low activity levels scintillation cocktail was still required. Finally, particles and resins were used in low level contaminated SGW which contained composition was based on typical  $^{90}\text{Sr}^{2+}$  and  $^{137}\text{Cs}^+$  activity levels found around the Sellafield site. All surfaces managed to detect low level signal, but error bars were notably smaller when traditional scintillation cocktail was added.

## **5 : High surface area nanofibres as affinity sorbents**

---

## 5.1 Chapter overview

Successful growth of functionalised nanoparticles was detailed in Chapter 4. It showed that using functional silanes to nucleate and modify nano- or micro- particles with chelating groups was possible. However, attempts to encapsulate particles into a support matrix proved challenging. Alternative approaches is to condense functional silanes onto a range of solid, high surface area surfaces that will allow direct analyte flowed over for analyte extraction and quantification. A range of bulk metal oxide and silica dioxide surfaces were functionalised and binding capacities compared to those of the chelator nanoparticles. In a similar manner, electrospun nanofibres were also investigated for this purpose, and used as high surface area sorbents. A hierarchy of the methods used in this chapter is summarised in Figure 5-1.

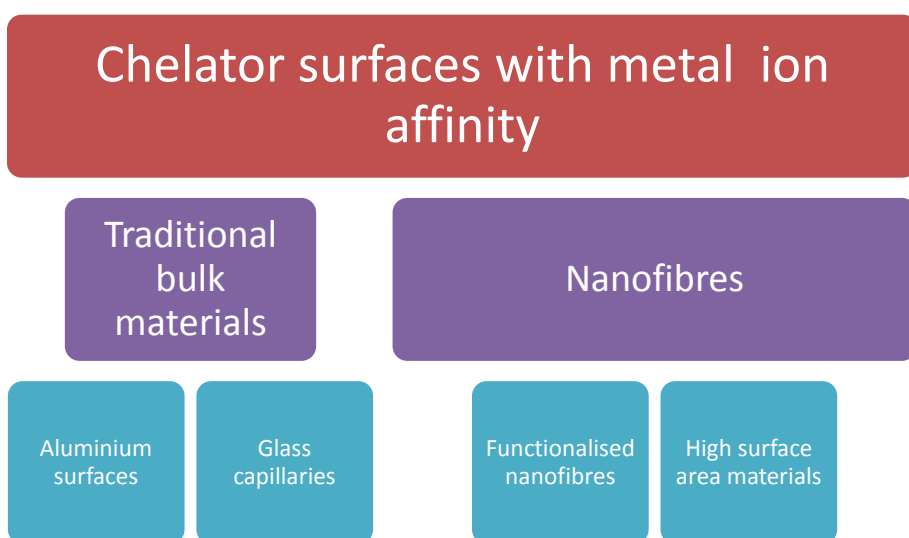


Figure 5-1 - Chapter five hierarchy, outlining the methods used to deposit chelator groups using functional silanes onto a range of surfaces including electrospun nanofibres for high surface area sorbents.

## 5.2 Silane reaction methods

Detailed silane reaction mechanisms have been shown for silica nanoparticle growth (section 4.5). However, to instigate surface condensation rather than solution nucleation a modified protocol was used.

Silanes can be reacted in two phase systems in a range of protocols available; (I) Organic/aqueous suspensions with low (v/w) water content plus acid added to aid slow hydrolysis. (II) Direct aqueous dissolution if the silane is water soluble, with careful control of the reaction time. Bulk silanes are initially immiscible in water and will form two separate phases until the alkoxy groups hydrolyse and the silanes begin to dissolve. If reacted for too long, the silanol intermediates will inter-react and polymerise creating milky suspensions and will subsequently not react at the desired surface interface. As a result, protocols typically used an organic solvent or organic/aqueous mix with typically only a few per cent (v/v) of water. (III) Organic solvent only deposition can be used only with specific highly reactive silanes (chloro- amino- and methoxy-) but not ethoxysilanes which require prior hydrolysis (Figure 5-2). As well as aqueous-aqueous phase deposition, (IV) vapour phase deposition is possible, where the silane is placed in a sealed glass chamber, under heat and vacuum, to react completely within the vessel.

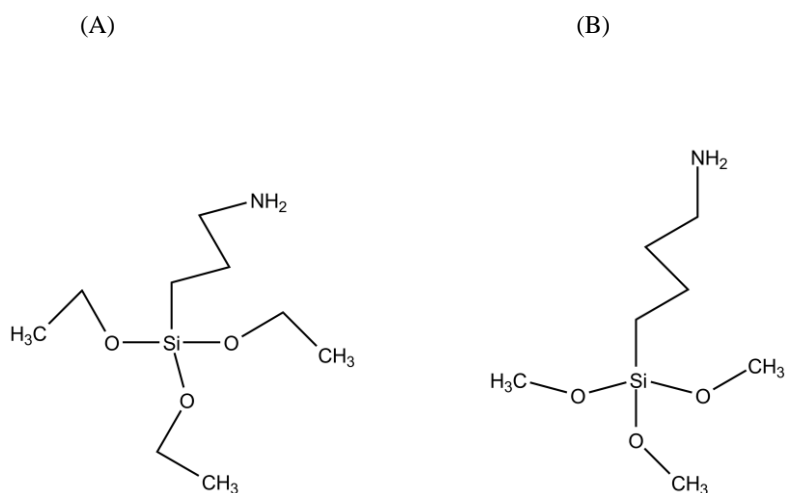


Figure 5-2 – Examples of hydrolysable functionalised silanes; (A), 3-aminopropyltriethoxysilane (APTES) and (B), 3-aminopropyltrimethoxysilane (APTMS).

For attachment of the hydrolysable methyl ether or ethyl ether, a reactive intermediate is generated before reaction with the substrate surface. This can be aided by heating or reaction with a catalyst.

The reaction of these intermediates with a hydroxyl layer forms organo-siloxane bonds. The thickness of this layer is proportional to the water and silane coupling agent concentrations. These properties were varied to create different functionalised surfaces.

#### **5.2.1.1 Substrate preparation – coating surfaces with a hydroxyl base layer**

Glass is comprised of 75 % (w/v) silica (SiO<sub>2</sub>) plus Na<sub>2</sub>O, CaO and other additives. It is optically transparent in the UV-visible spectrum and readily available, which makes it an ideal material for scalable functionised materials that can be used easily in combination with scintillation counting for radionuclides. To successfully silanise a surface, a dense hydroxyl layer will give optimum coverage. Glass and silica surfaces undergo disassociation of silanol groups, acquiring a negative surface charge according to Equation 5-1:



(5-1)

SiO<sub>2</sub> groups are considered inert and cannot act as binding sites. The degree of protonation on surfaces depends on the ionic strength and pH of the solution. To estimate the surface density of hydroxyl groups, application of the basic Stern model on silica nanoparticles and titration with acid can be used. By accurately measuring the number of protons transferred across an interface in highly acidic environments, this method has been shown, to yield fairly accurate surface estimations. However, this is only the case for non-porous, aqueous silica colloids containing high salt concentrations [216]. A number of traditional methods to quantify surface density of hydroxyls all fail under low ionic strength. These include streaming potential measurements, conductimetry and electroacoustic methods [217] and only recently have models allowed accurate bulk silica protonation estimation. An extensive theoretical derivation of silica surface charge is available [218] and a summary of the effects of pH on surface charge given in Figure 5-3.

At a pH lower than 4, the calculated surface charge-silica model [216] states that the surface charge of a silica surface approaches zero as surface silanol groups all become protonated. This will be optimal for maximum hydroxyl coating and for subsequent silane deposition.

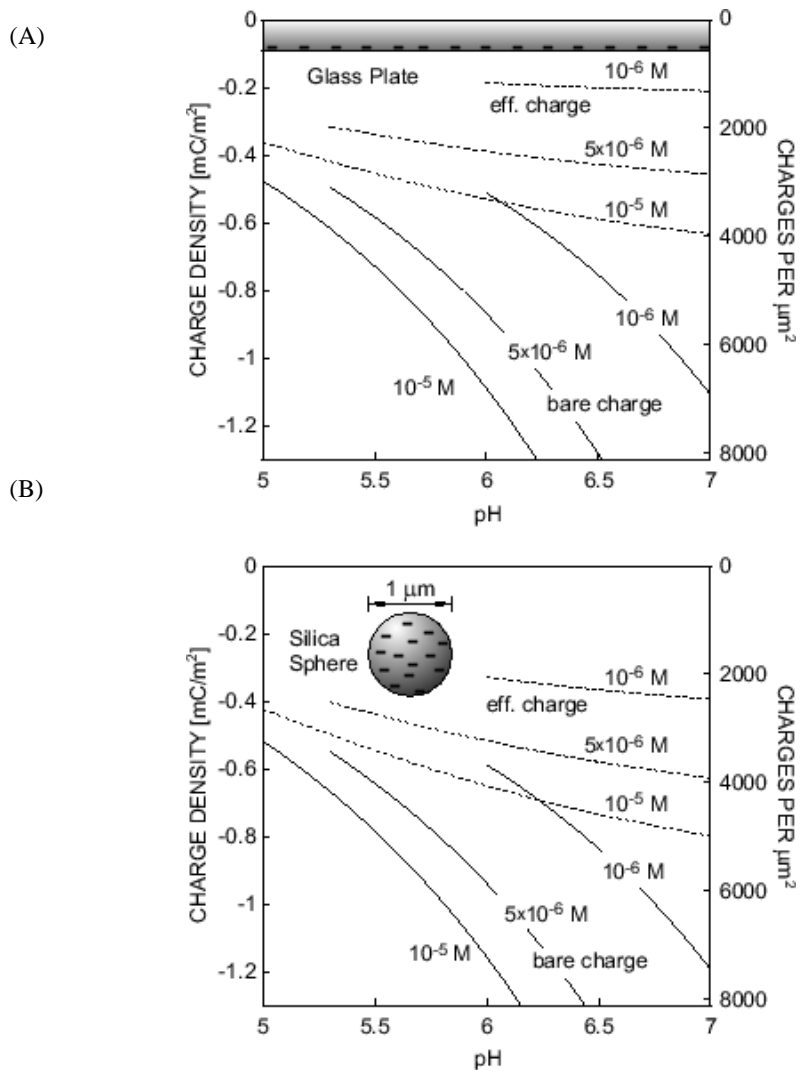


Figure 5-3 - The bare (—) and effective charge densities (----) of a planar glass substrate according to Hiemstra *et al* [212]. (A), solid surfaces used; (B), a 1 μm silica sphere, assuming a density 8 nm<sup>-2</sup> of chargeable sites, a pK value of 7.5 for the silanol dissociation, and a Stern capacity of 2.9 F/m<sup>2</sup> [216].

Because of the difficulties to experimentally calculate the surface density of hydroxyls, the theoretical model was used as an estimate. On μm sized silica particles, in μM buffer at pH 5.5 (SGW conditions), unfunctionalised hydroxyls will deprotonate leaving a maximum

2400 negative  $\text{SiO}^-$  available which increase to nearly 4000 charges per  $\mu\text{m}^{-2}$  at neutral pH. A bulk planar glass surface under the same conditions will have 2600 charges per  $\mu\text{m}^{-2}$  at pH 5.5 and approximately 2700 charges  $\mu\text{m}^{-2}$  at pH 7. A comparison of the two estimates reveals that bulk surfaces are less sensitive to changes in pH. This phenomenon explains the higher nonspecific absorption of cations at increasingly alkaline conditions observed experimentally.

## 5.3 Experimental

### 5.3.1 Experimental overview

A range of bulk surfaces (glass slides, glass capillaries, glass anti bumping granules, aluminium substrates), and high surface area nanofibres were functionalised with organosilanes bearing a range of functional chelating groups. These were characterised by FTIR, miniSIMS and FEG-TEM to confirm functionality, structure and surface properties. These surfaces were then used in radioisotope binding experiments to quantify binding efficiency.

### 5.3.2 Reagents

Tetramethyl orthosilicate (TEMOS), tetraethyl orthosilicate (TEOS); 3-(trimethoxysilyl)propyl methacrylate, 3-(triethoxysilyl)propyl isocyanate, (3-mercaptopropyl)trimethoxysilane were obtained from Aldrich. O-(propargyloxy)-N-(triethoxysilylpropyl)urethane; was bought from ABCR. 3-aminopropyltriethoxysilane sourced from Acros Organics. 3-[(trimethoxysilyl)propyl]ethylenediaminetriacetic acid, sodium and triethoxysilylpropylmaleamic acid were sourced from Silar laboratories.

Scintillants and their sources were atracene (Aldrich), 1,4-bis(5-phenyloxazol-2-yl) benzene (POPOP) (Sigma), 2,5-Diphenyloxazole (PPO) (Sigma), 1,1,4,4-tetraphenyl-1,3-butadiene (TPB) (Across organics) Triton X-100 (Sigma), p-terphenyl (Aldrich), methylstyrene/vinyl toluene (Aldrich). Ammonium hydroxide solution, all other solvents and acids were sourced from Fisher scientific unless otherwise stated.

Silication surfaces and their sources; glass capillaries (Ring caps for reflowtron 32  $\mu$ l) were purchased from VWR international. Blue star microslide glass microscope slides (76 by 62 mm, 1.2 mm thick) were purchased from Chance Proper Ltd. Nanofibres were produced by the Micro and Nanotechnology Centre, STFC Rutherford Appleton Laboratory. 5 mm diameter glass anti bumping granules were sourced from Sigma Aldrich. Nanofibres were supplied by Professor Bob Stevens, Smart Materials and Devices, School of Science and Technology, Nottingham Trent University.

## 5.4 Methodology

### 5.4.1 Surface preparation

All surfaces were washed in a 10 % (v/v) HCl solution to remove non-specific metal ions ( $\text{Na}^+$ ,  $\text{Mg}^+$ ,  $\text{Cs}^+$ ). Glass slides (76 by 62 mm, 1.2 mm thick) were cut into approximately 5 mm squares using a diamond tip pen. These squares or 32  $\mu\text{m}$  capacity glass capillaries were piranha washed for 30 min to remove organic contamination and create a dense surface hydroxyl layer for silane condensation.

Aluminium stubs were prepared by coating with a diamond stick resin and smoothing with abrasive paper before a 2 min wash in dilute piranha solution (25 % (v/v) sulphuric and 15 % (v/v) hydrogen peroxide) was carried out before reaction with the appropriate silane.

Nanofibres were washed in ethanol, then piranha solution washed for 30 min and neutralised with  $\text{dH}_2\text{O}$ . All binding experiments were performed against an unsilanised control to account for nonspecific binding.

### 5.4.2 Silane condensation for functional surface coatings

3-5 % (v/v) water in ethanol solution was adjusted to pH 4.5 – 5.5 with acetic acid. Silane coupling agent was then dissolved with stirring to a final concentration of 2 to 5 % (v/v). Hydrolysis was allowed to proceed for 5 min at room temperature to create the active silanol compound. The various hydroxyl coated substrates were then reacted for different periods of time ranging from mins to hrs, on a shaker, then washed with ethanol repeatedly to remove excess silane. Curing of the substrate at 110 °C for 30 mins under vacuum was performed to remove water and form siloxane bonds. The optimised conditions were found to be pH 5.5, 4 h deposition with 5 % (v/v) silane, 2 % (v/v) water in ethanol. An example of EDTA loaded surface preparation is shown in Figure 5-4. To functionalise glass capillaries, they were submerged in this solution with capillary force aspirating the liquid for complete internal coverage. This method however resulted in inhomogeneous silane coverage and explained the significant variation between capillary batches.

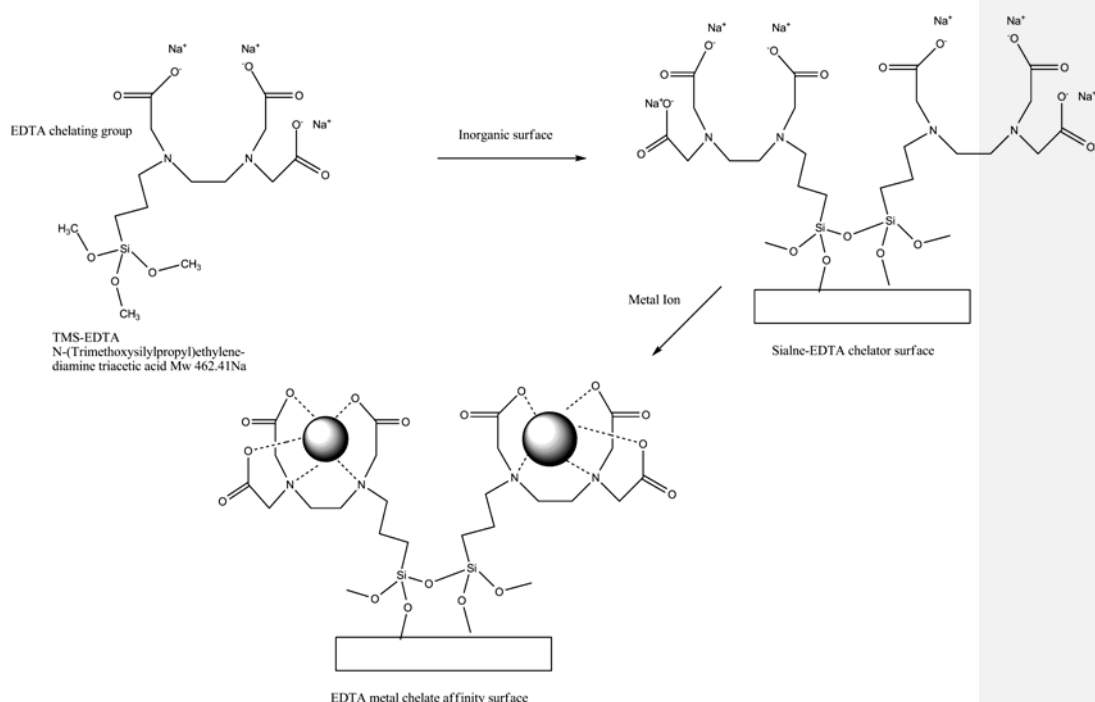


Figure 5-4 - EDTA affinity surface preparation from two dimensional silane condensation on planar hydroxyl coated surfaces.

### 5.4.3 Nanofibre formation

The nanofibres were supplied by Professor Bob Stevens of Nottingham Trent University. A brief knowledge of their production method and limitations is important to understand the batch irreproducibility. Briefly, fibres were grown by forcing a jet of electrically charged polymer solution between two electrodes under high voltage. A polymer drop forms on the end of the capillary and is pulled into a wet fibre by electrostatic forces. Wet fibres carry surface charges which condense as the fibre dries, the charge density increases until at a point. Here, self-extension occurs and the fibre extends to produce nanoscale fibres producing a non-woven continuous matrix with no long range order [219]. A summary of the five fibre types used for subsequent functionalisation and their growth conditions are summarised in Table 5-1.

Table 5-1 – Growth conditions controlled during nanofibres growth: polymer injection rate, growth temperature and relative humidity.

<b>Fibre type</b>	<b>Growth injection rate (<math>\mu\text{l} / \text{h}</math>)</b>	<b>Temperature ( <math>^{\circ}\text{C}</math>)</b>	<b>% Relative humidity</b>
1	1000	25	25
2	1000	25	25
3	1000	25	70
4	1500	25	25
5	1000	40	70

## 5.5 Analytical methods

### 5.5.1 Nanofibre diameter sizing analysis via FEG-TEM microscopy

Nanofibres were prepared by cutting the supplied samples into 2 cm x 2 cm squares and modifying as required. Because of difficulty in handling, samples were left on the foil backing and modified in six well plates on a low setting shaker with multiple washing steps between stages. For FEGTEM, 'short' sample stubs were mounted with 12 mm carbon tabs (Agar scientific) and the samples attached. Two or three carbon ink (< 1 % (v/v) xylene) perimeter coatings were added and dried which minimised sample charging. Initial samples were sputter coated with 2 x 30 nm gold layers using a Ar purged EMScope sputter coater. Whilst removing charging, the coating created gold aggregates that lost fine detail on the nanofibres at high magnification. The best sputter coating alternative found was a single 10 nm, 80 mA platinum coat using an AGAR high resolution sputter coater. Typical settings used for high resolution images were a 3 keV accelerating voltage, 20  $\mu\text{m}$  aperture, working distance of 3-6 mm,  $n = 21$  line integrals at a scan speed of 5 and a cycle time of 1.4 s.

### 5.5.2 Fourier transform infrared spectroscopy analysis of bulk surfaces

All FTIR, regardless of sample preparation of the bulk surfaces, was performed on a liquid  $\text{N}_2$  Perkin-Elmer Spectrum-100 FTIR spectrometer with averages of 30 spectra averages per point. Typically 3 regions were analysed and averaged per scan. A range of 4000 to 750  $\text{cm}^{-1}$  and resolution of 2  $\text{cm}^{-1}$  was used. For imaging of functionality density, the specified wave numbers chosen were used to scan a 100 x 100  $\mu\text{m}$  sample area, with 30 scans averaged per measurement.

### 5.5.3 Focused ion beam analysis for silane deposition depth

To estimate the thickness of the deposited silane layers a focused ion beam (FIB) etching technique was combined with TEM. Samples were mounted on a SEM metal stub with two sided carbon tape and onto which a conductive 50 nm platinum layer was deposited by thermal deposition. Imaging, etching and surface analysis was performed on a FEI Nova 200 dual beam SEM / FIB with INCA elemental analysis software. Etching was performed using a 10 kV gallium ion source using a silicon etching profile for the required depth estimations. A 1  $\mu\text{m}$  by 5  $\mu\text{m}$  protective platinum resist was deposited next to where the 5  $\mu\text{m}$  x 10  $\mu\text{m}$  trench was etched. The sample was then angled to allow lateral etching into the trench wall

to allow analysis of the bulk glass silicon dioxide, the organic deposition layer and the protective platinum resist.

#### **5.5.4 Secondary Ion Mass Spectroscopy of bulk surfaces for functionalisation**

MiniSIMS analysis was performed on a Millbrook SAI bench top machine using a 3 A current, 6 kV gallium source imaging a 10 nm<sup>2</sup> sample area, with SED integration of 4. Both positive and negative mode scans were used. Same stage heights were used between samples. Functional group density was estimated using a silicon etching profile and known elemental sensitivities.

## 5.6 Results and discussion

### 5.6.1 Secondary ion mass spectroscopy

Approximated atomic densities of functionalities deposited were calculated from known relative sensitivity factors and observed counts from multiple scans. Carboxylate and EDTA surfaces on aluminium substrates are shown in Figure 5-8. Negative scan ions (Figure 5-8 A) identified were  $\text{OH}^-$ ,  $\text{O}^-$ ,  $\text{AlO}_2^-$  and  $\text{Al}^+$  whilst positive ions were  $\text{K}^+$  and  $\text{Na}^+$  salts on the bare aluminium base (Figure 5-8 B). Deposition of carboxysilane was confirmed by a number of organic fragments detected (Figure 5-8 C). There were  $\text{CH}_3\text{O}^-$ ,  $\text{C}_2\text{H-CH}_3\text{O}^-$ ,  $\text{CH}^-$  ions in negative scans and  $\text{Al}^+$  and  $\text{Si}^+$ ,  $\text{CH}^+$ ,  $\text{CH}_3^+$  ions present in positive scans. Successful attachment of amino acid taurine (Figure 5-7D) and generation of a sulfonate surface was observed by  $\text{SH}^-$  groups rather than  $\text{SO}_3^-$  which was not observed at 80 AMU as this group is not easily ionised. Layer by layer deposition also showed the reduction in aluminium signal as the organic layer depth increased.

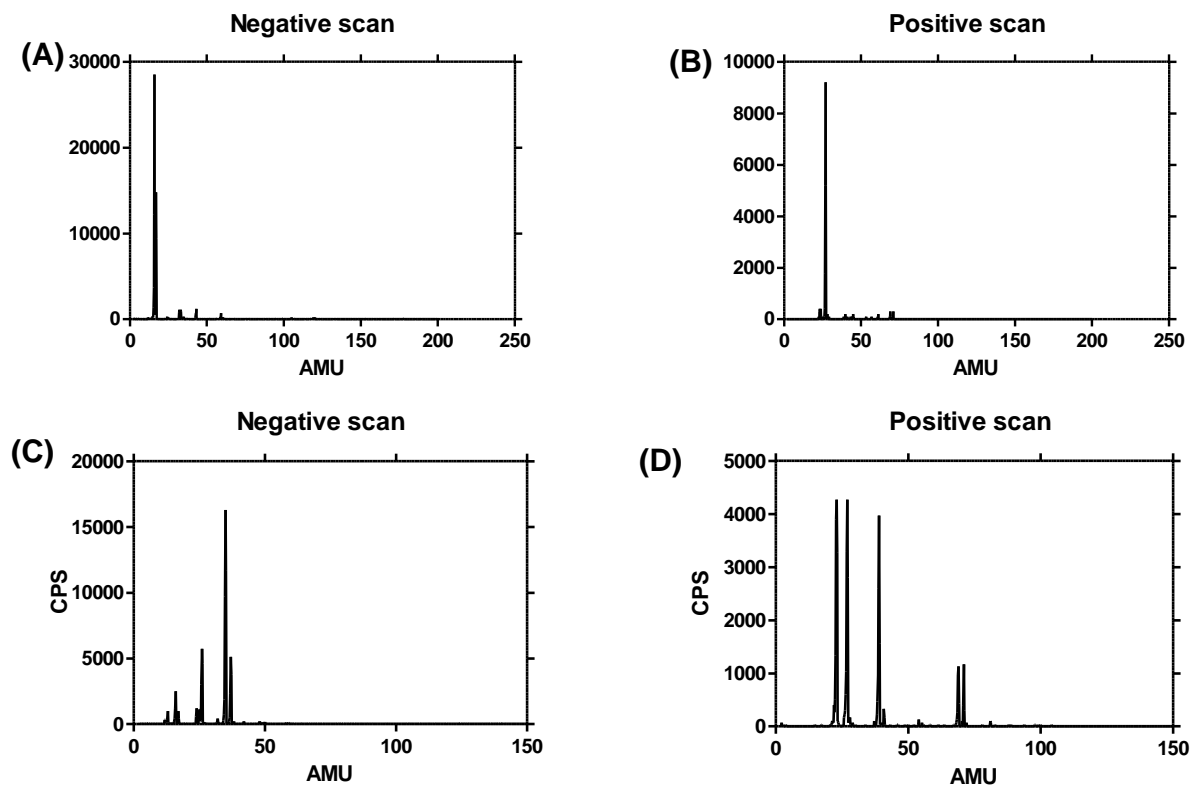


Figure 5-5 – Secondary ion mass spectroscopy analysis of functionalised surfaces. (A), positive and (B), negative scans of an aluminium base layer with generated hydroxyl base layer. An aluminium substrate was then modified with the desired functional silane including (C) carboxylate and (D), sulfonate.

### 5.6.2 Fourier transform infrared spectroscopy of surfaces

Surfaces were analysed using absorption peaks in the infrared region as was performed with the nanoparticles (Chapter 4). Microscopy images of the surfaces are presented in Figures 5-6 A, 7 A, 8 A, 9 A. FTIR spectra are presented in Figures 5-6 B, 5-7 B, 5-8 B and 5-9 B where 3 different regions per sample were averaged, 30 readings averaged per point.

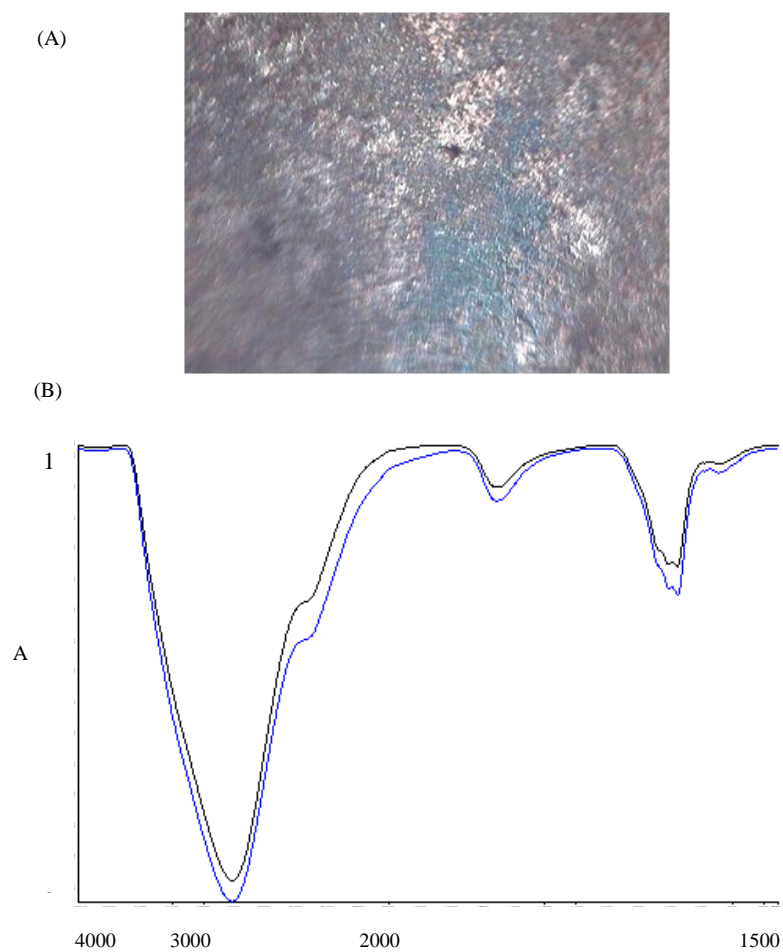


Figure 5-6 – Bare aluminium surface. (A), microscope image of aluminium surface, 1 min piranha treated hydroxyl layer. (B), triplicate FT-IR transmission mode scans of three different areas per sample. The sample was prepared by abrasion with 200  $\mu\text{m}$  diamond powder before a 1 min piranha wash to create a surface hydroxyl coating.

Bare oxide and hydroxyl surfaces were analysed to establish the unmodified surfaces and identify peaks present in all subsequent samples (Figure 5-6). New absorption peaks were then attributed to functionalisation of the surfaces.

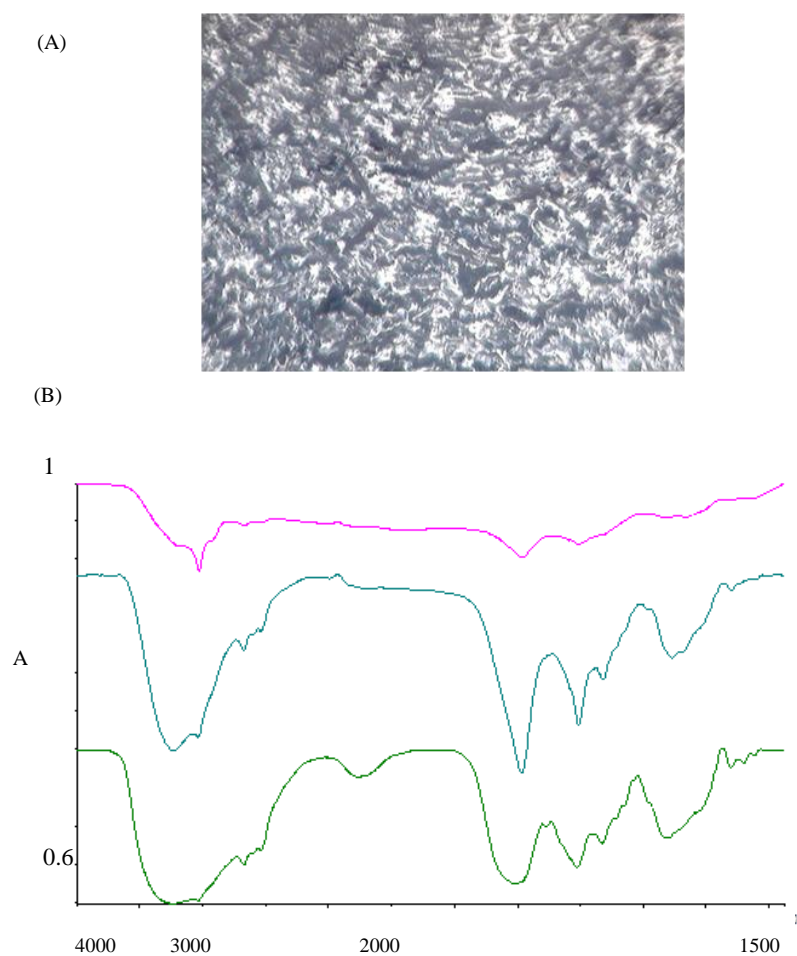


Figure 5-7 - Carboxysilane on aluminium substrate. Surfaces were prepared at pH 5.5, 4 h RT deposition of 5 % (v/v) silane, 2 % (v/v) water in ethanol. (A), microscope image of aluminium surface, 1 min piranha treated hydroxyl layer. (B), triplicate FT-IR transmission mode scans of three different areas per sample.

Large peaks attributed to  $\text{Al}_2\text{O}_3$  resulted in a broad absorbance at  $3100\text{ cm}^{-1}$ , which is known to be present in  $\text{M}_2\text{O}_3$  structures. The  $1050\text{-}1100\text{ cm}^{-1}$  absorption correspond to  $\text{Al}^{\text{IV}}\text{-O}$  bond stretching while  $850\text{-}900\text{ cm}^{-1}$  bulk stretching. A broad minor peak at  $3700\text{-}3800\text{ cm}^{-1}$  was attributed to five types of hydroxyl stretching [220].

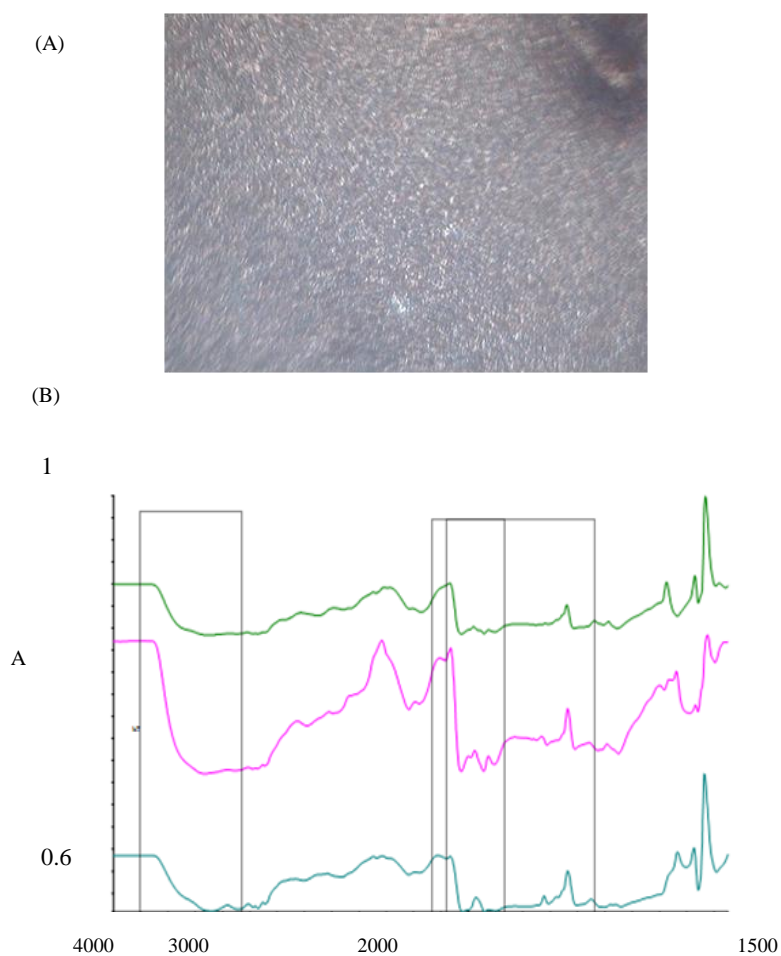


Figure 5-8 – EDTA silane on aluminium. (A), microscope image of aluminium surface imaged. (B), triplicate FT-IR transmission mode scans of three different areas per sample. Sample prepared as 5 % (v/v) EDTA-silane reacted in 2 % (v/v)  $\text{dH}_2\text{O}$  in ethanol as a 4 h surface condensation reaction to  $\text{AlOH}$  surface layer.

A number of peaks corresponded both to EDTA silane (Figure 5-8) and carboxysilane (Figure 5-9). The EDTA chelating group  $-N(CH_2COOH)_2$  is known to give strong bands in the range between  $1735$  and  $1550\text{ cm}^{-1}$  [221] due to  $C=O$  stretching vibration [222]. Peaks  $1268$ ,  $1336$ ,  $1409\text{ cm}^{-1}$  and two peaks at  $1600\text{ cm}^{-1}$  and  $1650\text{-}1680\text{ cm}^{-1}$  all correspond to FTIR spectra of the free acid and sodium salt forms of EDTA adsorbed on the surface of  $Al_2O_3$  [221].

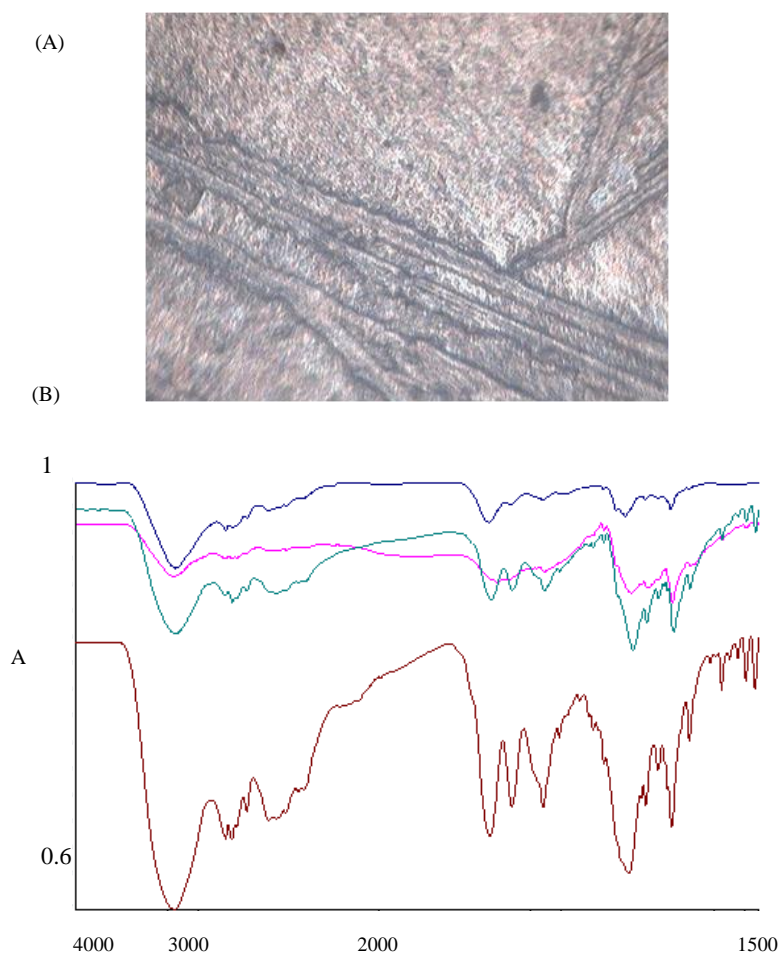


Figure 5-9 – Carboxysilane condensed on aluminium. (A), microscope image of aluminium surface. (B), triplicate FT-IR transmission mode scans of three different areas per sample. Samples were prepared as 5 % (v/v) carboxysilane reacted in 2 % (v/v)  $dH_2O$  in ethanol for 4 h. A EDAC/sulfo-NHS reaction to bond amino acid taurine was performed to form a sulfonic acid coated surface.

Broad peaks at 3000 – 3400  $\text{cm}^{-1}$  were presumed due to a combination of  $\text{Al}_2\text{O}_3$   $\text{cm}^{-1}$  and  $\text{SiOH}$  vibrational bonds, silica (3750  $\text{cm}^{-1}$  and 3742  $\text{cm}^{-1}$ ) or unreacted silanols (3200 -3600  $\text{cm}^{-1}$ ) [220].

The commercial sulfonate functionalised silane failed to undergo hydrolysis and silanol condensation. As result two alternative methods were used to create sulfonic acid surfaces. One was the oxidation of mercapto groups using sulphuric acid (see Chapter 4 section 4.11.3). The other was to peptide bond the sulfonate containing amino acid taurine via its free amine group to a carboxylic coated surface (Figure 5-9). Comparing the known free molecule taurine FTIR spectrum peaks from available spectra [204] 20 of the 23 expected peaks were observed between 700 to 1600  $\text{cm}^{-1}$ . However, the three peaks between 1400  $\text{cm}^{-1}$  and 1700  $\text{cm}^{-1}$  are noticeably broader and more intense. In comparison to the blank aluminium surface scans, large peaks attributed to  $\text{Al}_2\text{O}_3$ , broad absorbance at 3100  $\text{cm}^{-1}$  caused by  $\text{M}_2\text{O}_3$  structures have shifted to 3360  $\text{cm}^{-1}$ . The 1050-1100  $\text{cm}^{-1}$   $\text{Al}^{\text{IV}}\text{-O}$  bond stretching were present but overlap taurine peaks. 850-900  $\text{cm}^{-1}$  peaks corresponded to bulk stretching, with minor a peak at 3700-3800  $\text{cm}^{-1}$  attributed to five types of aluminium-hydroxyl stretching.

### 5.6.3 Thickness of deposited silane layers - FIB TEM analysis

Imaging organic samples via microscopy is always significantly more challenging than the analysis of inorganic layers. This is because they consist of low atomic elements than scatter the incident electron beam less, and also the tendency to result in sample charging with time during analysis causing blurring, drift and sample damage. However, perseverance and a modified FIB protocol allowed visual differentiation of bulk silica (Figure 5-10 A) and silane layers (Figure 5-10 B) on a supporting silica (glass) substrate. This involved a lateral cleaning etch to remove disturbed and redeposited organics after the initial etch, and a second platinum deposition into the exposed trench which removed charging which can often be mistakenly identified as organic layer deposition. EDX analysis of the bulk layer was similar to that seen with the nanoparticles, in than nitrogen could not be detected because of low atomic mass and little beam scattering. EDTA was identified by its chelation affects, with significant calcium and magnesium spikes that only occur at the EDTA interface (Figure 5-10). Because the etched depth is controlled with FIB, direct comparative quantification of elements between base glass layer and silanised layer is possible unlike with conversional SEM or TEM. A significant silicon peak was observed at the organic interface confirming deposition, also supported by a higher oxygen count from the TEOS silanol groups (Figure 5-10 B). A lateral etch performed on a smooth, level uniform area identified a 47.9 nm

organic layer (Figure 5-10 C), not dissimilar to that on silica EDTA nanoparticles grown for an equal time which ranged from 10 – 100 nm in diameter.

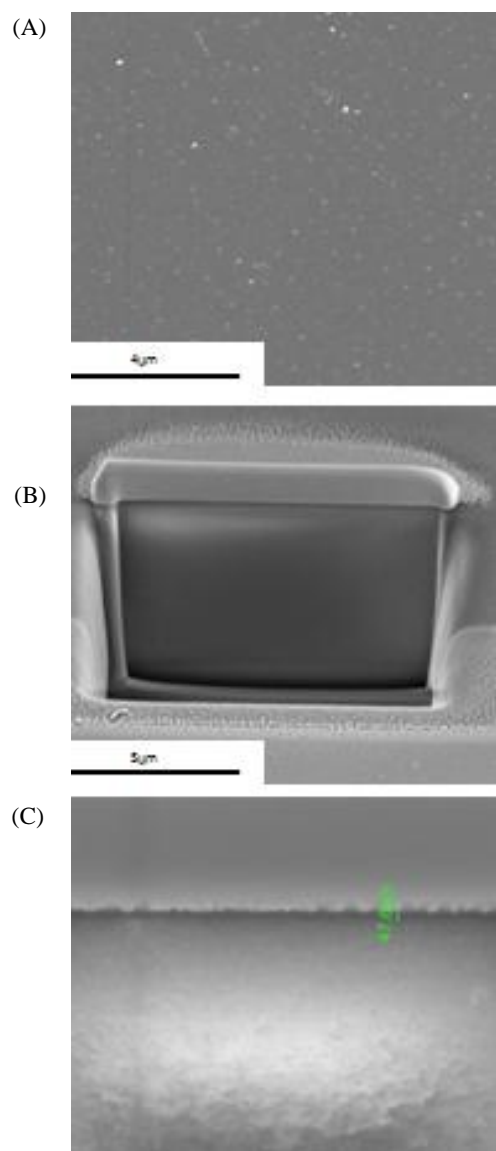


Figure 5-10 – FIB etching and cross section analysis of EDTA silane layer deposited onto silicon dioxide substrate. (A), surface overview; (B), trench etched into the sample with Pt resist layer; (C), magnification of the Pt-organic-silica interface and sizing of organic silane layer.

#### 5.6.4 Functionalised surfaces and binding of radionuclides

The various functionalised surfaces were tested for binding capacity under saturation conditions. Samples were pre-equilibrated in 1 M HCL containing 0.1 M NaCl solution before typically a 10 kBq stock of either  $^{90}\text{Sr}^{2+}$  or  $^{137}\text{Cs}^+$  was flowed over the surface continually for 1 h. The surfaces were then washed for 10 min with  $\text{dH}_2\text{O}$  to remove non-specifically bound ions, then the amount of radionuclide bound quantified using scintillation counting. For removal of analyte and rebinding experiments, an ethanol wash was used to remove scintillation fluid, the sample remounted into the flow rig and then the appropriate washing solution used. The sample was again counted with scintillation fluid before the whole cycle repeated.

##### 5.6.4.1 Functionalised capillaries and $^{90}\text{Sr}^{2+}$ binding

Figure 5-11 shows that there is significant variation in binding saturation between samples produced by the same method and within the same batch. While surfaces fail to bind  $^{90}\text{Sr}^{2+}$  at pH 1 due to nitrogens, carboxylates or glass silanols all being in protonated form, there is great variation at pH above 2. While the average CPM bound at pH 7 and pH 11 ranged from 322 to 458 CPM, the variation above and below this average were significant. The reason for this variation is most likely due to inhomogeneous silane deposition. The deposition solution, once aspirated into the capillaries by capillary force, was not uniform although the solution was static and covered the entire available surface area. Higher deposition often occurred around the edges of the tube and at the solution meniscus suggesting the higher surface tension resulted in higher rates of silanol condensation at the tube openings. These areas could be physically cut off from the end of the capillaries to increase uniformity. The average mg of strontium ions bound is summarised in Table 5-2. Significant variation between samples is observed particularly in increasingly acidic environments (pH 2) where increased protonation reduced the chelating ability of the surfaces.

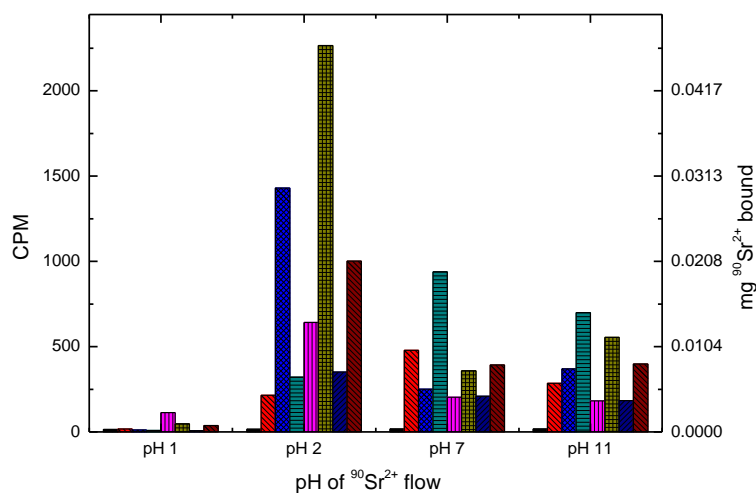


Figure 5-11 – Functionalised EDTA glass capillaries and saturation binding quantities of  $^{90}\text{Sr}^{2+}$  under analyte flow as a function of pH. Samples were background corrected and compared to an unfunctionalised capillary. •, scintillation fluid only control, •, unfunctionalised glass capillary control. Other bars are identically prepared EDTA functionalised capillaries (EDTA 1 - 5) are shown to illustrate inter batch variation.

Table 5-2 – Normalised background corrected saturation binding data of EDTA functionalised capillaries. Bound  $^{90}\text{Sr}^{2+}$  is extrapolated to counts per min or as a mass per  $\text{mm}^2$  of capillary surface.

	Average CPM	mg $^{90}\text{Sr}^{2+}$ bound	mg $^{90}\text{Sr}^{2+}$ bound per $\text{mm}^2$ area
pH 1	37.3	0.000777	$9.90 \times 10^{-7}$
pH 2	1002.0	0.0208	$2.65 \times 10^{-5}$
pH 7	392.3	0.00817	$1.04 \times 10^{-5}$
pH 11	397.9	0.00829	$1.05 \times 10^{-5}$

Mercapto and sulfonate surfaces tested under the same conditions were performed at pH 1 and 7. Minimal binding occurred at pH 1. However, reproducible behaviour was observed at pH 7 (Figure 5-12). The mercapto surfaces performed poorly compared to the nanoparticles binding less than  $1 \mu\text{g}$  of the radionuclide. This suggested that the binding capabilities of the nanoparticles came from the three dimensional conformations created by the condensation on to silica, as opposed to planar

geometries on two dimensional silica. Sulfonate surfaces managed to bind less than 4 µg per entire capillary. The normalised areas are summarised in Table 5-3.

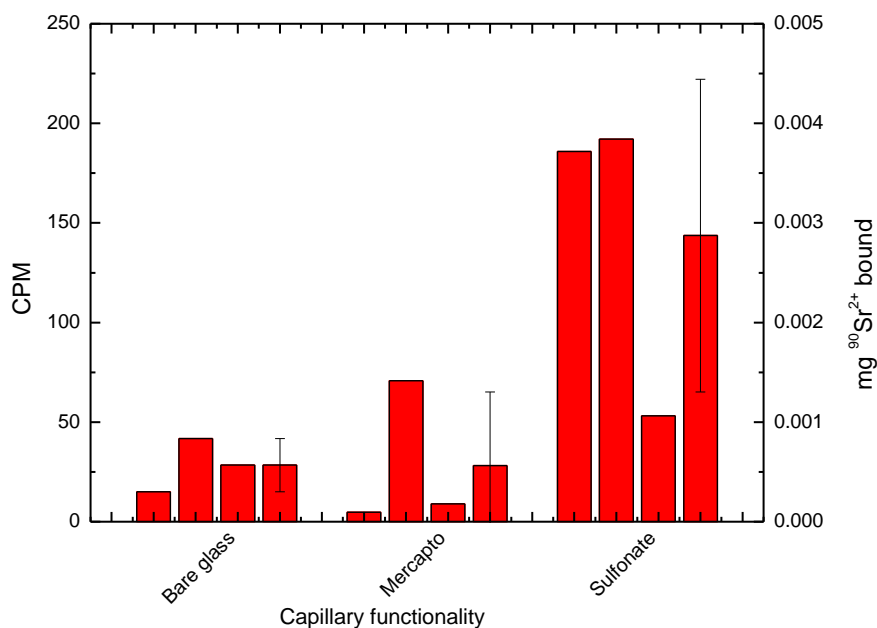


Figure 5-12 - Functionalised mercapto and sulfonate glass capillaries showing saturation binding of <sup>90</sup>Sr<sup>2+</sup> under analyte flow at pH 7. Samples triplicates versus an unfunctionalised glass capillary to account for nonspecific binding are shown.

Table 5-3 - Normalised saturation binding data of functionalised capillaries at pH 7. Bound <sup>90</sup>Sr<sup>2+</sup> is extrapolated to counts per min or as a mass per mm<sup>2</sup> of capillary surface area.

Capillary		mg <sup>90</sup> Sr bound	mg <sup>90</sup> Sr mm <sup>2</sup> area
Bare glass	28.42	5.92x10 <sup>-4</sup>	7.54 x10 <sup>-7</sup>
Mercapto	28.17	5.87 x10 <sup>-4</sup>	7.48 x10 <sup>-7</sup>
Sulfonate	143.67	2.99 x10 <sup>-3</sup>	3.81 x10 <sup>-6</sup>

#### 5.6.4.2 Functionalised capillaries and <sup>137</sup>Cs<sup>+</sup> saturation binding

In the case of binding <sup>137</sup>Cs<sup>+</sup> ions, deviation between triplicate samples was narrower (Figure 5-13) but the amount bound was between one and three magnitudes lower (Table 5-4) (10<sup>-7</sup> to 10<sup>-8</sup> mg mm<sup>2</sup>) compared to <sup>90</sup>Sr<sup>2+</sup> levels bound (10<sup>-5</sup> mg mm<sup>2</sup>).

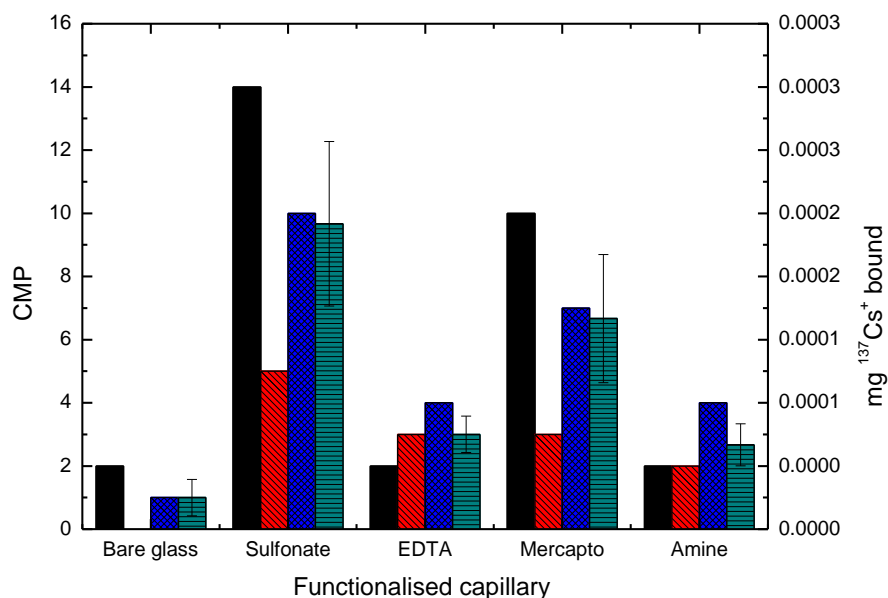


Figure 5-13 –Functionalised glass capillaries and saturation binding with  $^{137}\text{Cs}^+$  under analyte flow pH 7. ●, ●, ● are sample triplicates (functionalised capillary 1-3); ●, the average with SD to illustrate batch variation.

Table 5-4- Normalised saturation binding data of functionalised capillaries. Bound  $^{137}\text{Cs}^+$  is extrapolated to counts per min or as a mass per  $\text{mm}^2$  of capillary surface area.

Capillary	Average CPM	$\text{mg } ^{137}\text{Cs}^+$ bound	$\text{mg } ^{137}\text{Cs}^+$ $\text{mm}^2$ area
Bare glass	1.0	$2.08 \times 10^{-5}$	$2.65 \times 10^{-8}$
Sulfonate	9.7	$2.01 \times 10^{-4}$	$2.56 \times 10^{-7}$
EDTA	3.0	$6.25 \times 10^{-5}$	$7.96 \times 10^{-5}$
Mercapto	6.7	$1.38 \times 10^{-4}$	$1.76 \times 10^{-7}$
Amine	2.7	$6.66 \times 10^{-1}$	$8.49 \times 10^{-4}$

#### 5.6.4.3 Capillary recycling and poisoning

Capillary surfaces were flushed after binding with a 10 mM PBS pH 1 wash so that the chelation groups could reprotonate, and the high concentration of sodium ions within the PBS could competitively replace the bound radionuclide ions. After an initial wash 5 EDTA capillaries showed between 96.4 % and 98.4 % recovery and reduction in scintillation counts (Figure 5-14 A).

However, after a second cycle the removal of  $^{90}\text{Sr}^{2+}$  ions was significantly lower reducing the reusability of the capillaries. Further washes were used to elucidate if this poisoning effect was from incomplete competitive binding from the high salt buffer wash or that the length of the reprotonation wash was not long enough (Figure 5-15).

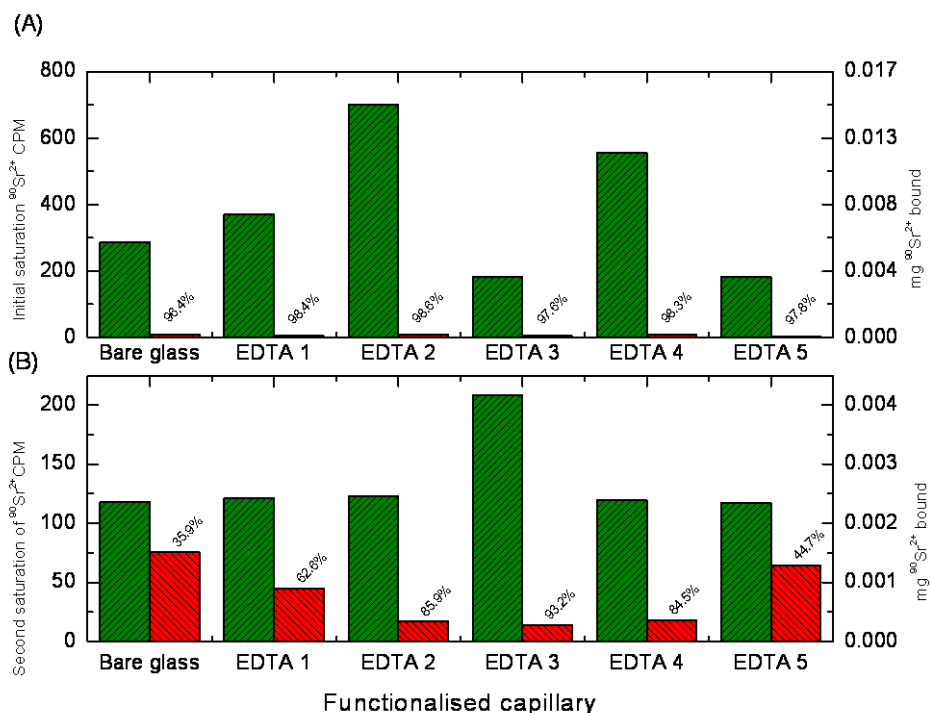


Figure 5-14 – Saturation binding and reusability of EDTA coated capillaries. Five identical samples (EDTA 1 – 5) were used in repeated binding and debinding experiments. Green bars show  $^{90}\text{Sr}^{2+}$  binding. Red bars show the amount remaining after a low pH acidic wash to reprotonate chelator sites. Percentages show the percent removal of  $^{90}\text{Sr}^{2+}$  ions after each wash. (A), the initial binding saturation of  $^{90}\text{Sr}^{2+}$  ions; (B), the second saturation amount of  $^{90}\text{Sr}^{2+}$  ions, of reused samples under identical conditions.

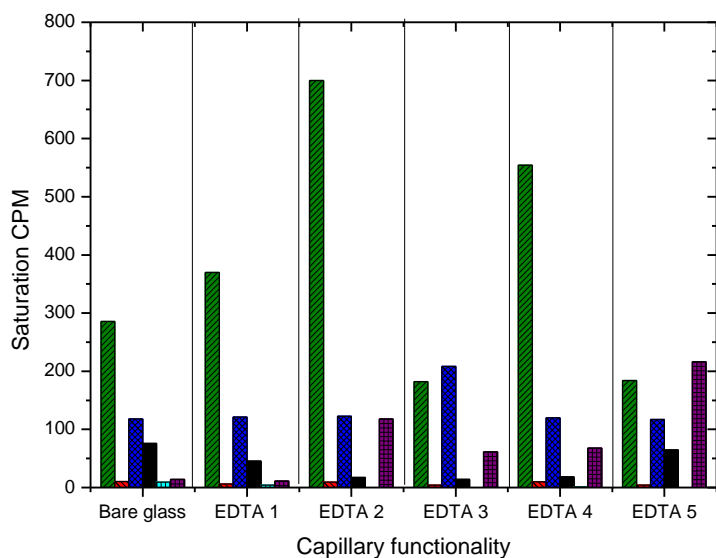


Figure 5-15 - Five identical EDTA capillaries under repeated saturation and washing. Bars correspond to; ●, initial incubation with  $^{90}\text{Sr}^{2+}$ ; ●, after a 10 min pH1 10 mM PBS wash; ●, second initial incubation with  $^{90}\text{Sr}^{2+}$ ; ●, a 20 mins pH 1 wash (no competing salt); ●, a 10 min 0.1 M HCl wash with 0.1M NaCl and ●, a third initial incubation with  $^{90}\text{Sr}^{2+}$ .

After the initial incubation with  $^{90}\text{Sr}^{2+}$ ; all capillaries recovered to above 95% capacity using a 10 min pH 1 wash which contained 10 mM PBS (Figure 5-15 green and red bars). However, the subsequent binding capacity which was reduced to below 50 % of the original maximum (blue bars). A more concentrated acid reprotonation wash did not significantly remove bound strontium ions (20 mins pH 1 wash, black bars), although a third wash of stronger acid and 10 x the competing salt concentration (10 min 0.1 M HCl wash with 0.1M NaCl) was enough to remove most of the bound  $^{90}\text{Sr}^{2+}$  ions on the capillaries and return the observed CPM close to zero (turquoise bars). However, when tested under a third  $^{90}\text{Sr}^{2+}$  incubation, four of the samples bound significantly lower amounts than the second  $^{90}\text{Sr}^{2+}$  binding. This suggests either damage or reduced efficacy of the capillaries from the high acid wash. This variation showed that capillaries may be reused several times but efficiency and binding density appears to drop with multiple uses even if the analyte is successfully removed using a high 0.1 M NaCl wash.

### 5.6.5 Fibre size visualisation and size change after silanisation

As well as the capillaries, functionalised nanofibres were produced to act as high surface area chelating sorbents. Five types of nanofibres, all consisting of a polyacrylonitrile base polymer, were produced under varying flow rates, relative humidity and temperature and were tested against the functionalised capillaries. Although types one and two were created under the same conditions, fibre type two showed a significantly lower fibre density, was difficult to handle and completely crumpled under solvent immersion making them unusable. They were not subsequently used in binding experiments. The remaining four fibre types were coated with a base layer formed from isocyanate silane which covalently bonds to available amines on the nanofibre polymeric backbone. This leaves three silanol groups per bound silane molecule exposed on the fibre surface that were then reacted with varying amounts of EDTA silane and sized using FEG TEM. The images of fibre type four are shown (Figure 5-16 A) which were typical of the other fibre types. The bare fibres and modification with isocyanate silane, and EDTA silane are shown. As well as the bulk physical property change, silanisation was able to be observed directly as the bare fibres had a visible surface roughness that is replaced with a smooth glass layer after reaction with silane (cf Figure 5-16 A with Figure 5-16 B - D).

For sizing of fibre types, three different regions per sample were chosen and a minimum of five sizing measurements per region were sized using analysis software, the average diameters summarised in Table 5-5 and Figure 5-17 A -B. Of the bare fibres, type four displayed the narrowest diameter ( $204.25 \pm 19.03$  nm) and five the widest ( $968.78 \pm 149.13$  nm). It can be seen that the faster the injection flow rate, the narrower the fibre diameter. Secondly, a higher growth temperature resulted in a wider fibre diameter. The same can be said for a more humid growth environment (Figure 5-17 A and B). The bare fibre diameters varied significantly, with fibre type five (FT 5) approaching  $1 \mu\text{m}$ , four times the size of the smallest FT 4. Base layer deposition of the isocyanate silane layer increased FT 3 and FT 4 controllably, both increasing diameter by approximately 800 nm. FT 1 and FT 5 showed an apparent decrease in size but widened SD error bars, showing regions of fibres grew significantly while others were not significantly altered by the deposition. Growth was not homogeneous in these cases.

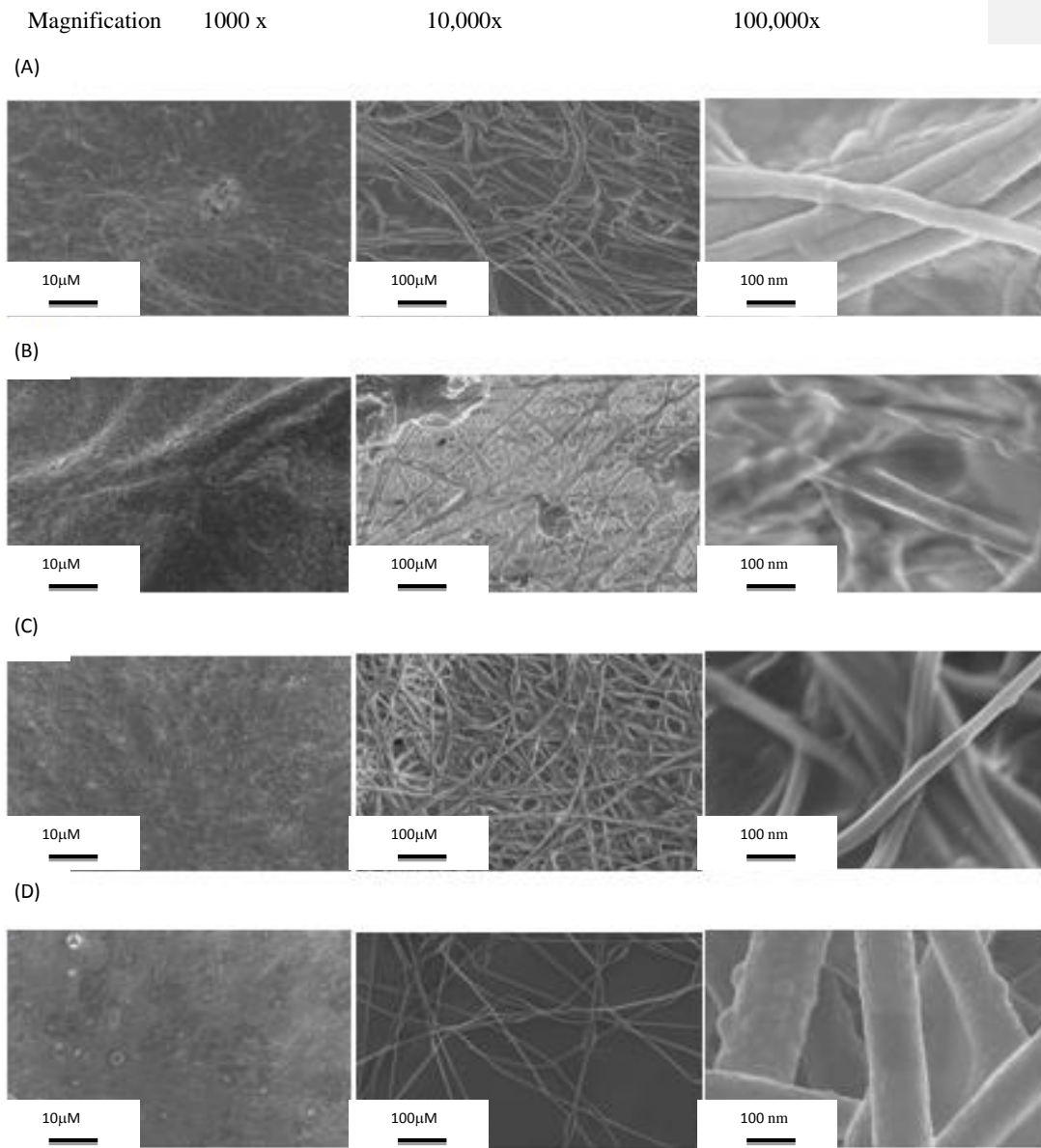
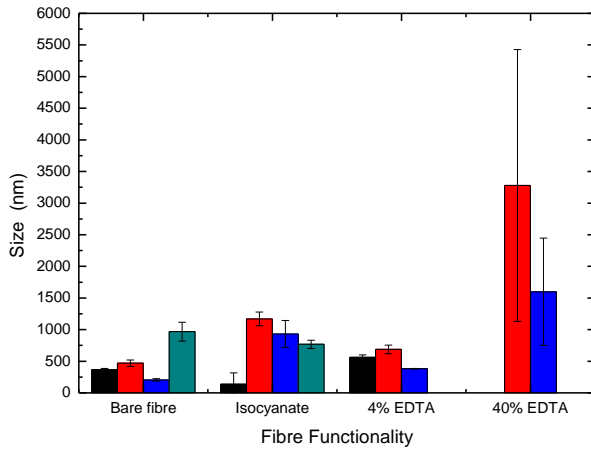


Figure 5-16 - FEG SEM images of FT 4 nanofibres. Left to right shows increasing magnification of fibres (1 k, 10 k and 100 k). Fibres used were (A), bare fibres; (B), as (A) with isocyanate modification; (C), as (B) with 4 % (v/v) EDTA silane; (D), as (B) with 40 % (v/v) EDTA silane.

(A)



(B)

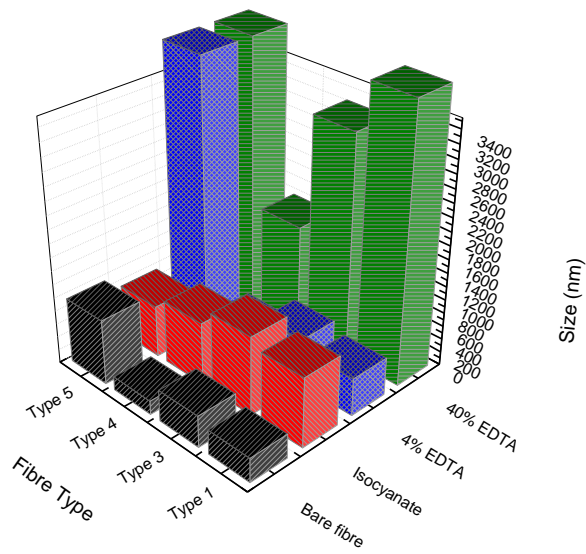


Figure 5-17 - Change in fibre diameter as a function of chemical modification. Diameters were averaged from a minimum of n=5 sampling at a 10,000 magnification. Fibre diameter sizing averages based on SEM analysis. (A), fibre diameter averages as a function of fibre modification. (B), diameter comparison of all fibre types as a function of silane modification.

Table 5-5 – Nanofibre diameter averages as a function of silane modification. Summary of Figure 5-17 B. Empty values are because fibre diameter grew too large.

Fibre functionality	FT 1 average (nm)	SD	FT 3 average (nm)	SD	FT 4 average (nm)	SD	FT 5 average (nm)	SD
Bare fibre	363.5	22.6	468.9	51.7	204.2	19.0	968.7	149.1
Isocyanate	136.2	181.2	1168.1	109.0	931.0	212.8	767.2	64.4
4% EDTA	561.1	38.1	686.7	67.9	381.7	5.1		
40% EDTA			3279.3	2148.1	1599.0	849.1		

Regardless of the inhomogeneous deposition of the silane layers, all fibres showed significant diameter growth upon addition of functional silane. Figure 5-17 B visually shows the direct comparison of diameter increase of all FT as a function of modification step. Fibres were then tested for radionuclide binding.

## 5.7 Functionalised nanofibres and radionuclide saturation binding

Binding experiments with  $^{90}\text{Sr}^{2+}$  or  $^{137}\text{Cs}^+$  further confirmed the variation between fibre batches as observed from TEM analysis. Although silanisation was confirmed both with TEM and FTIR, the binding capacity was significantly lower than with functionalised nanoparticles and comparable to that seen with capillaries (Figure 5-18). While the standard deviation between samples remained lower than with capillaries, at present the capacity would not be satisfactory for a reproducible sorbent surface.

The bare fibres showed erratic, but large amounts of radionuclide binding for both  $^{90}\text{Sr}^{2+}$  ions (Figure 5-18 A) and  $^{137}\text{Cs}^+$  ions (Figure 5-18 B) and despite washing steps (Figure 5-18 A black bars). This suggested the behaviour is based on an electrostatic attraction rather than non-specific binding. The bare fibres in fact bound far more  $^{137}\text{Cs}^+$  ions than the functionalised surfaces suggesting the silanisation was passivating an inherent electrostatic nature of the fibre polymer backbone. However, averages of  $^{90}\text{Sr}^{2+}$  binding were consistent, reproducible and significantly higher than the non-specific binding shown by bare fibres.

Comparison of  $^{90}\text{Sr}^{2+}$  (red bars) and  $^{137}\text{Cs}^+$  (green bars) binding (Figure 5-18 C) displayed the same behaviour as with NPs and capillaries. That is, that due to the ion valences, significantly greater amounts of  $^{90}\text{Sr}^{2+}$  bound (2-23 fold more bound than  $^{137}\text{Cs}^+$  ions).

FT 1 and FT 5 bound the most radionuclide, but FT 1 showed significant variation between samples. Only FT 5 showed a reproducible saturation limit. This behaviour correlates with the TEM fibre sizing which showed that FT 1 and 5 grew the most significantly, but inhomogeneously, which resulted in the inconsistent binding behaviour.

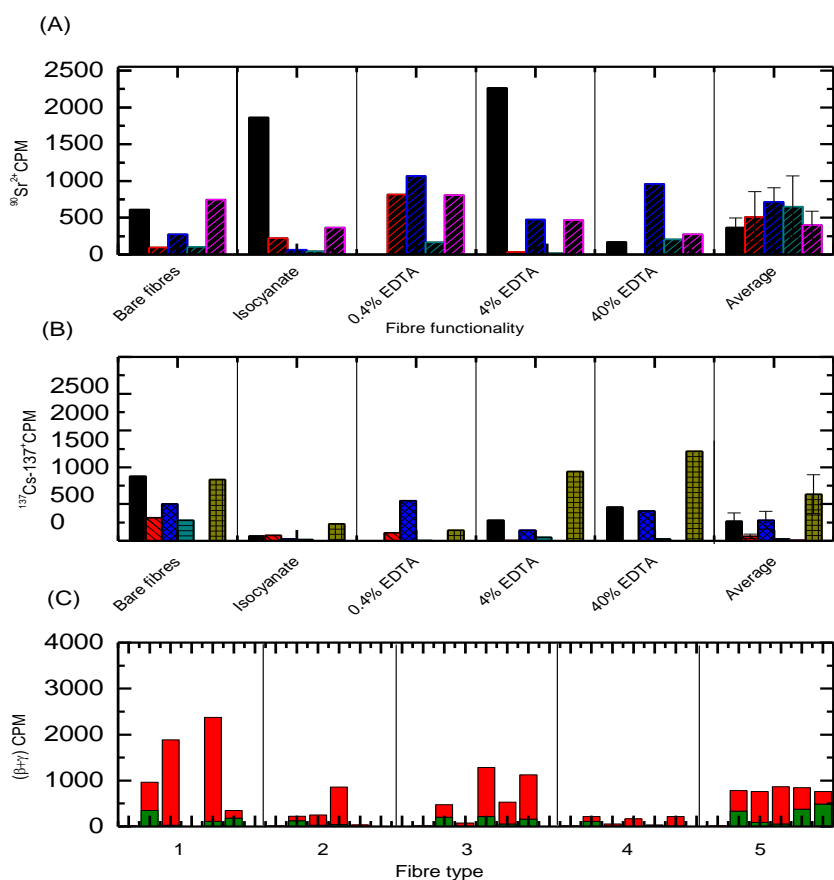


Figure 5-18 – Binding of  $^{90}\text{Sr}^{2+}$  and  $^{137}\text{Cs}^{+}$  ions by functionalised nanofibres. 2.5 cm square panels of fibres were incubated in synthetic ground water spiked with  $^{90}\text{Sr}^{2+}$  and  $^{137}\text{Cs}^{+}$  ions to give a total activity of 10 kBq. Samples were and incubated for 1 h. n=5 per sample. Black bars show binding of unfunctionalised bare fibres in comparison to 5 identical functionalised samples. (A), binding of  $^{137}\text{Cs}^{+}$  ions; (B), binding of  $^{90}\text{Sr}^{2+}$  ions; (C), relative amounts of  $^{90}\text{Sr}^{2+}$  (red bars) and  $^{137}\text{Cs}^{+}$  (green bars) bound.

## 5.8 Commercial resins and binding of radionuclides from contaminated synthetic ground water

All surfaces were tested in synthetic ground water to determine if very low levels of radionuclide could be bound from ground water containing a significant amount of co-contaminants and interfering analytes. Using SGW (section 1.2) spiked with  $1 \text{ kBq L}^{-1} \text{ }^{90}\text{Sr}^{2+}$  and  $0.1 \text{ kBq L}^{-1} \text{ }^{137}\text{Cs}^{+}$ , typical radionuclide contaminant levels observed in Sellafield groundwater, along with cocontaminants KCl,  $\text{MgSO}_4 \cdot \text{H}_2\text{O}$ ,  $\text{MCl}_2$ ,  $\text{H}_2\text{O}$ ,  $\text{CaCO}_3$  sodium silicate,  $\text{NaNO}_3$ ,  $\text{NaCl}$  and  $\text{NaHCO}_3$  at pH 7.35 [5].

All samples including the SGW stock were below the limits of the  $\gamma$  counter for  $^{137}\text{Cs}^{+}$  ions which gave a zero CPM average in spite of continual counts with time during analysis.  $^{90}\text{Sr}^{2+}$  could be quantified by scintillation counting, albeit counts were low. The data are shown in Figure 5-19.

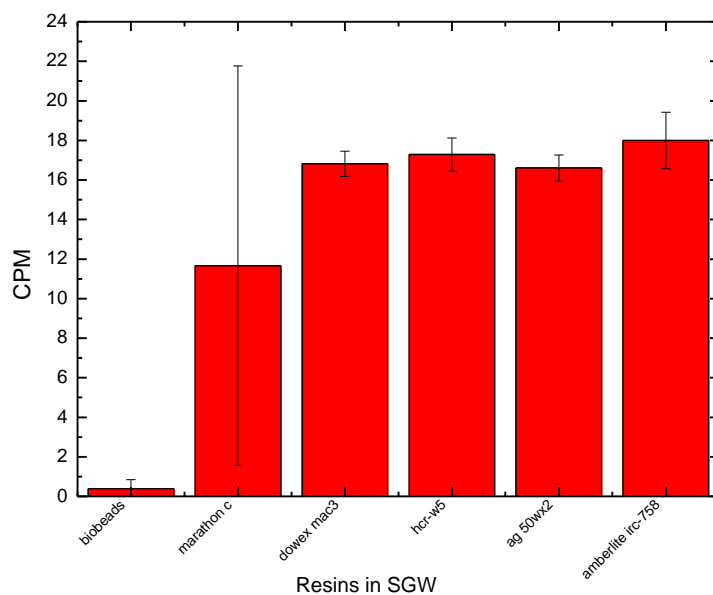


Figure 5-19 – Beta counting response of commercial resins incubated in Sellafield low level radioisotope contaminated synthetic ground water ( $n = 3$  per resin).  $50 \mu\text{l}$  of resin was incubated with  $50 \mu\text{l}$  of spiked SGW which contained  $1 \text{ kBq L}^{-1} \text{ }^{90}\text{Sr}^{2+}$  and  $0.1 \text{ kBq L}^{-1} \text{ }^{137}\text{Cs}^{+}$  ions.

The functionalised nanofibres and capillaries were unable to detect the required levels of radioactive contaminants typical of Sellafield groundwater. The commercial resins performed significantly better and were able to detect a reproducible amount of the  $^{90}\text{Sr}^{2+}$  ions present. Narrow standard deviations between four of the batches was achieved; Mac 3 ( $16.8 \pm 0.6$ ), Hdr-w5 ( $17.2 \text{ CPM} \pm 0.8$ ), Ag50wx2 ( $16.6 \text{ CPM} \pm 0.6$ ), Irc-758 ( $18.0 \text{ CPM} \pm 1.4$ ) CPM respectively. The only batch with significant error was the marathon resin C ( $11.6 \text{ CPM} \pm 10.1$ ) which showed poor reproducibility.

## 5.9 Conclusion

A range of silica surfaces were functionalised using two dimensional silanisation growth on glass capillaries or polymeric nanofibres. Capillaries showed moderate binding capacity but variation between batches was observed because of higher silanisation around the tube meniscus. Reusability was increased by recycling capillaries with a high salt – acid wash. Functionalised nanofibres were prepared in a similar manor with the aims of higher surface area specifically to give a higher binding capacity. Variation between these samples however was due to the random orientation of the fibres and inconsistent density of fibres. This however is a property of how the nanofibres are synthesised, only able to be produced in non woven disordered polymeric meshes.

In comparison, the solid scintillant NP managed to bind low levels of  $^{90}\text{Sr}^{2+}$  in contaminated synthetic ground water.

At such low levels of radionuclide, Emulsi Safe counting method was more reproducible with narrower variation between samples. For scintillation counting using either nanofibres or nanoparticles in a deployable device, an accumulation sensor which would continually bind analyte to well within detectable levels would be needed to increase reproducibility and reduce variation between batches. At saturation binding conditions and optimum pH (pH 2 – 11) EDTA NP bound 50 % of their own mass, an impressive loading capacity. Surprisingly, amines too while in protonated form bound a high amount of  $^{90}\text{Sr}^{2+}$  ions, between 10 and 45 % their own mass.

The nanofibres were also compared to the commercial resins Mac 3, Hdr-w5, Ag50wx2 and Irc-758 which performed superiorly to the functionalised surfaces which were able to bind low levels, but reproducible amounts of radioactive analyte from synthetic ground water.

## **6 : Conclusions, discussion and future work**

---

## 6.1 Project summary

The aim of the project was to design a number of surfaces with ion specificity to radionuclide contaminants common in U.K legacy waste sites such as those at Sellafield. Ideally, these surfaces were to allow specificity and selectivity to the radionuclides which were focused on  $\text{UO}_2^{2+}$ ,  $^{137}\text{Cs}^+$ , and  $^{90}\text{Sr}^{2+}$ . These binding mechanisms were to be coupled to a signal transducer which would convert the bind event into a quantifiable signal for real time monitoring.

In respects to these criteria, particular success was achieved for uranyl ions with the development of an impedance based biosensor. A novel uranyl biosensor for aqueous uranyl  $\text{UO}_2^{2+}$  ions used tethered surface layer proteins on gold substrates, interrogated by EIS at low frequency. The sensor showed minor interference from a number of divalent interferent ions  $\text{Ni}^{2+}$ ,  $\text{Cs}^+$ ,  $\text{Cd}^{2+}$  and  $\text{Co}^{2+}$ . Chemical modification of the JG-A12 binding protein by blocking of the phosphate and carboxyl groups prevented  $\text{UO}_2^{2+}$  binding, showing that both moieties were involved in the recognition to  $\text{UO}_2^{2+}$ .

Two bespoke tethering mechanisms based on short molecular linkers that created porous conductive membranes were developed that allowed potentially any biological receptor to be tethered to a gold electrode for use as a sensor component. However, due to the lack of available metal binding proteins for the desired analytes an alternative approach was taken for the other radionuclides.

A number of synthetic crown ether hosts were identified that had high specificity for  $\text{Cs}^+$ , and  $\text{Sr}^{2+}$  ions. These were either synthesised or a modification of commercially sourced crown ethers. These host molecules were combined with SAM surfaces and interrogated using a range of analytical methods in an attempt to monitor real time binding of analytes. This included EIS, real time CV and mass based gravimetry. While a number of interfacial phenomena were observed, a method of real time direct quantification of analyte binding was not achieved. An approximate mass based system for  $\text{Sr}^{2+}$  detection used a resorcinol calixarene - SAM format was shown to function in an 'on' or 'off' state, but was not sensitive enough to quantify the amount of analyte bound.

As a result, an alternative approach of creating high capacity surfaces, rather than those with specificities, was used to create functional chelators biosilica particles and nanofibres. The binding capacity and reproducibility of these surfaces were compared to the performance of a number of commercial chelating resins. Functionalised EDTA, sulfonate and amine particles showed excellent binding of  $^{90}\text{Sr}^{2+}$  ions at all pHs above pH 1, and were found to bind magnitudes more radionuclide ions than the commercial resins.

$^{137}\text{Cs}^+$  however bound in significantly lower amounts, with saturation amounts being lower than the commercial resins available. The same silanisation method was shown applicable to creating high surface bulk surfaces by coating of nanofibres. Functionalisation of nanofibres was confirmed but was found to be inhomogeneous across larger areas of the fibres because of variable fibre density. As a result the fibre binding performances were found to be variable, with poor reproducibility. This was also attributed to the inconsistent fibre density per unit area which is an unfortunate characteristic attributed to the electrospinning production method and not the functionalisation method.

A unique simultaneous condensation reaction also showed it was possible to create bifunctional silica particles which incorporated both chelator functionality and solid scintillant directly onto the particles, thus removing the need for scintillation cocktail for scintillation counting of  $\beta$  radiation. When tested in SGW containing radionuclide levels typical of U.K legacy sites detection of  $^{90}\text{Sr}^{2+}$  was possible, but  $^{137}\text{Cs}^+$  levels were below the sensitivity limits of available equipment. A more expensive environmental analysis grade machine would not be within the scope of a field implementable device.

In summary, a range of functionalised chelator surfaces were successfully made with affinity to  $\text{UO}_2^{2+}$ , and  $^{90}\text{Sr}^{2+}$ . The commercial resins remained the most successful as  $^{137}\text{Cs}^+$  sorbants. Further work is needed to utilise these surfaces to incorporate them into a field implementable device.

## 6.2 Future work

It is important to develop the prototype devices and sorbent surfaces reported within this thesis to field deployable devices. As such, they were tested in synthetic ground water under typical temperature, pH co-contaminant conditions. Future work will incorporate these into a bespoke microfluidics system, currently being developed by colleagues in the School of Civil Engineering at the University of Leeds. Ideally an automated assembly process would reduce variation between electrode and particle batches and could be combined with bespoke software for data analysis and interrogation.

Nanoparticles were grown in 50 ml container volumes yielding milligrams to grams. For large scale monodisperse particle production it has been shown that the growth of inorganic silica by use of a cross flow system via a slotted membrane can produce kilograms of monodisperse particles [223], and it would be interesting to see if this method will work with the biosilica particles.

While several particle functionalities have been demonstrated using methoxy condensation reactions, these particles are limited by the availability of the desired hydrolysable silanes. One alternative approach, with potential scalable yield is to use the alkyne particles as the precursor for click chemistry based reactions. Click chemistry is an emerging branch of chemistry that allows discrete molecular synthesis quickly and efficiently in high yields using thermodynamically driven reactions. While the number of reactions and practical chemistry is limited, the potential for controlled conjugated bio-, macro- and synthetic molecules is huge. Currently the most common of these reactions is Cu-catalysed azide-alkyne cycloaddition (CuAAC), ring open polymerisation (ROP), ring opening metathesis polymerisation (ROMP) cationic polymerisation, nitric oxide-mediated radical polymerisation (NMP), atom transfer radical polymerisation (ATRP) and reversible addition fragmentation chain transfer polymerisation (RAFT) [194, 215]. The range of molecules available for these reactions is far more than the available methoxy silanes and would allow a huge range of bespoke particles or surface functionalisations.

The nanofibres in current form showed poor reproducibility due to inconsistent fibre density, a product of the non-woven fibre production via the electrospinning process. However, as the nanoparticles showed, high surface area functionalised materials have great potential for chelator and remediation technologies, and an alternative nanofibre production method may alleviate these problems.

In particular, the success of the uranyl binding biosensor using SLP JG-A12 and the development of the two porous membrane linkers holds great potential for bespoke metal ion biosensors by screening microbiological species and extraction of relevant proteins for use as the sensing component. To date, there are few references to other sub nanomolar metal ion biosensors with specificity; the only prominent example being the MerR protein for  $\text{Hg}^{2+}$  ions [78]. MerR functions by undergoing a conformational change upon ion binding. The discovery or directed evolution of new metal ion binding proteins is clearly an area where potential for device development and commercialisation exists.

## 7 References

---

1. McBeth, J., et al., *Technetium Reduction and Reoxidation in Aquifer Sediments*. Geomicrobiology Journal, 2007. **24**: p. 189.
2. Keith-Roach, M.J., The speciation, stability, solubility and biodegradation of organic co-contaminant radionuclide complexes: A review. Science of The Total Environment, 2008. **396**(1): p. 1.
3. Nedeltcheva, T., et al., Determination of mobile form contents of Zn, Cd, Pb and Cu in soil extracts by combined stripping voltammetry. Analytica Chimica Acta, 2005. **528**(2): p. 143.
4. Bath, A., et al., *Geochemical indicators of deep groundwater movements at Sellafield, UK*. Journal of Geochemical Exploration. **90**(1-2): p. 24-44.
5. Wilkins, M.J., et al., The influence of microbial redox cycling on radionuclide mobility in the subsurface at a low-level radioactive waste storage site. Geobiology, 2007. **5**: p. 293.
6. Westlakes Scientific, C., A practicable and integrated groundwater monitoring programme proposed for the sellafield site. 2005.
7. WHO, Water Sanitation and Health (WSH) Water for health:WHO Guidelines for Drinking-water Quality (2010). 2010, World Health Organisation (WSH).
8. Sellafield, *Groundwater Annual report*. 2010: Seascale.
9. Roehl, R., K.E.; Meggyes, T.; Simon, F.G.; Stewart, D.I.K.E.; *Long-term Performance of Permeable Reactive Barriers*. 2005: p. 244.
10. Martinko, J.M., *Brock Biology of Microorganisms*. Eleventh edition ed. 2006: Pearson Prentice Hall.
11. Gherman, V.D., et al., The Sulphur and Iron Metabolism in Acidophilic Microbial Gelatinous Formations from an Auriferous Sulphides Mine from the South-West of Romania. Revista De Chimie, 2008. **59**(10): p. 1164-1168.
12. Bienert, G.P., M.D. Schuessler, and T.P. Jahn, *Metalloids: essential, beneficial or toxic? Major intrinsic proteins sort it out*. Trends In Biochemical Sciences, 2008. **33**(1): p. 20-26.

13. Imkus, R., et al., *Oscillatory luminescence from lux-gene engineered bacteria*. Biotechnology Techniques, 1999. **13**: p. 529.
14. Tauriainen, S., et al., *Luminescent bacterial sensor for cadmium and lead*. Biosensors and Bioelectronics, 1998. **13**(9): p. 931.
15. Barchiesi, D., N. Lidgi-Guigui, and M.L.d. la Chapelle, *Functionalization layer influence on the sensitivity of surface plasmon resonance (SPR) biosensor*. Optics Communications, 2012. **285**(6): p. 1619-1623.
16. Sun, Y., et al., Preparation of titania sol-gel matrix for the immunoassay by SPR biosensor with magnetic beads. Sensors and Actuators B: Chemical, 2008. **134**(2): p. 566-572.
17. Wang, R., et al., Regenerative Surface Plasmon Resonance (SPR) biosensor: Real-time measurement of fibrinogen in undiluted human serum using the competitive adsorption of proteins. Biosensors and Bioelectronics, 2011. **28**(1): p. 304-307.
18. Huang, C., et al., Detection of duck hepatitis virus serotype1 by biosensor based on imaging ellipsometry. Current Applied Physics, 2011. **11**(3): p. 353-357.
19. Liu, L., et al., Improvement for sensitivity of biosensor with total internal reflection imaging ellipsometry (TIRIE). Thin Solid Films, 2011. **519**(9): p. 2758-2762.
20. Jin, G., et al., Development of biosensor based on imaging ellipsometry and biomedical applications. Thin Solid Films, 2011. **519**(9): p. 2750-2757.
21. Dzyadevych, S.V., et al., *Amperometric enzyme biosensors: Past, present and future*. IRBM, 2008. **29**(2-3): p. 171-180.
22. Pchelintsev, N.A. and P.A. Millner, Development of surface activated screen-printed carbon transducers for biosensors application. Analytical Letters, 2007. **40**(7): p. 1317-1332.
23. Clark, L., *Monitor and control of blood and tissue oxygen tensions*. Trans Am Soc Artif Intern Organs 1956. **2**: p. 41-8.
24. He, P., et al., The studies of performance of the Au electrode modified by Zn as the anode electrocatalyst of direct borohydride fuel cell. International Journal of Hydrogen Energy, 2011. **36**(15): p. 8857-8863.
25. Cass, A., Biosensors. A practical approach. Theoretical methods for analysing biosensor performance 1990: Oxford University Press.

26. Romero, M.R., F. Garay, and A.M. Baruzzi, Design and optimization of a lactate amperometric biosensor based on lactate oxidase cross-linked with polymeric matrixes. *Sensors and Actuators B: Chemical*, 2008. **131**(2): p. 590-595.
27. Hnaïen, M., F. Lagarde, and N. Jaffrezic-Renault, A rapid and sensitive alcohol oxidase/catalase conductometric biosensor for alcohol determination. *Talanta*, 2010. **81**(1-2): p. 222-227.
28. Hu, S., et al., Biosensor for detection of hypoxanthine based on xanthine oxidase immobilized on chemically modified carbon paste electrode. *Analytica Chimica Acta*, 2000. **412**(1-2): p. 55-61.
29. Guerrieri, A., T.R.I. Cataldi, and R. Ciriello, The kinetic and analytical behaviours of an l-lysine amperometric biosensor based on lysine oxidase immobilised onto a platinum electrode by co-crosslinking. *Sensors and Actuators B: Chemical*, 2007. **126**(2): p. 424-430.
30. Bolton James, R. and D. Archer Mary, Basic Electron-Transfer Theory, in *Electron Transfer in Inorganic, Organic, and Biological Systems*. 1991, American Chemical Society. p. 7-23.
31. Yeh P, K., Reversible electrode reaction of cytochrome c. *Chem Lett*: p. 1145-8.
32. Ghindilis, A.L., et al., Potentiometric biosensors for cholinesterase inhibitor analysis based on mediatorless bioelectrocatalysis. *Biosensors and Bioelectronics*, 1996. **11**(9): p. 873-880.
33. Tkac, J., et al., Membrane-bound dehydrogenases from *Gluconobacter* sp.: Interfacial electrochemistry and direct bioelectrocatalysis. *Bioelectrochemistry*, 2009. **76**(1-2): p. 53-62.
34. Trashin, S.A., et al., Improvement of direct bioelectrocatalysis by cellobiose dehydrogenase on screen printed graphite electrodes using polyaniline modification. *Bioelectrochemistry*, 2009. **76**(1-2): p. 87-92.
35. Wang, H., et al., A hydrogen peroxide biosensor based on the bioelectrocatalysis of hemoglobin incorporated in a kieselgubr film. *Sensors and Actuators B: Chemical*, 2002. **84**(2-3): p. 214-218.
36. Nelson, A., N. Auffret, and J. Borlakoglu, *Interaction of hydrophobic organic compounds with mercury adsorbed dioleoylphosphatidylcholine monolayers*. *Biochimica et Biophysica Acta (BBA) - Biomembranes*, 1990. **1021**(2): p. 205.

37. Miller, I.R., The effect of interactions in the head groups on monolayer structure and permeability I.R. Miller, *Bioelectrochemistry and Bioenergetics*. *Bioelectrochemistry and Bioenergetics*, 1988. **19**: p. 551-567.
38. Nelson, L.A., Interaction of hydrophobic organic compounds with mercury adsorbed dioleoylphosphatidylcholine monolayers *Biophysica Acta*, 1990. **1021**: p. 205-216
39. Nelson, L.A. and N. Auffret, Phospholipid monolayers of di-oleoyl lecithin at the mercury/water interface. *J. Electroanal. Chem.* **244**: p. 99-113.
40. Nelson, A., Conducting Gramicidin Channel Activity in Phospholipid Monolayers. *Biophysical Journal*, 2001. **80**: p. 2694-2703.
41. Conroy, P.J., et al., *Antibody production, design and use for biosensor-based applications*. *Seminars in Cell & Developmental Biology*, 2009. **20**(1): p. 10-26.
42. Mosiello, L., et al., Development of a monoclonal antibody based potentiometric biosensor for terbuthylazine detection. *Sensors and Actuators B: Chemical*, 2003. **95**(1-3): p. 315-320.
43. Ercole, C., et al., A biosensor for Escherichia coli based on a potentiometric alternating biosensing (PAB) transducer. *Sensors and Actuators B: Chemical*, 2002. **83**(1-3): p. 48-52.
44. Sergeyeva, T.A., et al.,  *$\beta$ -Lactamase label-based potentiometric biosensor for  $\alpha$ -2 interferon detection*. *Analytica Chimica Acta*, 1999. **390**(1-3): p. 73-81.
45. Bard, A.J. and F. L.R., *Electrochemical methods Fundamentals and applications*. Second ed. 2001: Wiley.
46. Bockris, J.O.M. and S.U.M. Khan, *Surface Electrochemistry - A Molecular Level Approach*. 1993, Newyork and London: Plenum.
47. Bard, A.J. and L.R. Faulkner, *Electrochemical Methods Fundamentals and Applications*. Second ed. 2001: Wiley. 833.
48. Israelachvili, J., *Intermolecular and surface forces*. Second ed. 1991: Academic Press.
49. Esteban, M., et al., Voltammetry of metal ion--macromolecule interactions: Application to speciation problems. *TrAC Trends in Analytical Chemistry*, 1993. **12**(7): p. 276.
50. Chapman, C.S. and C.M.G. van den Berg, *Anodic stripping voltammetry using a vibrating electrode*. *Electroanalysis*, 2007. **19**(13): p. 1347-1355.

51. Castillo, J., et al., *Biosensors for life quality: Design, development and applications*. Sensors and Actuators B: Chemical, 2004. **102**(2): p. 179.
52. Marks, R.S. and D. Cullen, *Handbook of Biosensors and Biochips*. **1**: p. 686.
53. Salaun, P., B. Planer-Friedrich, and C.M.G. van den Berg, *Inorganic arsenic speciation in water and seawater by anodic stripping voltammetry with a gold microelectrode*. Analytica Chimica Acta, 2007. **585**(2): p. 312-322.
54. Salaun, P. and C.M.G. van den Berg, *Voltammetric detection of mercury and copper in seawater using a gold microwire electrode*. Analytical Chemistry, 2006. **78**(14): p. 5052-5060.
55. Locatelli, C. and G. Torsi, Simultaneous square wave anodic stripping voltammetric determination of Cr, Pb, Sn, Sb, Cu, Zn in presence of reciprocal interference: application to meal matrices. Microchemical Journal, 2004. **78**(2): p. 175-180.
56. Men, H., et al., *Novel All-State Heavy Metal Sensors and Analysis Instrument*. 2008 Chinese Control And Decision Conference, Vols 1-11, 2008: p. 1801-1805.
57. Van Den Berg, C.M.G. and Z. Qiang Huang, Determination of uranium(VI) in sea water by cathodic stripping voltammetry of complexes with catechol. Analytica Chimica Acta, 1984. **164**: p. 209.
58. Kefala, G., A. Economou, and A. Voulgaropoulos, Adsorptive stripping voltammetric determination of trace uranium with a bismuth-film electrode based on the U(VI)  $\rightarrow$  U(V) reduction step of the uranium-cupferron complex. Electroanalysis, 2006. **18**(3): p. 223-230.
59. Monk, P., Wiley Fundamentals of Electro analytical Chemistry. 2001: p. 185.
60. Marta C. Diaz, Supramolecular Pseudo-Rotaxane Type Complexes from pi-Extended TTF Dimer Crown Ether. ChemInform, 2006. **37**(18).
61. Arena, G., et al., Two Calix-Crown Based Stationary Phases. Synthesis, Chromatographic Performance and X-ray Photoelectron Spectroscopy Investigation. Journal of Supramolecular Chemistry, 2002. **2**(6): p. 521.
62. Woods, M., Z. Kovacs, and A.D. Sherry, *Targeted Complexes of Lanthanide(III) Ions as Therapeutic and Diagnostic Pharmaceuticals*. Journal of Supramolecular Chemistry, 2002. **2**(1-3): p. 1.
63. Ueda, M. and A. Tanaka, *Genetic immobilization of proteins on the yeast cell surface*. Biotechnology Advances, 2000. **18**(2): p. 121.

64. Cherian, S., et al., Detection of heavy metal ions using protein-functionalized microcantilever sensors. *Biosensors & Bioelectronics*, 2003. **19**(5): p. 411-416.
65. Guimarães-Soares, L., et al., Metal-binding proteins and peptides in the aquatic fungi *Fontanospora fusiramosa* and *Flagellospora curta* exposed to severe metal stress. *Science of The Total Environment*, 2006. **372**(1): p. 148.
66. Gupta, R.K., et al., *Metallothistins: A new class of plant metal-binding proteins*. *Journal Of Protein Chemistry*, 2002. **21**(8): p. 529-536.
67. Lee, M.H., S.B. Mulrooney, and R.P. Hausinger, Purification, characterization, and in vivo reconstitution of *Klebsiella aerogenes* urease apoenzyme. *J. Bacteriol.*, 1990. **172**(8): p. 4427-4431.
68. Kim, J.K., S.B. Mulrooney, and R.P. Hausinger, *The UreEF fusion protein provides a soluble and functional form of the UreF urease accessory protein*. *Journal Of Bacteriology*, 2006. **188**(24): p. 8413-8420.
69. Busenlehner, L.S., et al., Elucidation of Primary ([alpha]3N) and Vestigial ([alpha]5) Heavy Metal-binding Sites in *Staphylococcus aureus* pI258 CadC: Evolutionary Implications for Metal Ion Selectivity of ArsR/SmtB Metal Sensor Proteins. *Journal of Molecular Biology*, 2002. **319**(3): p. 685.
70. Branco, R., A.P. Chung, and P.V. Morais, Sequencing and expression of two arsenic resistance operons with different functions in the highly arsenic-resistant strain *Ochrobactrum tritici* SCII24(T). *Bmc Microbiology*, 2008. **8**.
71. Li, S., et al., Evidence for cooperativity between the four binding sites of dimeric ArsD, an As(III)-responsive transcriptional regulator. *Journal Of Biological Chemistry*, 2002. **277**(29): p. 25992-26002.
72. Lin, Y.F., A.R. Walmsley, and B.P. Rosen, *An arsenic metallochaperone for an arsenic detoxification pump*. *Proceedings Of The National Academy Of Sciences Of The United States Of America*, 2006. **103**(42): p. 15617-15622.
73. Kotrba, P., et al., Enhanced Bioaccumulation of Heavy Metal Ions by Bacterial Cells Due to Surface Display of Short Metal Binding Peptides. *Appl. Environ. Microbiol.*, 1999. **65**(3): p. 1092-1098.
74. Bae, W., et al., Genetic Engineering of *Escherichia coli* for Enhanced Uptake and Bioaccumulation of Mercury. *Appl. Environ. Microbiol.*, 2001. **67**(11): p. 5335-5338.

75. Salem, M., et al., *Perspectives on microbial cell surface display in bioremediation*. Biotechnology Advances, 2008. **26**(2): p. 151-161.
76. Luczkowski, M., et al., *Design of Thiolate Rich Metal Binding Sites within a Peptidic Framework*. Inorganic Chemistry, 2008. **47**(23): p. 10875-10888.
77. Hamza, I., et al., *Interaction of the copper chaperone HAH1 with the Wilson disease protein is essential for copper homeostasis*. Proceedings of the National Academy of Sciences of the United States of America, 1999. **96**(23): p. 13363-13368.
78. Bontidean, I., et al., *Detection of Heavy Metal Ions at Femtomolar Levels Using Protein-Based Biosensors*. Analytical Chemistry, 1998. **70**(19): p. 4162-4169.
79. Bell, C.F, *Introduction - Principals and applications of metal chelation*. Oxford Chemistry Series. 1977: Oxford Press.
80. Bell, C.F., *14 Properties of ligands and chelate rings, in Principles and applications of metal chelation*. 1977, Oxford University Press.
81. Bell, C.F., *Aminopolycarboxylic acids - principals and applications of metal chelation*. Oxford chemistry series. 1977, Oxford: Oxford Press.
82. Basolo, F. and R.C. Johnson, *Coordination Chemistry*. Second ed. 1986, Oxford: Science Reviews.
83. Nakajima, A. and T. Sakaguchi, *Selective accumulation of heavy metals by microorganisms*. Applied Microbiology and Biotechnology, 1986. **24**(1): p. 59.
84. Šmarda, J., et al., *S-layers on cell walls of cyanobacteria*. Micron, 2002. **33**(3): p. 257-277.
85. Beveridge, T.J., et al., *V. Functions of S-layers*. FEMS Microbiology Reviews, 1997. **20**(1–2): p. 99-149.
86. Bahl, H., et al., *IV. Molecular biology of S-layers*. FEMS Microbiology Reviews, 1997. **20**(1–2): p. 47-98.
87. Merroun, M.L., et al., *Complexation of Uranium by Cells and S-Layer Sheets of Bacillus sphaericus JG-A12*. Appl. Environ. Microbiol., 2005. **71**(9): p. 5532-5543.
88. Pollmann, K., et al., *Novel surface layer protein genes in Bacillus sphaericus associated with unusual insertion elements*. Microbiology, 2005. **151**(9): p. 2961-2973.

89. Sanchez, E.F., C.R. Diniz, and M. Richardson, The complete amino acid sequence of the haemorrhagic factor LHFII, a metalloproteinase isolated from the venom of the bushmaster snake (*Lachesis muta muta*). *FEBS Letters*, 1991. **282**(1): p. 178.
90. MacCordick, H., et al., *Interaction of uranyl ions with snake venom proteins from Lachesis muta muta*. *Journal of Radioanalytical and Nuclear Chemistry*, 1997. **223**(1): p. 187.
91. Sánchez, E.F., A. Magalhães, and C.R. Diniz, Purification of a hemorrhagic factor (LHF-I) from the venom of the bushmaster snake, *Lachesis muta muta*. *Toxicon*, 1987. **25**(6): p. 611.
92. Pourbaix, M., *Atlas of electrochemical equilibria in aqueous solution*. 1966, London: Pergamon Press.
93. Billah, M., H.C.W. Hays, and P.A. Millner, Development of a myoglobin impedimetric immunosensor based on mixed self-assembled monolayer onto gold. *Microchimica Acta*, 2008. **160**: p. 447.
94. Hays, H.C.W., P.A. Millner, and M.I. Prodromidis, *Development of capacitance based immunosensors on mixed self-assembled monolayers*. *Sensors and Actuators B: Chemical*, 2006. **114**(2): p. 1064.
95. *Bioconjugate Techniques*. Second ed, ed. G.T. Hermanson. 2008: Hermanson.
96. Gomez-Rodriguez, J.M., *Nanotech, your AFM manufacturer*. Review of scientific instruments, 2007. **78**(013705).
97. Lingane, J.J. and W.D. Larson, *The Standard Electrode Potential of Silver*. *Journal of the American Chemical Society*, 1936. **58**(12): p. 2647-2648.
98. EMBL-EBI, PDBeChEM small molecule database - Dictionary of chemical components (ligands, small molecules and monomers). 2012.
99. Billah, M., H.C.W. Hays, and P.A. Millner, Development of a myoglobin impedimetric immunosensor based on mixed self-assembled monolayer onto gold. *Microchimica Acta*, 2008. **160**(4): p. 447-454.
100. Caygill, R.L., G.E. Blair, and P.A. Millner, *A review on viral biosensors to detect human pathogens*. *Analytica Chimica Acta*, 2010. **681**(1-2): p. 8-15.
101. Bergveld, P., Reference Field Effect Transistors based on Chemically Modified ISFETS. *Analytica Chimica Acta*, 1990. **230**: p. 67-73.

102. Schasfoort, R.B.M.S., G. J., Bergveld, P., and R.P.H.G. Kooyman, J, *Influence of an immunological precipitate on dc and ac behaviour of an ISFET*. Sensors & Actuators 1989. **18**: p. 119-29.
103. Crown compounds Towards future applications, ed. S.R. Cooper. 1992: VCH.
104. Tsukube, H., et al., Ag<sup>+</sup>-Specific Pyridine Podands: Effects of Ligand Geometry and Stereochemically Controlled Substitution on Cation Complexation and Transport Functions. The Journal of Organic Chemistry, 1998. **63**(12): p. 3884-3894.
105. Aziz, S., Chemistry of Pyrones, Part 5: New Crown Ether and Podand Derivatives of 3,5-Bis(bromomethyl)-2,6-diphenyl-4H-pyran-4-one. Molecules, 2001(6): p. 721-727.
106. Lindoy, L.F. and M.I. Atkinson, *Self-Assembly in Supramolecular Systems*, in *Monographs in Supramolecular Chemistry*. 2000, Royal Society of Chemistry. p. 224.
107. Walkowiak, W. and C.A. Kozłowski, Macrocyclic carriers for separation of metal ions in liquid membrane processes--a review. Desalination, 2009. **240**(1-3): p. 186.
108. Steed, J. and Atwood L. Jerry, *Supramolecular Chemistry*. 2000: Wiley. 745.
109. Tamaki, K., et al., *Fabrication of luminescent polymeric nanoparticles doped with a lanthanide complex by self-organization process*. Colloids and Surfaces A: Physicochemical and Engineering Aspects, 2006. **284-285**: p. 355-358.
110. Anderson, C.J. and M.J. Welch, *Radiometal-Labeled Agents (Non-Technetium) for Diagnostic Imaging*. Chemical Reviews, 1999. **99**(9): p. 2219.
111. Wängler, C., et al., Improved syntheses and applicability of different DOTA building blocks for multiply derivatized scaffolds. Bioorganic & Medicinal Chemistry, 2008. **16**(5): p. 2606.
112. Pier Lucio, A., et al., Sulfonamide-Functionalized Gadolinium DTPA Complexes as Possible Contrast Agents for MRI: A Relaxometric Investigation. European Journal of Inorganic Chemistry, 2000. **2000**(4): p. 625-630.
113. De Leon-Rodriguez, L.M., et al., *Magnetic Resonance Imaging Detects a Specific Peptide-Protein Binding Event*. Journal of the American Chemical Society, 2002. **124**(14): p. 3514.

114. Horwitz, E.P., M.L. Dietz, and D.E. Fisher, *SREX: new crown ether for the extraction and recovery of strontium from acidic nuclear waste stream*. Solvent Extraction and Ion Exchange, 1991. **9**(1): p. 1 - 25.
115. Rawat, N., et al., Evaluation of a supported liquid membrane containing a macrocyclic ionophore for selective removal of strontium from nuclear waste solution. Journal of Membrane Science, 2006. **275**(1-2): p. 82-88.
116. McDowell, W.J., Synergistic and solvent effects in the extraction of strontium and sodium by di(2-ethylhexyl) phosphate. Journal of Inorganic and Nuclear Chemistry, 1968. **30**(4): p. 1037-1049.
117. Moyer, B.A., et al., Complexation of strontium in the synergistic extraction system dicyclohexano-18-crown-6, versatic acid, carbon tetrachloride. Solvent Extraction and Ion Exchange, 1986. **4**(1): p. 83 - 93.
118. Moyer, B.A., et al., Further complexation of strontium in cyclohexano-18-crown-6 in organic media. Solvent Extraction and Ion Exchange, 1990. **6**: p. 172-182.
119. Dozol, H., et al., Nitro derivatives of 1,3-calix[4]arene bis-crown-6. Synthesis, structure and complexing properties. Tetrahedron Letters, 2001. **42**(47): p. 8285-8287.
120. Dietz, M.L., Stereochemical effects on the mode of facilitated ion transfer into room-temperature ionic liquids. Green Chemistry, 2007(10): p. 174–176.
121. Eroglu, et al., *Extraction of strontium ions with emulsion liquid membrane technique*. Journal of Membrane Science, 1993. **80**(1): p. 319-325.
122. Abdelghani, A., et al., *Impedance spectroscopy on xerogel layer for chemical sensing*. Materials Science & Engineering C-Biomimetic and Supramolecular Systems, 2006. **26**(2-3): p. 542-545.
123. Yamato, K., et al., Improved stereospecific synthesis of the trans-isomers of dicyclohexano-18-crown-6 and the solid-state structure of the trans-syn-trans-isomer. Tetrahedron Letters, 2002. **43**(12): p. 2153-2156.
124. Pellet-Rostaing, S., et al., *Synthesis and caesium complexing properties of water-soluble cavitands*. Tetrahedron Letters, 1999. **40**(50): p. 8793-8796.
125. Council, N.R., Research needs for high level waste stored in tanks and bins at US department of energy sites. 2001: National Academy Press.

126. Anelli, Pier L., et al., Sulfonamide-Functionalized Gadolinium DTPA Complexes as Possible Contrast Agents for MRI: A Relaxometric Investigation. *European Journal of Inorganic Chemistry*, 2000. **2000**(4): p. 625-630.
127. Warta, A.M., W.A. Arnold, and E.L. Cussler, *Permeable Membranes Containing Crystalline Silicotitanate As Model Barriers for Cesium Ion*. *Environmental Science & Technology*, 2005. **39**(24): p. 9738-9743.
128. Kaminski, M.D., et al., Cesium separation from contaminated milk using magnetic particles containing crystalline silicotitanates. *Separation and Purification Technology*, 2000. **21**(1-2): p. 1-8.
129. Bruggenwert, M.G.M. and A. Kamphorst, Chapter 5: Survey of Experimental Information on Cation Exchange in Soil Systems, in *Developments in Soil Science*, G.H. Bolt, Editor. 1979, Elsevier. p. 141-203.
130. Gaur, S., Determination of Cs-137 in environmental water by ion-exchange chromatography. *Journal of Chromatography A*, 1996. **733**(1-2): p. 57-71.
131. Strelow, F.W.E., Distribution coefficients and ion-exchange selectivities for 46 elements with a macroporous cation-exchange resin in hydrochloric acid-acetone medium. *Talanta*, 1988. **35**(5): p. 385-395.
132. Fanning, J.C., The solubilities of the alkali metal salts and the precipitation of Cs<sup>+</sup> from aqueous solution. *Coordination Chemistry Reviews*, 1995. **140**: p. 27-36.
133. Hsu, C.-I.W. and T.L. White, Development of high-performance liquid chromatographic methods for measuring tetraphenylborate decomposition products in radioactive alkaline solutions. *Journal of Chromatography A*, 1998. **828**(1-2): p. 461-467.
134. Ungaro, R., et al., 1,3-Dialkoxycalix[4]arene crowns-6 in 1,3-Alternate Conformation: Cesium-Selective Ligands that Exploit Cation-Arene Interactions. *Angewandte Chemie International Edition in English*, 1994. **33**(14): p. 1506-1509.
135. Keipert, S.J., C.B. Knobler, and D.J. Cram, Host-guest complexation : 43. Synthesis and binding properties of a macrocycle composed of two phenanthrolines and two sulfonamide units. *Tetrahedron*, 1987. **43**(21): p. 4861-4874.
136. Raut, D.R., et al., Evaluation of polymer inclusion membranes containing calix[4]-bis-2,3-naphtho-crown-6 for Cs recovery from acidic feeds: Transport behaviour, morphology and modeling studies. *Journal of Membrane Science*, (0).

137. Law, J.D., et al., The universal solvent extraction (unex) process using crown ethers. ii. flowsheet - development and demonstration of the unex procrown ethers for separation of crown ethersium, strontium, and actinides from actual acidic radioactive waste. *Solvent Extraction and Ion Exchange*, 2001. **19**(1): p. 23-36.
138. Sahmsipur, M., et al., Competitive cesium-133 NMR spectroscopic study of complexation of different metal ions with dibenzo-21-crown-7 in acetonitrile-dimethylsulfoxide and nitromethane-dimethylsulfoxide mixtures. *Spectrochimica Acta Part A: Molecular and Biomolecular Spectroscopy*, 2008. **69**(4): p. 1265-1270.
139. Olander, D., *Nuclear fuels – Present and future*. *Journal of Nuclear Materials*, 2009. **389**(1): p. 1-22.
140. Ozawa, M., et al., Separation of actinides and fission products in high-level liquid wastes by the improved TRUEX process. *Journal of Alloys and Compounds*, 1998. **271–273**(0): p. 538-543.
141. Dong, S. and Y. Wang, Anodic stripping voltammetric determination of trace lead with a nafion/crown-ether film electrode. *Talanta*, 1988. **35**(10): p. 819-821.
142. Desai, P., R. Kotkar, and A. Srivastava, Electrochemical behaviour of pyridoxine hydrochloride (vitamin B<sub>6</sub>) at carbon paste electrode modified with crown ethers. *Journal of Solid State Electrochemistry*, 2008. **12**(9): p. 1067-1075.
143. Moore, A.J., et al., New Crown Annelated Tetrathiafulvalenes: Synthesis, Electrochemistry, Self-Assembly of Thiol Derivatives, and Metal Cation Recognition. *The Journal of Organic Chemistry*, 2000. **65**(24): p. 8269-8276.
144. Cavalleri, O., et al., Self-assembled monolayers of organosulphur molecules bearing calix[4]arene moieties. *Bioelectrochemistry*, 2004. **63**(1-2): p. 3-7.
145. Gokel, G.W., et al., Steroidal lariat ethers: a new class of macrocycles and the crystal structure of N-(cholesteryloxycarbonyl)aza-15-crown-5. *The Journal of Organic Chemistry*, 1987. **52**(14): p. 2963-2968.
146. Gehin, D., P.A. Kollman, and G. Wipff, *Anchoring of ammonium cations to an 18-crown-6 binding site: molecular mechanics and dynamics study*. *Journal of the American Chemical Society*, 1989. **111**(8): p. 3011-3023.

147. Wagner-Wysiecka, E., E. Luboch, and J.F. Biernat, *Chromoionophores with Chromophores as Integral Part(s) of the Macrocycle in Crown Ethers*. Journal of Inclusion Phenomena and Macrocyclic Chemistry, 2001. **41**(1): p. 19-22.
148. Hayashita, T., et al., *Chromoionophores Based on Crown Ethers and Related Structures for Alkali Metal Ion Sensing in Aqueous Media*. Journal of Inclusion Phenomena and Macrocyclic Chemistry, 1998. **32**(2): p. 251-265.
149. Danks, I.P. and I.O. Sutherland, *Potassium selective chromoionophores*. Journal of Inclusion Phenomena and Macrocyclic Chemistry, 1992. **12**(1): p. 223-236.
150. Nishi, T., et al., *Detection of chirality by colour*. Journal of the Chemical Society, Chemical Communications, 1991(5): p. 339-341.
151. Hollmann, G. and F. Vögtle, *Kationen-Selektivität neuer Chromoionophore mit stark lösungsmittelabhängiger Lichtabsorption. Zur optischen Enantiomeren-Differenzierung mit chiralen Chromoionophoren*. Chemische Berichte, 1984. **117**(4): p. 1355-1363.
152. Shinkai, S., et al., *Crown-metal interactions in cholesteric liquid crystals*. Journal of the Chemical Society, Chemical Communications, 1990(4): p. 303-304.
153. Ariga, K., *Supramolecular Chemistry - Fundamentals and applications*. 2006: p. 208.
154. Constable, E.C., *Coordination Chemistry of Macrocyclic Compounds*. Oxford Chemistry primers. Vol. 72. 1999: Oxford Science Publications.
155. Walden, P., *Bull. Acad. Imper. Sci*, 1914: p. 1800.
156. Turner, M.B., et al., *Production of Bioactive Cellulose Films Reconstituted from Ionic Liquids*. Biomacromolecules, 2004. **5**(4): p. 1379-1384.
157. Zhao, F., et al., *Electrochemical and Bioelectrochemistry Properties of Room-Temperature Ionic Liquids and Carbon Composite Materials*. Analytical Chemistry, 2004. **76**(17): p. 4960-4967.
158. Fukushima, T., et al., *Molecular Ordering of Organic Molten Salts Triggered by Single-Walled Carbon Nanotubes*. Science, 2003. **300**(5628): p. 2072-2074.
159. Franzoi, A.C., et al., *Development of biosensors containing laccase and imidazolium bis(trifluoromethylsulfonyl)imide ionic liquid for the determination of rutin*. Analytica Chimica Acta, 2009. **639**(1-2): p. 90-95.

160. Maleki, N., A. Safavi, and F. Tajabadi, *High-Performance Carbon Composite Electrode Based on an Ionic Liquid as a Binder*. Analytical Chemistry, 2006. **78**(11): p. 3820-3826.
161. Shiddiky, M.J.A. and A.A.J. Torriero, *Application of ionic liquids in electrochemical sensing systems*. Biosensors and Bioelectronics, 2011. **26**(5): p. 1775-1787.
162. Sun, N., et al., Ferrocene Peapod Modified Electrodes: Preparation, Characterization, and Mediation of H<sub>2</sub>O<sub>2</sub>. Analytical Chemistry, 2006. **78**(17): p. 6050-6057.
163. Ding, C., et al., An electrochemical biosensor for  $\alpha$ -fetoprotein based on carbon paste electrode constructed of room temperature ionic liquid and gold nanoparticles. Talanta, 2009. **78**(3): p. 1148-1154.
164. Chen, P.-Y. and C.L. Hussey, Electrodeposition of cesium at mercury electrodes in the tri-1-butylmethylammonium bis((trifluoromethyl)sulfonyl)imide room-temperature ionic liquid. Electrochimica Acta, 2004. **49**(28): p. 5125-5138.
165. Chen, P.-Y. and C.L. Hussey, Electrochemistry of ionophore-coordinated Cs and Sr ions in the tri-1-butylmethylammonium bis((trifluoromethyl)sulfonyl)imide ionic liquid. Electrochimica Acta, 2005. **50**(12): p. 2533-2540.
166. Chen, P.-Y., The assessment of removing strontium and cesium cations from aqueous solutions based on the combined methods of ionic liquid extraction and electrodeposition. Electrochimica Acta, 2007. **52**(17): p. 5484-5492.
167. Parker, D., *Macrocyclic Synthesis A Practical Approach*. Practical approach in chemistry, ed. L.M. Harwood and C.J. Moody. 1996: Oxford University Press.
168. Coldrick, Z., et al., Phospholipid monolayer coated microfabricated electrodes to model the interaction of molecules with biomembranes. Electrochimica Acta, 2009. **54**(22): p. 4954-4962.
169. Chen, P.-Y. and C.L. Hussey, Electrodeposition of cesium at mercury electrodes in the tri-1-butylmethylammonium bis((trifluoromethyl)sulfonyl)imide room-temperature ionic liquid. Electrochimica Acta, 2004. **49**(28): p. 5125.
170. Disley, D.M., et al., Covalent coupling of immunoglobulin G to self-assembled monolayers as a method for immobilizing the interfacial-recognition layer of a surface plasmon resonance immunosensor. Biosensors and Bioelectronics, 1998. **13**(11): p. 1213-1225.
171. Bard, A.J. and R. Parsons, *Standard potentials in aqueous solution*, ed. A.J. Bard. 1985, Oxford: Dekker.

172. Tourwé, E., R. Pintelon, and A. Hubin, Extraction of a quantitative reaction mechanism from linear sweep voltammograms obtained on a rotating disk electrode. Part I: Theory and validation. *Journal of Electroanalytical Chemistry*, 2006. **594**(1): p. 50-58.
173. Chen, P.-Y. and C.L. Hussey, Electrochemistry of ionophore-coordinated Cs and Sr ions in the tri-1-butylmethylammonium bis((trifluoromethyl)sulfonyl)imide ionic liquid. *Electrochimica Acta*, 2005. **50**(12): p. 2533.
174. Chen, P.-Y., The assessment of removing strontium and cesium cations from aqueous solutions based on the combined methods of ionic liquid extraction and electrodeposition. *Electrochimica Acta*, 2007. **52**(17): p. 5484.
175. Nelson, A., *Electrochemical analysis of a phospholipid phase transition*. *Journal of Electroanalytical Chemistry*, 2007. **601**(1-2): p. 83-93.
176. British Standards Institute, (2005) *PAS71 Vocabulary. Nanoparticles*. Publicly Available Specification (PAS) PAS 71:2011 Vocabulary - Nanoparticles,
177. Mondloch, J.E., E. Bayram, and R.G. Finke, *A review of the kinetics and mechanisms of formation of supported-nanoparticle heterogeneous catalysts*. *Journal of Molecular Catalysis A: Chemical*, 2012. **355**(0): p. 1-38.
178. Silar catalogue. 2009.
179. Barton, A.C., et al., Labelless AC impedimetric antibody-based sensors with pg ml<sup>-1</sup> sensitivities for point-of-care biomedical applications. *Biosensors and Bioelectronics*, 2009. **24**(5): p. 1090-1095.
180. Pepe, A., et al., Synthesis of hybrid silica sol-gel coatings containing Zn particles on carbon steel and Al/Zn coated carbon steel. *Materials Letters*, 2005. **59**(29-30): p. 3937-3940.
181. Zhang, Q., et al., Synthesis of poly[2-methoxy-5-(2-ethylhexyloxy)-1,4-phenylenevinylene-silica core-shell particles with a self-templating method and their fluorescent properties. *European Polymer Journal*, 2008. **44**(12): p. 3957-3962.
182. Li, Z.-Z., et al., Fabrication of porous hollow silica nanoparticles and their applications in drug release control. *Journal of Controlled Release*, 2004. **98**(2): p. 245-254.
183. Khani, O., et al., Synthesis and characterizations of ultra-small ZnS and Zn(1-x)FexS quantum dots in aqueous media and spectroscopic study of their interactions with bovine serum

- albumin. *Spectrochimica Acta Part A: Molecular and Biomolecular Spectroscopy*, 2011. **79**(2): p. 361-369.
184. Zhao, B., et al., Size control of monodisperse nonporous silica particles by seed particle growth. *Particuology*, 2011. **9**(3): p. 314-317.
185. Lee, M.H., F.L. Beyer, and E.M. Furst, Synthesis of monodisperse fluorescent core-shell silica particles using a modified Stöber method for imaging individual particles in dense colloidal suspensions. *Journal of Colloid and Interface Science*, 2005. **288**(1): p. 114-123.
186. Stöber, W., A. Fink, and E. Bohn, *Controlled growth of monodisperse silica spheres in the micron size range*. *Journal of Colloid and Interface Science*, 1968. **26**(1): p. 62-69.
187. Kruis, F.E. and R.K. Joshi, Nanoparticle design and handling — challenges for engineers and particle technologists. *China Particuology*, 2005. **3**(1-2): p. 99-104.
188. Srisombat, L., A.C. Jamison, and T.R. Lee, *Stability: A key issue for self-assembled monolayers on gold as thin-film coatings and nanoparticle protectants*. *Colloids and Surfaces A: Physicochemical and Engineering Aspects*, 2011. **390**(1-3): p. 1-19.
189. Roy, D., et al., *On shelf stability of freeze-dried poly(methylidene malonate 2.1.2) nanoparticles*. *International Journal of Pharmaceutics*, 1997. **148**(2): p. 165-175.
190. Abdelwahed, W., G. Degobert, and H. Fessi, A pilot study of freeze drying of poly(epsilon-caprolactone) nanocapsules stabilized by poly(vinyl alcohol): Formulation and process optimization. *International Journal of Pharmaceutics*, 2006. **309**(1-2): p. 178-188.
191. Schwarz, C. and W. Mehnert, *Freeze-drying of drug-free and drug-loaded solid lipid nanoparticles (SLN)*. *International Journal of Pharmaceutics*, 1997. **157**(2): p. 171-179.
192. Socrates, G., *Infrared and Raman characteristic group frequencies*. Third ed. 2001, New York: Wiley.
193. Millner, P.A., Are guanine nucleotide-binding proteins involved in regulation of thylakoid protein kinase activity? *FEBS Letters*, 1987. **226**(1): p. 155-160.
194. Achatz, D.E., et al., Colloidal silica nanoparticles for use in click chemistry-based conjugations and fluorescent affinity assays. *Sensors and Actuators B: Chemical*, 2010. **150**(1): p. 211-219.
195. Reichardt, C., *Solvents and Solvent Effects in Organic Chemistry*. 3 rd ed. 2003: Wiley-VCH Publishers.

196. Wituck, G.L., *A silane primer : chemistry and applications of alkoxy silanes*. Coatings technology, 1993. **65**(822): p. 0361-8773.
197. Lim, A.Y., et al., Doped amorphous silica nanoparticles as enhancing agents for surface-assisted time-of-flight mass spectrometry. *Analyst*, 2011. **136**(13): p. 2775-2785.
198. Hou, S., et al., *Highly Sensitive and Selective Dopamine Biosensor Fabricated with Silanized Graphene*. *The Journal of Physical Chemistry C*, 2010. **114**(35): p. 14915-14921.
199. Tien, P. and L.-K. Chau, Novel Sol–Gel-Derived Material for Separation and Optical Sensing of Metal Ions: Propyl-ethylenediamine Triacetate Functionalized Silica. *Chemistry of Materials*, 1999. **11**(8): p. 2141-2147.
200. Francesca, C. and et al., Enzyme-functionalized polymer brush films on the inner wall of silicon–glass microreactors with tunable biocatalytic activity. *Lab on a Chip*, 2010. **10**(24): p. 3407.
201. Esquena, J., et al., *Preparation of monodisperse silica particles in emulsion media*. *Colloids and Surfaces A: Physicochemical and Engineering Aspects*, 1997. **123-124**: p. 575-586.
202. Bruzzoniti, M.C., et al., *MCM41 functionalized with ethylenediaminetriacetic acid for ion-exchange chromatography*. *Journal of Materials Chemistry*, 2011. **21**(2): p. 369-376.
203. Naka, Y., Y. Komori, and H. Yoshitake, One-pot synthesis of organo-functionalized monodisperse silica particles in W/O microemulsion and the effect of functional groups on addition into polystyrene. *Colloids and Surfaces A: Physicochemical and Engineering Aspects*, 2010. **361**(1-3): p. 162-168.
204. Aldrich, S. (1986) Aldrich FTIR Ramen Transmission database.
205. Scott, A. and J.E. Gray-Munro, The surface chemistry of 3-mercaptopropyltrimethoxysilane films deposited on magnesium alloy AZ91. *Thin Solid Films*, 2009. **517**(24): p. 6809-6816.
206. Ishida, H., C.-h. Chiang, and J.L. Koenig, The structure of aminofunctional silane coupling agents: 1.  $\gamma$ -Aminopropyltriethoxysilane and its analogues. *Polymer*, 1982. **23**(2): p. 251-257.
207. Brito, R., et al., Adsorption of 3-mercaptopropyltrimethoxysilane and 3-aminopropyltrimethoxysilane at platinum electrodes. *Journal of Electroanalytical Chemistry*, 2002. **520**(1–2): p. 47-52.
208. Zhang, N. and B. Hu, Cadmium (II) imprinted 3-mercaptopropyltrimethoxysilane coated stir bar for selective extraction of trace cadmium from environmental water samples followed by

inductively coupled plasma mass spectrometry detection. *Analytica Chimica Acta*, 2012. **723**(0): p. 54-60.

209. Bell, *Principles and applications of metal chelation*. Oxford Chemistry series, ed. P.W. Atkins. 1977, Oxford: Oxford.

210. Reich, H.J., *Organic Chemistry pKa reference database*. 2004, University of Wisconsin-Madison.

211. van Olphen, H., *An introduction to clay colloid chemistry*. Second ed. 1977, Washington: John Wiley and sons.

212. Vakurov, A., R. Brydson, and A. Nelson, *Electrochemical Modeling of the Silica Nanoparticle–Biomembrane Interaction*. *Langmuir*, 2011. **28**(2): p. 1246-1255.

213. Kim, J., J. Wainaina, and J.S. Na, Synthesis of Amphiphilic Silica/Polymer Composite Nanoparticles As Water-dispersible Nano-absorbent for Hydrophobic Pollutants. *Journal of Industrial and Engineering Chemistry*. In Press, Accepted Manuscript.

214. Frances, N. and et al., Novel one-pot synthesis and characterization of bioactive thiol-silicate nanoparticles for biocatalytic and biosensor applications. *Nanotechnology*, 2009. **20**(5): p. 055612.

215. Lahann, J., *Click chemistry for biotechnology and material sciences*. 2009, Sussex: Wiley.

216. Hiemstra, T., J.C.M. De Wit, and W.H. Van Riemsdijk, Multisite proton adsorption modeling at the solid/solution interface of (hydr)oxides: A new approach: II. Application to various important (hydr)oxides. *Journal of Colloid and Interface Science*, 1989. **133**(1): p. 105-117.

217. Hiemstra, T., P. Venema, and W.H.V. Riemsdijk, *Intrinsic Proton Affinity of Reactive Surface Groups of Metal (Hydr)oxides: The Bond Valence Principle*. *Journal of Colloid and Interface Science*, 1996. **184**(2): p. 680-692.

218. S. H. Behrens and D. G. Grier, *The charge on glass and silica surfaces*. *Journal of Chemical Physics*, 2001. **115**: p. 6716-6721.

219. Stevens, B. (2008) *Intelligent materials to revolutionise surgical implants*. Science and Technology research Funding Council, bulletin 5584.

220. Davydov, A., *Molecular Spectroscopy of Oxide Catalyst Surfaces*. 2003: Wiley.

221. Ryczkowski, J., FT-IR study of the adsorption of some complexones and of EDTA alkaline salts into alumina. *Vibrational Spectroscopy*, 2000. **22**(1-2): p. 55-62.
222. Bellamy, L.J., *The Infrared Spectra of Complex Molecules*. 1958, New York.
223. Dragosavac, M.M., R.G. Holdich, and G.T. Vladisavljević, *Continuous Flow Stirred Cell Microfiltration of Ion Exchange Media to Determine Mass Transfer Kinetics and Equilibrium Data*. *Industrial & Engineering Chemistry Research*, 2011. **50**(4): p. 2408-2417.

## **8 Appendix – Publications**

---

## 8.1 Young investigator of the year nomination

### Bioanalysis

July 2011, Vol. 3, No. 13, Pages 1439-1440 , DOI 10.4155/bio.11.139

(doi:10.4155/bio.11.139)

Young Investigator: David JR Conroy

*David JR Conroy & Paul Millner*

Sections:

#### ABSTRACT

##### Supervisor's supporting comments

As a graduate nanotechnologist, MSc bio-nanotechnologist David is one of the new breed of young scientists who only progress if they are prepared to develop a wide skill base and engage in a multiplicity of new techniques and approaches cutting right across the full range of scientific disciplines. David has shown himself to be a creative and lateral thinker who is totally committed to finding (and training in) the techniques he needs to accomplish his aim, which is translational research aimed at producing real world analytical devices that lean heavily on the new opportunities offered by bionanotechnology. The uranyl sensor he developed (now published work) really does show the way to remote environmental monitoring of pollutants. In fact, this makes possible an environmental surveillance approach that has hitherto been impossible except with huge expense and infrastructure. His work is likely to change current practice in a big way and he would be a very worthy recipient of a young investigator award.

**Q What drove you to choose a career in \_\_\_\_\_  
bioanalysis?**

My undergraduate course in nanotechnology here at Leeds University was a multidisciplinary mix of biochemistry, chemistry, physics, electronics and materials. As a result I wanted a research project that was both cutting edge, novel and interdisciplinary allowing me the potential to create a functional biotechnological device with potential for large-scale development rather than research for the sake of research.

**Q Describe the main highlights of your bioanalytical research, & its importance to the bioanalytical community both now & in the future**

A biosensor is the integration of biological recognition elements with electronic components to create a signal transduction mechanism, for example; current, optical or impedametric to create a superior sensing device. Applications are vast, from toxicology, cancer and medical diagnostics to pharmaceuticals and cosmetics.

In my own work I use bionanotechnology to integrate organic or synthetic components including proteins, antibodies or calixarenes onto functionalized surfaces. In this way, highly functionalized and responsive surfaces are coupled to real-time analysis methods with the hopes of creating a bio-/chemo-sensor that has a higher specificity or selectivity to what is currently commercially or practically available for field-active devices. My PhD project primarily for environmental and defense technologies is to detect groundwater contamination from UK nuclear legacy sites that has escaped into the environment. Within 18 months of starting my PhD I have managed to create a completely new, novel functioning prototype for groundwater uranium by tethering purified surface layer proteins from bacteria evolved in radioactive contaminated waste sites. With the current problems in Japan and large-scale groundwater radioactive contamination it is unfortunate that my project was not started a few years ago and is not closer to commercialization. However this shows the significant need for such devices.

**Q Where do you see your career in bioanalysis taking you?**

As bionanotechnology is an emerging field I plan to use my unique skills to establish truly interdisciplinary research laboratories for the integration of a wide range of science and engineering to focus on practical problems. For my future work I see myself potentially looking for a postdoctoral position in either China (if my language skills improve to a conversational level) or in the USA, as these are currently the two leading countries in terms of original research with significant funding in nanotechnology. In the next month I am visiting China on a nanomedicine conference to instigate inter-university research, student exchange between laboratories, and to look at potential postdoctoral routes and take the first steps towards achieving my ideal career. Ideally, this will include a combined laboratory of medics, scientists and engineers focusing on

areas such as drug delivery, medical diagnostics, functionalizing nanoparticles and biosensing.

## Q How do you envisage the field of bioanalysis evolving in the future?

I see the field moving away from the traditional branches of science such as biology, biochemistry, chemistry and the likes. While these will still exist in their own right, more and more disciplines are overlapping; genetics and bioinformatics, and biotechnology and material engineering are current examples. Without the broadening and merging of research minds from structured and traditional ways of thinking, research will stagnate and limit the potential possible. As an example; medics would be consulted to identify the symptoms and markers of illnesses, genetic disorders or disease such as cancer. Biochemists and geneticists would then identify potential disease biomarkers and the antibodies against them. Nanotechnologists will create functionalized nanoparticles in parallel with biotechnologists so the devices are biocompatible. Material scientists will test drug loading, release and delivery of the nanoparticles that have been conjugated with the produced antibodies. In this way, a nanoparticle designed for a specific illness, loaded with an appropriate drug, is functionalized with a desired receptor molecule to be delivered via the patient's bloodstream. Problems will be approached from different perspectives with the same goal, from problem identification and theory to product design and application, leading to testing, scaling and finally production.

## Representative publication

- Conroy DJR, Millner PA, Stewart DI, Pollmann K. Biosensing for the environment and defense: aqueous uranyl detection using bacterial surface layer proteins. *Sensors* 10(5), 4739–4755 (2010).

Financial & competing interests disclosure

*The authors have no relevant affiliations or financial involvement with any organization or entity with a financial interest in or financial conflict with the subject matter or materials discussed in the manuscript. This includes employment, consultancies, honoraria, stock ownership or options, expert testimony, grants or patents received or pending, or royalties.*

*No writing assistance was utilized in the production of this manuscript.*

Affiliations

David JR Conroy

Position PhD researcher (3rd year); PhD Bio- and chemo-sensors for groundwater radionuclides; Research area Bionanotechnology; biosensors and functionalized nanoparticles; Biosensors & Biocatalysis Group, Research Institute of Membrane & Systems Biology, Garstang Building, University of Leeds, Leeds LS2 9JT, UK. [sms4dc@leeds.ac.uk](mailto:sms4dc@leeds.ac.uk)

*Paul Millner*

Professor of Bionanotechnology, IMSB/FBS Garstang Building, University of Leeds, Leeds, LS2 9JT, UK. [p.a.millner@leeds.ac.uk](mailto:p.a.millner@leeds.ac.uk)

## 8.2 Sensors publication

*Sensors* **2010**, *10*, 1-x manuscripts; doi:10.3390/s90x0000x

OPEN ACCESS

**sensors**

ISSN 1424-8220

www.mdpi.com/journal/sensors

Article

### Biosensing for the Environment and Defence: Aqueous Uranyl Detection Using Bacterial Surface Layer Proteins

David J.R. Conroy <sup>1\*</sup>, Paul A. Millner <sup>2</sup>, Douglas I. Stewart <sup>3</sup>, Katrin Pollmann <sup>4</sup>

<sup>1,2</sup> Biosensors and Biocatalysis Group, Institute of Membranes and Systems Biology, University of Leeds, Leeds, LS2 9JT, UK; E-Mail: p.a.millner@leeds.ac.uk (P.A.M.)

<sup>3</sup> School of Civil Engineering, University of Leeds, Leeds LS2 9JT, UK; E-Mail: d.i.stewart@leeds.ac.uk (D.I.S.)

<sup>4</sup> Institute of Radiochemistry, Forschungszentrum Dresden, Rossendorf, Germany; E-Mail: k.pollmann@fzd.de (K.P.)

\* Author to whom correspondence should be addressed; E-Mail: sms4dc@leeds.ac.uk; Tel.: +44-(0)113-3433-162.

Received: 5 March 2010; in revised version: 22 April 2010/Accepted: 27 April 2010/

Published:

---

**Abstract:** The fabrication of novel uranyl ( $\text{UO}_2^{2+}$ ) binding protein based sensors is reported. The new biosensor responds to picomolar levels of aqueous uranyl ions within minutes using *Lysinibacillus sphaericus* JG-A12 S-layer protein tethered to gold electrodes. In comparison to traditional self assembled monolayer based biosensors the porous bioconjugated layer gave greater stability, longer electrode life span and a denser protein layer. Biosensors responded specifically to  $\text{UO}_2^{2+}$  ions and showed minor interference from  $\text{Ni}^{2+}$ ,  $\text{Cs}^+$ ,  $\text{Cd}^{2+}$  and  $\text{Co}^{2+}$ . Chemical modification of JG-A12 protein phosphate and carboxyl groups prevented  $\text{UO}_2^{2+}$  binding, showing that both moieties are involved in the recognition to  $\text{UO}_2^{2+}$ .

**Keywords:** S-layer; surface layer; protein biosensor; uranium; uranyl; metal ion; sequestering; impedance spectroscopy

---

## Introduction

### Toxicology of Uranium

Toxicologically, the uranyl ion is hazardous due to rapid adsorption through the gastrointestinal tract. In the bloodstream most uranyl is carried as soluble bicarbonate while the remainder is bound to plasma proteins. Whilst typically 60% is excreted within 24 h approximately 25 % has been shown to undergo incorporation to bone [224]. Historic experiments in human test participants showed systemic exposure above levels of 0.1 mg/kg body weight results in acute renal tubular damage that can be fatal. There are currently no diagnostic tests available and no proven methods for reducing the chronic effects of uranyl exposure [225] which is why the application of biosensing for early detection of contaminated aqueous systems would be advantageous.

**Comment [MSOffice1]:** The location of the uranyl under discussion is unclear

### Environmental Effects of Uranium

In the UK uranium based hazards arise from fuels, materials and wastes produced from United Kingdom Atomic Energy Authority (UKAEA) and British Nuclear Fuels plc (BNFL) dating back to the 1940s and 1960s as well as Magnox power stations from the 1950s to 1970s. High level radioactive waste is buried with the intention of radioactive decay reducing activity over significant periods of time. Even minor leakage and radionuclide migration through container vessels can result in disastrous environmental ramifications [2]. Sellafield Ltd (previously British Nuclear Fuels) is a U.K nuclear processing site, and one of the few UK sites that publicly discloses information on soil analysis and allows a realistic model of the environmental contamination to be made. By-products from the nuclear fission process are the radionuclides U-238, Tc-99, Sr-90 and Cs-137. Of the five oxidation states of uranium only +4 and +6 are stable for practical considerations. The +6 species forms the water soluble uranyl ( $\text{UO}_2^{2+}$ ) ion and is the most commonly encountered form.

**Comment [MSOffice2]:** I think that Drigg is a low level waste repository site where they wish to construct a deep underground repository. Reprocessing is carried out at the Sellafield site.

### Current Sensing Technologies

Three remediation strategies currently used for ground water remediation; (i) natural attenuation systems use reactive elemental reducing agents that induce abiotic degradation of substances (ii) wetland and mine effluents sorption systems and (iii) permeable reactive barriers (PRB) for ground water remediation that act as large scale sorption or reductive-precipitation barriers that sequester contaminants in situ over extended time scales. Economical and political restrictions often resist implementation of these methods. In such situations as these, the application of biosensing technologies is the most practical solution to continually monitor a target site where a complete remediation strategy is not possible.

Current metal ion detection systems are limited, often with poor specificity and are limited to laboratory analyses. Chemical modification of surfaces to create chelator coatings can work as sorption barriers but they tend to lack specificity for analytes [226]. Alternative mass based systems use microcantilevers that monitor concentration changes of metal ions present as a function of frequency dampening have been developed [64] but lack specificity; if a conformational change in the binding protein occurs as a result of analyte binding [71] monitoring such a mechanism is relatively easy. If binding induces structural changes in a protein then even fM concentrations of the analyte can result in large mass and interface changes that are readily measurable [78]. For example, at a magnitude of size smaller, oligonucleotide sequences generated by PCR can be identified using enzymes and chronocoulometry [227]. The current limitation for these approaches is simply that too few analyte specific binding proteins have been discovered. Similarly enzyme based systems that use metal ions to enhance or inhibit a reaction in a quantifiable analyte specific manner has been shown [228] but are limited in number. Most proteins do not undergo a conformational change on binding and so analyte binding cannot simply be monitored by a change in interface mass.

**Comment [MSOffice3]:** I've tried to join-up this sentence with the previous one, because otherwise it is a non-sequitur.

**Comment [MSOffice4]:** I'm assuming that this sentence is an illustration of the previous sentence (otherwise it needs further clarification)

#### Bacillus Sphaericus S-layer Proteins

While a few bacterial strains have been identified e.g *Pseudomonasstutzeri*, *Neurospora sitophila*, *Streptomycesalbus* and *Streptomyces viridochromogenes* [83] that are tolerant to, and able to sequester uranyl ions, the specific mechanisms and bindings sites are poorly understood. Bacteria regulate their response to specific metals by a number of mechanisms. Membrane pumps use an active potential to translocate ions from the cell by pumping out metal ions from the bacteria and maintain ion concentrations below toxic levels. However, many bacterial species have evolved specific proteins, externally or internally, that that bind and sequester metal ions to minimise uptake [12]. *Bacillus sphaericus* strain JG-A12 has evolved naturally under chronic exposure to uranium mining waste within piles near the town of Johanngeorgenstadt (Saxony, Germany [229]). This strain shows an intrinsic tolerance to the radioactive compound [88]. Compared to similar strains, JG-A12 was reported to bind uranyl ions with higher specificity. Early reports [20] claimed JG-A12 showed specificity only for  $UO_2^{2+}$  making it an ideal metal receptor. However subsequent work [87] monitored the interaction of this strain with 19 heavy metals (Al, Ba, Cd, Co, Cr, Cs, Cu, Fe, Ga, Mn, Ni, Rb, Si, Sn, Sr, Ti, U, and Zn). While failing to bind a number of divalent ions that similar strains could bind, JG-A12 bound Cu, Pb, Al, and Cd to a small extent as well as  $UO_2^{2+}$  [230]. Thus, while not offering complete specificity to uranium it binds to a fewer number of interfering cations than related species and has a significantly higher affinity for  $UO_2^{2+}$ .

**Comment [MSOffice5]:** Make this change unless "resilience" has a very specific and well understood meaning in this context

**Comment [MSOffice6]:** This is an incomplete comparison statement. To complete it, it is necessary to know other strains bind uranium (i.e. is it higher level of uranyl binding or more specific uranyl binding)?

## Electrochemical Biosensors

Electrochemical biosensors typically employ a binding protein of some sort as the recognition element and are of increasing interest due their simplicity of operation and low cost of fabrication. They also show potential for near real-time detection and excellent specificity [231]. Current examples include, but are not limited to, medical diagnostics and serodiagnosis [232] tumour marker analysis [233], early identification of tissue damage [234] and cardiac marker analysis. However, most of these biosensors are designed to quantify larger analytes such as proteins. For much smaller analytes such as metal ions, several classes of proteins exist that chelate, transport or remove them, either as a natural function or to avoid cytotoxicity. Metallothioneins are a recent class of histidine rich metal binding proteins found in the plant *Alnus glutinosa* [66]. Phyto-chelatins are metal chelating peptides important for heavy metal regulation in certain plants, fungi and bacteria containing the binding sequence ( $\gamma$ -Glu-Cys) $_n$ -Gly [66] and some have been found to bind Cu and Zn for storage in both eukaryotes and prokaryotes [65]. A range of bacteria and some eukaryotic algae contain a highly ordered array of surface layer proteins (SLP) or glycoproteins creating a porous outer shell. The biological roles can be specific to the organism but can include cell adhesion, protection from predation, virulence factor, antigenic properties, anchoring sites for exoenzymes or porin function [235], typically the layer lattice is 5–10 nm deep with pores of 2–6 nm diameter. Upon isolation, purification and re-suspension these form ordered 2 dimensional arrays on lipid or solid supports with crystalline arrays of oblique (p1, p2), tetragonal (p4), or hexagonal (p3, p6) symmetry with between 1 and 6 protein subunits [236]. The anchoring mechanisms of these proteins to cells vary, but include interactions with hydrophobic mycolic acid tails, template support layers on the cell surface or orientated nanogrooves for protein assembly and ordering [237].

## Electrochemical Impedance Spectroscopy

Electrochemical impedance spectroscopy (EIS) is a method of interrogating surfaces and interfaces as a function of current dissipation with frequency. Specifically to biosensing, the changes in resistance and capacitance in response to an analyte-interface interaction can be observed. Impedance is the ratio of current change to a incremental applied voltage and has emerged as a powerful technique for monitoring interfacial changes at a solid-liquid or liquid-liquid interface for a number of biosensing mechanisms including membrane-analyte interactions [36], ion channels [238], interfacial capacitance changes [94] and antibody/antigen interactions [93].

Models of EIS idealise an electrode interface as a series of electronic circuit components which are used to model current dissipation with frequency. Models of increasing complexity use resistors and capacitors in series and parallel to represent the resistance and capacitance

changes at an electrode interface due to mass transport phenomena or reaction transfer kinetics of species at the interface. Bulk impedance ( $Z$ ) can be expressed as a complex function represented as the sum of the real  $Z'(\omega)$  and imaginary  $-Z''(\omega)$ . These are the resistance and capacitance components respectively and is typically represented as a Nyquist plot which shows the imaginary  $-Z''$  part on the Y axis and the real  $Z'$  part on the X axis. Interpreting the Nyquist plot using a representative equivalent circuit model shows changes in impedance from interfacial phenomena such as analyte binding as a function of solution resistance, interfacial resistance and layer capacitance [47].

**Comment [MSOffice7]:** I may not have got this sentence completely right, but it certainly needs some changes.

## Results and Discussion

### Surface Preparation

Two alternative protein tethering mechanisms of SLP were performed. However, it is essential a clean uniform base gold layer is prepared for repeatable layer by layer depositions and subsequent biosensor construction. Thus a number of surface cleaning routines were performed. Ozone and chemical etchants, produced the cleanest electrodes compared to surfactant and solvent washes, but caused significant surface damage with repeated use. The effects on surface roughness and area change these methods induced were calculated using the Cottrell equation which relates the current decay of a potential ramped electrode in solution with an electro active species [239]. Up to 2 min in piranha solution (a highly exothermic and corrosive mixture of 7:3 (v/v)  $H_2SO_4$  and  $H_2O_2$ ) yielded clean electrodes with minimal surface damage, whilst 15 min piranha washes created surface roughness factors showing up to a tenfold increase in surface area. As a result, a 2 min piranha wash followed by a rinse with methanol and isopropyl gave the optimal gold layer.

**Comment [MSOffice8]:** I found this paragraph unclear, and am therefore unable to make suggestions. However my recommendation is that you start with a clear and simple statement of a result. The conditional statement "while shown" in the first sentence is confusing

**Comment [MSOffice9]:** Define piranha solution.

### Analysis of Sensor Fabrication

Two methods of tethering the SLP were optimised; a mixed self assembled monolayer (mSAM) was compared to a porous membrane bioconjugation method. Incorporation of surface layer protein (SLP) was optimised using increasing ratios of 16-mercaptohexadecanoic acid (MHDA) to 1,2-dipalmitoyl-sn-glycero-3-phosphoethanolamine-N-(cap biotinyl) (biotin-caproyl-DPPE) in the mSAM. An increased ratio of biotin-caproyl-DPPE showed an increase in the binding sites of the docking protein Neutravidin and thus the binding density of biotinylated SLP. However beyond a 50% (mol/mol) ratio a breakdown of the mSAM was seen and caused the formation of independent stable domains of the mSAM components [94]. A 20% (mol/mol) ratio of biotin-caproyl-DPPE to MHDA) was determined to be the optimal amount for

**Comment [MSOffice10]:** define mSAM

mSAM stability. Successful Neutravidin adsorption onto the mSAM was monitored by quartz crystal microbalance (QCM). System instability occurred upon SLP tethering to a biotin tagged mSAM. The possibility that the S-layer protein was directly inserting into the mSAM was unlikely due to the JG-A12 SLP isoelectric point theoretically calculated as pH 5. At pH 7 both protein and mSAM are negatively charged. Extensive X-ray reflectivity studies on similar SLPs from bacterial strains CCM2177 and E38-66 on DPPE (a cationic lipid that binds to negative protein regions) did show protein adsorption onto the lipid head groups resulting in some intercalation at least up to the phosphate moieties and probably further [240]. It is unlikely that the SLP was disrupting the mSAM and the instability was most likely due to the viscoelastic nature of the linkers introducing dispersion affects. Addition and tethering of biotinylated-SLP could not be achieved reproducibly and thus a bioconjugation approach was chosen for the optimised biosensor.

Comment [MSOffice11]: Define QCM

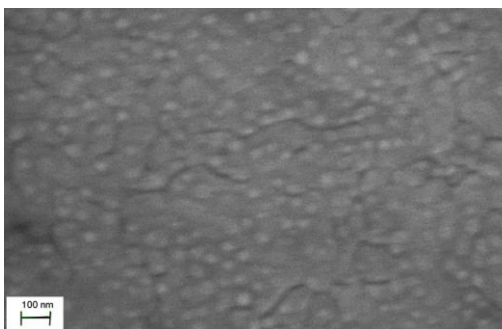
Successful layer by layer deposition of the bioconjugated tethering layer was confirmed by EIS. Nyquist analysis showed that while 4-aminothiophenol (4-ATP) binds within the first hour, stabilisation and ordering of the molecular layer to an ordered SAM occurred beyond 4 hrs, thus a minimum of 4 hrs incubation was required. To covalently attach the cross linker 4-(N-maleimidomethyl)cyclohexane-1-carboxylic acid 3-sulfo-N-hydroxysuccinimide ester (sulfo-SMCC) which reacts with the amine moiety of the 4-ATP SAM coated electrodes, a further incubation in 5 mM sulfo-SMCC PBS pH 7 solution at least 1 h was performed. The free maleimide groups present bound to free cysteine sulfhydryl groups on the SLP creating a covalently tethered protein layer. SEM analysis of the electrode surface after deposition of the SLP (Figure 1A) produced a very uniform image. This is because a dense protein layer was successfully covalently linked to the bioconjugation layer separated by flat regions that acted as boundaries between protein domains. Extended imaging resulted in charging burns that caused permanent damage to the bilayer but confirmed the successfully covalently bonded protein layer. Atomic force microscopy allowed analysis of the sensor surface physical properties. The 4-aminothiophenol layer created a planar layer of linkers separated by their own electrostatic charge from the aromatic ring. These were linked to the linear sulfo-SMCC groups creating a total linker approximately 1.5 nm in length. However rather than acting as a solid anchor to tether the protein the linker sulfo-SMCC appears to have acted as a flexible spring-like linker shown by the lateral and compressive deviation in tip tapping mode analysis. As a result the proteins deviated from the microscope probe resulting in trough formation parallel to the scanning direction. This suggests an almost fluid like interface rather than solid linkers. The total bioconjugated linker layer at preferred orientation extends approximately 1.5 nm from the gold surface. Also, due to the repulsive nature of the probe in regards to the protein's negative charge above its isoelectric point some degree of protein deviation was expected. The soft-fluid interfacial data supports a model in which the surface acts as a porous membrane interface and also explains the need for electrode equilibration with each batch of electrodes which took at least 30 min upon immersion in electrolyte. X-ray photoelectron spectroscopy (XPS) analysis (Figure 1B) demonstrated

successful deposition of each incubation layer and also allowed phosphate and carboxylate modification to be followed. Protein attachment was observed as a significant gold Au 4f to carbon C 1s peak ratio. A significant carbon increase, on average 30.2% carbon C 1s to gold 4f peak ratio increase on chemically modified SLP biosensors, supports the idea that phosphate binding groups were, as intended, successfully modified by acylation, as were carboxylate binding groups by tris(hydroxymethyl)aminomethane modification.

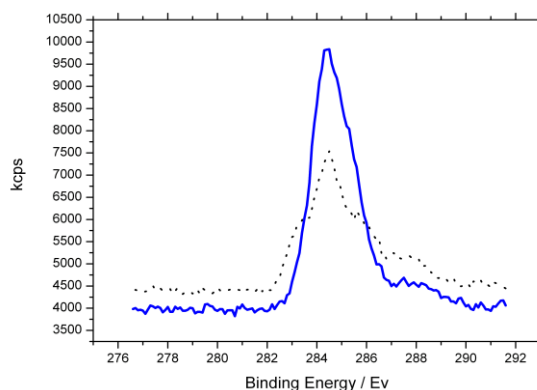
Comment [MSOffice12]: I don't understand this sentence

**Figure 1.** (A) SEM image of organic SLP biosensor layer bound to a gold working electrode. Dense protein layer covalently bound with boundaries between protein domains. (B) XPS analysis of surface composition of top 5nm of bound protein layer before (—) and after (---) chemical modification of phosphate and carboxylate groups. The data show a 30.2% carbon C 1s to gold 4f peak ratio increase confirming successful modification of analyte binding sites.

(A)



(B)



### Binding of $\text{UO}_2^{2+}$ to the SLP Biosensor

Binding of a reversible protein layer under an electric field adds an additional capacitive component [241]. Covalently linking such a layer creates a more stable interrogatable interface. In addition to protein capacitance, the capacitance between electrode and an ion in solution and the electrode is modelled as series of capacitors (equation (1)):

$$\frac{1}{C} = \frac{1}{C_{\text{mod}}} + \frac{1}{C_{\text{dl}}} \quad (2)$$

Where  $C_{\text{mod}}$  is the modifier layer of absorbed species and  $C_{\text{dl}}$  the capacitance of the natural double layer occurring at a liquid-electrode interface as modelled by Gouy Chapman–Stern theory [47]. Simple mSAM based systems can often be modelled by use of a parallel capacitor and resistor in series to a second resistor (the Randles circuit). Comparison of

modified and unmodified layers can be used to show the distribution of defects, pinholes, the effect of linked redox probes and the kinetics and mechanism of the monolayer formation process [242]. However, increasing model complexity by adding increasing components to accurately model organic-metallic interfaces is not usually justified because many of the imperfections of natural surfaces and roughness of electrode substrates [243]. In addition, lateral inhomogeneities between mSAM component molecules means multiple equivalent circuits often fit impedance data without accurately modelling the system [244]. Binding nanomolar levels of atoms to the Stern layer will cause a small disruption to the outer Helmholtz plane of the Guoy-Chapman model. Because these processes occurred on the nanometer scale they are difficult to detect over other dominating processes. Use of buffer concentrations magnitudes greater than the analyte monitored allowed agreement between Gouy–Chapman–Stern (GCS) model and experimental results observed in dilute solutions near the point of zero charge [245], minimising the changes in  $C_{dl}$  in response to analyte addition. Binding of analytes to the absorbed molecular layers thus caused an increase in modified layer capacitance (extending the closest distance of approach of a molecule, increasing the resistive component of the inner Helmholtz Plane (IHP) and a decrease in double layer capacitance due to a compression in the double layer. Equation (2) shows the dominant of these opposing processes will determine if binding causes an increase or decrease in  $C_{dl}$ , the double layer capacitance,  $C_{protein}$ , the additional capacitance component from the protein layer, and  $C_{analyte}$ , the capacitance from addition of a charge species binding at the interface.

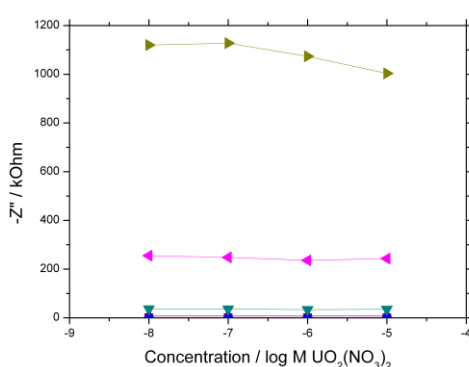
$$\frac{1}{C_{dl}} = \frac{1}{C_{protein}} + \frac{1}{C_{analyte}} \quad (3)$$

Analyte binding caused a disruption in the interfacial double layer by disrupting the hydrated salt layer in the outer Helmholtz plane (OHP). By plotting the Nyquist data as a function of concentration response to different frequencies (Figure 2) a mass transport response is observed at low frequencies.

Figure 2 shows a significant decrease in the imaginary component of impedance at lower frequencies in response to increasing analyte concentration. Poration of the interface between proteins allowed charged analyte to be delivered to and from the interface. Successful binding to the protein layer with increasing analyte concentration increases the charge density across the interface, increasing the layer capacitance and decreasing the imaginary impedance component. As a result more information can be obtained about interface mechanisms at low frequencies as mass transport to the interface is the limiting step compared to the electron transfer kinetics at high frequencies.

**Comment [MSOffice13]:** I didn't understand this sentence. I think there may be some assumed knowledge which it might be better to state explicitly.

**Figure 2.** Dependence of imaginary component of impedance on uranyl ion concentration. The JG-A12 SLP based sensors were exposed to  $\text{UO}_2(\text{NO}_3)_2$  and stirred continuously for 15 mins before a 30 min equilibration period. EIS scans were performed in 10 mM PBS at 0V vs Ag /AgCl at a perturbation of 10 mV. The signals at (■ 10 kHz, ● 1 kHz, ▲ 100 Hz, ▼ 10 Hz, ◆ 1 Hz, ► 0.1 Hz) are shown. 10kHz–100Hz all overlay each other close to zero due to the system exhibiting high resistive and low capacitive behaviour at high frequency.



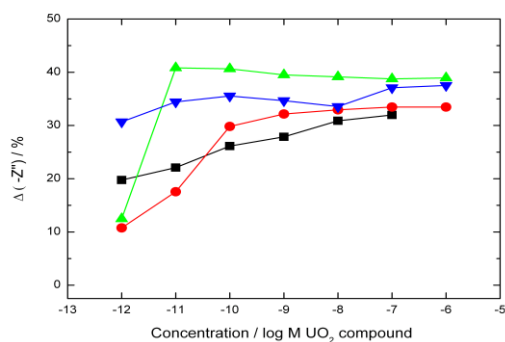
**Comment [MSOffice14]:** My word processor has lost the shape of these symbols, which makes interpretation of B&W printed pages difficult

Data from low frequency scans with a response to a range of  $\text{UO}_2^{2+}$  compounds is shown in (Figure 3A). EIS data for aqueous binding systems is almost always sigmoidal be it antibody, protein or chemo-receptor based systems. This is a logical consequence of the relationship between receptor-ligand complex and ligand concentration in contrast to linear responses that are often observed with amperometric systems in which a direct analyte to product current is generated. The result of analyte binding to the protein layer caused an increasing charge build up at the interface building to saturation. Experimental repeats all lay within an average curve with error bars of  $\pm 2$  standard deviations. Within the centre region  $10^{-11}\text{M}$  to  $10^{-7}\text{M}$ , between biosensor lower limit and saturation point respectively a linear response is observed. The sensor is still functional above and below this range but yields a less accurate response. However, if a sample gives a response outside the linear range it could either be diluted or concentrated to lie within the linear range on the calibration plot.

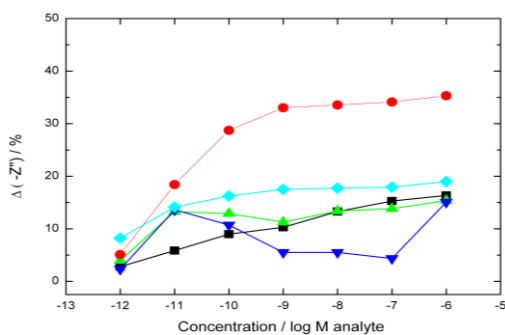
Binding of uranyl ions to the protein layer resulted in a large decrease in the imaginary impedance component, significantly more than other interfering divalent cations (Figure 3B). Significant charge build up at the interface from analyte binding appeared to compress the molecular double layer showing the greater selectivity of the JG-A12 SLP to  $\text{UO}_2^{2+}$  than other analytes (Ni, Cs, Cd, Co on Figure 3B). Analytes for which JG-A12 SLP had a lower affinity caused a smaller decrease in imaginary impedance, typically around 10–20 %. To confirm this apparent selectivity for  $\text{UO}_2^{2+}$  was due to binding by the JG-A12 SLP a number

of controls were performed using alternative protein layers and binding site modification (Figure 4).

**Figure 3.** Real time capacitance response to analytes. Sensors were exposed to increasing concentrations of analyte and stirred continuously for 15 mins before a 30 min equilibration period. EIS scans were performed in 10 mM PBS at 0V vs Ag /AgCl at a perturbation of 10 mV at 0.1 Hz. (A) –Response of biosensor to different uranyl compound response (■ Uranyl nitrate on 6 hr old electrode, ● uranyl nitrate response from a 7 d old electrode, ▲ natural uranyl nitrate response ▼ uranyl acetate response). The data shows no differentiation between uranyl compounds as all are able to bind with the  $\text{UO}_2^{2+}$  in the +6 oxidation state. (B) –Response of biosensor to a range of interfering divalent cations (■ nickel nitrate, ▲ caesium sulphate, ▼ cadmium nitrate, ◆ cobalt chloride, ● average uranyl response).



(A)

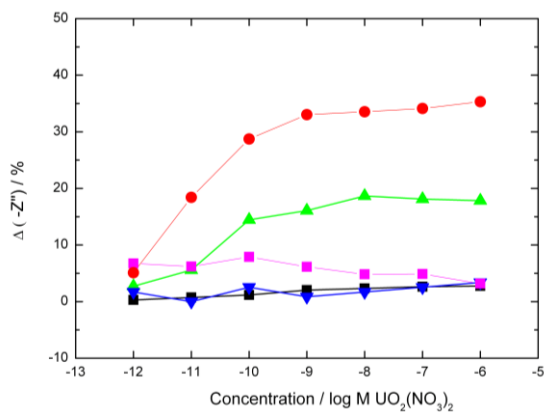


(B)

Sequential uranyl aliquots were added to a bare electrode in buffer in comparison showed a  $-Z''$  response 3 orders of magnitude lower showing that which there is some double layer capacitive component from unbound uranyl ion-gold interaction it is significantly lower than the main signal. The signal stability of a bare electrode in only buffer was monitored over 6 hrs and was stable within 2% of the base signal during this time. Sensors constructed of other proteins that lacked the uranyl binding specificity of JG-A12 SLP showed a lower binding response (Figure 4A). The phosphoprotein casein was used to further elucidate if the sequestering ability of JG-A12 SLP originated via a monodentate mechanism using phosphate groups or a bidentate mechanism involving both phosphate and carboxylate groups. This is because the JG-A12 SLP is similarly a highly phosphorylated protein. Bovine serum albumin (BSA), a relatively stable and inert protein often used to block non specific analyte binding was similarly used as a control. There was virtually no response from the casein sensors which showed that in spite of a high degree of phosphorylation, the protein did not manage to bind a significant amount of uranyl. This supports the idea that the JG-A12 SLP was responsible for the specific  $UO_2^{2+}$  binding. BSA gave an intermediate response due to the non-specific electrostatic binding of  $UO_2^{2+}$  to the proteins negative surface charge. These two alternate protein sensors support the specific binding of JG-A12 SLP to uranyl in a bidentate manner. Figure 4b shows individual and combined functional group blocking on a functioning SLP biosensor. While there is some limited response when only 1 binding site is chemically blocked suggesting some monodentate binding, the complete binding inhibition by blocking both functional groups supports a dominating bidentate mechanism. Experiments also showed that uranyl binding was reversible as would be predicted since the interaction mechanism is non-covalent. Previously uranyl saturated biosensors that had brief buffer washes showed complete removal of uranyl ions which strongly implies rapid on and off rates for the  $UO_2^{2+}$  binding to the SLP.

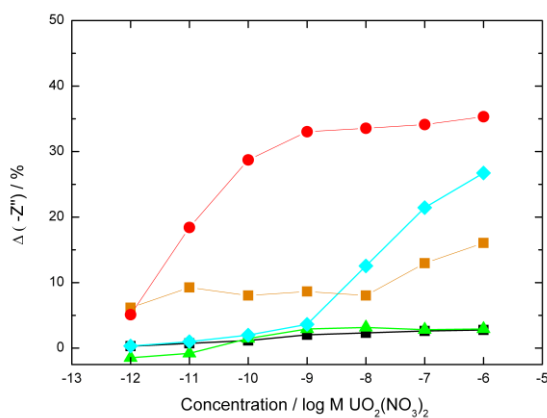
**Comment [MSOffice15]:** This paragraph assumes that the reader has read the figure captions (a poor assumption it is necessary to break off from the text to read captions). Thus you need to explain about the BSA (define BSA) and Casein. Why were these compounds chosen for developing comparison sensors?

**Figure 4.** Effect of using non-specific proteins as the sensing agent. (A) Biosensors were constructed and the response to  $UO_2^{2+}$  monitored (▼ Casein sensor response, ▲ BSA sensor response, ■ BSA sensor response with carboxylates blocked, ● average uranyl response of SLP biosensor for comparison). The percentage decrease in  $-Z''$  was calculated as previously. Sequential analyte injections were performed over a 6 hr period. (■ A control sensor with no analyte added showed only a 2% drift in base signal over the same period). (B) Modified SLP protein response to  $UO_2^{2+}$  (▲ Both carboxylates and phosphates moieties blocked ◆ carboxylates only blocked, ◆ phosphates only blocked, ■ base signal drift over a 6 h period, ● average uranyl response of SLP biosensor for comparison).



(A)

Figure 4. Cont.



(B)

## Materials and Methods

### Chemicals and Reagents

SLP from strain *Lysinibacillus sphaericus* JG-A12 was provided by Dr Katrin Pollmann, Institute of Radiochemistry, Forschungszentrum Dresden - Rossendorf, Germany. Transducers used were design P3 [93] comprising a 1 mm diameter gold working electrode

fabricated on a SiO<sub>2</sub> coated Si wafer over a Ti adhesion layer. These were sourced from the Tyndall institute, Cork. 4-aminothiophenol (4-ATP), 4-(N-maleimidomethyl)cyclohexane-1-carboxylic acid 3-sulfo-N-hydroxysuccinimide ester sodium salt (sulfo-SMCC), 16-mercaptohexadecanoic acid (MHDA) and biotin-N-Hydroxysulfosuccinimide (biotin-NHS) were obtained from Sigma-Aldrich. Biotin-caproyl-DPPE was obtained from Avanti Polar lipids whilst Neutravidin was acquired from Pierce. All other solvents and buffers unless stated obtained from Sigma-Aldrich.

Comment [MSOffice16]: Define NHS

### Electrochemical Setup

EIS was performed on PGSTAT100 FRA and microAutolabIII/FRA2 systems. Experiments were performed with a gold P3 working electrode, an Ag /AgCl reference electrode and a solid platinum counter electrode, in a classic 3 electrode system. Phosphate buffered saline solution at pH 7.0 comprising 140 mM NaCl, 2.7 mM KCl, 0.1 mM Na<sub>2</sub>HPO<sub>4</sub> and 1.8 mM KH<sub>2</sub>PO<sub>4</sub> was used as the supporting electrolyte. A range of cleaning methods was used for preparation of the gold electrodes and then the amperometric response monitored by cyclic voltammetry scans in 5 mM potassium ferricyanide as the redox probe. Cleaning protocols tested were ethanol wash and sonication, 15 min UV irradiation followed by ethanol wash, ozone treatment followed by an ethanol wash, 2 mins in a piranha solution (7:3 v/v sulphuric : hydrogen peroxide), 5 mins in a 7:3 (v/v) piranha solution, 15 mins in a 1:1 piranha solution. Piranha solution, gives an aggressive treatment that erodes metal with excessive use, and thus reduced electrode life span with extended use, but also offers the most powerful organic removal from electrode surfaces. The optimum method (see Results) was 2 min clean in a 7:3 (v/v) piranha solution.

### SLP Tethering Mechanisms

Two alternative tethering mechanisms of the SLP were performed, a schematic representation shown in (Figure 5A), Neutravidin-biotin mSAM tethering and (Figure 5B), the gold bioconjugation method.

### Biotin-Neutravidin mSAM preparation

For mSAM preparation initially a 10 : 1 (M/M) biotin-caproyl-DPPE to MHDA ratio was used. For this 44 µL of 10 mg/ml MHDA in CHCl<sub>3</sub> was added to 10 ml EtOH to form a 0.5 mM/500 µM stock solution. To this 52.5 µL of biotin-caproyl-DPPE was added from a 10 mM stock in CHCl<sub>3</sub> to create a total working concentration of 50 µM biotin-caproyl-DPPE and a 10:1 molar ratio of MHDA : biotin-caproyl-DPPE. Electrodes were incubated overnight

to prepare the mSAM. Biotinylated SLP was bound to a Neutravidin protein layer that was preassembled on a MHDA:DPPE mSAM [94]. In the present work n-hydroxysuccinimide activated carboxy biotin was used to biotinylate the SLP. The protein was dialysed for 24 hrs against PBS to remove interferants. Biotin/S-layer protein ratios tested were 1000, 100 and 10 to 1. A 10 : 1 ratio with a 30 min incubation time was found to be optimal for binding. Bound and unbound complexes purified by a PD-10 Desalting column (Sephadex G-25).

#### mSAM stability measurements at varying MHDA : biotin-caproyl-DPPE

Varying ratios of biotin-caproyl-DPPE : MHDA were prepared in 10 ml ethanol to be absorbed on gold P3 electrodes. The mSAM was interrogated over a frequency range 250 kHz to 0.25 Hz. Fifty data points were measured to monitor self assembly. Readings were taken immediately upon electrode immersion into the component solution to monitor adsorption, assembly or stability as a function of capacitance.

#### Bioconjugation layer preparation

Cleaned electrodes were incubated in 10 mM 4-ATP in ethanol solution for 4 hrs. Hourly Nyquist scans showed that while a significant amount of 4-ATP bound within the first hr, stabilisation and molecular ordering occurred sometime after 4 hrs. To attach sulfo-SMCC the electrodes were then incubated in a 5 mM sulfo-SMCC in PBS pH 7.0 for a minimum of 1 hr. Sulfo-SMCC binds to amine groups of the 4-ATP monolayer; its maleimide groups are then free to bind cysteine thiol groups on the SLP. Once the supporting layer had been prepared, the electrodes were further incubated for a minimum of 1 hr in 1 mg/ml protein and stored in 10 mM PBS at room temperature. Electrodes were interrogated after each deposition step to confirm successful layer deposition.

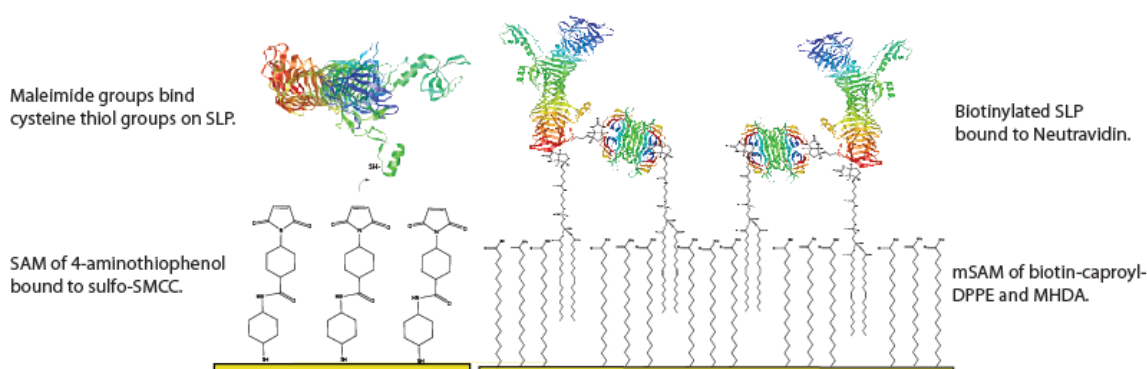
**Figure 5.** Schematic showing the two alternate tethering methods for SLP incorporation on to gold surfaces. (A) mSAM incorporation of SLP by MHDA/biotin-caproyl-DPPE mSAM, deposited with a Neutravidin layer that binds to pre-biotinylated SLP. (B) Porous membrane model with molecular linkers of 1.5 nm length binding SLP through a stable permeable membrane as maleimide groups covalently bind to thiols on protein cysteine residues.

(A)

(B)

### Blocking S-the SLP Chelating Sites

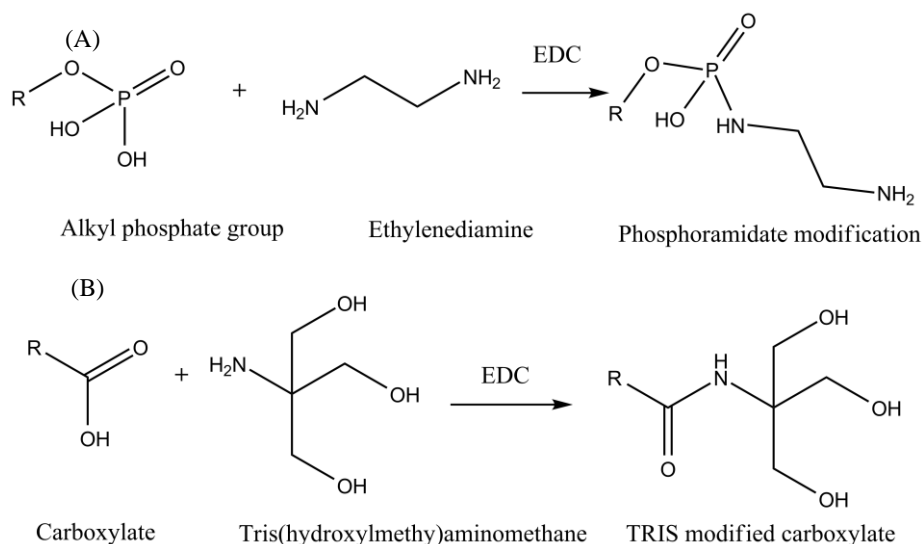
The proposed binding mechanism of uranyl ions to JG-A12 SLP is through carboxyl and phosphate groups in a bidentate manner or via phosphate groups with monodentate



orientation, the mechanism unique to JG-A12 SLP [87]. To confirm the impedance response change was due to the specificity of JG-A12 SLP to uranyl ions these sites were chemically modified (Figure 6). Carboxyl groups were blocked using acylation that created 3 terminal hydroxyls that introduced electrostatic and steric hindrance to analyte cations that attempted to bind. This was achieved by incubating an SLP bound electrode in 0.1 M MES pH 4.7 with 0.1 M TRIS with 10 mg/ml 1-ethyl-3-(3-dimethylaminopropyl) carbodiimide for 4 hrs at room temperature. Phosphate blocking was achieved by phosphoramidate modification which added an amine to phosphate groups. This was performed by incubating at S-layer coated electrode in 5 mM ethylenediamine with 1-ethyl-3-(3-dimethylaminopropyl) carbodiimide under alkaline conditions (pH 7–10).

**Comment [MSOffice17]:** It is unclear whether the proposed binding mechanism involves a bidentate site, a monodentate site, two different sites acting independently (i.e. the sensor would probably have a bilinear response) or the two sites acting together (essentially a tridentate site). This is important, so needs to be clear.

**Figure 6.** Schematic of the protocols used to modify proposed SLP analyte binding carboxylates and phosphates sites. (A) Phosphate modification by carbodiimide reaction in the presence of amine. (B) Modification of carboxylates with TRIS using carbodiimide mediated process.



## Surface and Construction Analysis

Atomic force microscopy was performed using a Nanoscope IV Pico scope force module. Scanning electron microscopy was performed on a Philips XL30 SEM. X-ray photoelectron spectroscopy was performed on a VG Escalab 250 XPS using a 500  $\mu\text{m}$  spot size and 150 W power. QCM analysis was carried out using a Maxtek RQCM instrument using 5 MHz, 1 in. diameter AT cut crystals with Au coated surfaces. Real time deposition studies were obtained by setting up a flow through system using a 100  $\mu\text{L}$  flow chamber and flow speed of 220  $\mu\text{L}$  min.

## Conclusions

It has been shown that by tethering protein layers to metal surfaces via bioconjugation it is possible to create a dense protein layer without denaturing the protein. Coating surfaces with proteins such as the JG-A12 SLP can create bio-functional surfaces; in the present report the SLP coated surface shows high specificity to  $\text{UO}_2^{2+}$  ions. While mSAMs create stable environments for a number of enzymes and proteins, this was not the case for JG-A12 SLP and a more direct bioconjugation procedure proved more effective. Biosensors were shown to

respond to sub-nM levels of aqueous uranyl with this response inhibited by chemical modification of proposed binding sites. The response from surfaces coated with control proteins supported our contention that the binding specificity was conferred by the JG-A12 SLP. Moreover chemical modification of carboxy and phosphate groups on the SLP abrogates uranyl recognition, indicating that the previous suggested binding mechanism [87] was correct. The current biosensor detection limit is  $10^{-12}$ M. While a number of experiments were performed to  $10^{-15}$ M these are currently difficult to reproduce and highly sensitive to system noise. A limit of  $10^{-12}$ M and above has been reproducible across numerous protein and electrode batches. Our approach provides a new means of fabricating metal ion biosensors, and it is possible that SLP isolates from bacteria surviving in other metal polluted sites may provide the sensing components for fabrication of other metal ion biosensors.

#### Acknowledgements

Thanks to Sabine Kutschke of the Institute of Radiochemistry, Forschungszentrum, Dresden, Rossendorf for producing the SLP. AFM analysis was performed with Dr Chris Hodges. XPS analysis performed with the aid of Dr Alex Walton. Valuable advice given by Prof Rik Brydson on surface analysis techniques. This work was funded by the EPSRC through grant number EP/F055412/1, DIAMOND: Decommissioning, Immobilisation And Management Of Nuclear wastes for Disposal.

#### References and Notes

1. McBeth, J., et al., *Technetium Reduction and Reoxidation in Aquifer Sediments*. Geomicrobiology Journal, 2007. **24**: p. 189.
2. Keith-Roach, M.J., *The speciation, stability, solubility and biodegradation of organic co-contaminant radionuclide complexes: A review*. Science of The Total Environment, 2008. **396**(1): p. 1.
3. Nedelcheva, T., et al., *Determination of mobile form contents of Zn, Cd, Pb and Cu in soil extracts by combined stripping voltammetry*. Analytica Chimica Acta, 2005. **528**(2): p. 143.
4. Bath, A., et al., *Geochemical indicators of deep groundwater movements at Sellafield, UK*. Journal of Geochemical Exploration. **90**(1-2): p. 24-44.
5. Wilkins, M.J., et al., *The influence of microbial redox cycling on radionuclide mobility in the subsurface at a low-level radioactive waste storage site*. Geobiology, 2007. **5**: p. 293.
6. Westlakes Scientific, C., *A practicable and integrated groundwater monitoring programme proposed for the sellafield site*. 2005.
7. WHO, *Water Sanitation and Health (WSH) Water for health:WHO Guidelines for Drinking-water Quality (2010)*. 2010, World Health Organisation (WSH).
8. Sellafield, *Groundwater Annual report*. 2010: Seascale.
9. Roehl, R., K.E.; Meggyes, T.; Simon, F.G.; Stewart, D.I.K.E., *Long-term Performance of Permeable Reactive Barriers*. 2005: p. 244.

10. Martinko, J.M., *Brock Biology of Microorganisms*. Eleventh edition ed. 2006: Pearson Prentice Hall.
11. Gherman, V.D., et al., *The Sulphur and Iron Metabolism in Acidophilic Microbial Gelatinous Formations from an Auriferous Sulphides Mine from the South-West of Romania*. *Revista De Chimie*, 2008. **59**(10): p. 1164-1168.
12. Bienert, G.P., M.D. Schuessler, and T.P. Jahn, *Metalloids: essential, beneficial or toxic? Major intrinsic proteins sort it out*. *Trends In Biochemical Sciences*, 2008. **33**(1): p. 20-26.
13. Imkus, R., et al., *Oscillatory luminescence from lux-gene engineered bacteria*. *Biotechnology Techniques*, 1999. **13**: p. 529.
14. Tauriainen, S., et al., *Luminescent bacterial sensor for cadmium and lead*. *Biosensors and Bioelectronics*, 1998. **13**(9): p. 931.
15. Barchiesi, D., N. Lidgi-Guigui, and M.L.d. la Chapelle, *Functionalization layer influence on the sensitivity of surface plasmon resonance (SPR) biosensor*. *Optics Communications*, 2012. **285**(6): p. 1619-1623.
16. Sun, Y., et al., *Preparation of titania sol-gel matrix for the immunoassay by SPR biosensor with magnetic beads*. *Sensors and Actuators B: Chemical*, 2008. **134**(2): p. 566-572.
17. Wang, R., et al., *Regenerative Surface Plasmon Resonance (SPR) biosensor: Real-time measurement of fibrinogen in undiluted human serum using the competitive adsorption of proteins*. *Biosensors and Bioelectronics*, 2011. **28**(1): p. 304-307.
18. Huang, C., et al., *Detection of duck hepatitis virus serotype1 by biosensor based on imaging ellipsometry*. *Current Applied Physics*, 2011. **11**(3): p. 353-357.
19. Liu, L., et al., *Improvement for sensitivity of biosensor with total internal reflection imaging ellipsometry (TIRIE)*. *Thin Solid Films*, 2011. **519**(9): p. 2758-2762.
20. Jin, G., et al., *Development of biosensor based on imaging ellipsometry and biomedical applications*. *Thin Solid Films*, 2011. **519**(9): p. 2750-2757.
21. Dzyadevych, S.V., et al., *Amperometric enzyme biosensors: Past, present and future*. *IRBM*, 2008. **29**(2-3): p. 171-180.
22. Pchelintsev, N.A. and P.A. Millner, *Development of surface activated screen-printed carbon transducers for biosensors application*. *Analytical Letters*, 2007. **40**(7): p. 1317-1332.
23. Clark, L., *Monitor and control of blood and tissue oxygen tensions*. *Trans Am Soc Artif Intern Organs* 1956. **2**: p. 41-8.
24. He, P., et al., *The studies of performance of the Au electrode modified by Zn as the anode electrocatalyst of direct borohydride fuel cell*. *International Journal of Hydrogen Energy*, 2011. **36**(15): p. 8857-8863.
25. Cass, A., *Biosensors. A practical approach. Theoretical methods for analysing biosensor performance* 1990: Oxford University Press.
26. Romero, M.R., F. Garay, and A.M. Baruzzi, *Design and optimization of a lactate amperometric biosensor based on lactate oxidase cross-linked with polymeric matrixes*. *Sensors and Actuators B: Chemical*, 2008. **131**(2): p. 590-595.
27. Hnaïen, M., F. Lagarde, and N. Jaffrezic-Renault, *A rapid and sensitive alcohol oxidase/catalase conductometric biosensor for alcohol determination*. *Talanta*, 2010. **81**(1-2): p. 222-227.
28. Hu, S., et al., *Biosensor for detection of hypoxanthine based on xanthine oxidase immobilized on chemically modified carbon paste electrode*. *Analytica Chimica Acta*, 2000. **412**(1-2): p. 55-61.

29. Guerrieri, A., T.R.I. Cataldi, and R. Ciriello, *The kinetic and analytical behaviours of an l-lysine amperometric biosensor based on lysine oxidase immobilised onto a platinum electrode by co-crosslinking*. Sensors and Actuators B: Chemical, 2007. **126**(2): p. 424-430.
30. Bolton James, R. and D. Archer Mary, *Basic Electron-Transfer Theory*, in *Electron Transfer in Inorganic, Organic, and Biological Systems*. 1991, American Chemical Society. p. 7-23.
31. Yeh P, K., *Reversible electrode reaction of cytochrome c*. Chem Lett: p. 1145-8.
32. Ghindilis, A.L., et al., *Potentiometric biosensors for cholinesterase inhibitor analysis based on mediatorless bioelectrocatalysis*. Biosensors and Bioelectronics, 1996. **11**(9): p. 873-880.
33. Tkac, J., et al., *Membrane-bound dehydrogenases from Gluconobacter sp.: Interfacial electrochemistry and direct bioelectrocatalysis*. Bioelectrochemistry, 2009. **76**(1-2): p. 53-62.
34. Trashin, S.A., et al., *Improvement of direct bioelectrocatalysis by cellobiose dehydrogenase on screen printed graphite electrodes using polyaniline modification*. Bioelectrochemistry, 2009. **76**(1-2): p. 87-92.
35. Wang, H., et al., *A hydrogen peroxide biosensor based on the bioelectrocatalysis of hemoglobin incorporated in a kieselgubr film*. Sensors and Actuators B: Chemical, 2002. **84**(2-3): p. 214-218.
36. Nelson, A., N. Auffret, and J. Borlakoglu, *Interaction of hydrophobic organic compounds with mercury adsorbed dioleoylphosphatidylcholine monolayers*. Biochimica et Biophysica Acta (BBA) - Biomembranes, 1990. **1021**(2): p. 205.
37. Miller, I.R., *The effect of interactions in the head groups on monolayer structure and permeability* I.R. Miller, *Bioelectrochemistry and Bioenergetics*. Bioelectrochemistry and Bioenergetics, 1988. **19**: p. 551-567.
38. Nelson, N.A., *Interaction of hydrophobic organic compounds with mercury adsorbed dioleoylphosphatidylcholine monolayers* Biophysica Acta, 1990. **1021**: p. 205-216
39. Nelson, A. and N. Auffret, *PHOSPHOLIPID MONOLAYERS OF DI-OLEOYL LECITHIN AT THE MERCURY/WATER INTERFACE* A. NELSON and N. AUFFRET. J. Electroanal. Chem. **244**: p. 99-113.
40. Nelson, A., *Conducting Gramicidin Channel Activity in Phospholipid Monolayers*. Biophysical Journal, 2001. **80**: p. 2694-2703.
41. Conroy, P.J., et al., *Antibody production, design and use for biosensor-based applications*. Seminars in Cell & Developmental Biology, 2009. **20**(1): p. 10-26.
42. Mosiello, L., et al., *Development of a monoclonal antibody based potentiometric biosensor for terbuthylazine detection*. Sensors and Actuators B: Chemical, 2003. **95**(1-3): p. 315-320.
43. Ercole, C., et al., *A biosensor for Escherichia coli based on a potentiometric alternating biosensing (PAB) transducer*. Sensors and Actuators B: Chemical, 2002. **83**(1-3): p. 48-52.
44. Sergeyeva, T.A., et al.,  *$\beta$ -Lactamase label-based potentiometric biosensor for  $\alpha$ -2 interferon detection*. Analytica Chimica Acta, 1999. **390**(1-3): p. 73-81.
45. Bard, A.J. and F. L.R., *Electrochemical methods Fundamentals and applications*. Second ed. 2001: Wiley.
46. Bockris, J.O.M. and S.U.M. Khan, *Surface Electrochemistry - A Molecular Level Approach*. 1993, Newyork and London: Plenum.
47. Bard, A.J. and L.R. Faulkner, *Electrochemical Methods Fundamentals and Applications*. Second ed. 2001: Wiley. 833.

48. Israelachvili, J., *Intermolecular and surface forces*. Second ed. 1991: Academic Press.
49. Esteban, M., et al., *Voltammetry of metal ion--macromolecule interactions: Application to speciation problems*. TrAC Trends in Analytical Chemistry, 1993. **12**(7): p. 276.
50. Chapman, C.S. and C.M.G. van den Berg, *Anodic stripping voltammetry using a vibrating electrode*. Electroanalysis, 2007. **19**(13): p. 1347-1355.
51. Castillo, J., et al., *Biosensors for life quality: Design, development and applications*. Sensors and Actuators B: Chemical, 2004. **102**(2): p. 179.
52. Marks, R.S. and D. Cullen, *Handbook of Biosensors and Biochips*. **1**: p. 686.
53. Salaun, P., B. Planer-Friedrich, and C.M.G. van den Berg, *Inorganic arsenic speciation in water and seawater by anodic stripping voltammetry with a gold microelectrode*. Analytica Chimica Acta, 2007. **585**(2): p. 312-322.
54. Salaun, P. and C.M.G. van den Berg, *Voltammetric detection of mercury and copper in seawater using a gold microwire electrode*. Analytical Chemistry, 2006. **78**(14): p. 5052-5060.
55. Locatelli, C. and G. Torsi, *Simultaneous square wave anodic stripping voltammetric determination of Cr, Pb, Sn, Sb, Cu, Zn in presence of reciprocal interference: application to meal matrices*. Microchemical Journal, 2004. **78**(2): p. 175-180.
56. Men, H., et al., *Novel All-State Heavy Metal Sensors and Analysis Instrument*. 2008 Chinese Control And Decision Conference, Vols 1-11, 2008: p. 1801-1805.
57. Van Den Berg, C.M.G. and Z. Qiang Huang, *Determination of uranium(VI) in sea water by cathodic stripping voltammetry of complexes with catechol*. Analytica Chimica Acta, 1984. **164**: p. 209.
58. Kefala, G., A. Economou, and A. Voulgaropoulos, *Adsorptive stripping voltammetric determination of trace uranium with a bismuth-film electrode based on the U(VI) -> U(V) reduction step of the uranium-cupferron complex*. Electroanalysis, 2006. **18**(3): p. 223-230.
59. Monk, P., Wiley *Fundamentals of Electro analytical Chemistry*. 2001: p. 185.
60. Marta C. Diaz, B.M.I.N.M.J.F.S.M.A.C.J.J.-B.G.S.D.M.G., *Supramolecular Pseudo-Rotaxane Type Complexes from pi-Extended TTF Dimer Crown Ether and C<SUB><FONT SIZE='1'>60</FONT></SUB>*. ChemInform, 2006. **37**(18).
61. Arena, G., et al., *Two Calix-Crown Based Stationary Phases. Synthesis, Chromatographic Performance and X-ray Photoelectron Spectroscopy Investigation*. Journal of Supramolecular Chemistry, 2002. **2**(6): p. 521.
62. Woods, M., Z. Kovacs, and A.D. Sherry, *Targeted Complexes of Lanthanide(III) Ions as Therapeutic and Diagnostic Pharmaceuticals*. Journal of Supramolecular Chemistry, 2002. **2**(1-3): p. 1.
63. Ueda, M. and A. Tanaka, *Genetic immobilization of proteins on the yeast cell surface*. Biotechnology Advances, 2000. **18**(2): p. 121.
64. Cherian, S., et al., *Detection of heavy metal ions using protein-functionalized microcantilever sensors*. Biosensors & Bioelectronics, 2003. **19**(5): p. 411-416.
65. Guimarães-Soares, L., et al., *Metal-binding proteins and peptides in the aquatic fungi Fontanospora fusiformis and Flagellospora curta exposed to severe metal stress*. Science of The Total Environment, 2006. **372**(1): p. 148.
66. Gupta, R.K., et al., *Metallothioneins: A new class of plant metal-binding proteins*. Journal Of Protein Chemistry, 2002. **21**(8): p. 529-536.
67. Lee, M.H., S.B. Mulrooney, and R.P. Hausinger, *Purification, characterization, and in vivo reconstitution of Klebsiella aerogenes urease apoenzyme*. J. Bacteriol., 1990. **172**(8): p. 4427-4431.

68. Kim, J.K., S.B. Mulrooney, and R.P. Hausinger, *The UreEF fusion protein provides a soluble and functional form of the UreF urease accessory protein*. Journal Of Bacteriology, 2006. **188**(24): p. 8413-8420.
69. Busenlehner, L.S., et al., *Elucidation of Primary ([alpha]3N) and Vestigial ([alpha]5) Heavy Metal-binding Sites in Staphylococcus aureus pI258 CadC: Evolutionary Implications for Metal Ion Selectivity of ArsR/SmtB Metal Sensor Proteins*. Journal of Molecular Biology, 2002. **319**(3): p. 685.
70. Branco, R., A.P. Chung, and P.V. Morais, *Sequencing and expression of two arsenic resistance operons with different functions in the highly arsenic-resistant strain Ochrobactrum tritici SCII24(T)*. BMC Microbiology, 2008. **8**.
71. Li, S., et al., *Evidence for cooperativity between the four binding sites of dimeric ArsD, an As(III)-responsive transcriptional regulator*. Journal Of Biological Chemistry, 2002. **277**(29): p. 25992-26002.
72. Lin, Y.F., A.R. Walmsley, and B.P. Rosen, *An arsenic metallochaperone for an arsenic detoxification pump*. Proceedings Of The National Academy Of Sciences Of The United States Of America, 2006. **103**(42): p. 15617-15622.
73. Kotrba, P., et al., *Enhanced Bioaccumulation of Heavy Metal Ions by Bacterial Cells Due to Surface Display of Short Metal Binding Peptides*. Appl. Environ. Microbiol., 1999. **65**(3): p. 1092-1098.
74. Bae, W., et al., *Genetic Engineering of Escherichia coli for Enhanced Uptake and Bioaccumulation of Mercury*. Appl. Environ. Microbiol., 2001. **67**(11): p. 5335-5338.
75. Salem, M., et al., *Perspectives on microbial cell surface display in bioremediation*. Biotechnology Advances, 2008. **26**(2): p. 151-161.
76. Luczkowski, M., et al., *Design of Thiolate Rich Metal Binding Sites within a Peptidic Framework*. Inorganic Chemistry, 2008. **47**(23): p. 10875-10888.
77. Hamza, I., et al., *Interaction of the copper chaperone HAH1 with the Wilson disease protein is essential for copper homeostasis*. Proceedings of the National Academy of Sciences of the United States of America, 1999. **96**(23): p. 13363-13368.
78. Bontidean, I., et al., *Detection of Heavy Metal Ions at Femtomolar Levels Using Protein-Based Biosensors*. Analytical Chemistry, 1998. **70**(19): p. 4162-4169.
79. Bell, C.F., *Introduction - Principals and applications of metal chelation*. Oxford Chemistry Series. 1977: Oxford Press.
80. Bell, C.F., *14 Properties of ligands and chelate rings*, in *Principles and applications of metal chelation*. 1977, Oxford University Press.
81. Bell, C.F., *Aminopolycarboxylic acids - principals and applications of metal chelation*. Oxford chemistry series. 1977, Oxford: Oxford Press.
82. Basolo, F. and R.C. Johnson, *Coordination Chemistry*. Second ed. 1986, Oxford: Science Reviews.
83. Nakajima, A. and T. Sakaguchi, *Selective accumulation of heavy metals by microorganisms*. Applied Microbiology and Biotechnology, 1986. **24**(1): p. 59.
84. Šmarda, J., et al., *S-layers on cell walls of cyanobacteria*. Micron, 2002. **33**(3): p. 257-277.
85. Beveridge, T.J., et al., *V. Functions of S-layers*. FEMS Microbiology Reviews, 1997. **20**(1-2): p. 99-149.
86. Bahl, H., et al., *IV. Molecular biology of S-layers*. FEMS Microbiology Reviews, 1997. **20**(1-2): p. 47-98.
87. Merroun, M.L., et al., *Complexation of Uranium by Cells and S-Layer Sheets of Bacillus sphaericus JG-A12*. Appl. Environ. Microbiol., 2005. **71**(9): p. 5532-5543.

88. Pollmann, K., et al., *Novel surface layer protein genes in Bacillus sphaericus associated with unusual insertion elements*. Microbiology, 2005. **151**(9): p. 2961-2973.
89. Sanchez, E.F., C.R. Diniz, and M. Richardson, *The complete amino acid sequence of the haemorrhagic factor LHFII, a metalloproteinase isolated from the venom of the bushmaster snake (Lachesis muta muta)*. FEBS Letters, 1991. **282**(1): p. 178.
90. MacCordick, H., et al., *Interaction of uranyl ions with snake venom proteins from Lachesis muta muta*. Journal of Radioanalytical and Nuclear Chemistry, 1997. **223**(1): p. 187.
91. Sánchez, E.F., A. Magalhães, and C.R. Diniz, *Purification of a hemorrhagic factor (LHF-I) from the venom of the bushmaster snake, Lachesis muta muta*. Toxicon, 1987. **25**(6): p. 611.
92. Pourbaix, M., *Atlas of electrochemical equilibria in aqueous solution*. 1966, London: Pergamon Press.
93. Billah, M., H.C.W. Hays, and P.A. Millner, *Development of a myoglobin impedimetric immunosensor based on mixed self-assembled monolayer onto gold*. Microchimica Acta, 2008. **160**: p. 447.
94. Hays, H.C.W., P.A. Millner, and M.I. Prodromidis, *Development of capacitance based immunosensors on mixed self-assembled monolayers*. Sensors and Actuators B: Chemical, 2006. **114**(2): p. 1064.
95. *Bioconjugate Techniques*. Second ed, ed. G.T. Hermanson. 2008: Hermanson.
96. Gomez-Rodriguez, J.M., *Nanotech, your AFM manufacturer*. Review of scientific instruments, 2007. **78**(013705).
97. Lingane, J.J. and W.D. Larson, *The Standard Electrode Potential of Silver*. Journal of the American Chemical Society, 1936. **58**(12): p. 2647-2648.
98. EMBL-EBI, *PDBeChEM small molecule database - Dictionary of chemical components (ligands, small molecules and monomers)*. 2012.
99. Billah, M., H.C.W. Hays, and P.A. Millner, *Development of a myoglobin impedimetric immunosensor based on mixed self-assembled monolayer onto gold*. Microchimica Acta, 2008. **160**(4): p. 447-454.
100. Caygill, R.L., G.E. Blair, and P.A. Millner, *A review on viral biosensors to detect human pathogens*. Analytica Chimica Acta, 2010. **681**(1-2): p. 8-15.
101. Bergveld, P., *Reference Field Effect Transistors based on Chemically Modified ISFETS*. Analytica Chimica Acta, 1990. **230**: p. 67-73.
102. Schasfoort, R.B.M.S., G. J., Bergveld, P., and R.P.H.G. Kooyman, J., *Influence of an immunological precipitate on dc and ac behaviour of an ISFET*. Sensors & Actuators 1989. **18**: p. 119-29.
103. *Crown compounds Towards future applications*, ed. S.R. Cooper. 1992: VCH.
104. Tsukube, H., et al., *Ag<sup>+</sup>-Specific Pyridine Podands: Effects of Ligand Geometry and Stereochemically Controlled Substitution on Cation Complexation and Transport Functions*. The Journal of Organic Chemistry, 1998. **63**(12): p. 3884-3894.
105. Aziz, S., *Chemistry of Pyrones, Part 5: New Crown Ether and Podand Derivatives of 3,5-Bis(bromomethyl)-2,6-diphenyl-4H-pyran-4-one*. Molecules, 2001(6): p. 721-727.
106. Lindoy, L.F. and M.I. Atkinson, *Self-Assembly in Supramolecular Systems*, in *Monographs in Supramolecular Chemistry*. 2000, Royal Society of Chemistry. p. 224.
107. Walkowiak, W. and C.A. Kozłowski, *Macrocyclic carriers for separation of metal ions in liquid membrane processes--a review*. Desalination, 2009. **240**(1-3): p. 186.
108. Steed, J. and Atwood L. Jerry, *Supramolecular Chemistry*. 2000: Wiley. 745.

109. Tamaki, K., et al., *Fabrication of luminescent polymeric nanoparticles doped with a lanthanide complex by self-organization process*. Colloids and Surfaces A: Physicochemical and Engineering Aspects, 2006. **284-285**: p. 355-358.
110. Anderson, C.J. and M.J. Welch, *Radiometal-Labeled Agents (Non-Techneium) for Diagnostic Imaging*. Chemical Reviews, 1999. **99**(9): p. 2219.
111. Wängler, C., et al., *Improved syntheses and applicability of different DOTA building blocks for multiply derivatized scaffolds*. Bioorganic & Medicinal Chemistry, 2008. **16**(5): p. 2606.
112. Pier Lucio, A., et al., *Sulfonamide-Functionalized Gadolinium DTPA Complexes as Possible Contrast Agents for MRI: A Relaxometric Investigation*. European Journal of Inorganic Chemistry, 2000. **2000**(4): p. 625-630.
113. De Leon-Rodriguez, L.M., et al., *Magnetic Resonance Imaging Detects a Specific Peptide-Protein Binding Event*. Journal of the American Chemical Society, 2002. **124**(14): p. 3514.
114. Horwitz, E.P., M.L. Dietz, and D.E. Fisher, *SREX: A NEWPROCESS FOR THE EXTRACTION AND RECOVERY OF STRONTIUM FROM ACIDIC NUCLEAR WASTE STREAMS*. Solvent Extraction and Ion Exchange, 1991. **9**(1): p. 1 - 25.
115. Rawat, N., et al., *Evaluation of a supported liquid membrane containing a macrocyclic ionophore for selective removal of strontium from nuclear waste solution*. Journal of Membrane Science, 2006. **275**(1-2): p. 82-88.
116. McDowell, W.J., *Synergistic and solvent effects in the extraction of strontium and sodium by di(2-ethylhexyl) phosphate*. Journal of Inorganic and Nuclear Chemistry, 1968. **30**(4): p. 1037-1049.
117. Moyer, B.A., et al., *COMPLEXATION OF STRONTIUM IN THE SYNERGISTIC EXTRACTION SYSTEM DICYCLOHEXANO-18-CROWN-6, VERSATIC ACID, CARBON TETRACHLORIDE*. Solvent Extraction and Ion Exchange, 1986. **4**(1): p. 83 - 93.
118. Moyer, B.A., et al., *COMPLEXATION OF STRONTIUM IN THE SYNERGISTIC EXTRACTION SYSTEM DICYCLOHEXANO-18-CROWN-6, VERSATIC ACID, CARBON TETRACHLORIDE*. Solvent Extraction and Ion Exchange, 1986. **4**(1): p. 83-93.
119. Dozol, H., et al., *Nitro derivatives of 1,3-calix[4]arene bis-crown-6. Synthesis, structure and complexing properties*. Tetrahedron Letters, 2001. **42**(47): p. 8285-8287.
120. Dietz, M.L., et al., *Stereochemical effects on the mode of facilitated ion transfer into room-temperature ionic liquids*. Green Chemistry, 2007(10): p. 174-176.
121. Erog, et al., *Extraction of strontium ions with emulsion liquid membrane technique*. Journal of Membrane Science, 1993. **80**(1): p. 319-325.
122. Abdelghani, A., et al., *Impedance spectroscopy on xerogel layer for chemical sensing*. Materials Science & Engineering C-Biomimetic and Supramolecular Systems, 2006. **26**(2-3): p. 542-545.
123. Yamato, K., et al., *Improved stereospecific synthesis of the trans-isomers of dicyclohexano-18-crown-6 and the solid-state structure of the trans-syn-trans-isomer*. Tetrahedron Letters, 2002. **43**(12): p. 2153-2156.
124. Pellet-Rostaing, S., et al., *Synthesis and caesium complexing properties of water-soluble cavitands*. Tetrahedron Letters, 1999. **40**(50): p. 8793-8796.
125. Council, N.R., *Research needs for high level waste stored in tanks and bins at US department of energy sites*. 2001: National Academy Press.

126. Anelli, Pier L., et al., *Sulfonamide-Functionalized Gadolinium DTPA Complexes as Possible Contrast Agents for MRI: A Relaxometric Investigation*. European Journal of Inorganic Chemistry, 2000. **2000**(4): p. 625-630.
127. Warta, A.M., W.A. Arnold, and E.L. Cussler, *Permeable Membranes Containing Crystalline Silicotitanate As Model Barriers for Cesium Ion*. Environmental Science & Technology, 2005. **39**(24): p. 9738-9743.
128. Kaminski, M.D., et al., *Cesium separation from contaminated milk using magnetic particles containing crystalline silicotitanates*. Separation and Purification Technology, 2000. **21**(1-2): p. 1-8.
129. Bruggenwert, M.G.M. and A. Kamphorst, *Chapter 5: Survey of Experimental Information on Cation Exchange in Soil Systems*, in *Developments in Soil Science*, G.H. Bolt, Editor. 1979, Elsevier. p. 141-203.
130. Gaur, S., *Determination of Cs-137 in environmental water by ion-exchange chromatography*. Journal of Chromatography A, 1996. **733**(1-2): p. 57-71.
131. Strelow, F.W.E., *Distribution coefficients and ion-exchange selectivities for 46 elements with a macroporous cation-exchange resin in hydrochloric acid-acetone medium*. Talanta, 1988. **35**(5): p. 385-395.
132. Fanning, J.C., *The solubilities of the alkali metal salts and the precipitation of Cs+ from aqueous solution*. Coordination Chemistry Reviews, 1995. **140**: p. 27-36.
133. Hsu, C.-I.W. and T.L. White, *Development of high-performance liquid chromatographic methods for measuring tetraphenylborate decomposition products in radioactive alkaline solutions*. Journal of Chromatography A, 1998. **828**(1-2): p. 461-467.
134. Ungaro, R., et al., *1,3-Dialkoxycalix[4]arene-crowns-6 in 1,3-Alternate Conformation: Cesium-Selective Ligands that Exploit Cation-Arene Interactions*. Angewandte Chemie International Edition in English, 1994. **33**(14): p. 1506-1509.
135. Keipert, S.J., C.B. Knobler, and D.J. Cram, *Host-guest complexation : 43. Synthesis and binding properties of a macrocycle composed of two phenanthrolines and two sulfonamide units*. Tetrahedron, 1987. **43**(21): p. 4861-4874.
136. Raut, D.R., et al., *Evaluation of polymer inclusion membranes containing calix[4]-bis-2,3-naphtho-crown-6 for Cs recovery from acidic feeds: Transport behaviour, morphology and modeling studies*. Journal of Membrane Science, (0).
137. Law, J.D., et al., *THE UNIVERSAL SOLVENT EXTRACTION (UNEX) PROCESS. II. FLOWSHEET DEVELOPMENT AND DEMONSTRATION OF THE UNEX PROCESS FOR THE SEPARATION OF CESIUM, STRONTIUM, AND ACTINIDES FROM ACTUAL ACIDIC RADIOACTIVE WASTE*. Solvent Extraction and Ion Exchange, 2001. **19**(1): p. 23-36.
138. Sahmsipur, M., et al., *Competitive cesium-133 NMR spectroscopic study of complexation of different metal ions with dibenzo-21-crown-7 in acetonitrile-dimethylsulfoxide and nitromethane-dimethylsulfoxide mixtures*. Spectrochimica Acta Part A: Molecular and Biomolecular Spectroscopy, 2008. **69**(4): p. 1265-1270.
139. Olander, D., *Nuclear fuels – Present and future*. Journal of Nuclear Materials, 2009. **389**(1): p. 1-22.
140. Ozawa, M., et al., *Separation of actinides and fission products in high-level liquid wastes by the improved TRUEX process*. Journal of Alloys and Compounds, 1998. **271–273**(0): p. 538-543.
141. Dong, S. and Y. Wang, *Anodic stripping voltammetric determination of trace lead with a nafion/crown-ether film electrode*. Talanta, 1988. **35**(10): p. 819-821.

142. Desai, P., R. Kotkar, and A. Srivastava, *Electrochemical behaviour of pyridoxine hydrochloride (vitamin B<sub>6</sub>) at carbon paste electrode modified with crown ethers*. Journal of Solid State Electrochemistry, 2008. **12**(9): p. 1067-1075.
143. Moore, A.J., et al., *New Crown Annelated Tetrathiafulvalenes: Synthesis, Electrochemistry, Self-Assembly of Thiol Derivatives, and Metal Cation Recognition*. The Journal of Organic Chemistry, 2000. **65**(24): p. 8269-8276.
144. Cavalleri, O., et al., *Self-assembled monolayers of organosulphur molecules bearing calix[4]arene moieties*. Bioelectrochemistry, 2004. **63**(1-2): p. 3-7.
145. Gokel, G.W., et al., *Steroidal lariat ethers: a new class of macrocycles and the crystal structure of N-(cholesteryloxycarbonyl)aza-15-crown-5*. The Journal of Organic Chemistry, 1987. **52**(14): p. 2963-2968.
146. Gehin, D., P.A. Kollman, and G. Wipff, *Anchoring of ammonium cations to an 18-crown-6 binding site: molecular mechanics and dynamics study*. Journal of the American Chemical Society, 1989. **111**(8): p. 3011-3023.
147. Wagner-Wysiecka, E., E. Luboch, and J.F. Biernat, *Chromoionophores with Chromophores as Integral Part(s) of the Macrocycle in Crown Ethers*. Journal of Inclusion Phenomena and Macrocyclic Chemistry, 2001. **41**(1): p. 19-22.
148. Hayashita, T., et al., *Chromoionophores Based on Crown Ethers and Related Structures for Alkali Metal Ion Sensing in Aqueous Media*. Journal of Inclusion Phenomena and Macrocyclic Chemistry, 1998. **32**(2): p. 251-265.
149. Danks, I.P. and I.O. Sutherland, *Potassium selective chromoionophores*. Journal of Inclusion Phenomena and Macrocyclic Chemistry, 1992. **12**(1): p. 223-236.
150. Nishi, T., et al., *Detection of chirality by colour*. Journal of the Chemical Society, Chemical Communications, 1991(5): p. 339-341.
151. Hollmann, G. and F. Vögtle, *Kationen-Selektivität neuer Chromoionophore mit stark lösungsmittelabhängiger Lichtabsorption. Zur optischen Enantiomeren-Differenzierung mit chiralen Chromoionophoren*. Chemische Berichte, 1984. **117**(4): p. 1355-1363.
152. Shinkai, S., et al., *Crown-metal interactions in cholesteric liquid crystals*. Journal of the Chemical Society, Chemical Communications, 1990(4): p. 303-304.
153. Ariga, K., *Supramolecular Chemistry - Fundamentals and applications*. 2006: p. 208.
154. Constable, E.C., *Coordination Chemistry of Macrocyclic Compounds*. Oxford Chemistry primers. Vol. 72. 1999: Oxford Science Publications.
155. Walden, P., Bull. Acad. Imper. Sci, 1914: p. 1800.
156. Turner, M.B., et al., *Production of Bioactive Cellulose Films Reconstituted from Ionic Liquids*. Biomacromolecules, 2004. **5**(4): p. 1379-1384.
157. Zhao, F., et al., *Electrochemical and Bioelectrochemistry Properties of Room-Temperature Ionic Liquids and Carbon Composite Materials*. Analytical Chemistry, 2004. **76**(17): p. 4960-4967.
158. Fukushima, T., et al., *Molecular Ordering of Organic Molten Salts Triggered by Single-Walled Carbon Nanotubes*. Science, 2003. **300**(5628): p. 2072-2074.
159. Franzoi, A.C., et al., *Development of biosensors containing laccase and imidazolium bis(trifluoromethylsulfonyl)imide ionic liquid for the determination of rutin*. Analytica Chimica Acta, 2009. **639**(1-2): p. 90-95.
160. Maleki, N., A. Safavi, and F. Tajabadi, *High-Performance Carbon Composite Electrode Based on an Ionic Liquid as a Binder*. Analytical Chemistry, 2006. **78**(11): p. 3820-3826.

161. Shiddiky, M.J.A. and A.A.J. Torriero, *Application of ionic liquids in electrochemical sensing systems*. *Biosensors and Bioelectronics*, 2011. **26**(5): p. 1775-1787.
162. Sun, N., et al., *Ferrocene Peapod Modified Electrodes: Preparation, Characterization, and Mediation of H<sub>2</sub>O<sub>2</sub>*. *Analytical Chemistry*, 2006. **78**(17): p. 6050-6057.
163. Ding, C., et al., *An electrochemical biosensor for  $\alpha$ -fetoprotein based on carbon paste electrode constructed of room temperature ionic liquid and gold nanoparticles*. *Talanta*, 2009. **78**(3): p. 1148-1154.
164. Chen, P.-Y. and C.L. Hussey, *Electrodeposition of cesium at mercury electrodes in the tri-1-butylmethylammonium bis((trifluoromethyl)sulfonyl)imide room-temperature ionic liquid*. *Electrochimica Acta*, 2004. **49**(28): p. 5125-5138.
165. Chen, P.-Y. and C.L. Hussey, *Electrochemistry of ionophore-coordinated Cs and Sr ions in the tri-1-butylmethylammonium bis((trifluoromethyl)sulfonyl)imide ionic liquid*. *Electrochimica Acta*, 2005. **50**(12): p. 2533-2540.
166. Chen, P.-Y., *The assessment of removing strontium and cesium cations from aqueous solutions based on the combined methods of ionic liquid extraction and electrodeposition*. *Electrochimica Acta*, 2007. **52**(17): p. 5484-5492.
167. Parker, D., *Macrocyclic Synthesis A Practical Approach*. Practical approach in chemistry, ed. L.M. Harwood and C.J. Moody. 1996: Oxford University Press.
168. Coldrick, Z., et al., *Phospholipid monolayer coated microfabricated electrodes to model the interaction of molecules with biomembranes*. *Electrochimica Acta*, 2009. **54**(22): p. 4954-4962.
169. Chen, P.-Y. and C.L. Hussey, *Electrodeposition of cesium at mercury electrodes in the tri-1-butylmethylammonium bis((trifluoromethyl)sulfonyl)imide room-temperature ionic liquid*. *Electrochimica Acta*, 2004. **49**(28): p. 5125.
170. Disley, D.M., et al., *Covalent coupling of immunoglobulin G to self-assembled monolayers as a method for immobilizing the interfacial-recognition layer of a surface plasmon resonance immunosensor*. *Biosensors and Bioelectronics*, 1998. **13**(11): p. 1213-1225.
171. Bard, A.J. and R. Parsons, *Standard potentials in aqueous solution*, ed. A.J. Bard. 1985, Oxford: Dekker.
172. Tourwé, E., R. Pintelon, and A. Hubin, *Extraction of a quantitative reaction mechanism from linear sweep voltammograms obtained on a rotating disk electrode. Part I: Theory and validation*. *Journal of Electroanalytical Chemistry*, 2006. **594**(1): p. 50-58.
173. Chen, P.-Y. and C.L. Hussey, *Electrochemistry of ionophore-coordinated Cs and Sr ions in the tri-1-butylmethylammonium bis((trifluoromethyl)sulfonyl)imide ionic liquid*. *Electrochimica Acta*, 2005. **50**(12): p. 2533.
174. Chen, P.-Y., *The assessment of removing strontium and cesium cations from aqueous solutions based on the combined methods of ionic liquid extraction and electrodeposition*. *Electrochimica Acta*, 2007. **52**(17): p. 5484.
175. Nelson, A., *Electrochemical analysis of a phospholipid phase transition*. *Journal of Electroanalytical Chemistry*, 2007. **601**(1-2): p. 83-93.
176. British Standards Institution and U.D.o.T.a.I.D.i.c.w.t.B.S.I. (BSI) (2005) *PAS71 Vocabulary. Nanoparticles*. Publicly Available Specification (PAS) **PA 71**.
177. Mondloch, J.E., E. Bayram, and R.G. Finke, *A review of the kinetics and mechanisms of formation of supported-nanoparticle heterogeneous catalysts*. *Journal of Molecular Catalysis A: Chemical*, 2012. **355**(0): p. 1-38.
178. *Silar catalogue*. 2009.

179. Barton, A.C., et al., *Labelless AC impedimetric antibody-based sensors with pg ml<sup>-1</sup> sensitivities for point-of-care biomedical applications*. *Biosensors and Bioelectronics*, 2009. **24**(5): p. 1090-1095.
180. Pepe, A., et al., *Synthesis of hybrid silica sol-gel coatings containing Zn particles on carbon steel and Al/Zn coated carbon steel*. *Materials Letters*, 2005. **59**(29-30): p. 3937-3940.
181. Zhang, Q., et al., *Synthesis of poly[2-methoxy-5-(2-ethylhexyloxy)-1,4-phenylenevinylene-silica core-shell particles with a self-templating method and their fluorescent properties*. *European Polymer Journal*, 2008. **44**(12): p. 3957-3962.
182. Li, Z.-Z., et al., *Fabrication of porous hollow silica nanoparticles and their applications in drug release control*. *Journal of Controlled Release*, 2004. **98**(2): p. 245-254.
183. Khani, O., et al., *Synthesis and characterizations of ultra-small ZnS and Zn(1-x)FexS quantum dots in aqueous media and spectroscopic study of their interactions with bovine serum albumin*. *Spectrochimica Acta Part A: Molecular and Biomolecular Spectroscopy*, 2011. **79**(2): p. 361-369.
184. Zhao, B., et al., *Size control of monodisperse nonporous silica particles by seed particle growth*. *Particuology*, 2011. **9**(3): p. 314-317.
185. Lee, M.H., F.L. Beyer, and E.M. Furst, *Synthesis of monodisperse fluorescent core-shell silica particles using a modified Stöber method for imaging individual particles in dense colloidal suspensions*. *Journal of Colloid and Interface Science*, 2005. **288**(1): p. 114-123.
186. Stöber, W., A. Fink, and E. Bohn, *Controlled growth of monodisperse silica spheres in the micron size range*. *Journal of Colloid and Interface Science*, 1968. **26**(1): p. 62-69.
187. Kruis, F.E. and R.K. Joshi, *Nanoparticle design and handling — challenges for engineers and particle technologists*. *China Particuology*, 2005. **3**(1-2): p. 99-104.
188. Srisombat, L., A.C. Jamison, and T.R. Lee, *Stability: A key issue for self-assembled monolayers on gold as thin-film coatings and nanoparticle protectants*. *Colloids and Surfaces A: Physicochemical and Engineering Aspects*, 2011. **390**(1-3): p. 1-19.
189. Roy, D., et al., *On shelf stability of freeze-dried poly(methylidene malonate 2.1.2) nanoparticles*. *International Journal of Pharmaceutics*, 1997. **148**(2): p. 165-175.
190. Abdelwahed, W., G. Degobert, and H. Fessi, *A pilot study of freeze drying of poly(epsilon-caprolactone) nanocapsules stabilized by poly(vinyl alcohol): Formulation and process optimization*. *International Journal of Pharmaceutics*, 2006. **309**(1-2): p. 178-188.
191. Schwarz, C. and W. Mehnert, *Freeze-drying of drug-free and drug-loaded solid lipid nanoparticles (SLN)*. *International Journal of Pharmaceutics*, 1997. **157**(2): p. 171-179.
192. Socrates, G., *Infrared and Raman characteristic group frequencies*. Third ed. 2001, New York: Wiley.
193. Millner, P.A., *Are guanine nucleotide-binding proteins involved in regulation of thylakoid protein kinase activity?* *FEBS Letters*, 1987. **226**(1): p. 155-160.
194. Achatz, D.E., et al., *Colloidal silica nanoparticles for use in click chemistry-based conjugations and fluorescent affinity assays*. *Sensors and Actuators B: Chemical*, 2010. **150**(1): p. 211-219.
195. Reichardt, C., *Solvents and Solvent Effects in Organic Chemistry*. 3 rd ed. 2003: Wiley-VCH Publishers.
196. WITUCKI, G.L., *A silane primer : chemistry and applications of alkoxy silanes*. *Coatings technology*, 1993. **65**(822): p. 0361-8773.

197. Lim, A.Y., et al., *Doped amorphous silica nanoparticles as enhancing agents for surface-assisted time-of-flight mass spectrometry*. *Analyst*, 2011. **136**(13): p. 2775-2785.
198. Hou, S., et al., *Highly Sensitive and Selective Dopamine Biosensor Fabricated with Silanized Graphene*. *The Journal of Physical Chemistry C*, 2010. **114**(35): p. 14915-14921.
199. Tien, P. and L.-K. Chau, *Novel Sol–Gel-Derived Material for Separation and Optical Sensing of Metal Ions: Propyl-ethylenediamine Triacetate Functionalized Silica*. *Chemistry of Materials*, 1999. **11**(8): p. 2141-2147.
200. Francesca, C. and et al., *Enzyme-functionalized polymer brush films on the inner wall of silicon–glass microreactors with tunable biocatalytic activity*. *Lab on a Chip*, 2010. **10**(24): p. 3407.
201. Esquena, J., et al., *Preparation of monodisperse silica particles in emulsion media*. *Colloids and Surfaces A: Physicochemical and Engineering Aspects*, 1997. **123-124**: p. 575-586.
202. Bruzzoniti, M.C., et al., *MCM41 functionalized with ethylenediaminetriacetic acid for ion-exchange chromatography*. *Journal of Materials Chemistry*, 2011. **21**(2): p. 369-376.
203. Naka, Y., Y. Komori, and H. Yoshitake, *One-pot synthesis of organo-functionalized monodisperse silica particles in W/O microemulsion and the effect of functional groups on addition into polystyrene*. *Colloids and Surfaces A: Physicochemical and Engineering Aspects*, 2010. **361**(1-3): p. 162-168.
204. Aldrich, S. (1986) *Aldrich FTIR Ramen Transmission database*.
205. Scott, A. and J.E. Gray-Munro, *The surface chemistry of 3-mercaptopropyltrimethoxysilane films deposited on magnesium alloy AZ91*. *Thin Solid Films*, 2009. **517**(24): p. 6809-6816.
206. Ishida, H., C.-h. Chiang, and J.L. Koenig, *The structure of aminofunctional silane coupling agents: 1.  $\gamma$ -Aminopropyltriethoxysilane and its analogues*. *Polymer*, 1982. **23**(2): p. 251-257.
207. Brito, R., et al., *Adsorption of 3-mercaptopropyltrimethoxysilane and 3-aminopropyltrimethoxysilane at platinum electrodes*. *Journal of Electroanalytical Chemistry*, 2002. **520**(1–2): p. 47-52.
208. Zhang, N. and B. Hu, *Cadmium (II) imprinted 3-mercaptopropyltrimethoxysilane coated stir bar for selective extraction of trace cadmium from environmental water samples followed by inductively coupled plasma mass spectrometry detection*. *Analytica Chimica Acta*, 2012. **723**(0): p. 54-60.
209. Bell, *Principles and applications of metal chelation*. Oxford Chemistry series, ed. P.W. Atkins. 1977, Oxford: Oxford.
210. Reich, H.J., *Organic Chemistry pKa reference database*. 2004, University of Wisconsin-Madison.
211. van Olphen, H., *An introduction to clay colloid chemistry*. Second ed. 1977, Washington: John Wiley and sons.
212. Vakurov, A., R. Brydson, and A. Nelson, *Electrochemical Modeling of the Silica Nanoparticle–Biomembrane Interaction*. *Langmuir*, 2011. **28**(2): p. 1246-1255.
213. Kim, J., J. Wainaina, and J.S. Na, *Synthesis of Amphiphilic Silica/Polymer Composite Nanoparticles As Water-dispersible Nano-absorbent for Hydrophobic Pollutants*. *Journal of Industrial and Engineering Chemistry*. **In Press, Accepted Manuscript**.

214. Frances, N. and et al., *Novel one-pot synthesis and characterization of bioactive thiol-silicate nanoparticles for biocatalytic and biosensor applications*. Nanotechnology, 2009. **20**(5): p. 055612.
215. Lahann, J., *Click chemistry for biotechnology and material sciences*. 2009, Sussex: Wiley.
216. Hiemstra, T., J.C.M. De Wit, and W.H. Van Riemsdijk, *Multisite proton adsorption modeling at the solid/solution interface of (hydr)oxides: A new approach: II. Application to various important (hydr)oxides*. Journal of Colloid and Interface Science, 1989. **133**(1): p. 105-117.
217. Hiemstra, T., P. Venema, and W.H.V. Riemsdijk, *Intrinsic Proton Affinity of Reactive Surface Groups of Metal (Hydr)oxides: The Bond Valence Principle*. Journal of Colloid and Interface Science, 1996. **184**(2): p. 680-692.
218. S. H. Behrens and D. G. Grier, *The charge on glass and silica surfaces*. Journal of Chemical Physics, 2001. **115**: p. 6716-6721.
219. Stevens, B. ((2008)) *Intelligent materials to revolutionise surgical implants*. STFC **2008**, 5584.
220. Davydov, A., *Molecular Spectroscopy of Oxide Catalyst Surfaces*. 2003: Wiley.
221. Ryczkowski, J., *FT-IR study of the adsorption of some complexones and of EDTA alkaline salts into alumina*. Vibrational Spectroscopy, 2000. **22**(1-2): p. 55-62.
222. Bellamy, L.J., *The Infrared Spectra of Complex Molecules*. 1958, New York.
223. Dragosavac, M.M., R.G. Holdich, and G.T. Vladislavljević, *Continuous Flow Stirred Cell Microfiltration of Ion Exchange Media to Determine Mass Transfer Kinetics and Equilibrium Data*. Industrial & Engineering Chemistry Research, 2011. **50**(4): p. 2408-2417.
224. Klaassen, C.D., *Casarett and Doull's toxicology* Seventh ed, ed. C.D. Klaassen. 2008: McGraw-Hill. 1275.
225. Dart, R.C., *Medical Toxicology*. Third ed, ed. R.C. Dart. 2004: Williams & Wilkins.
226. Shervedani, R.K., A. Farahbakhsh, and M. Bagherzadeh, *Functionalization of gold cysteamine self-assembled monolayer with ethylenediaminetetraacetic acid as a novel nanosensor*. Analytica Chimica Acta, 2007. **587**(2): p. 254.
227. Lucarelli, F., G. Marrazza, and M. Mascini, *Enzyme-based impedimetric detection of PCR products using oligonucleotide-modified screen-printed gold electrodes*. Biosensors and Bioelectronics, 2005. **20**(10): p. 2001.
228. Yang, Y. and S.B. Khoo, *Fabrication of self-assembled monolayer of 8-mercaptoquinoline on polycrystalline gold electrode and its selective catalysis for the reduction of metal ions and the oxidation of biomolecules*. Sensors and Actuators B: Chemical, 2004. **97**(2-3): p. 221.
229. Pollmann, K., et al., *Metal binding by bacteria from uranium mining waste piles and its technological applications*. Biotechnology Advances. **24**(1): p. 58.
230. Sonja, S.-P., et al., *Selective accumulation of heavy metals by three indigenous Bacillus strains, B. cereus, B. megaterium and B. sphaericus, from drain waters of a uranium waste pile*. FEMS Microbiology Ecology, 1999. **29**(1): p. 59-67.
231. Hu, S., Q. Lu, and Y. Xu, *Biosensors based on direct electron transfer of protein*, in *Electrochemical Sensors, Biosensors and their Biomedical Applications*. 2008, Academic Press: San Diego. p. 531.
232. Jiang, L., et al., *Development of a fluorescent and colorimetric detection methods-based protein microarray for serodiagnosis of TORCH infections*. Biosensors and Bioelectronics, 2008. **24**(3): p. 376.

233. Chen, H., et al., *Protein chips and nanomaterials for application in tumor marker immunoassays*. Biosensors and Bioelectronics, 2009. **24**(12): p. 3399.
234. Chan, C.P.Y., et al., *Rapid analysis of fatty acid-binding proteins with immunosensors and immunotests for early monitoring of tissue injury*. Biosensors and Bioelectronics, 2005. **20**(12): p. 2566.
235. Terrance, J.B., et al., *V. Functions of S-layers*. FEMS Microbiology Reviews, 1997. **20**(1-2): p. 99-149.
236. Debabov, V.G., *Bacterial and archaeal S-layers as a subject of nanobiotechnology*. Molecular Biology, 2004. **38**(4): p. 482-493.
237. Dupres, V.e.a., *In Vivo Imaging of S-Layer Nanoarrays on Corynebacterium glutamicum*. Langmuir letter, 2009. **25**(17): p. 9653-9655.
238. Whitehouse, C., et al., *Interaction of Gramicidin Derivatives with Phospholipid Monolayers*. Langmuir, 2004. **20**(21): p. 9291-9298.
239. Wang, J., *Analytical Electrochemistry*. Third Edition ed. 2006: Wiley-VCH. 250.
240. Weygand, M., et al., *Bacterial S-Layer Protein Coupling to Lipids: X-Ray Reflectivity and Grazing Incidence Diffraction Studies*. 1999. **76**(1): p. 458.
241. Bergveld, P., *A critical evaluation of direct electrical protein detection method*. Biosensors and Bioelectronics, 1991. **6**(1): p. 55-72.
242. Campuzano, S., et al., *Characterization of alkanethiol-self-assembled monolayers-modified gold electrodes by electrochemical impedance spectroscopy*. Journal of Electroanalytical Chemistry, 2006. **586**(1): p. 112.
243. Fawcett, W.R., et al., *Application of the ac admittance technique to double-layer studies on polycrystalline gold electrodes*. Journal of Electroanalytical Chemistry, 1992. **326**(1-2): p. 91.
244. Breyer, B. and H.H. Bauer, *Electrochemical cells as electrical circuit elements*. Journal of Electroanalytical Chemistry. **12**(5-6): p. 411.
245. Rivera-Gandía, J. and C.R. Cabrera, *Self-assembled monolayers of 6-mercapto-1-hexanol and mercapto-n-hexyl-poly(dT)18-fluorescein on polycrystalline gold surfaces: An electrochemical impedance spectroscopy study*. Journal of Electroanalytical Chemistry, 2007. **605**(2): p. 145.

© 2010 by the authors; licensee MDPI, Basel, Switzerland. This article is an open-access article distributed under the terms and conditions of the Creative Commons Attribution license (<http://creativecommons.org/licenses/by/3.0/>).